UNIVERSITY OF SOUTHAMPTON

Faculty of Engineering and the Environment
Institute of Sound and Vibration

Numerical investigation of a supercritical aerofoil with wavy leading edges in transonic flows

by

Enrico Degregori

A thesis for the degree of
Doctor of Philosophy

January 2023

University of Southampton

Abstract

Faculty of Engineering and the Environment
Institute of Sound and Vibration

Doctor of Philosophy

Numerical investigation of a supercritical aerofoil with wavy leading edges in transonic flows

by Enrico Degregori

High fidelity numerical simulations are conducted to investigate wavy leading edges (WLEs) in transonic flows. In particular the focus is on the mitigation of shock buffet and its radiated noise. The main objective of this work is to give a comprehensive overview of the aerodynamic and aeroacoustic performance of this passive technique previously studied only in subsonic flows. Due to the novelty of this study, a preliminary analysis is conducted slowly varying the incidence angles. This gives information about the aerodynamic performance and the leading edge flow structures. After that, the shock buffet condition is analysed in details focusing first on the unsteady phenomena and then on the radiated noise. The aerodynamic and aeroacoustic performance analyses are conducted including the effect of the WLE amplitude. Finally, a sweep angle is introduced in order to investigate an aeronautical application of this passive technique. Two wavy swept configurations are studied. In the first one, the WLE direction has a sweep angle with respect to the upstream flow, while in the second one, the WLE direction is parallel to the upstream flow. The focus is on the mitigation of shock buffet and the additional unsteady phenomena introduced by the three dimensional configuration. Moreover, the leading edge flow structures are inspected and compared with the unswept case. The study shows that wavy leading edges over supercritical aerofoils represent a promising passive technique to mitigate the shock oscillations and it paves the ground for further studies.

Contents

List of Figures

List of Tables

Declaration of Authorship

I declare that this thesis and the work presented in it is my own and has been generated by me as the result of my own original research.

I confirm that:

1. This work was done wholly or mainly while in candidature for a research degree at this University;
2. Where any part of this thesis has previously been submitted for a degree or any other qualification at this University or any other institution, this has been clearly stated;
3. Where I have consulted the published work of others, this is always clearly attributed;
4. Where I have quoted from the work of others, the source is always given. With the exception of such quotations, this thesis is entirely my own work;
5. I have acknowledged all main sources of help;
6. Where the thesis is based on work done by myself jointly with others, I have made clear exactly what was done by others and what I have contributed myself;
7. Parts of this work have been published as:

Signed:..... Date:.....

Acknowledgements

Firstly and foremost I would like to thank my supervisor Dr Jae-Wook Kim for his continual support and guidance throughout the project. I have thoroughly enjoyed my time in Southampton, and I am grateful that you encouraged me to pursue a PhD. I would also like to thank Dr Jacob Turner for the useful discussions about aerofoil's aeroacoustics. I also gratefully acknowledge the support of the NGCM (Next Generation Computational Modelling) CDT (Center for Doctoral Training) through ESPRC (Engineering and Physical Sciences Research Council) grant. In addition I acknowledge the support of the high-performance computing facilities and services of the University of Southamptons local supercomputing facility IRIDIS5, as well as the UK national supercomputer ARCHER. Lastly, but not least, I would like to thank my family for their continued support and encouragement throughout the past years.

Definitions and Abbreviations

Roman characters

a	Speed of sound
e	Internal energy
f	Frequency
h	Amplitude
M	Mach number
p	Pressure
q	Heat flux
Re	Reynolds number
S	Sponge zone forcing term
St	Strouhal number
t	Time
T	Period
u, v, w	Streamwise, vertical and spanwise velocities
x, y, z	Cartesian coordinates

Greek characters

δ	Displacement thickness
γ	Ratio of specific heats
λ	Wavelength
μ	Dynamic viscosity
ρ	Density
ξ, η, ζ	Body fitted coordinates

Superscript and subscript

$()_\infty$	Free-stream quantity
$()_c$	Chordwise
$()_w$	Wall quantity

Coefficients

C_p	Pressure coefficient
C_f	Skin friction coefficient

C_L	Lift coefficient
C_D	Drag coefficient
C_{Dp}	Pressure drag coefficient
C_{Df}	Skin friction drag coefficient

Abbreviations

AoA	Angle of Attack
BL	Boundary Layer
DNS	Direct Numerical Simulation
IDW	Inverse Distance Weighting
ILES	Implicit Large Eddy Simulation
LE	Leading Edge
LES	Large Eddy Simulation
LSB	Laminar Separation Bubble
L-T	Laminar-Turbulent
SBLI	Shock wave Boundary Layer Interaction
SCB	Shock Control Bump
SLE	Straight Leading Egde
St_B	Strouhal number of shock buffet
St_{VS}	Strouhal number of vortex shedding
St_{BB}	Strouhal number of bubble breathing
SV	Streamwise Vortex
TE	Trailing Edge
TED	Trailing Edge Device
V2C	Laminar-flow profile designed by Dassault Aviation
VG	Vortex Generator
WLE	Wavy Leading Edge
WLEc1	Wavy Leading Edge configuration 1 (swept case)
WLEc2	Wavy Leading Edge configuration 2 (swept case)

Chapter 1

Introduction

1.1 Motivation

Aircraft flight in a transonic speed regime represents a huge challenge in terms of fuel consumption, fluid-structure interaction and noise emission. The reason is related to a decreased efficiency caused by a drag divergence and to an unsteady loading because of shock wave oscillations. Some supercritical aerofoils to alleviate these issues can be found in commercial aviation aircraft wings, helicopter rotor blades, and compressor blades. In addition, control devices exist to improve the aerodynamic performance in transonic flow, which can be classified into three main categories:

- trailing edge devices (TEDs)
- vortex generators
- shock control bumps

TEDs were originally studied for shock oscillation control because a common feature among the classic models governing the buffet phenomenon is the coupling between the large scale excursions of the shock and the pressure fluctuations at the trailing edge. Static trailing edge flap deflections can modify the flow field and stabilize it. In transonic flows, they can diminish significantly the buffet lift response, indicating that the aerodynamic coefficients can be controlled by prescribed structural motions under this condition (Iovnovich and Raveh (2012)). The drawbacks are drag penalties and longitudinal instability, but they can be tackled with a feedback loop control (Gao et al. (2016)).

Vortex generators energize and stabilize the boundary layer, promoting attached flow and inhibiting shock induced separation, which is a key feature of the buffet phenomenon. Previous studies show that VGs over an aerofoil improve the

aerodynamic performance at incidence close to buffet onset with the downside of drag penalty addition at lower angles of attack (Huang et al. (2012)).

Two-dimensional shock control bumps (SCBs) were originally studied for pressure wave drag reduction (Stanewsky et al. (2013); Birkemeyer et al. (2000)). The working principle is the split of a normal shock into a λ-shape shock because, in this way, the total pressure losses are decreased. SCBs work properly in design condition, but they perform poorly off design. Two-dimensional SCBs can delay transonic buffet onset by introducing a region of attached flow between the shock wave and the trailing edge of a supercritical wing, postponing complete flow breakdown (Bruce and Colliss (2015)). They can achieve this if they are placed between the shock wave and the wing trailing edge, where they do not offer any drag benefit.

Recent studies have analysed three dimensional shock control bumps to both control shock buffet oscillation and decrease drag divergence (Mayer et al. (2019)). They are used as 'smart' vortex generators because they creates streamwise vorticity (as standard vortex generators) but they do not introduce discountinuity in the aerofoil geometry. The main issue is that the optimal position for wave drag reduction is always different from the one for shock buffet suppression. A trade-off is needed to improve the overall mean and unsteady characteristics of an aerofoil.

The main challenge in transonic flow is to find a passive device which mitigates the shock buffet oscillation at high angles of attack and improve or at least does not decrease the wing efficiency at low angles of attack.

Wavy Leading Edges (WLEs) have been applied to improve the stall performance of aerofoils in subsonic flows (Perez Torro and Kim (2017); Hansen et al. (2016); Siconolfi et al. (2015)). The results show that WLEs allow to improve both time-averaged and unsteady aerodynamic performance in stall condition. In particular, pressure drag is decreased while skin friction drag is increased. The drawback is that the aerodynamic efficiency is decreased at low and moderate angles of attack. WLEs seem to work properly when pressure drag is the dominant component. This is the main reason why they should be analysed also in transonic flows which are dominated by pressure drag. Both the stall condition in low speed flows and the shock buffet in high speed flows are dominated by the pressure drag, thus WLEs are expected to work consistently in controlling the pressure drag in these two different conditions. In addition, Plante et al. (2019) have proved a similitude between 3D cellular patterns on a swept wing in these conditions. The flow analysis in the leading edge region shows that streamwise vorticity is generated at the trough. Thus, WLEs can also be considered 'smart' vortex generators and this concept is the current state of the art in transonic flow research.

1.2 Research aims and objectives

The drag reduction in transonic flows and the mitigation of shock buffet have been extensively studied over the years, but Wavy Leading Edges have never been applied to address these problems. The principle aim of this research is then to develop a comprehensive understanding of WLE performance in transonic flows. The goal is broken into four major categories which are as follows:

- Provide a preliminary performance of WLEs over a range of incidence angles and define the main flow characteristics.
- Analyse the unsteady performance of modified aerofoils and study the influence of wavy amplitude on it.
- Study the aeroacoustics of WLEs at high incidence angles and the influence of wavy amplitude on sound propagation.
- Analyse swept wing sections with two wavy configurations at high incidence angles.

The preliminary analysis is necessary because of the lack of previous studies on this topic and the novelty of the work. The limit of the slow heaving motion analysis is that it does not allow to analyse in details the unsteady phenomena on the aerofoils. Since the mitigation of shock oscillations on an aerofoil in transonic flows is crucial, the second and third categories aim to provide a detailed analysis of the aerodynamic and aeroacoustic performance of the modified aerofoil in shock buffet condition. Finally, having an understanding of the modified aerofoil in an unswept configuration, the aerodynamic performance is investigated in an aeronautical case, considering swept wing sections.

1.3 Thesis outline

Chapter 2 illustrates both aerodynamic and aeroacoustic characteristics of WLEs in subsonic flows. Then, the main aspects of transonic flows are displayed, the shock wave boundary layer interaction, the turbulent separation bubble and the shock buffet oscillation and its control. Finally, some details about important flow characteristics are given. In particular, the laminar bubble and the laminar-turbulent transition are treated.

Chapter 3 explains in details the methodology which includes grid generation and numerical methods. High-fidelity simulations are exploited throughout the thesis because the author believes that they allow to fully understand the flow complexity.

First of all, the generation of a multi-block structured mesh is described. Then, the numerical methods used to solve and filter the compressible Navier-Stokes equations are explained. Finally, the boundary conditions and the additional non reflective treatments are illustrated.

The results are presented as a collection of four papers. Below are details of the work conducted for each paper.

Chapter 4 - **Preliminary results slowly varying incidence angle** contains the paper first presented in:

Degregori, E., & Kim, J. W. (2020). "An investigation on a supercritical aerofoil with a wavy leading edge in a transonic flow". Physics of Fluids, 32(7), 076105.

Abstract A compressible large-eddy simulation is performed to study the effects of a wavy leading edge (WLE) applied on a supercritical aerofoil in a transonic flow at $Re_\infty = 5.0 \times 10^5$ and $M_\infty = 0.7$. The wavelength and peak-to-trough amplitude of the WLE used in this study are 5% and 2.5%, respectively, of the mean aerofoil chord. The primary aim of this study is to understand the aerodynamic characteristics of the modified aerofoil over a range of incidence angles. For this reason, a slow heaving motion is imposed where the geometric angle of attack is gradually increased from $\alpha_g = 2^o$ to 7^o without a significant dynamic (added mass) effect, i.e., a quasi-linear range. The new transonic flow study shows significantly different findings (with some similar features) to the previous low-speed flow studies. It is observed in the quasi-linear range that the modified aerofoil achieves a performance improvement at low and moderate angles because of a drag reduction in the leading edge region and downstream of the laminar-turbulent (L-T) transition point. The leading edge (LE) analysis shows that the maximum pressure coefficient remains equal to that of the baseline case only at the trough and peak sections. The relative decrease in pressure at the LE results in the drag reduction. The transonic flow at the LE is analyzed in further detail to show a reversed flow region at the trough and its influence on the boundary layer development over the aerofoil. In addition, the spanwise variation of the boundary layer characteristics over the modified aerofoil is evaluated and analyzed. One of the most notable findings in this paper is that the flow at the trough becomes supersonic even at low angles of attack, and this results in an enhanced LE flow acceleration spread across the span, which seems facilitated by using a short WLE wavelength. This flow behavior is qualitatively explained by using an analogy between a channeling effect and a convergent-divergent nozzle in a transonic flow. Another notable observation is that there is an upstream movement of the laminar-turbulent transition point seemingly related to the flow distortion around the WLE. Interestingly, the flow distortion introduces a three dimensionality into the laminar boundary layer, but it keeps the flow laminar, so the benefits of the laminar supercritical aerofoil are not lost. These LE phenomena have a major impact on the

shock structure at high incidence angles where the more energetic laminar boundary layer changes the shock structure over the modified aerofoil. This can be crucial to control the shock buffet phenomenon.

Chapter 5 - **Mitigation of transonic shock buffet** contains the paper:

Degregori, E., & Kim, J. W. (2021). "Mitigation of transonic shock buffet on a supercritical aerofoil through wavy leading edges". Physics of Fluids, 33(2), 026104.

Abstract Mitigation of shock buffet phenomenon over a supercritical aerofoil by means of wavy leading edges (WLEs) is analysed with implicit large eddy simulations (ILES). A Dassault Aviations V2C aerofoil is simulated in a transonic flow with $Re_\infty = 5.0 \times 10^5$ and $M_\infty = 0.7$ at $\alpha = 7.0^o$. This aerofoil profile is designed for transonic flows, delaying the onset of wave drag and decreasing the skin friction drag. The results of this upstream flow condition on a straight aerofoil is a large oscillation of lift and drag coefficients. In the first part, time-averaged aerodynamic characteristics over a straight leading edge (SLE) aerofoil and three modified aerofoils with different wavy amplitudes are compared. The results show that overall WLE aerofoils are more efficient than SLE ones and the aerofoil with the lowest amplitude ($h = 0.0075$) is the most efficient, increasing lift coefficient and decreasing drag coefficient. The flow unsteadiness has a key role for aerofoils in transonic flows at moderate and high angles of attack. Hence, the second part of the paper is a detailed unsteady analysis of flow phenomena. The starting point is an investigation of unsteady aerodynamic performance. It is observed that WLE aerofoils are capable of significantly decreasing low-frequency oscillations' amplitude, identified with shock buffet. The best performance is obtained with $h = 0.0125$ where a high-frequency oscillation becomes the dominant unsteady phenomenon. High-frequency oscillations are identified through the application of a frequency filtering method to the flow field. It is proved that the oscillation on the SLE aerofoil is related to vortex shedding, while the one on WLE aerofoils is related to laminar separation bubble (LSB) breathing. Overall, the unsteady analysis shows a connection between shock buffet and LSB breathing phenomena on wavy aerofoils and identifies the WLE amplitude as a key parameter to control this relation and mitigate the shock buffet.

Chapter 6 - **Shock buffet aeroacoustics** contains the paper:

Degregori, E., & Turner, J. M., & Kim, J. W. (2022). "Effect of Wavy Leding Edges on Shock Buffet noise", *Preprint*

Abstract Aerofoil self-noise produced during the shock buffet phenomenon and its mitigation through wavy leading edge (WLEs) is investigated with regard to the dipole noise sources utilising high-fidelity numerical simulations. A Dassault Aviation's V2C aerofoil is simulated in a transonic flow with $Re_\infty = 5.0 \times 10^5$ and $M_\infty = 0.7$ at $\alpha = 7.0^o$. Large shock wave oscillations are observed on the straight

aerofoil with this upstream flow conditions. In the first part, the radiated spectra and the directivity trends of the straight aerofoil and three wavy ones are compared. WLE aerofoils with amplitude $h = 0.0075$ and $h = 0.0125$ show similar aeroacoustic performance, decreasing the radiated noise mainly in the region upstream and above the aerofoil and having comparable noise emission with the SLE in the region downstream. In particular, the pressure fluctuations downstream are decreased in the low frequency range ($St < 0.5$) and they are increased in the medium frequency range ($0.5 < St < 1.2$). On the contrary, the wavy aerofoil with higher amplitude ($h = 0.0250$) significantly improves the aeroacoustic performance in all the directions. In the second part, the far-field pressure fluctuations sources are investigated at the frequency of the main unsteady phenomena. The sources are located in the region of shock wave oscillations at the shock buffet frequency. On the contrary, at the laminar bubble breathing frequency the sources are located at the shock boundary layer interaction (SBLI) region and in the region downstream where the boundary layer is fully turbulent. Finally, the vortex shedding on the straight aerofoil displays strong pressure fluctuations sources at the trailing edge region, as expected from the physical nature of the unsteadiness.

Chapter 7 - **Swept wing effects** contains the paper:

Degregori, E., & Kim, J. W. (2022). "Swept wing effects on Wavy Leading Edges performance in a transonic flow", *Preprint*

Abstract The swept wing effects on Wavy Leading Edges (WLEs) performance is analysed with implicit large eddy simulations (LES). A Dassault Aviation V2C aerofoil is simulated with a sweep angle $\Lambda = 25^o$ and $M_\infty = M_{2D\infty}/\cos\Lambda$, where $M_{2D\infty} = 0.7$. Two wavy configurations are simulated and compared with the baseline case. On the first one (WLEc1), the WLE direction has a sweep angle with respect to the upstream flow direction, while on the second one (WLEc2), the WLE direction is parallel to the upstream flow direction. The mean aerodynamic performance analysis displays that both wavy configurations increase the lift coefficient of the swept wing sections. On the contrary, WLEc1 is able to also decrease the drag coefficient because of the reduction of pressure drag coefficient, while WLEc2 slightly increases the drag coefficient with respect to the straight counterpart. The second part of the paper is a detailed analysis of flow unsteadiness. The wavy configurations are able to decrease the low frequency unsteadiness related to the shock buffet even if the shock oscillation amplitude is larger on WLEc2. The local unsteady analysis displays high frequency unsteady phenomena on the two wavy configurations which appear to be stronger on WLEc2. The origin of this unsteadiness is in the laminar BL upstream the SBLI region and, as a result, vortical structures are generated downstream the SBLI. Finally, the leading edge flow structures are investigated. The leading edge flow channelling is modified with respect to the unswept case because of the asymmetry introduced by the sweep angle and the different location of the stagnation points. Vortical flow

structures are generated by the leading edge waviness and they develop downstream convected in the spanwise direction. On WLEc1, the vortical structures generate close to the LE and then downstream they detach from the surface, while on WLEc2, the vortical structures generate further downstream and they stay close to the wing section surface.

1.3.1 List of publications

Journal papers-accepted

- Degregori, E., & Kim, J. W. (2020). "An investigation on a supercritical aerofoil with a wavy leading edge in a transonic flow", *Physics of Fluids, 32*(7), 076
- Degregori, E., & Kim, J. W. (2020). "Mitigation of transonic shock buffet on a supercritical aerofoil through wavy leading edges", *Physics of Fluids, 33*(2), 026104

Journal papers-in preparation

- Degregori, E., & Turner, J. M., & Kim, J. W. (2022). "Effect of Wavy Leding Edges on Shock Buffet noise", *Preprint*
- Degregori, E., & Kim, J. W. (2022). "Swept wing effects on Wavy Leading Edges performance in a transonic flow", *Preprint*

Chapter 2

Literature Review

The flow around an aerofoil and the transonic flow are characterised by complex physical phenomena. This chapter presents the previous studies and analyses about Wavy Leading Edges aerodynamic and acoustic performance, the shock boundary layer interaction and shock buffet oscillation, the laminar separation bubble and the laminar-turbulent interaction. This gives a complete overview on the phenomena that will be analysed in this study.

2.1 Wavy Leading Edge aerofoils

The Wavy Leading Edges (WLEs) are a passive control technique that can lead to increased lift at high angles of attack and decreased noise emission. In this section, a detailed review of the aerodynamic and aeroacoustic characteristics of this modified aerofoil is presented in order to show the current knowledge and the area of research still uncovered.

First of all, the geometric characteristics and the terminology that will be used throughout the all thesis are introduced. Figure 2.1 shows a section of an infinite span aerofoil with leading edge protuberances. The main parameters are reported in the figure, L_c is the mean chord length and L_z is the aerofoil's span. The leading edge is modelled as a sinusoidal profile of h_{LE} amplitude and λ_{LE} wavelength. The sections of maximum and minimum chord are referred as peaks and troughs, while the sections with chord equal to the mean chord are referred as middle sections or hills herein.

2.1.1 Aerodynamics

The mean aerodynamic characteristics of WLE aerofoils have been analysed extensively in the past. Hansen et al. (2009), Rostamzadeh et al. (2014), Custodio et al.

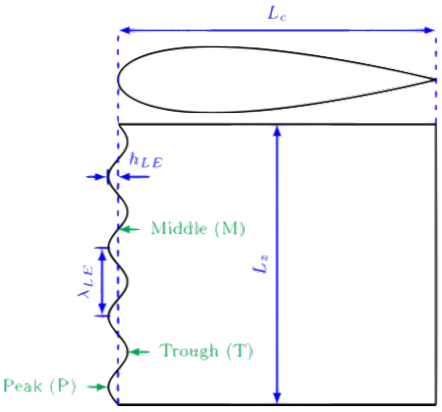

FIGURE 2.1: Main parameters of WLE geometry extracted from Perez Torro (2015).

(2015), Yoon et al. (2011) and Perez Torro and Kim (2017) showed that the maximum lift coefficient ($C_{L_{max}}$) decreases with leading edge tubercles and the stall characteristics are less abrupt than straight leading edge (SLE) aerofoils. Hence, LE tubercles on aerofoils improve the efficiency (L/D) after stall, while at lower angles of attack the straight aerofoil is generally more efficient. The lift is increased in post-stall regime because of the larger attached flow region at the peaks sections. The drag is increased near stall because streamwise vortices are generated and the shear stress grows, but it can decrease in post-stall regime. In pre-stall regime the lift is slightly decreased with respect to the SLE aerofoils and the drag is close to the SLE case one. The flow is highly three-dimensional on WLE aerofoils. The lift is larger at the peaks sections, while the opposite is observed at the throughs sections.

The parametric study shows that the wavelength reduction is advantageous for both pre-stall and post-stall regimes. The amplitude increase generates smoother stall characteristics, but the downside is a fall in $C_{L_{max}}$ and a decrease in maximum stall angle. In general the wavelength decrease is more beneficial than the amplitude raise. Rostamzadeh et al. (2017) analysed the effect of Reynolds number variation over the flow topology induced by leading edge waviness. The flow at the peaks sections moves towards the troughs, driven by low pressure regions at the troughs (spanwise pressure gradients). The outcome is a distribution of periodic LSBs in the throughs regions. When the Reynolds number increases, the LSB size decreases because the streamtubes of streamwise vorticity are closer to the surface in a high Reynolds number flow. Custodio et al. (2015) studied the aerodynamic performance of WLE aerofoils with finite span and with a non-zero swept angle. A different lift behaviour between the full span and the finite span aerofoil is reported. The finite span wing stall is delayed without a relevant lift loss prior to stall. The drag characteristics of the finite wing are consistent with those of the full span model, thus overall the efficiency is higher. The leading edge waviness on a swept wing reduces the abrupt stall and increases the angle of maximum lift.

The beneficial behaviour of WLEs is strictly related to the induced spanwise periodic flow field. On the one hand, a two dimensional LSB that spans the whole upper surface is formed on SLE aerofoils close to the leading edge. On the other hand, WLE aerofoils exhibit LSBs periodically generated at the trough sections. More details about the characteristics of transitional flows and laminar separation bubbles will be provided in section 2.3 because they are necessary to understand the flow topology and behaviour over the modified aerofoil.

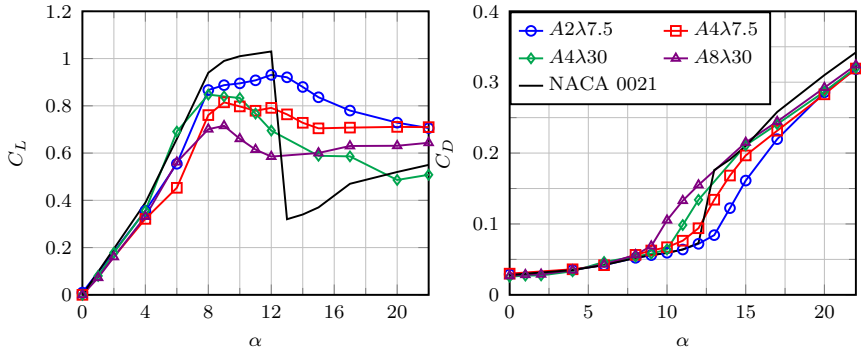

FIGURE 2.2: Comparison of lift and drag coefficients for WLE aerofoils with different amplitudes and wavelengths extracted from Hansen et al. (2010).

Hansen et al. (2016), Serson et al. (2017), Rostamzadeh et al. (2014) and Perez Torro and Kim (2017) studied the flow around WLE aerofoils in order to understand the physics and to explain the benefits of these models. Between tubercles peaks, streamwise vortices are formed and they enhance the momentum exchange within the boundary layer. This is a key aerodynamic characteristic of WLEs. The streamwise vorticity is skew-induced when existing vorticity turns in the streamwise direction. This mechanism was observed on both laminar and turbulent flows. Alternatively, the vorticity is stress-induced when it arises from anisotropy of the turbulence. The main steps of this process are observed near the leading edge of the aerofoil:

- vorticity production caused by spanwise pressure gradients
- decay of peak vorticity activated by the velocity gradients
- vorticity spreading because of adverse pressure gradients (APGs) on the suction side

Hansen et al. (2016) and Perez Torro and Kim (2017) illustrated the development of different vorticity regions close to the LE. The main one is a primary vorticity region and it is spread downstream. The peak of vorticity decreases and the area over which it is distributed increases (Kelvin circulation theory). A secondary vorticity region with opposite sign is annihilated by the primary one. Finally, there are the wall vortices, adjacent to the primary ones and with opposite rotation.

Perez Torro and Kim (2017) analysed also the unsteady characteristics of a deep stalled aerofoil with WLEs. First of all, the lift and drag fluctuations are reduced. The von-Karman vortex shedding in the rear wake is weakened and the peak on the spectra appears at higher frequencies. The vortex shedding has a very limited influence on the aerodynamic force fluctuations in the WLE case. The deteriorated vortex shedding can be explained by the loss of coherence in the spanwise direction, related to the highly three dimensional flow. Secondly, the turbulent energy spectra rapidly broaden and decay because of the leading edge vortex dynamics.

All the previous results were obtained experimentally and computationally with low Mach number flows. Preliminary analyses about the mean aerodynamics in transonic flows were illustrated by Asghar et al. (2017) and Filho et al. (2018) using a NACA 0012 aerofoil. The critical Mach number is improved and the efficiency increases, the drawback is a decrease in aerodynamic efficiency at high angles of attack because of bubbles bursting.

2.1.2 Aeroacoustics

The WLE aerofoils show significant benefits also on the mitigation of acoustic emissions. The aerodynamic sound generation of an aerofoil can be divided into two main categories: aerofoil-turbulence interaction (ATI) noise or aerofoil-gust interaction (AGI) noise, where pressure waves are generated when upstream turbulence hits the leading edge, and aerofoil self noise, where sound waves are scattered when the boundary layer meets the trailing edge (TE). These phenomena can be studied separately with numerical simulations, considering an inviscid flow with upstream synthetic turbulence for ATI noise and viscous flow without upstream disturbances for self noise. When these phenomena are studied experimentally it is not possible to completely separate them. However, the contribution is on different frequency ranges. The ATI noise appears on low frequencies, while the self noise on high frequencies.

In this section, the main aeroacoustic characteristics of WLEs are introduced and explained in details. First of all, a flat plate with upstream perturbations is considered in order to understand the acoustic source location and strength in the simplest case. Then, an aerofoil is introduced and both sound generation types are analysed.

Flat plate

When vortical structures impinge on a surface, the normal velocity component is forced to zero and pressure fluctuations start propagating. The radiation of these pressure waves is the ATI noise. The mechanism of pressure fluctuations suggests that the use of a flat plate can tackle the complexity of the aeroacoustic problem.

Narayanan et al. (2015), Kim et al. (2016) and Chaitanya et al. (2017) studied this problem both numerically and experimentally. A comparison of the ATI noise from SLE and WLE plates is illustrated in Figure 2.3. ATI noise is generated by the rapid twist of the vorticity field impinging on the surface. The pressure waves are significantly lessened in the hill region of WLEs, whereas the peak and root regions show a level of fluctuations similar to the SLE case (Figure 2.4). The reason is that the hill region exhibits a local sweep angle higher than the peak and root ones. The difference between the root and peak sections is the frequency range. In the former, low frequency components are dominant, in the latter high frequency components are stronger. SLE spectrum represents an envelope of the spectra from the peak and the root combined. WLEs yield a de-synchronised gust response in span along the LE of the plate. As a consequence, the unsteady forces acting on the surface are globally reduced.

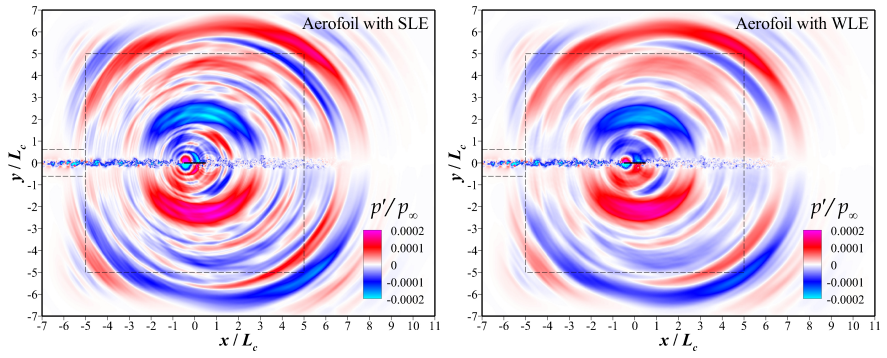

FIGURE 2.3: ATI noise propagation from SLE and WLE plates extracted from Kim et al. (2016).

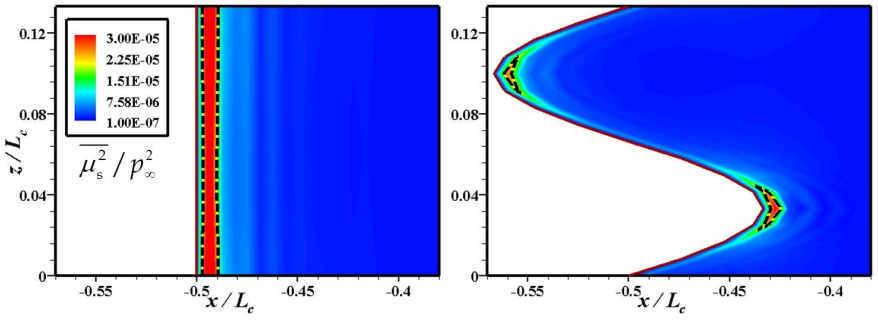

FIGURE 2.4: Acoustic source strength on the plate surface extracted from Kim et al. (2016).

The parametric study of Lau and Kim (2013) shows that the most important parameter to characterise the acoustic performance of WLEs is the ratio between the peak-to-peak amplitude (LEA) and the longitudinal wavelength of incident gust (λ_g). The sound pressure level (SPL) decreases when LEA increases due to the destructive interference along the leading edge (weaker correlation of surface pressure fluctuations). The power level (PWL) is proportional to $1/h^n$, where n is a frequency-dependent constant and h is the waviness amplitude. Chaitanya et al. (2017) reported that the maximum

noise reduction is obtained when $\lambda_o/\Lambda_t = 4$, where λ_o is the optimum wavelength and Λ_t is a turbulence length scale. If the WLE wavelength is lower than the optimal one, the sound power is dominated by coherence. On the contrary, if the wavelength is greater than the optimal one, the sound power is dominated by source strength.

Turner and Kim (2017) tried to deeply understand the relations between the vortex induced velocity perturbations and the wall pressure fluctuations on the WLE geometry. The objective was to explain the aeroacoustic performance of the flat plate through a fundamental understanding of the physics. An horseshoe-like vortex system is created twice when a single vortex impinges on a wavy plate. As a consequence, the source strength is weaker at the peak, while it is similar to that of the SLE at the root, independently of LEA. However, the source strength is correlated with the mean vertical velocity signal, not with the local one. This proves the difference between the spectra at the root and those of the SLE, changing the amplitude. Increasing the amplitude, both the vertical velocity component and the wall pressure fluctuation at the peak tend to saturation.

Aerofoil

The aerodynamic noise generated by an aerofoil is governed by more complicated phenomena. From an aeroacoustic point of view, there are two main differences with the previous analysis over a flat plate.

- The TE self noise contribution is higher because of a more energetic boundary layer driven by adverse pressure gradients.
- The LE profile distorts the incoming turbulence due to mean flow gradients.

Narayanan et al. (2015) and Chaitanya et al. (2017) compared the flat plate and the aerofoil noise generation. The SPL of the flat plate is higher than the one of the aerofoil. However, the noise reduction mechanisms applied to flat plates can also be employed with the aerofoils, even though the flow topology at the LE is more complicated and highly three dimensional. Both interaction and self noise reduction were reported by Narayanan et al. (2015), Chaitanya et al. (2017) and Chong et al. (2015). The self noise mitigation is achieved because of boundary layer distortion at the LE.

Lau and Kim (2013) and Gea Aguilera et al. (2017) solved the linear Euler equations (LEEs) neglecting self noise contribution. The ATI phenomenon was studied by Lau and Kim (2013) introducing an upstream vortex and by Gea Aguilera et al. (2017) and Fan et al. (2018) injecting isotropic and anisotropic synthetic turbulence inside the domain. Stretching turbulence structures in the spanwise direction enhances the

amplitude of spectra in the high frequencies range. On the contrary, an increment in the streamwise direction increases the amplitude in the low frequencies range. The effectiveness of LE waviness is more negatively affected by anisotropy in the spanwise direction.

Hansen et al. (2010) study is focused on tonal noise. If the boundary layer is laminar, the tonal noise is related to the periodic vortex shedding. Instabilities in a laminar BL on the pressure surface can trigger a feedback loop. A lateral oscillation of the wake causes acoustic wave emission in all directions. The aeroacoustic feedback loop is between maximum velocity point and TE. Hansen et al. (2010) showed that tonal noise is closely related to a region of separated flow near the TE, this suggests a dependence on a separation bubble. WLE aerofoils with small wavelength and large amplitude are the most effective to reduce tonal noise. The frequency is increased by the waviness and the SPL is decreased. The parametric analysis also proves that the amplitude is more effective than the wavelength in self noise mitigation.

2.2 Transonic flow

The study of an aerofoil in a transonic flow involves the interaction of shock waves with turbulent boundary layers. A fundamental understanding of the complex physical phenomena involved in the interaction is extremely important in order to control their detrimental effects. Thus, the interaction was initially isolated in order to deeply understand its physics. Then, the original problem was studied both experimentally and numerically. In this section, the main findings of the shock-wave boundary layer interaction (SBLI) problem are illustrated and then the shock buffet phenomenon, strictly related to the transonic flow over an aerofoil, is presented.

2.2.1 Shock wave boundary layer interaction

The phenomenon of SBLI can be isolated and practically studied experimentally or numerically using two kinds of configurations, a compression ramp or a reflection of an incident shock wave (Figure 2.5). The two configurations show similar flow behaviour such as a low frequency motion of the shock when the shock intensity is strong enough to separate the boundary layer.

The interaction can be weak or strong depending on the mean separation behaviour of the boundary layer. Souverein et al. (2010) showed the influence of the interaction on the flow unsteadiness. In a weak interaction, a fan of compression waves arises upstream of the nominal shock impingement and it generates a quasi normal rear shock, which brings the flow to subsonic conditions. The mean flow is not separated,

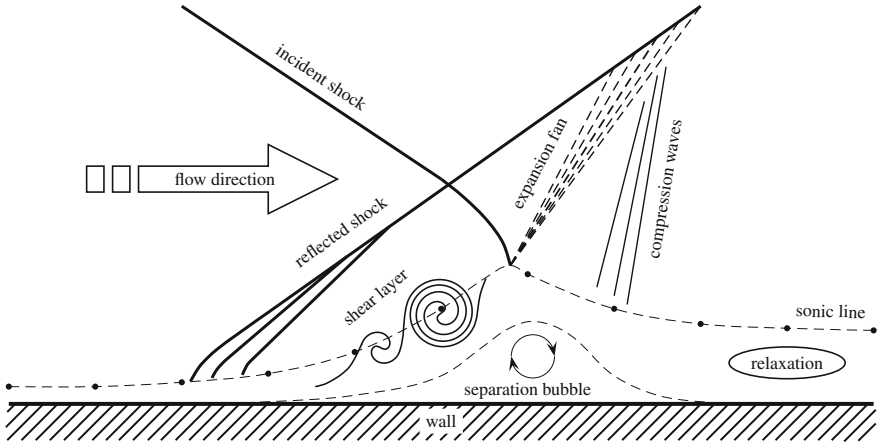

FIGURE 2.5: Reflection of incident shock wave extracted from Touber and Sandham (2009).

but it shows scattered spots of instantaneous and intermittent separation. The unsteady characteristics of the interaction are governed by upstream events. In a strong interaction, it is observed a leading shock generated by compression waves and a region of supersonic flow past the rear shock. The intersection of the leading shock with the rear shock forms the lambda shock pattern. The flow is governed by downstream unsteadiness related to turbulent separation bubbles. A borderline case is the incipient separation, where a superposition of different mechanisms is observed, involving time scales that can vary by one order of magnitude.

Pirozzoli et al. (2010), Bernardini et al. (2011), Sartor et al. (2012) and Dupont et al. (2006) identified different zones in the interaction:

- a zero pressure gradient (ZPG) region upstream the origin of interaction, where a canonical boundary layer develops with a balance of production and dissipation
- a supersonic adverse pressure gradient (APG) region close to the interaction point, where the boundary layer is out of equilibrium and does not present the Kolmogorov turbulence decay because of the amplification of the Reynolds stress components
- a subsonic adverse pressure gradient region downstream the interaction, where the boundary layer is again in equilibrium and the velocity profiles are self similar (flow relaxation)

The analysis of the pressure signal allows to locate the acoustic sources in the different regions. A pressure source presents a slow term related to high frequencies and a rapid term related to low frequencies. In ZPG and subsonic APG regions, the pressure sources terms are located close to the wall and the slow term is the dominant contribution. The source distribution is more heterogeneous close to the interaction.

The pressure sources are located both in the proximity of the wall, where the slow term is dominant, and in the mixing layer, where the contribution is provided by the rapid term. The oscillations of the reflected shock are driven by low frequencies as demonstrated by Wollblad et al. (2006), Touber and Sandham (2009) and Dupont et al. (2006). An unstable global mode in the span and time averaged flow field is found. Sartor et al. (2012) and Delery (1983) have shown that the first part of the interaction process (supersonic region) involves a large turbulence production, which mainly affects the streamwise component and generates anisotropic turbulence, this explains the non canonical turbulence decay. During the relaxation (subsonic region) a gradual return to isotropic turbulence is observed.

2.2.1.1 Turbulent separation bubble

The SBLI can present a mean separated flow in the supersonic flow region that interacts with the incident shock. This creates a turbulent separation bubble which drives the unsteady behaviour of the shock when the interaction is strong enough. A separated turbulent boundary layer is characterised by a fluctuation of detachment and reattachment points. Skote and Henningson (2002) compared the separated and the attached BLs. They showed that the near wall scaling theory can not be applied to the separated one, the near wall streaks vanish at separation and the turbulence energy is negative at positions upstream of reattachment (destruction of turbulence energy).

Kiya and Sasaki (1983, 1985) found two types of unsteadiness in the separation bubble: a weak and regular vortex shedding from the main body of the bubble and a large scale unsteadiness responsible for the shrinkage and the enlargement. The large scale unsteadiness is the dominant flow feature in the reattaching zone, but it is strictly related to the vortex shedding. Indeed, Kiya and Sasaki (1983) explained that the vortex shedding accumulates vorticity inside the bubble, this enhances the bubble length and size. When a sufficient amount of vorticity is accumulated, a large vortex is shed from the bubble and, as a consequence, the bubble rapidly shrinks. The large scale unsteadiness is characterised by the flapping of shear layer, it moves outward during the enlargement and inward during the shrinkage. Kiya and Sasaki (1985) analysed the reverse flow unsteadiness and its connection with the large scale one. The reverse flow boundary definition allows to introduce two types of zeros,

$$\begin{cases} \overline{u} = 0 & \frac{\partial \overline{u}}{\partial t} < 0 & \frac{\partial \overline{u}}{\partial x} > 0 & \text{I type zero} \\ \overline{u} = 0 & \frac{\partial \overline{u}}{\partial t} > 0 & \frac{\partial \overline{u}}{\partial x} < 0 & \text{II type zero} \end{cases} \tag{2.1}$$

where $\overline{u}$ is a short time average velocity.

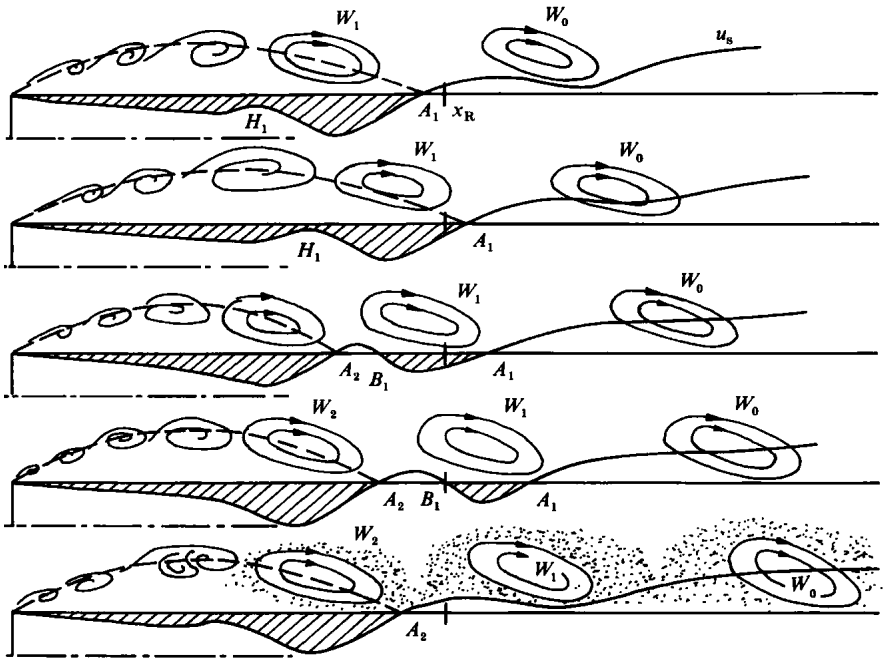

FIGURE 2.6: Sketch of large scale unsteadiness extracted from Kiya and Sasaki (1985).

The large scale cycle is illustrated in Figure 2.6, where the hatched areas indicate the reverse flow regions and the dotted area reveals the poorly correlated region around vortices.

- A large scale vortex W_0 is shed and another vortex W_1 approaches the reattaching zone. There is not a reverse flow underneath W_0, thus it accelerates and its strength decays. In this initial configuration there is only one zero of first type A_1 at the reattaching point.
- The vortex W_1 and the zero A_1 move downstream and the maximum H_1 increases.
- The maximum H_1 keeps increasing and it gives rise to two new zeros, A_2 and B_1. A distinct reverse flow region is beneath the vortex W_1.
- The zero B_1 moves faster than A_1 and A_2, thus the forward flow region A_2B_1 is extended and the reverse flow region A_1B_1 is contracted.
- When B_1 reaches A_1, the reverse flow region disappears and another cycle begins.

The vortices shed during the bubble shrinkage are stronger than those shed during the enlargement. The bubble length is determined by the balance between the entrainment rate and the reinjection rate, an imbalance can cause the expansion or contraction of the bubble. The low frequency correlation along the separation line decays slower than the high frequency one, thus the low frequency unsteadiness has a

larger spanwise length scale. On the contrary, the low frequency correlation decays faster on the reattachment line than on the upstream separation line and the low frequency pressure fluctuations have a lower level than the high frequency fluctuations. This result implies that the low frequency unsteadiness is most strongly felt upstream the reattachment. The relatively constant periodicity of the low frequency oscillations indicates a feedback of disturbances from the reattaching zone to the shear layer near the separation point. The disturbances are generated by the change of vortex strength in the reattaching zone, propagating upstream as pressure waves. Na and Moin (1998) showed with numerical simulations that turbulent structures upstream of the separation bubble move away from the wall into the shear layer in the detachment region and turn around the bubble. Then, they impinge on the wall in the reattachment region.

Downstream the reattachment, a relaxation process is observed and analysed by Alving and Fernholz (1996). The large scale structures in the outer layer play a role in flow relaxation. It is observed that the skewness becomes more negative and the flatness becomes larger, thus the free stream fluid is entrained more deeply into the BL. The inner layer flow is quite distorted, lacking canonical inner layer structure. In particular, $\overline{u}^2$ and $\overline{w}^2$ form a plateau near the wall which can be explained in terms of inviscid vortex dynamics, while the $\overline{v}^2$ and $\overline{uv}$ components do not show it. These findings imply the presence of instantaneous vorticity in the inner region, not necessarily organised into vortex structures. The main outcome of Alving and Fernholz (1996) is that the outer layer is the dominant factor in the inner/outer interaction after reattachment, while it was previously thought the inner layer to be dominant.

2.2.2 Shock buffet

The shock buffet is a low frequency oscillation of a shock wave over an aerofoil in a transonic flow. Lee (2001) and Giannelis et al. (2017) proposed a review of this physical phenomenon. There are two main types of shock buffet. The Type I oscillation appears on biconvex aerofoils and the shock wave is on both sides of the aerofoil with a phase shift of π. The Type II oscillation appears on modern supercritical aerofoils and the shock wave is only on the suction side. In this case there are two modes of separation. Mode A consists of a shock induced separation bubble, while Mode B includes an additional trailing edge separation, it can be a rear separation caused by a bubble, a shock or it can be present from the outset.

It is possible to have three kinds of shock oscillations.

- Type A, sinusoidal shock oscillation across upper surface (acoustic propagation feedback loop).

- Type B, similar to Type A but with higher shock strength variation.
- Type C, shock travels upstream, initially strengthening and then weakening but continuing to move forward, eventually propagating into the oncoming flow as a free shock wave.

This section will focus mainly on the sinusoidal motion of the shock. A phase locked motion of the shock and the separated boundary layer was observed by Szubert et al. (2015), Sartor et al. (2014), Hartmann et al. (2013) and Crouch et al. (2009, 2018). The shear layer thins as the shock moves downstream and thickens during the upstream excursion. The shock oscillations should be considered as acoustic phenomena, the noise generation at the TE governs the shock motion. A sketch of the shock wave motion and its interaction with the boundary layer is shown in Figure 2.7.

- At the beginning of the cycle the shock is at the most downstream position. The main characteristics of the flow are the separation bubble at the shock foot and the rear separation.
- An unstable interaction with the high pressure bubble pushes the shock upstream, as a consequence, von Karman instability starts and it gives rise to vortex shedding. Kutta type waves are generated at the TE and propagate upstream.
- During the upstream excursion, the shock length grows and the separated shear layer thickens. The shock strengthening driving mechanisms are the wedge effects, the dynamic effects and the aerofoil curvature effects.
- Close to the most upstream excursion, curvature effects are dominant. They weaken the shock and allow reattachment at the shock foot.
- During the shear layer reattachment, the shock strengthens and it makes a downstream excursion. Full reattachment is obtained when the shock is already moving downstream, hence vortex shedding disappears and acoustic waves generation is attenuated.

The driving mechanism of the feedback loop is the emission of waves at the TE. The separation is larger when the noise generation at the TE is lower because of the lower vorticity in the near wall region, this allows the shock to move downstream. The interaction between the sound waves and the shock governs the whole physical phenomenon. The shock strength is higher at the origin of SBLI and it diminishes increasing the normal distance from the wall. A weaker shock is more sensitive to upstream propagating sound waves. Thus the main interaction region is the upper end of the shock wave as it is shown in Figure 2.8.

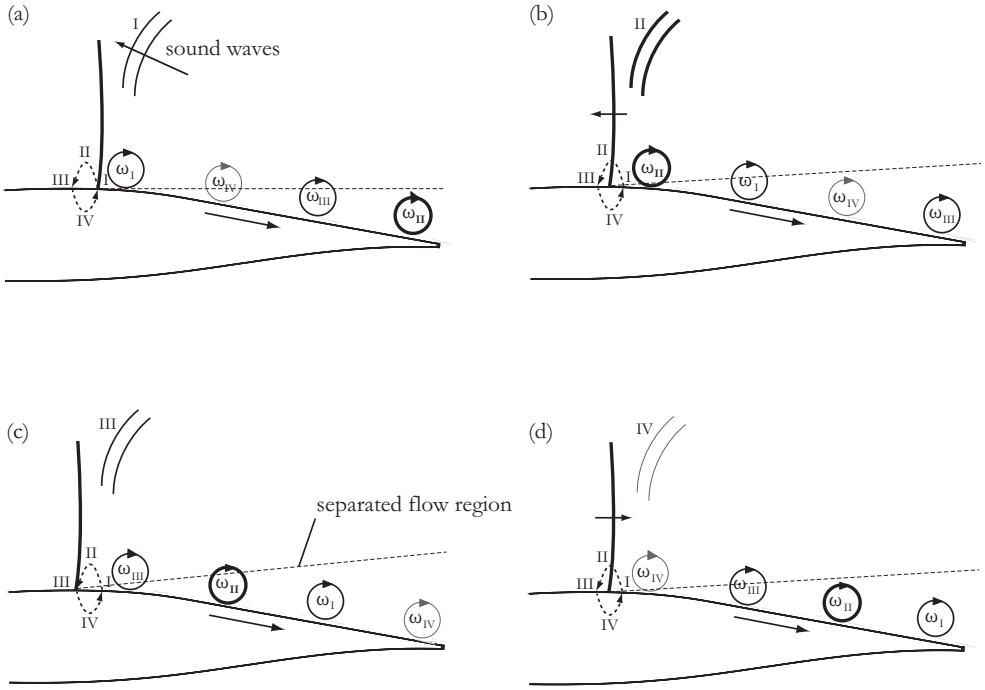

FIGURE 2.7: Sketch of shock wave motion extracted from Hartmann et al. (2013).

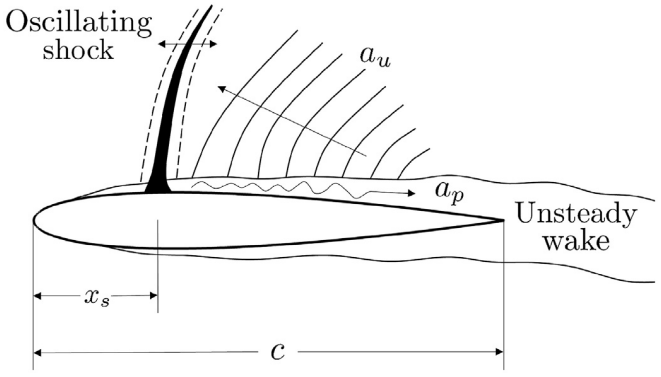

FIGURE 2.8: Sketch of interaction between sound waves and shock wave extracted from Giannelis et al. (2017).

Crouch et al. (2009) and Sartor et al. (2014) proved with a linear stability analysis that the phenomenon is driven by a global unstable mode and the onset of the oscillation is due to a Hopf bifurcation. The unstable mechanism is driven by Kelvin Helmholtz (KH) instabilities which operate in the medium frequency range, affecting the mixing layer downstream the region of separation and downstream the trailing edge in the wake. KH instabilities give a broadband contribution in the frequency domain. At the most upstream position, the spectra do not show predominance in a frequency range, while at the most downstream position, the turbulence content is richer in the high frequency range. When the shock moves downstream, the bubble contracts and vice versa. Large scale fluctuations of eddy viscosity, which propagate in the wake, is due to the contraction and expansion of the recirculation bubble, related to shock displacement.

The previous results are obtained using unsteady Reynolds averaged Navier-Stokes (URANS) simulations or detached eddy simulations (DES). Zauner et al. (2018a,b) analysed the unsteady flow over a laminar supercritical aerofoil using direct numerical simulations (DNS). It is considered the particular flow condition of buffet onset. There is not a strong shock wave oscillation but weak shock waves are generated by the pressure waves gathering and they move upstream. In this case the interaction between shock waves and acoustic waves is the key and thus only high fidelity simulations can properly describe the phenomenon.

Dandois et al. (2018b) and Brion et al. (2017) studied the shock buffet over a laminar supercritical aerofoil both numerically and experimentally. They observed that the interaction of the shock wave with a laminar separation bubble increases the frequency of oscillation. Laminar transonic buffet is driven by the separation bubble breathing phenomenon occurring at the shock foot.

Crouch et al. (2018) and Ohmichi et al. (2018) compared the shock buffet phenomenon over a straight wing and a swept one. Two types of instability are observed on the straight wing, an unsteady mode localised in the shock region and in the downstream shear layer and a steady spatial mode. Both modes become unstable at roughly the same conditions. The spatial modes provide a three dimensional structure to the nominally two dimensional unsteady flow. In the swept wing the spatial mode becomes unsteady and the primary instability mode is different from the unswept wing one. The oscillating shock wave is driven by two dimensional flow mechanisms, but its behaviour is affected by three dimensional interactions. As a consequence a broadband frequency peak is observed instead of the clear peak of the straight case. Ohmichi et al. (2018) observed periodic spatial structures in the spanwise direction and periodic pressure fluctuations generated in the shock region propagating from the root to the tip. These spatial structures are called buffet cells and they are the most dominant fluid phenomena on a swept wing. Buffet cells move upstream until they reach the shock wave, then they travel at an angle in the spanwise direction.

Sartor et al. (2014) performed receptivity and sensitivity analysis of shock buffet flows in order to localise the most sensitive region to manipulate and control the phenomenon. The adjoint global mode highlights the region where an harmonic forcing has the strongest effect on the dynamics of the unstable global mode. The analysis shows that the most sensitive regions are the boundary layer upstream of the shock foot and the recirculation bubble. A streamwise force in the upstream boundary layer or in the recirculation bubble has a stabilising effect on the flow field. Only the supersonic region that is connected to the separation point through a characteristic line can affect the separation location. The pressure disturbances that propagate along the left characteristic line from the profile to the sonic line have less influence on the buffet phenomenon than the same disturbances localised on the right characteristic

line. The results obtained in the receptivity and sensitivity analysis are fundamental to understand the working principles of the different control techniques.

2.2.2.1 Control of shock oscillations

The previous section explains the governing physics of the shock buffet phenomenon in details and the coupling between large scale excursions of the shock and pressure waves radiation from the trailing edge. Control of this instability can be obtained modulating the flow field at the SBLI zone or at the TE. Giannelis et al. (2017), Dandois et al. (2013) and Raghunathan et al. (2008) reviewed several control methodologies:

- trailing edge flap
- fluidic trailing edge device (TED)
- mechanical vortex generator (VG)
- fluidic VG with continuous or pulsated flow rate
- streamwise slot
- synthetic jet actuator
- shock bump
- wall cooling

This section provides further details about the passive mechanical control methodologies (Figure 2.9) because they can be easily compared with the WLE.

Static trailing edge flap deflections may alter the flow field and stabilise it, but these beneficial effects are often combined with detrimental aerodynamic effects such as drag penalties. Iovnovich and Raveh (2012) observed that large prescribed flap motions diminish significantly the buffet lift response and suppress completely the resonance lift response. This result suggests that the flap excitation can change the nature of the flow and can control the aerodynamic responses. However, it can also increase the pitching moment responses (longitudinal instability), thus it may not be the optimal flow control technique. Gao et al. (2016) designed a control loop system in order to overcome the reported drawbacks of the passive technique. The control strategy works well in the buffet flow with a combination of three control parameters: balanced lift coefficient, gain and delay time.

Both mechanical and fluidic vortex generators can be used in the suppression of transonic shock oscillations. They have been studied experimentally to analyse the effect on the SBLI by Rybalko et al. (2012), Titchener and Babinsky (2013) and Holden

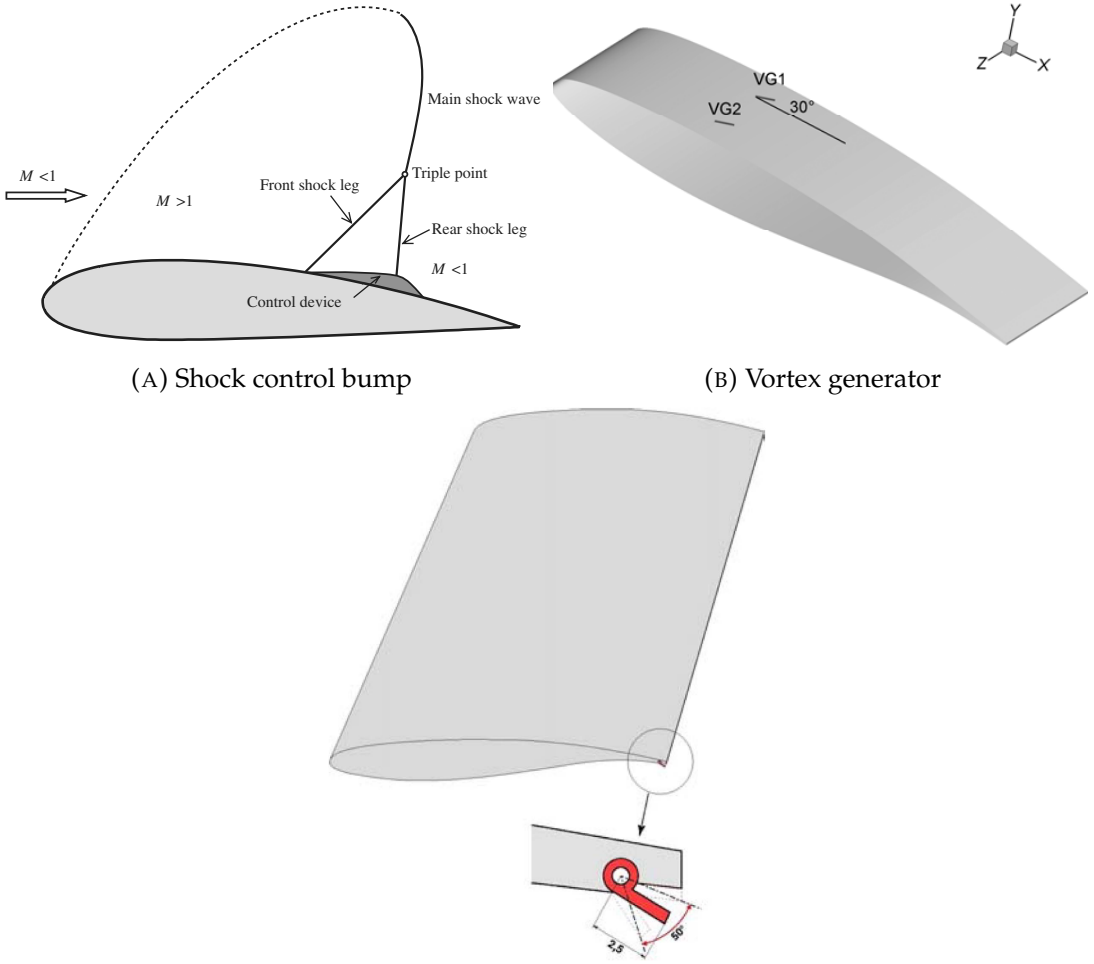

(A) Shock control bump

(B) Vortex generator

(C) Trailing edge device

FIGURE 2.9: Passive mechanical shock buffet control methodologies extracted from Ogawa et al. (2008), Huang et al. (2012) and Giannelis et al. (2017).

and Babinsky (2007). Vortex generators energise and stabilise the boundary layer, promoting attached flow and inhibiting shock induced separation which is a key feature of buffet phenomenon.

The vortex generators installed on an aerofoil bring an improvement to the aerodynamic performance at incidence close to buffet onset. However they also bring drag penalties at lower angles of attack. Huang et al. (2012) showed that the shock wave is moved downstream over the modified aerofoil and the shock location is almost fixed. Downstream the shock, an overall reduction of the energy levels is observed due to the damping of the unsteadiness in the separated region. The VGs deform the shock in the spanwise direction, leading to a very complex but almost periodic three dimensional shock-vortices interaction. Streamwise vortices detach from vortex generators and interact with the shock wave, which is significantly deformed near the wall. As a consequence of the interaction, many small scale structures are generated. Molton et al. (2013) compared the performance of passive

mechanical VGs with active fluidic ones and they found out that the shock is located more downstream with fluidic VGs. Fluidic actuators are as effective as mechanical ones without the drawback of drag increase in cruise conditions.

The two dimensional shock control bumps (SCBs) have been studied extensively for wave drag reduction by König et al. (2009), Wong et al. (2008) and Bruce and Babinsky (2012). They work for drag reduction because the bumps generate a λ shape shock and the total pressure losses through multiple shocks are always less than those through a single one. Ogawa et al. (2008) analysed three dimensional wedge and rounded bumps with different shapes. The possibility to decrease the drag with three dimensional bumps can be estimated in terms of total pressure recovery and average boundary layer thickness, which are indicators for wave drag and viscous drag, respectively. The outcomes show that the wave drag is decreased and the viscous drag is slightly increased.

Recent studies show that the bumps can be used for shock buffet control and in this case the working principle of two dimensional and three dimensional SCBs is different. In the former, the idea is the same of wave drag reduction but the bump's geometry and position are optimised for the shock oscillation control. In the latter, the bumps are employed as smart vortex generators that suppress the shock oscillation limiting the aerodynamic detriment of conventional VGs. The shock structure over the bumps largely depends on the shock location and this is one of the main constraints of this control technique, both for wave drag reduction and shock buffet suppression. The off-design conditions are more deleterious for two dimensional bumps. When the shock wave is upstream the design point, the flow is re-accelerated because of convex curvature at the front of the bump ridge and because of contraction effect, related to the increased cross sectional area of the bump behind the main shock system. Consequently, a second supersonic region similar to a supersonic tongue arises behind the main shock structure and it forms a secondary λ shock system that enhances significantly the wave drag (Figure 2.10). On the contrary, a λ shock structure located downstream the design point can undergo another type of re-acceleration. The supersonic flow in the λ region speeds up due to re-expansion at the front bump ridge and this leads to another shock system, which quickens boundary layer separation. The consequence is a secondary bifurcated shock system and boundary layer thickening, both sources of total pressure loss (Figure 2.10).

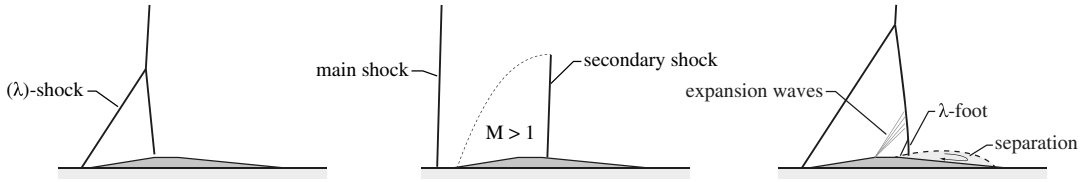

FIGURE 2.10: Shock control bump operating principle extracted from Colliss et al. (2016).

The optimal shape of the bumps is different for wave drag reduction and shock buffet suppression as shown by Mayer et al. (2019). They obtained good results with 2D bumps optimised for drag reduction and for buffet damping. However, the 3D bumps optimised for both the objectives work only for drag reduction because they are positioned too close to the shock wave. The control of oscillations is successful when the shock waves move significantly aft of the 3D bumps during buffet onset.

During the shock buffet phenomenon, the SCBs work in off-design conditions. In case of 3D bumps, primary streamwise vortex pairs are enclosed in the region immediately downstream of the bump and secondary vortex pairs exist in the outer region. Streamwise vortices are beneficial in case of separation downstream of the SBLI. For this reason, it is necessary to know the flow topology over the bumps. Colliss et al. (2016) and Wong et al. (2008) analysed the vortical structures generated by three dimensional SCBs. They showed that the flow control potential of a bump is separated from its influence on the boundary layer, which is governed by the tail. Indeed, the inspected bumps worked as vortex generators, creating a rotationally similar structure, even when the boundary layer separation on the tail altered their effective aerodynamic shape. Colliss et al. (2016) compared the flow topology over different bumps shapes and they found out that it is the flow on the ramp that governs the development of streamwise vortices in the wake rather than the flow on the tail.

2.3 Laminar bubble and transition

The aerodynamic benefits of WLE aerofoils are closely related to the modification of the flow field in the laminar-turbulent transition region and the transformation of the LSB shape. Hence, the understanding of laminar bubbles and laminar-turbulent transition is fundamental in order to comprehend the main features of this control technique.

The laminar separation bubble was studied in details by Jones et al. (2010), Alam and Sandham (2000), Pröbsting and Yarusevych (2015) and Yarusevych et al. (2009). When a laminar boundary layer over a solid surface encounters an APG, it separates and a bubble is formed. The separated shear layer undergoes transition to turbulence and the resulting flow can reattach to the surface and develop an attached turbulent BL (Figure 2.11). The transition process promotes momentum exchange between the inner and the outer regions of the wall bounded shear layer, leading to flow reattachment. LSBs can be classified by their size, short bubbles have a limited influence on the external potential flow, long bubbles alter the overall pressure distribution around the aerofoil. Before the stall condition, the transition from laminar to turbulent BL is fixed by the bubble. The stall of the aerofoil is determined by the bursting of the bubble and the flow no longer attaches to the surface or reattaches

much further downstream. In Figure 2.12, a sketch of the flow behaviour on the suction side is shown at incidence below and above the stall configuration.

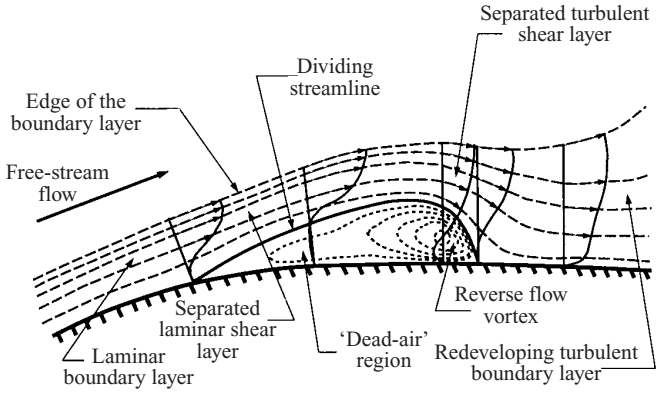

FIGURE 2.11: Sketch of laminar separation bubble extracted from Alam and Sandham (2000).

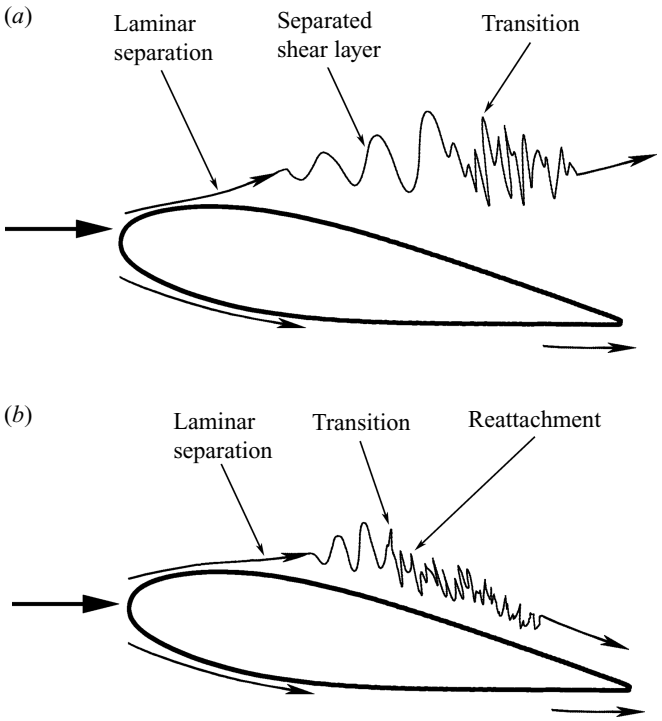

FIGURE 2.12: Sketch of the two possible flows over an aerofoil at low Reynolds numbers extracted from Yarusevych et al. (2009).

The transition is driven by external perturbations such as vortical structures or sound waves interacting with the boundary layer. The process starts with the growth of instability waves at an exponential rate (primary instability). Jones et al. (2010) distinguishes two forms of primary instabilities:

- Convective instability. A flow is perturbed at a certain point and the perturbation growth rate and velocity are such that the perturbation amplitude at that point decays in time as $t \to \infty$.

- Absolute instability. A flow is perturbed at a certain point and the perturbation growth rate and velocity are such that the perturbation amplitude at that point grows in time as $t \to \infty$. It can be predicted with linear stability theory (LST).

When primary instability perturbations reach nonlinear amplitudes, secondary instabilities advance upon the primary structures and this causes the breakdown to small scales and the development of turbulent flows. Evidences of local absolute instability were not observed with cusp map analysis. Primary instability growth is well understood and predictable, while the receptivity process is less known even if it is crucial for transition's forecast. The receptivity process allows to evaluate the initial amplitudes of primary instabilities and it also plays a role in the development of an acoustic feedback loop. The feedback loop was described and analysed by Jones et al. (2010) and Alam and Sandham (2000) and it is represented schematically in Figure 2.13.

1. Primary amplification mechanism is related to an inviscid KH instability.
2. Due to growing disturbances, the transitioning shear layer rolls up into periodically 2D shed vortices.
3. The 2D shear layer roll up is followed by 3D deformation of the vortices and breakdown into smaller structures.
4. The vortical structures reach the TE and the unsteady pressure fluctuations scatter because of the discontinuity, leading to sound waves radiation.
5. The sound waves propagate upstream to the location of receptivity and amplify the instability waves within the BL.

The amplitude of both hydrodynamic instabilities and acoustic waves increases during each cycle. The behaviour is globally unstable even if LST does not predict local absolute instability. The frequency of the feedback loop is lower than that of the convectively amplified waves and it is comparable with that of the vortex shedding. Increasing the Reynolds number, the feedback loop is disrupted due to a loss of coherence of the vortical structures and a lower amplitude of the scattered acoustic waves. The consequence is an abrupt change in shedding frequency. The frequency selection follows that expected for the transition process in separated shear layers (local convective instability).

Watmuff (1999), Marxen et al. (2004) and Pauley (1994) analysed the behaviour of LSB over a flat plate, focusing on the role of disturbances with strong spanwise variation. When the level of fluctuations in time is low, the transition process is driven by a large amplification of these disturbances. The large amplification starts in the adverse pressure gradient region and the saturation leads to shear layer roll up and vortex

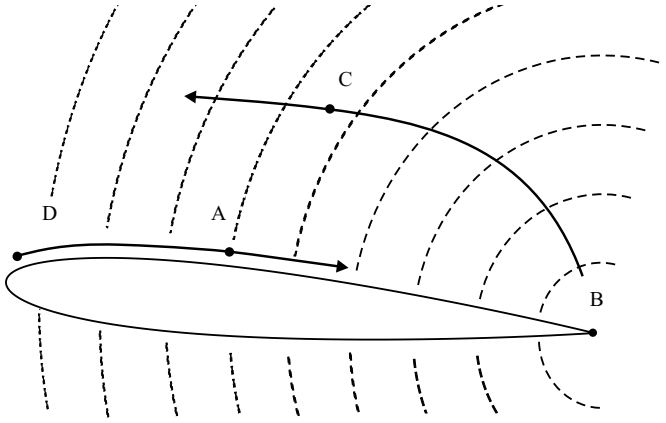

FIGURE 2.13: Sketch of acoustic feedback loop extracted from Jones et al. (2010).

shedding. This amplification is the result of a transformation from viscous wall instability (TS) to inviscid free shear layer type instability (KH). Watmuff (1999) observed steady and highly fluctuating three dimensional disturbances. The former ones are related to Gortler vortices and they are amplified by streamline curvature, the latter ones are related to a secondary instability known as K type boundary layer transition. Marxen et al. (2004) considered both steady and unsteady spanwise harmonic disturbances. A limited effect on the development of the two dimensional instability wave is observed. Pauley (1994) considered random perturbations and spanwise harmonic disturbances. The former ones have negligible effects on the structure of the LSB, the latter ones increase the length of the bubble and lessen the strength of the shed vortices.

Chapter 3

Methodology

High fidelity simulations are used to analyse WLEs in transonic flow. This chapter gives an overview about the grid generation and computational methodology, giving details about governing equations, compact finite difference schemes and high fidelity compact filters, parallelisation methods and boundary conditions. Further details can be found in Appendix A, where the grid interfaces are further explained, the matrices are explicitly written and the different boundary conditions are described.

3.1 Grid generation

A multi-block structured mesh is generated using an algebraic method. When a body is introduced inside the domain, a body-fitted curvilinear mesh is created. The starting point is the definition and the discretisation of the blocks' boundaries. Then, the interior grid points are obtained through a two dimensional interpolation technique. Figure 3.1 shows an example of a body-fitted multi-block domain, where the body is an aerofoil in the middle of the domain. The multivariate interpolation can be applied after the definition of the horizontal and vertical interfaces, domain edges and aerofoil shape.

The aerofoil is interpolated using Lagrange interpolation. The Lagrange basis polynomials

$$L_i(x) = \prod_{j=0, j\neq i}^{n} \frac{x - x_j}{x_i - x_j} \tag{3.1}$$

are linearly combined to obtain the interpolation polynomial

$$p(x) = \sum_{i=0}^{n} y_i L_i(x) \tag{3.2}$$

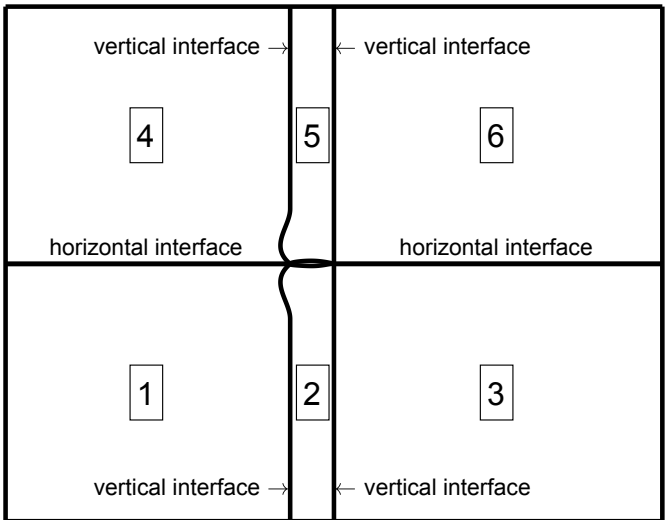

FIGURE 3.1: Multi-block grid example.

where x is the coordinate in the chordwise direction. The leading edge and the trailing edge of the aerofoil can present a slope that tends to infinity. In this case, the y coordinates are evaluated as

$$y_i = y_{i-1} + (-1)^n \Delta\eta_{min} k \tag{3.3}$$

where y is the coordinate in the vertical direction and $n = 0$ for the lower surface and $n = 1$ for the upper surface, $\Delta\eta_{min}$ is the minimum dimension of a cell in the η direction (computational space coordinate) and k is a constant equal to 0.8.

Once the body is interpolated, the other boundaries are evaluated.

1. Firstly, the x (or y) coordinate is computed, depending on the type of boundary.
2. Then, the other coordinate is evaluated as $y(x)$ (or $x(y)$), giving the desired shape to the interface.

The first step is very important because it defines the points' distribution and it has to ensure the continuity of the cells dimensions between two contiguous lines. Hence, the input parameters are the first point coordinate x_0, the last point coordinate x_1 and the derivatives of the grid at those points, dx_0 and dx_1. The points are distributed using a fifth order polynomial function $x(\xi)$, where $\xi \in [0, 1]$ and $x \in [x_0, x_1]$. A fifth order polynomial function has six free parameters, thus the following conditions are imposed

$$\begin{cases} x(0) = x_0 & x(1) = x_1 \\ \frac{dx}{d\xi}(0) = dx_0 & \frac{dx}{d\xi}(1) = dx_1 \\ \frac{d^2x}{d\xi^2}(0) = 0 & \frac{d^2x}{d\xi^2}(1) = 0 \end{cases} \tag{3.4}$$

The values of the derivative at the extremes have to be defined because the spacing between the nodes is controlled by the first derivative of the distribution function. This method allows to distribute the points with a large freedom and to have a continuous first derivative which is an essential requirement for the mesh. The continuity requirement is related to the grid metrics which appear inside the governing equations in generalised form. The distribution function imposes also the continuity of the second derivative which is always set to zero.

Once the boundary points for each block are defined and computed, the interior grid points can be obtained through an interpolation method. It is used a two dimensional multivariate interpolation method because it has the advantage that the boundary points are not changed; this is an essential requirement for a multi-block grid. The drawback is that undesired grid overlapping can be obtained when the interior points are computed. In this case, it is necessary to work on the points distribution and the interfaces shape. The freedom provided by the coordinates distribution becomes essential to obtain an accurate mesh. For example, if the domain is large, the vertical interface shape tends to create an overlapping grid. The solution is to apply the vertical interface function to a limited zone with a relatively small height and then use a vertical line that connects the interface extreme with the domain upper edge (Figure 3.1).

3.1.1 Grid metrics

When body fitted grids are used, it is necessary to transform the discretised governing equations so that they can be solved on the curvilinear grid. A curvilinear grid in physical space x,y,z (Cartesian coordinates) is transformed into a rectangular grid in computational space ξ, η, ζ (Generalised coordinates) with uniform spacing $\Delta\xi$, $\Delta\eta$, $\Delta\zeta$. The transformed equations are solved in the computational space and this requires that the partial derivatives in physical space are transformed into partial derivatives in computational space. As a consequence, the grid metrics appear in the governing equations (Section 3.2).

The matrix containing the grid metrics can be explicitly written as

$$\mathbf{D}^{-1} = \begin{bmatrix} \xi_x & \xi_y & \xi_z & \xi_t \\ \eta_x & \eta_y & \eta_z & \eta_t \\ \zeta_x & \zeta_y & \zeta_z & \zeta_t \\ 0 & 0 & 0 & 1 \end{bmatrix} = J \begin{bmatrix} (y_\eta z_\zeta - y_\zeta x_\eta) & -(x_\eta z_\zeta - x_\zeta z_\eta) & (x_\eta y_\zeta - x_\zeta y_\eta) & CF_{41} \\ -(y_\xi z_\zeta - y_\zeta z_\xi) & (x_\xi z_\zeta - x_\zeta z_\xi) & -(x_\xi y_\zeta - x_\zeta y_\xi) & CF_{42} \\ (y_\xi z_\eta - y_\eta z_\xi) & -(x_\xi z_\eta - x_\eta z_\xi) & (x_\xi y_\eta - x_\eta y_\xi) & CF_{43} \\ 0 & 0 & 0 & 1/J \end{bmatrix} \tag{3.5}$$

where

$$\begin{cases} CF_{41} &= -x_t(y_\eta z_\zeta - y_\zeta z_\eta) - y_t(x_\zeta z_\eta x_\eta z_\zeta) - z_t(x_\eta y_\zeta - x_\zeta y_\eta) \\ CF_{42} &= x_t(y_\xi z_\zeta - y_\zeta z_\xi) + y_t(x_\zeta z_\xi - x_\xi z_\zeta) + z_t(x_\xi y_\zeta - x_\zeta y_\xi) \\ CF_{43} &= -x_t(y_\xi z_\eta - y_\eta z_\xi) - y_t(x_\eta z_\xi - x_\xi z_\eta) - z_t(x_\xi y_\eta - x_\eta y_\xi) \end{cases} \tag{3.6}$$

The Jacobian of the transformation J is defined to be

$$J = \frac{\partial(\xi, \eta, \zeta, t)}{\partial(x, y, z, t)} = \begin{vmatrix} \xi_x & \xi_y & \xi_z & \xi_t \\ \eta_x & \eta_y & \eta_z & \eta_t \\ \zeta_x & \zeta_y & \zeta_z & \zeta_t \\ 0 & 0 & 0 & 1 \end{vmatrix} \tag{3.7}$$

Therefore,

$$\frac{1}{J} = \frac{\partial(x, y, z, t)}{\partial(\xi, \eta\zeta, t)} \tag{3.8}$$

3.2 Governing equations

The governing equations are the compressible Navier-Stokes equations. They are a set of partial differential equations (PDEs) and in conservation form can be expressed as

$$\frac{\partial \mathbf{Q}}{\partial t} + \frac{\partial \mathbf{E}}{\partial x} + \frac{\partial \mathbf{F}}{\partial y} + \frac{\partial \mathbf{G}}{\partial z} = \mathbf{S_v} \tag{3.9}$$

where $\mathbf{Q}$ is the conservative variables vector, $\mathbf{E}$, $\mathbf{F}$, $\mathbf{G}$ are the inviscid flux terms and $\mathbf{S_V}$ contains the viscous flux terms. These vectors can be explicitly written as

$$\mathbf{Q} = [\rho, \rho u, \rho v, \rho w, e_t]^T \tag{3.10}$$

$$\begin{cases} \mathbf{E} &= [\rho u, \rho u^2 + p, \rho uv, \rho uw, (\rho e_t + p)u]^T \\ \mathbf{F} &= [\rho v, \rho uv, \rho v^2 + p, \rho vw, (\rho e_t + p)v]^T \\ \mathbf{G} &= [\rho w, \rho uw, \rho vw, \rho w^2 + p, (\rho e_t + p)w]^T \end{cases} \tag{3.11}$$

$$\mathbf{S_v} = \frac{M_\infty}{Re_\infty}\left(\frac{\partial \mathbf{E_v}}{\partial x} + \frac{\partial \mathbf{F_v}}{\partial y} + \frac{\partial \mathbf{G_v}}{\partial z}\right) \tag{3.12}$$

where

$$\begin{cases} \mathbf{E_v} &= [0, \tau_{xx}, \tau_{xy}, \tau_{xz}, (u\tau_{xx} + v\tau_{xy} + w\tau_{xz} + q_x)]^T \\ \mathbf{F_v} &= [0, \tau_{xy}, \tau_{yy}, \tau_{yz}, (u\tau_{xy} + v\tau_{yy} + w\tau_{yz} + q_y)]^T \\ \mathbf{G_v} &= [0, \tau_{xz}, \tau_{yz}, \tau_{zz}, (u\tau_{xz} + v\tau_{yz} + w\tau_{zz} + q_z)]^T \end{cases} \tag{3.13}$$

ρ is the density of the flow, u, v and w are the x velocity component, the y velocity component and the z velocity component respectively and e_t is the total energy. The

stress tensor τ_{ij} and the heat fluxes q_i are defined as

$$\tau_{ij} = \mu\left(\frac{\partial u_i}{\partial x_j} + \frac{\partial u_j}{\partial x_i}\right) + \delta_{ij}\lambda\frac{\partial u_i}{\partial x_i} \tag{3.14}$$

$$q_i = \frac{\mu}{(\gamma-1)Pr}\frac{\partial T}{\partial x_i} \tag{3.15}$$

where μ is the dynamic viscosity, $\lambda = -2/3\mu$ is the bulk viscosity coefficient and Pr is the Prandtl number. All variables introduced in this Chapter are dimensionless. Length scales are normalised by the aerofoil mean chord L_c, time scales by L_c/a_∞, velocities by a_∞ and pressure by $\rho_\infty a_\infty^2$, while density, temperature and viscosity are normalised by their own ambient values ρ_∞, T_∞ and μ_∞ respectively.

3.2.1 Implicit LES

The flow is investigated using an implicit LES method, which means that a low-pass filter is applied to the numerical solution of Navier-Stokes equations. The governing equations are solved numerically and then filtered every time step so that the oscillations beyond the cut-off wavenumber are removed from the actual solution. This technique does not require a sub-grid scale (SGS) model that enforces dissipation of smaller scales. Garmann et al. (2013) compared the solution of transitional flows using both a SGS model and an implicit method. They showed that the ILES is capable to reproduce the flow physics halving the computational cost. The eddy viscosity coefficient was limited or ramped at the beginning of the simulation in order to stabilise the system. The adjustment of coefficients is not needed in ILES, this is a proof of its robustness.

3.2.2 Generalised equations

The set of governing equations expressed by Equation 3.9 is transformed before being numerically solved. The transformation to generalised coordinates is commonly used with finite difference schemes because it allows to set the boundary conditions easily and to stretch the grid. The drawback is the potential introduction of additional errors and the computational cost.

The coordinates transformation is given by

$$\begin{cases} \xi &= \xi(x,y,z,t) \\ \eta &= \eta(x,y,z,t) \\ \zeta &= \zeta(x,y,z,t) \end{cases} \tag{3.16}$$

Using the chain rule, Equation 3.9 can be written

$$\frac{\partial \hat{\mathbf{Q}}}{\partial t} + \frac{\partial \hat{\mathbf{E}}}{\partial \xi} + \frac{\partial \hat{\mathbf{F}}}{\partial \eta} + \frac{\partial \hat{\mathbf{G}}}{\partial \zeta} = \hat{\mathbf{S}}_{\mathbf{v}} \tag{3.17}$$

where

$$\hat{\mathbf{S}}_{\mathbf{v}} = \frac{M_\infty}{Re_\infty}\left(\frac{\partial \hat{\mathbf{E}}_{\mathbf{v}}}{\partial \xi} + \frac{\partial \hat{\mathbf{F}}_{\mathbf{v}}}{\partial \eta} + \frac{\partial \hat{\mathbf{G}}_{\mathbf{v}}}{\partial \zeta}\right) \tag{3.18}$$

The variables in cartesian coordinates are related to the ones in generalised coordinates by the following relations

$$\begin{gathered}
\hat{\mathbf{Q}} = \frac{\mathbf{Q}}{J} \\
\hat{\mathbf{E}} = \frac{\xi_x \mathbf{E} + \xi_y \mathbf{F} + \xi_z \mathbf{G}}{J} \quad \hat{\mathbf{F}} = \frac{\eta_x \mathbf{E} + \eta_y \mathbf{F} + \eta_z \mathbf{G}}{J} \quad \hat{\mathbf{G}} = \frac{\zeta_x \mathbf{E} + \zeta_y \mathbf{F} + \zeta_z \mathbf{G}}{J} \\
\hat{\mathbf{E}}_{\mathbf{v}} = \frac{\xi_x \mathbf{E}_{\mathbf{v}} + \xi_y \mathbf{F}_{\mathbf{v}} + \xi_z \mathbf{G}_{\mathbf{v}}}{J} \quad \hat{\mathbf{F}}_{\mathbf{v}} = \frac{\eta_x \mathbf{E}_{\mathbf{v}} + \eta_y \mathbf{F}_{\mathbf{v}} + \eta_z \mathbf{G}_{\mathbf{v}}}{J} \quad \hat{\mathbf{G}}_{\mathbf{v}} = \frac{\zeta_x \mathbf{E}_{\mathbf{v}} + \zeta_y \mathbf{F}_{\mathbf{v}} + \zeta_z \mathbf{G}_{\mathbf{v}}}{J}
\end{gathered} \tag{3.19}$$

Equation 3.17 is discretised in space using a compact finite difference scheme and then the obtained result is discretised in time using a Runge-Kutta method.

3.3 Numerical schemes

3.3.1 Compact finite difference schemes

High fidelity simulations try to solve the governing equations numerically with a high level of accuracy. Spectral methods can solve the equations on the whole range of scales. The drawbacks are the restrictions on geometry complexity and boundary conditions. The compact finite difference schemes provide an accurate representation of the shorter length scales without the spectral methods limitations.

The general expression for the approximation of the first derivative is

$$\beta \overline{f}'_{i-2} + \alpha \overline{f}'_{i-1} + \overline{f}'_i + \alpha \overline{f}'_{i+1} + \beta \overline{f}'_{i+2} = \frac{1}{\Delta x} \sum_{m=1}^{3} a_m (f_{i+m} - f_{i-m}) \tag{3.20}$$

where f_i and f'_i represent an objective function and its spatial derivative, while $\overline{f}'_i$ represents the numerical approximation of the derivative. The spatial interval Δx is a constant because all the grid points are equally spaced. Matching the coefficients with the Taylor series expansion up to the tenth order brings to the following conditions

(Lele (1992))

$$\begin{aligned}
1+2(\alpha+\beta) &= 2\sum_{m=1}^{3} m a_m && \text{second order} \\
3(\alpha+4\beta) &= 2\sum_{m=1}^{3} m^3 a_m && \text{fourth order} \\
10(\alpha+16\beta) &= 2\sum_{m=1}^{3} m^5 a_m && \text{sixth order} \\
14(\alpha+64\beta) &= 2\sum_{m=1}^{3} m^7 a_m && \text{eighth order} \\
18(\alpha+256\beta) &= 2\sum_{m=1}^{3} m^9 a_m && \text{tenth order}
\end{aligned} \tag{3.21}$$

The coefficients for a pentadiagonal eighth-order scheme with five-point stencil are

$$\begin{gathered}
\alpha = \frac{4}{9} \quad \beta = \frac{1}{36} \\
a_1 = \frac{40}{54} \quad a_2 = \frac{25}{216} \quad a_3 = 0
\end{gathered} \tag{3.22}$$

Depending on the formal accuracy, different families of schemes with different sets of parameters are obtained, they present different characteristics in terms of resolution when analysed in the wavenumber domain. High order schemes have more restrictions and thus the number of free parameters decreases. For instance, the tenth order scheme has a closed set of equations. On the contrary, a lower order model has some free parameters that can be used to add constraints and improve the resolution characteristics.

3.3.2 High order compact filters

The high order compact FD schemes represent the analytical differentiation up to high wavenumbers. However, the numerical method formulated so far presents different sources of error:

1. the FD schemes do not cover the entire spectra
2. the grid topology is directly included in the governing equations through the grid metrics, thus spurious waves can easily develop in the zones where the grid is not smooth enough
3. the boundary schemes are dissipative at high wavenumbers but the interior schemes are not dissipative because of the central formulation

For these reasons, it is necessary to introduce a numerical treatment that avoids spurious solutions to develop and makes the algorithm stable before time

discretisation. The method is based on the application of high order compact filters introduced by Kim (2010) that damp the spurious solutions up to a defined cut-off wavenumber κ_c.

The present method is based on a pentadiagonal type of compact filter with a seven-point stencil that can be expressed as

$$\beta\hat{\Delta}f_{i-2} + \alpha\hat{\Delta}f_{i-1} + \hat{\Delta}f_i + \alpha\hat{\Delta}f_{i+1} + \beta\hat{\Delta}f_{i+2} = \sum_{m=1}^{3} a_m(f_{i-m} - 2f_i + f_{i+m}) \tag{3.23}$$

where $\hat{\Delta}f_i = \hat{f}_i - f_i$ is the difference between the filtered and the original functions. Once Equation 3.23 is solved in the entire domain, the filtered values $\hat{f}_i = f_i + \hat{\Delta}f_i$ are determined subsequently.

There are five unknown coefficients in Equation 3.23. Imposing a sixth order formal accuracy, the number of free coefficients is reduced to three. The remaining coefficients are defined as a function of the cut-off wavenumber. First, the transfer function $T(\kappa)$ is introduced. It is the ratio of the filtered value to the original one at a certain wavenumber, where $T(\kappa) = 1$ is no filtering and $T(\kappa) = 0$ is complete filtering. The definition of the cut-off wavenumber is obtained by the following relation

$$T(\kappa) = k_r \qquad 0 < \kappa < \pi \tag{3.24}$$

It is possible to obtain the coefficients as a function of the cut-off wavenumber κ_c and the constant k_r

$$\begin{aligned}
\alpha &= A(\kappa_c)k_r(20(2k_r-1) - 30\cos(\kappa_c) + 12(2k_r-1)\cos(2\kappa_c) - 2\cos(3\kappa_c)) \\
\beta &= \frac{A(\kappa_c)}{2}k_r(2(13-8k_r) + (33-48k_r)\cos(\kappa_c) + 6\cos(2\kappa_c) - \cos(3\kappa_c)) \\
a_1 &= A(\kappa_c)60(1-k_r)k_r\cos^4(\kappa_c/2) \qquad a_2 = -A(\kappa_c)\frac{2a_1}{5} \qquad a_3 = \frac{a_1}{15} \\
A(\kappa_c) &= \frac{1}{30 + 5(7-16k_r)\cos(\kappa_c) + 2(1+8k_r)\cos(2\kappa_c) - 3\cos(3\kappa_c)}
\end{aligned} \tag{3.25}$$

In the following simulations, the coefficient k_r is always set to 0.5.

3.3.3 Artificial dissipation

High order and high resolution numerical schemes are formulated to be less dissipative and dispersive than low order standard ones. As a consequence, they are less suitable for the computation of non linear waves solutions, in particular when a discontinuity is present. The non linear wave steepening process corresponds to an energy cascade process in the wavenumber domain. Low wavenumber components are transferred into high wavenumber range. The central differences generally

produce spurious spatial oscillations near the shock. These oscillations arise from the unresolved high wavenumber components generated by the non linear cascading process. The computed non linear wave remains accurate as long as the cascading process does not transfer wave components into the unresolved narrow band of high wavenumber range. For this reason an artificial dissipative model has to be introduced.

Kim and Lee (2001) proposed an improved artificial dissipation model for Computational Aeroacoustics (CAA), which removes the spurious numerical oscillations near the shock but hardly affects the linear acoustic waves. The artificial selective damping model proposed by Tam (1995) and the non linear artificial dissipation model proposed by Jameson et al. (1981) are combined to improve the shock capturing property progressively. Moreover, an adaptive control constant is introduced to adjust the local level of dissipation automatically, according to flow conditions and grid mesh.

In this case, a high order filter is applied as described in details in Section 3.3.2. The filter can be useful when the shock is weak, but it is not sufficient with a strong shock wave. The idea is to combine a filter with an artificial dissipation model that is activated by a discontinuity detector. In regions of strong discontinuity the shock capturing term dominates, but outside these regions it becomes negligible and the filter is dominant. The artificial dissipation is directly applied to the conservative variables. In a one dimensional problem, it can be written

$$\hat{\mathbf{Q}}_i = \underbrace{\mathbf{Q}_i + \hat{\Delta}\mathbf{Q}_i}_{\text{filtered conservative variables}} + \overbrace{\epsilon[k(\mathbf{Q}_{i-1} - 2\mathbf{Q}_i + \mathbf{Q}_{i+1}) - \hat{\Delta}\mathbf{Q}_i]}^{\text{artificial dissipation}} \tag{3.26}$$

where $k = 1/4$ and ϵ is the dissipation function

$$\epsilon = 1 - \frac{1}{1 + c_{sh}|\nu_i|} \tag{3.27}$$

c_{sh} is a function of Mach number, while ν_i is the shock detector, a function of pressure

$$\nu_i = p_{i-1} - 2p_i + p_{i+1} \tag{3.28}$$

$$c_{sh} = \frac{c_{sr}\sigma}{\gamma} \tag{3.29}$$

where $\sigma = \max(M_{max} - 1/3, 0)$ and c_{sr} is a user-defined constant. If c_{sr} is set equal to zero, the artificial dissipation is never introduced inside the system. If c_{sr} is too high, it decreases the actual Reynolds number inside the boundary layer and the flow becomes steady. Hence, this parameter should be set carefully taking into account that it can change the physics of the problem.

3.3.4 Parallelisation

Parallel computing is required when high-fidelity simulations are applied to real problems. In this code, the parallelisation is done using the Message Passing Interface (MPI) library. Thus, each processor executes the program independently on a portion of the domain. When it needs information from other parts of the domain, it receives this information from another processor. The advantage is that memory locality is encouraged, thus there is no shared memory space and the risk of race conditions is avoided. The main issue of using distributed architectures is that the algorithm of a numerical method usually has to be mathematically reformulated in order to minimise the communication between cores.

The strategy is to split each block of the grid into subdomains. The communication between subdomains can be performed using halo points as suggested by Kim and Sandberg (2012). They parallelised the compact finite difference scheme using halo points and the high order filter using a predictor-corrector method. Although this work shows a great improvement with respect to previous methods such as Sengupta et al. (2007), parallel artefacts are observed with vortex-driven flows.

In order to improve the solution at the subdomains boundaries, Kim (2013) proposed a set of differencing and filtering subdomain boundary (SB) schemes. The system of equations formed by the differencing and the filtering schemes, given by Equation 3.20 and 3.23, can be expressed in matrix-vector form

$$\begin{aligned} \mathbf{P}\bar{\mathbf{f}}' &= \frac{1}{\Delta x}\mathbf{Q}\mathbf{f} \qquad \text{differencing} \\ \mathbf{P}_F\hat{\Delta}\mathbf{f} &= \mathbf{Q}_F\mathbf{f} \qquad \text{filtering} \end{aligned} \tag{3.30}$$

where $\mathbf{f}$, $\bar{\mathbf{f}}'$ and $\hat{\Delta}\mathbf{f}$ are the objective function, the numerical derivative and the filter's contribution, respectively.

In order to perform parallel computations with the compact schemes and filters, it is necessary to allow independent inversion of the pentadiagonal matrices within each subdomain. This can be achieved if the matrix $\mathbf{P}$ is transformed into a modified matrix $\mathbf{R}$ that has no elements shared between two subdomains. The same can be written for a modified matrix $\mathbf{R}_F$ of the original matrix $\mathbf{P}_F$. The modified matrices for the differencing and the filtering can be written as

$$\begin{aligned} \mathbf{R} &= \left[\begin{array}{c|c} \mathbf{R}_A & \mathbf{0} \\ \hline \mathbf{0} & \mathbf{R}_B \end{array}\right] \\ \mathbf{R}_F &= \left[\begin{array}{c|c} \mathbf{R}_{FA} & \mathbf{0} \\ \hline \mathbf{0} & \mathbf{R}_{FB} \end{array}\right] \end{aligned} \tag{3.31}$$

The present approach considers two completely separated subdomains with no overlapped points. The defined matrices $\mathbf{R}$ and $\mathbf{R}_F$ can be applied to Equation 3.30 without affecting the solutions $\bar{\mathbf{f}}'$ and $\hat{\Delta}\mathbf{f}$.

$$\begin{aligned} \mathbf{R}\bar{\mathbf{f}}' &= \frac{1}{\Delta x}\mathbf{R}\mathbf{P}^{-1}\mathbf{Q}\mathbf{f} = \frac{1}{\Delta x}\mathbf{S}\mathbf{f} \\ \mathbf{R}_F\hat{\Delta}\mathbf{f} &= \mathbf{R}_F\mathbf{P}_F^{-1}\mathbf{Q}_F\mathbf{f} = \mathbf{S}_F\mathbf{f} \end{aligned} \tag{3.32}$$

The new matrices $\mathbf{S}$ and $\mathbf{S}_F$ can be written as

$$\begin{aligned} \mathbf{S} = \mathbf{R}\mathbf{P}^{-1}\mathbf{Q} &= \left[\begin{array}{c|c} \mathbf{S}_A & \mathbf{T}_B \\ \hline \mathbf{T}_A & \mathbf{S}_B \end{array}\right] \\ \mathbf{S}_F = \mathbf{R}_F\mathbf{P}_F^{-1}\mathbf{Q}_F &= \left[\begin{array}{c|c} \mathbf{S}_{FA} & \mathbf{T}_{FB} \\ \hline \mathbf{T}_{FA} & \mathbf{S}_{FB} \end{array}\right] \end{aligned} \tag{3.33}$$

The differencing matrices $\mathbf{R}$, $\mathbf{P}$ and $\mathbf{Q}$ and the filtering matrices $\mathbf{R}_F$, $\mathbf{P}_F$ and $\mathbf{Q}_F$ can be evaluated in each subdomain using the coefficients defined in Sections 3.3.1 and 3.3.2. After that, two quasi-disjoint systems can be solved for each subdomain in order to obtain $\bar{\mathbf{f}}'$ and $\hat{\Delta}\mathbf{f}$.

$$\begin{aligned} \text{subdomain A:} &\begin{cases} \mathbf{R}_A\bar{\mathbf{f}}'_A = \frac{1}{\Delta x}(\mathbf{S}_A\mathbf{f}_A + \mathbf{T}_B\mathbf{f}_B) \\ \mathbf{R}_{FA}\hat{\Delta}\mathbf{f}_A = \mathbf{S}_{FA}\mathbf{f}_A + \mathbf{T}_{FB}\mathbf{f}_B \end{cases} \\ \text{subdomain B:} &\begin{cases} \mathbf{R}_B\bar{\mathbf{f}}'_B = \frac{1}{\Delta x}(\mathbf{S}_B\mathbf{f}_B + \mathbf{T}_A\mathbf{f}_a) \\ \mathbf{R}_{FB}\hat{\Delta}\mathbf{f}_B = \mathbf{S}_{FB}\mathbf{f}_B + \mathbf{T}_{FA}\mathbf{f}_A \end{cases} \end{aligned} \tag{3.34}$$

3.4 Boundary conditions

In Section 3.3 the numerical methods that discretise spatial derivatives have been introduced. Boundary conditions have to be imposed to close the problem, they represent the solution outside the domain and its influence on the interior points. The key idea is that boundary conditions are imposed when a characteristic wave propagates towards the interior of the domain, while no conditions are needed when the wave propagates away from the domain.

Characteristic boundary conditions (CBCs) are imposed because accurate time dependent boundary conditions are needed in order to solve the entire conservation form governing equations at the body surface and at the far field plane. CBCs were presented originally by Thompson (1987, 1990). In this case, the governing equations are solved in a generalised form, thus the generalised characteristic boundary conditions (GCBCs) are introduced. They were illustrated in details by Kim and Lee (2000, 2004). The formulation described in this section is similar but it is a dimensionally consistent one.

First of all, the governing equations are transformed into a characteristic form, which is a decomposition of the conservation equations into locally one dimensional wave modes. The starting point is the conservation form in Cartesian coordinates given by Equation 3.9. It is transformed into a quasi-linear form using Jacobian matrices.

$$\frac{\partial \mathbf{Q}}{\partial t} + \mathbf{A}\frac{\partial \mathbf{Q}}{\partial x} + \mathbf{B}\frac{\partial \mathbf{Q}}{\partial y} + \mathbf{C}\frac{\partial \mathbf{Q}}{\partial z} = \mathbf{S_V} \tag{3.35}$$

where the Jacobian matrices are defined as

$$\mathbf{A} = \frac{\partial \mathbf{E}}{\partial \mathbf{Q}} \qquad \mathbf{B} = \frac{\partial \mathbf{F}}{\partial \mathbf{Q}} \qquad \mathbf{C} = \frac{\partial \mathbf{G}}{\partial \mathbf{Q}} \tag{3.36}$$

The equations are also written in terms of primitive variables.

$$\frac{\partial \mathbf{Q}'}{\partial t} + \mathbf{A}'\frac{\partial \mathbf{Q}'}{\partial x} + \mathbf{B}'\frac{\partial \mathbf{Q}'}{\partial y} + \mathbf{C}'\frac{\partial \mathbf{Q}'}{\partial z} = \mathbf{S}'_\mathbf{V} \tag{3.37}$$

These forms of the equations are related through the matrix $\mathbf{M} = \partial \mathbf{Q}/\partial \mathbf{Q}'$.

$$\begin{gathered} \mathbf{A}' = \mathbf{M}^{-1}\mathbf{A}\mathbf{M} \qquad \mathbf{B}' = \mathbf{M}^{-1}\mathbf{B}\mathbf{M} \qquad \mathbf{C}' = \mathbf{M}^{-1}\mathbf{C}\mathbf{M} \\ \mathbf{S_V}' = \mathbf{M}^{-1}\mathbf{S_V} \end{gathered} \tag{3.38}$$

The quasi-linear equations in terms of conservative and primitive variables are transformed in generalised coordinates. Applying the chain rule to Equation 3.35 and 3.37, it is obtained

$$\frac{\partial \mathbf{Q}}{\partial t} + \mathbf{K}_\xi\frac{\partial \mathbf{Q}}{\partial \xi} + \mathbf{K}_\eta\frac{\partial \mathbf{Q}}{\partial \eta} + \mathbf{K}_\zeta\frac{\partial \mathbf{Q}}{\partial \zeta} = \mathbf{S_V} \tag{3.39}$$

$$\frac{\partial \mathbf{Q}'}{\partial t} + \mathbf{K}'_\xi\frac{\partial \mathbf{Q}'}{\partial \xi} + \mathbf{K}'_\eta\frac{\partial \mathbf{Q}'}{\partial \eta} + \mathbf{K}'_\zeta\frac{\partial \mathbf{Q}'}{\partial \zeta} = \mathbf{S}'_\mathbf{V} \tag{3.40}$$

where the flux Jacobian matrices in generalised coordinates can be written as

$$\begin{aligned} \mathbf{K}_\xi &= \xi_x\mathbf{A} + \xi_y\mathbf{B} + \xi_z\mathbf{C} \\ \mathbf{K}'_\xi &= \xi_x\mathbf{A}' + \xi_y\mathbf{B}' + \xi_z\mathbf{C}' \end{aligned} \tag{3.41}$$

The same can be written in η and ζ directions. The relation between the conservative form and the primitive form of the matrix is again a function of matrix $\mathbf{M}$.

$$\mathbf{K}_\xi = \mathbf{M}\mathbf{K}'_\xi\mathbf{M}^{-1} \tag{3.42}$$

The flux Jacobian matrices can be diagonalised

$$\mathbf{K}_\xi = \mathbf{P}\mathbf{\Lambda}\mathbf{P}^{-1} \tag{3.43}$$

$$\mathbf{K}'_\xi = \mathbf{P}'\mathbf{\Lambda}\mathbf{P}'^{-1} \tag{3.44}$$

where $\mathbf{P}$ and $\mathbf{P}'$ are the eigenvector matrices, while $\mathbf{\Lambda}$ is the eigenvalues matrix and it

is the same for both flux Jacobian matrices. The relation between the two eigenvector matrices is again a function of the matrix $\mathbf{M}$.

$$\mathbf{P} = \mathbf{M}\mathbf{P}' \qquad \mathbf{P}^{-1} = \mathbf{P}'^{-1}\mathbf{M}^{-1} \tag{3.45}$$

The eigenvalues matrix is a diagonal matrix and it is given by

$$\mathbf{\Lambda} = \mathrm{diag}[U_{\tilde{\xi}}, U_{\tilde{\xi}}, U_{\tilde{\xi}}, U_{\tilde{\xi}} + c|\tilde{\xi}|, U_{\tilde{\xi}} - c|\tilde{\xi}|] \tag{3.46}$$

Equation 3.39 and 3.40 can be transformed in a characteristic form. It is considered only the equation in conservative variables, the same formulation can be written in primitive variables.

$$\frac{\partial \mathbf{Q}}{\partial t} + \mathbf{K}_{\tilde{\xi}} \frac{\partial \mathbf{Q}}{\partial \tilde{\xi}} = \mathbf{S}_{\mathbf{V}}^{*} = \mathbf{S}_{\mathbf{V}} - \left(\mathbf{K}_{\eta} \frac{\partial \mathbf{Q}}{\partial \eta} + \mathbf{K}_{\zeta} \frac{\partial \mathbf{Q}}{\partial \zeta} \right) \tag{3.47}$$

The equation is then multiplied with the matrix $\mathbf{P}^{-1}$ and a characteristic form is obtained

$$\mathbf{P}^{-1} \frac{\partial \mathbf{Q}}{\partial t} + \mathbf{L} = \mathbf{P}^{-1} \mathbf{S}_{\mathbf{V}}^{*} = \mathbf{S}_{\mathbf{C}} \tag{3.48}$$

where $\mathbf{L}$ is the amplitude variation of the characteristic waves and it can be written as

$$\mathbf{L} = \mathbf{\Lambda}\mathbf{P}^{-1} \frac{\partial \mathbf{Q}}{\partial \tilde{\xi}} = \mathbf{P}^{-1} \mathbf{K}_{\tilde{\xi}} \frac{\partial \mathbf{Q}}{\partial \tilde{\xi}} \tag{3.49}$$

It is introduced a characteristic variable $\mathbf{R}$ defined as

$$\delta \mathbf{R} = \mathbf{P}^{-1} \delta \mathbf{Q} \tag{3.50}$$

It is finally obtained the characteristic form in the direction normal to the computational boundary surface where $\tilde{\xi}$ keeps a constant value

$$\frac{\partial \mathbf{R}}{\partial t} + \mathbf{\Lambda} \frac{\partial \mathbf{R}}{\partial \tilde{\xi}} = \mathbf{S}_{\mathbf{C}} \tag{3.51}$$

The diagonal terms of the eigenvalues matrix represent entropy (first term), vorticity (second and third terms) and acoustic waves (fourth and fifth terms). Entropy and vorticity waves convect with flow velocity, whereas acoustic waves convection is a function of flow velocity and speed of sound. For subsonic flows, the first four waves enter inside the domain and the fifth one exits the domain at an inlet boundary ($\tilde{\xi} = 0$). At the outlet boundary, the fifth wave is the only incoming wave.
Equation 3.51 is the starting point of the GCBCs proposed by Kim and Lee (2000, 2004). The overall procedure is given by the following steps.

- Once the flux derivatives are evaluated using the numerical methods introduced in the previous section, the normal flux derivative $\partial \hat{\mathbf{E}} / \partial \tilde{\xi}$ on the boundary is

used as an initial guess.

- The initial guess of the characteristic convection term on the boundary is evaluated as

$$\mathbf{L} = \mathbf{P}^{-1} J \hat{\mathbf{D}} \tag{3.52}$$

where $\hat{\mathbf{D}}$ depends on the imposed condition. It is defined as $\hat{\mathbf{D}} = \frac{\partial \hat{\mathbf{E}}}{\partial \xi}$ for the non reflective conditions and as $\hat{\mathbf{D}} = \frac{\partial \hat{\mathbf{E}}}{\partial \xi} + \frac{\partial \hat{\mathbf{F}}}{\partial \eta} + \frac{\partial \hat{\mathbf{G}}}{\partial \zeta} - \hat{\mathbf{S}}_V$ for the wall conditions and the characteristic interface conditions (CICs).

- The characteristic convection term on the boundary is modified imposing the proper conditions, it is indicated as $\mathbf{L}^*$.

- The normal flux derivative is corrected adding $\frac{\mathbf{P}}{J}(\mathbf{L}^* - \mathbf{L})$.

3.5 Non reflective treatments

Sponge zone techniques can be used to derive both inflow and outflow BCs, they work for inflow forcing and outflow damping. The computational domain is divided into two parts:

1. the physical domain where the physical phenomena are simulated and analysed during the post-processing
2. the sponge zone where a source term is added on the right hand side (RHS) of the governing equations and a special treatment is applied

This treatment is widely used because it is effective in damping the reflections and the additional number of computations per point is low. The issue is the need of a nonphysical domain which, in same kinds of simulations, can be quite broad. For this reason, it is usually coupled with the CBCs at the boundary in order to decrease the width of the sponge layer.

In this section, it is presented the sponge condition proposed by Kim et al. (2010b,a) where the pressure is forced instead of the total energy and a weighting factor to the velocity forcing term is introduced. The first modification is made because the total energy forcing in the conventional sponge conditions overrides the density and velocity forcing of the other equations. The second modification generates a velocity forcing function which is stronger at the upstream boundary. This is done because when there is a solid body inside the domain and it is forced a gust through the sponge, the velocity distribution downstream of the body does not follow the function

imposed upstream, thus an excessive constraint should be avoided.

$$\mathbf{S}_{sponge} = -\sigma \frac{a_\infty}{L} \begin{bmatrix} \rho - \rho_{target} \\ \lambda(\rho u - \rho_{target} u_{target}) \\ \lambda(\rho v - \rho_{target} v_{target}) \\ \lambda(\rho w - \rho_{target} w_{target}) \\ p - p_{target} \end{bmatrix} \tag{3.53}$$

where σ is a function of space and it is set to zero inside the physical domain, while it grows smoothly inside the sponge layers. This parameter control the strength of the forcing and the damping. The weighting factor λ is also a function of space and it allows to have better control over the velocity forcing. The sponge coefficient profile and the weighting factor for a 2D problem are given by

$$\sigma(x,y) = \sigma_0 \frac{[1 + \cos(\pi A(x) B(y))]}{2} \tag{3.54}$$

$$A(x) = 1 - \max\Big(1 - \frac{x - x_{min}}{L_s}, 0\Big) - \max\Big(1 - \frac{x_{max} - x}{L_s}, 0\Big)$$

$$B(y) = 1 - \max\Big(1 - \frac{y - y_{min}}{L_s}, 0\Big) - \max\Big(1 - \frac{y_{max} - y}{L_s}, 0\Big)$$

and

$$\lambda = \lambda(x) = \frac{1 - \tanh(x/L_s) + \epsilon}{2 + \epsilon} \tag{3.55}$$

where x_{min} and x_{max} are the left and right boundaries of the domain respectively, while y_{min} and y_{max} are the bottom and top boundaries. L_s is the sponge dimension and ϵ is an ad-hoc constant to control the weighting in the downstream region and it is set to $2/9$. In Figure 3.2, a contour of the conventional profile of the sponge zone and the velocity forcing profile are illustrated. The first one is applied to density and pressure, while the second one to velocity components. The velocity forcing profile is stronger at the upstream inflow boundary and it diminishes smoothly to zero at a specified x location. This profile avoids excessive velocity constraints on the outflow condition.

3.6 Time discretisation

In Section 3.3, the methods for the spatial discretisation have been described extensively. Once the spatial derivatives are discretised, a system of ordinary differential equations (ODEs) needs to be solved. It can be written as

$$\frac{d\mathbf{Q}}{dt} = \mathbf{F}(\mathbf{Q}, t) \tag{3.56}$$

where $\mathbf{Q}$ is the vector of conservative variables and $\mathbf{F}$ contains all the fluxes. The system of ODEs is solved using an explicit fourth order Runge-Kutta scheme.

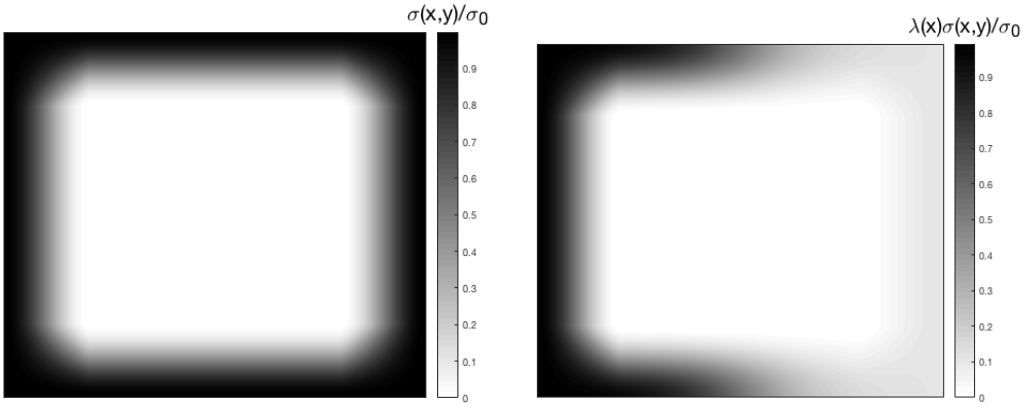

(A) (B)

FIGURE 3.2: The conventional sponge damping coefficient profile (a) and the damping coefficient profile for velocity forcing (b).

The time integration method is explicit, hence the time step needs to be carefully evaluated in order to avoid instabilities. In particular, the Courant-Friedrichs-Levy (CFL) condition should be respected.

$$CFL = \Delta t U_{\xi} + \Delta t U_{\eta} + \Delta t U_{\zeta} \leq 1 \tag{3.57}$$

where U_{ξ}, U_{η} and U_{ζ} are the characteristic wave's convection velocities in the three computational directions ξ, η and ζ, respectively. This condition avoids that the information crosses more than one cell per time step, it is a fundamental requirement for the stability of the system.

3.7 Grid validation

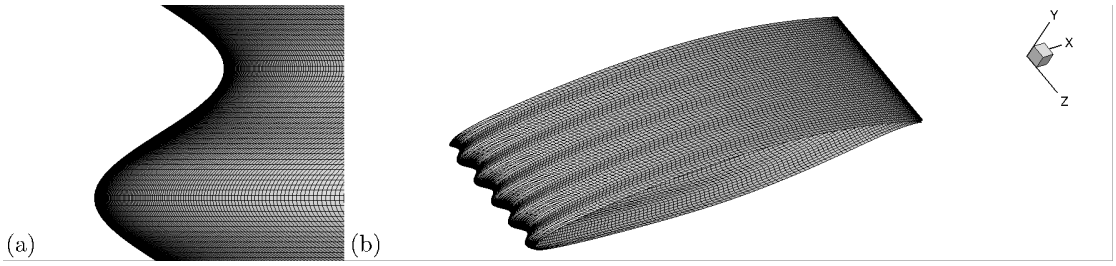

FIGURE 3.3: Leading edge view of wavy aerofoil ($h_{LE} = 0.0125L_c$) based on Dassault Aviations V2C profile with 100% of the points shown (a) and mesh over the all wavy aerofoil surface (repeated 5 times) with 20% of the points shown (b).

Both unswept and swept wing sections are simulated throughout this thesis with a Mach number normal to the wing of 0.7. The mesh is validated with an unswept straight aerofoil at $Re_{\infty} = 500,000$, $\alpha = 7.0^{o}$, where the Reynolds number is defined with respect to the aerofoil chord. A Dassault Aviations V2C profile (Figure 3.4b) is

used throughout this study, which is a laminar supercritical profile designed to delay the laminar-turbulent transition on the pressure and suction sides of the aerofoil, thus to minimise the skin friction drag.

The WLE aerofoil geometry (Figure 3.3) is given by

$$\begin{cases} x_B(z) = k_w(z)(x_A - x_{TE}) + x_{TE} \\ y_B(z) = k_w(z)(y_A - y_{TE}) + y_{TE} \end{cases} \tag{3.58}$$

where

$$k_w = 1 - \frac{h_{LE}}{L_c} \sin\left[\frac{2\pi(z - z_0)}{\lambda_{LE}}\right], \tag{3.59}$$

where (x_A, y_A) represents the coordinates of the original (unmodified) aerofoil section, and (x_B, y_B) the corresponding coordinates of the modified aerofoil section varying with the spanwise coordinate. This definition of WLE geometry provides the same volume on a wing section between the wavy and the straight case when an integer number of wavelengths is simulated.

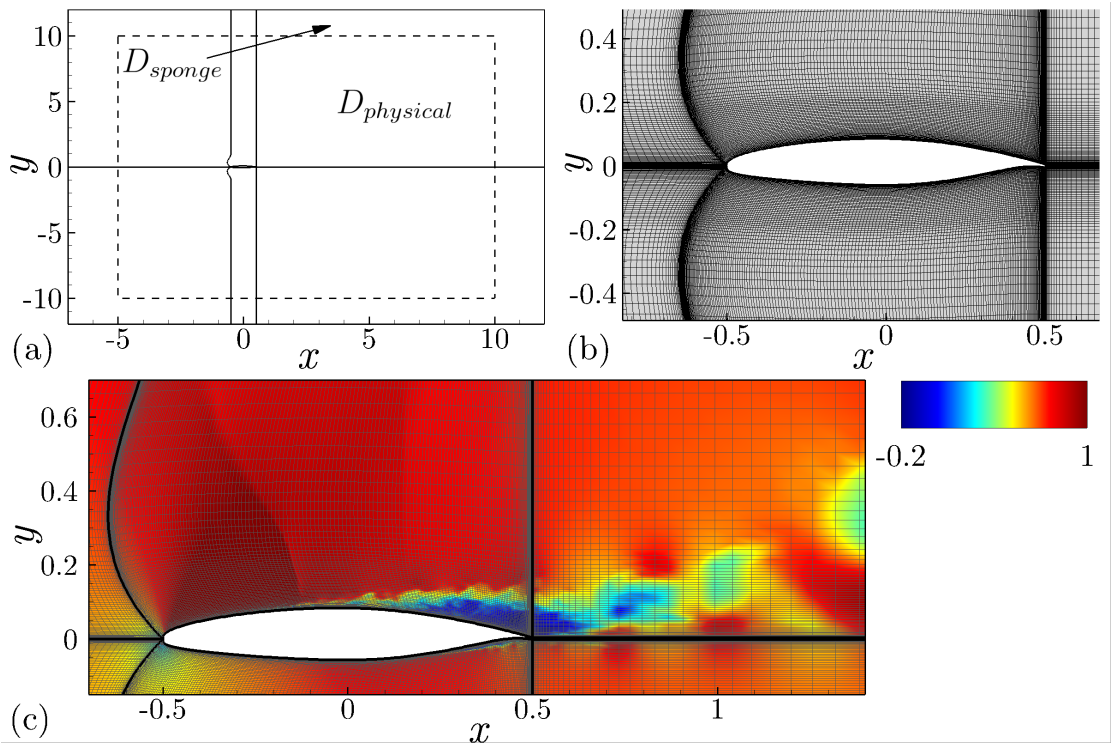

FIGURE 3.4: Computational domain highlighting physical domain and sponge layer (a), close up near the aerofoil and the wake with 25% of points shown and the streamwise velocity flow field (b), close up near the aerofoil with 25% of points shown (c) and mesh over the surface of the wavy aerofoil (repeated 5 times) with 50% of the points shown (d).

The computational domain is shown in Figure 3.4a, where the dashed line separates the physical domain from the sponge layer. A structured multi-block grid is used based on a H-topology, stretched in both streamwise and vertical directions. A very

	$n_{\xi AERO}$	n_ξ	n_η	n_ζ	$n_{tot}/10^6$
G1	800	1430	800	50	57.2
G2	1000	1630	800	50	65.2
G3	800	1430	800	75	85.8

TABLE 3.1: Details of grids used for validation of SLE aerofoil simulation at $\alpha = 7.0^o$ and $Re_\infty = 500,000$.

	G1	G2	G3
C_L	0.943	0.931	0.936
C_D	0.084	0.089	0.088
C_L/C_D	11.23	10.46	10.63

TABLE 3.2: Mean lift, drag and efficiency obtained during the grid validation for SLE aerofoil.

fine grid spacing is imposed close to block boundaries to avoid loss of accuracy due to boundary compact schemes (Figure 3.4b). Figure 3.4c shows that the grid cells are clustered vertically in the region $y = \pm 0.2$ in order to capture properly the interaction between the shock wave and the boundary layer. The spanwise domain size is denoted by L_z , and it is set to 0.05. Zauner et al. (2018b) have proved that this spanwise domain size is sufficient to investigate the aerodynamic unsteady phenomena on the Dassault Aviations V2C aerofoil in transonic flow with high fidelity simulations. The aerofoil is placed at the centre of the domain with the origin at the mid-chord location. The domain size is $x \in [-7, 12]$ in the streamwise direction, $y \in [-12, 12]$ in the vertical direction, and $z \in [-L_z/2, L_z/2]$ in the spanwise direction.

The grid is validated with three different grids on the straight aerofoil, they are reported in Table 3.1 where n_ξ, n_η and n_ζ are the number of points in the streamwise, vertical and spanwise direction, respectively. G1 is the grid used for all the analyses. Since no turbulence model is included, a sufficiently high level of near-wall grid resolution is maintained in order to properly resolve the boundary layers throughout the surface. The distribution of the mean wall variable in the normal direction is always below 1. In the streamwise direction it is between the direct numerical simulation (DNS) and the large eddy simulation (LES) range (Garmann et al. (2013)), while in the spanwise direction it is in the low LES range. In particular, in streamwise direction $\Delta x^+ < 40$ and in spanwise direction $\Delta z^+ < 20$. G2 is a grid refined in the streamwise direction increasing the number of cells on the aerofoil by 20%, while G3 is a grid refined in the spanwise direction by 50%. The value of the wall variables for the three grids are reported in Table 3.3.

The time and spanwise averaged pressure (C_p) and skin friction (C_f) coefficients obtained with the grids in Table 3.1 are compared in Figure 3.5a and 3.5b. For both variables, there is a close agreement, demonstrating a reasonable level of grid convergence. Since in this study there is a large unsteady analysis, Figure 3.5c and 3.5d display a comparison of lift coefficient time signal and PSD with respect to the

	G1	G2	G3
$\max(\Delta x^+)$	40	30	40
$\max(\Delta y^+)$	0.6	0.6	0.6
$\max(\Delta z^+)$	18	16	10

TABLE 3.3: Wall variables obtained during the grid validation for SLE aerofoil.

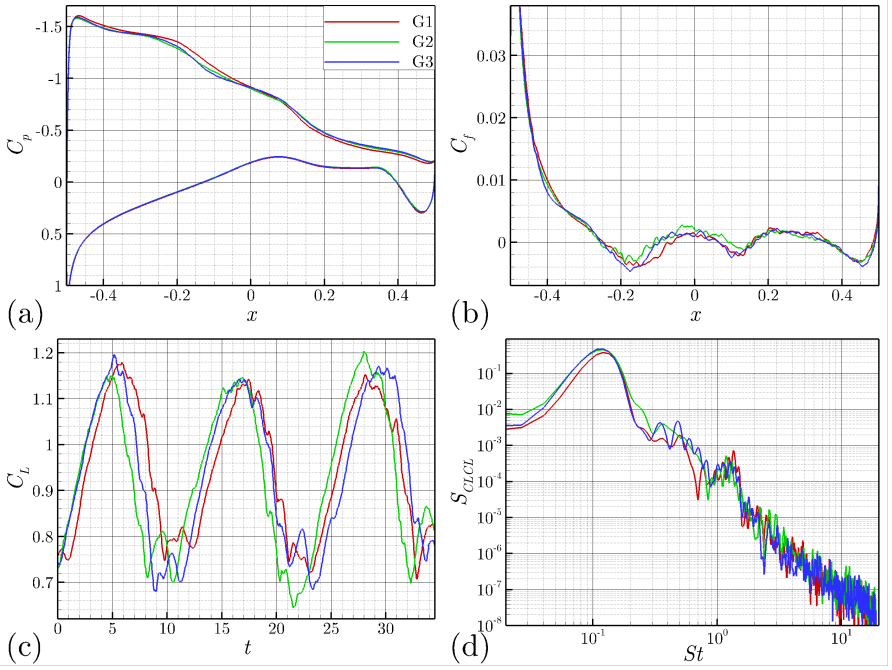

FIGURE 3.5: Grid validation for SLE aerofoil. Comparison of mean aerodynamic characteristics, mean pressure coefficient distribution (a) and mean skin friction coefficient distribution (b). Comparison of unsteady aerodynamic characteristics, lift coefficient time signal (c) and lift coefficient PSD with respect to the Strouhal number (d).

Strouhal number (St). The PSD shows a close agreement in the two maxima and the decay at high frequencies. The largest difference is in the decay between the first and the second peak, but the three results are consistent. Table 3.2 shows the overall aerodynamic characteristics which confirm the possibility to use G1 grid for the study. Figure 3.6 shows isosurfaces of spanwise vorticity at $t = 0.0$ for the three meshes coloured with velocity magnitude. Figure 3.6b shows the BL finer in streamwise direction, while Figure 3.6c the BL finer in spanwise direction.

Due to the imposed Reynolds number, the time step has an order of magnitude of 10^{-5}. The computational cost is 2 wall-clock hours per time unit using 2592 processor cores in the UK National Supercomputer ARCHER, which brings to a max of 26,500 points per processor.

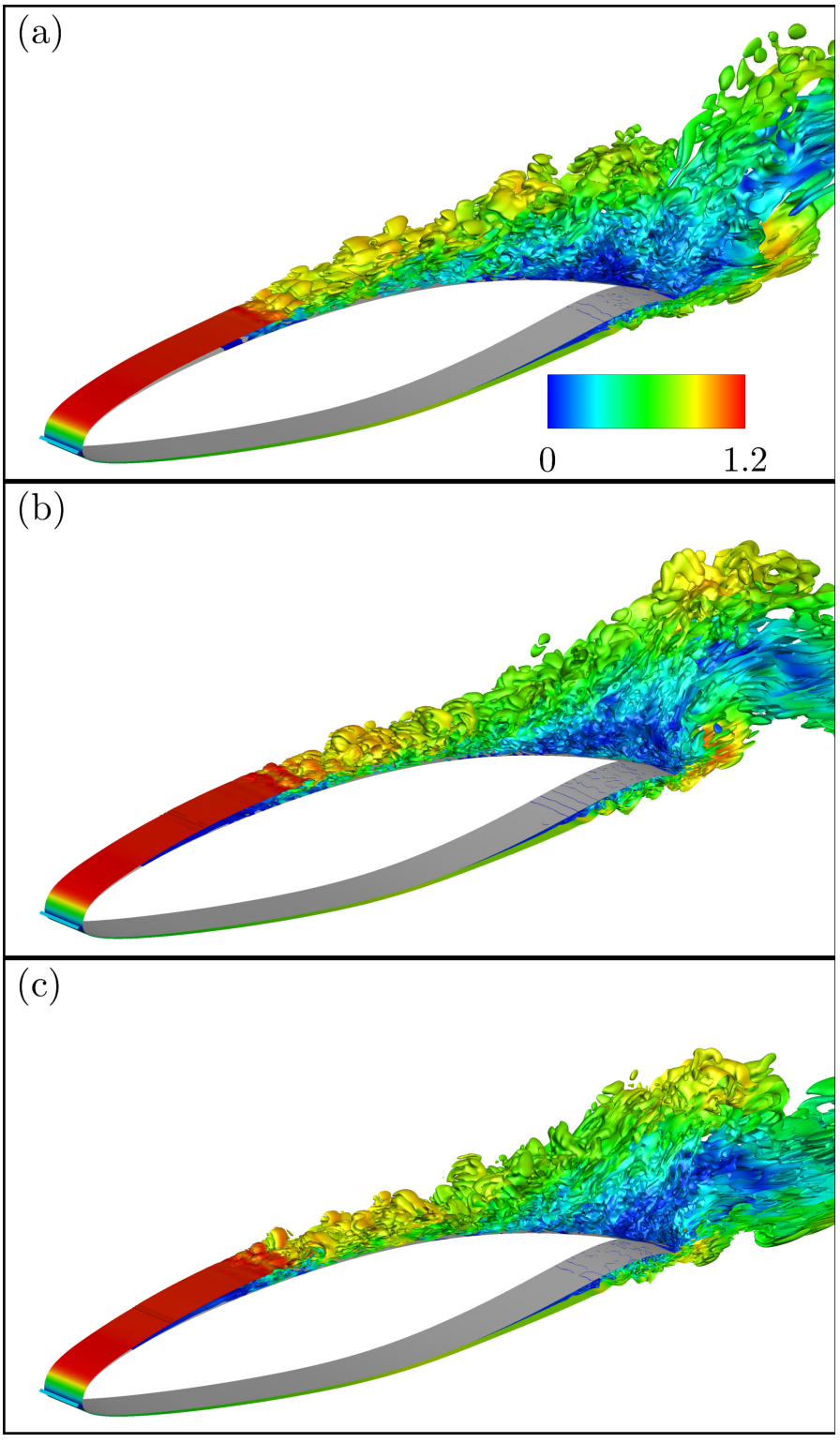

FIGURE 3.6: Grid validation for SLE aerofoil. Isosurfaces of instantaneous spanwise vorticity coloured with velocity magnitude contour at $t = 0.0$ for G1 (a), G2 (b) and G3 (c) aerofoils.

Chapter 4

Preliminary results slowly varying incidence angle

This chapter aims to apply for the first time WLEs to a supercritical aerofoil in a transonic flow. The first question is, will the common trend observed in the low speeds (decreased efficiency at low angles and increased efficiency at high angles when wavy aerofoils are used) still remain consistent in the high speed? The second question is, how does the flow field change in terms of counter rotating vortices and LSBs in the transonic speed? Since answers to these fundamental questions have not previously been available, it is necessary to perform a preliminary study to observe and understand how the wavy aerofoil responds to a range of angles of attack. A slowly heaving aerofoil is simulated for this purpose with a minimal effect of added mass (dynamic stall). The added mass is the inertia added to a system because an accelerating body moves a volume of surrounding fluid as it moves through it. As a consequence, an additional force is generated on the body because of the acceleration. The objective is to create a working frame for future studies at static incidence. This approach is driven by the fact that there is no knowledge about aerodynamic behavior of WLEs in high speed flows, and it would be computationally expensive to perform several different static simulations. The limitation of this strategy is that the unsteady characteristics of the aerofoils at a certain incidence angle may not be precisely determined. This restriction is accepted for now because the main goal is to investigate the overall aerodynamic performance, while some discussions about the unsteady load can be considered in a second step.

4.1 Simulation set-up

The simulations performed in this study are at $Re_\infty = 500,000$ and with a range of incidence angles between 2^o and 7^o. In this Chapter, the spanwise domain size is set to

$0.05L_c$, while $h_{LE} = 0.0125L_c$ and $\lambda_{LE} = 0.05L_c$, thus only one wavelength is simulated. The simulation of one wavelength is sufficient when there is no interaction between the laminar separation bubbles generated in the leading edge region around the trough sections, which means that the bubble is localised around the trough section. The size of the laminar separation bubble is a function of the Reynolds number and the angle of attack, in particular it decreases when the Reynolds number increases, thus the choice of a moderate Reynolds number is crucial to be able to obtain meaningful results with one wavelength simulations. In the results presented in this Chapter, it is clear that the bubble is localised around the trough section also at high incidence angles, thus the simulation of one wavelength is meaningful. However, the domain size represents the main limitation of this setup and it should be extended in future studies. The amplitude is chosen consistent with previous large eddy simulations in low speed flows (Perez Torro and Kim (2017); Skillen et al. (2015)). The amplitude has to be limited using a laminar supercritical aerofoil in order to not loose the benefits of the laminar boundary layer. The aspect ratio of the wavy geometry ($2h_{LE}/\lambda_{LE}$) is 0.5. The waviness at the leading edge stretches the grid cells, thus the computational cost increases. In particular, it is observed that an aspect ratio equal to one doubles the computational cost of the simulation compared with the baseline case. Both a compact filter and artificial dissipation are introduced for a clean shock capturing. The filtering cut-off wavenumber is set to $\kappa = 0.7\pi$ (Equation 3.24), while the artificial dissipation coefficient introduced in Equation 3.29 is set to $c_{sr} = 10^{-3}$. This means that a small amount of filtering is sufficient to stabilize the numerical solution of the Navier-Stokes equations, while a tiny amount of artificial dissipation is additionally introduced around the shock wave to remove the spurious numerical oscillations.

Since this is the first work about WLE performance in transonic flows, the choice is to conduct an analysis varying the angle of attack. The high computational cost of the simulation justifies the choice to perform a slow heaving motion to analyse the aerodynamic performance as a function of the incidence angle.

The upstream flow is given by $(u_\infty, v_\infty, w_\infty) = U_\infty(\cos\alpha, \sin\alpha, 0)$ with the aerofoil mean chord parallel to the x-axis. $\hat{u}_j = \{\hat{u}, \hat{v}, \hat{w}\}$ is the velocity of the moving frame relative to the mean flow velocity, in order to describe the slow heaving motion of the aerofoil, of which the derivation is found in Hoffmann and Chiang (2000). The current slow periodic heaving motion is given by

$$\hat{v}(t) = \frac{\epsilon U_\infty}{2}\left[\cos\left(2\pi\frac{t-t_0}{T}\right) - 1\right] \quad \text{with} \quad \hat{u}(t) = \hat{w}(t) = 0, \tag{4.1}$$

where ϵ is chosen to set the maximum geometric angle of attack to $\alpha_g = 7^\circ$, and the period of the heaving motion is $Ta_\infty/L_c = 50$ which corresponds to a Strouhal number

of 0.0285. The heaving motion is initiated from $t_0 a_\infty / L_c = 5$ when the mean flow has settled down after an initial condition.

Figure 4.1 illustrates the AoA profile. The extremes are chosen in order to obtain a wide range within the limits of the transonic regime. While there are extensive studies of V2C aerofoil at the upper incidence angle (Szubert et al. (2016)), the lower one has never been considered for this aerofoil.

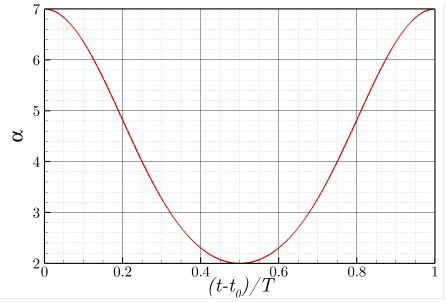

FIGURE 4.1: Angle of attack profile used for slow heaving motion simulations.

4.2 Aerodynamic performance in quasi-linear motion

The aerodynamic performance of the baseline and the modified aerofoils is analysed in details both in streamise and spanwise directions. In this study low incidence angles are considered in the range $\alpha_g \leq 3.5^o$, moderate angles in the range $3.5^o < \alpha_g < 5.0^o$ and high angles in the range $\alpha_g \geq 5.0^o$. Figure 4.2 illustrates the performance in quasi-linear range, showing the lift and drag coefficients variation with the angle of attack. The main outcome is that the modified aerofoil decreases the drag at low and moderate incidence angles, the result is an increased efficiency. Increasing the angle of attack, the drag coefficient of the two aerofoils tends to the same value, the same trend is observed for the efficiency. This suggests that the aerodynamic characteristics of WLEs in transonic flows are different from the ones in low-speed flows. A static analysis is required at higher angles of attack because of low frequency unsteadiness.

4.2.1 Streamwise aerodynamic performance details

The quasi-linear part of the heaving motion is analysed in detail trying to understand the flow behaviour and comparing the performance between the two aerofoils. The performance is evaluated considering the piecewise distributions of lift and drag increase/decrease along the chord ($d(\Delta C_L)/dx$ and $d(\Delta C_D)/dx$) between SLE and WLE cases.

Figure 4.3 represents the pressure gradient magnitude contour highlighting the supersonic region with a solid red line at different incidence angles of the quasi-linear

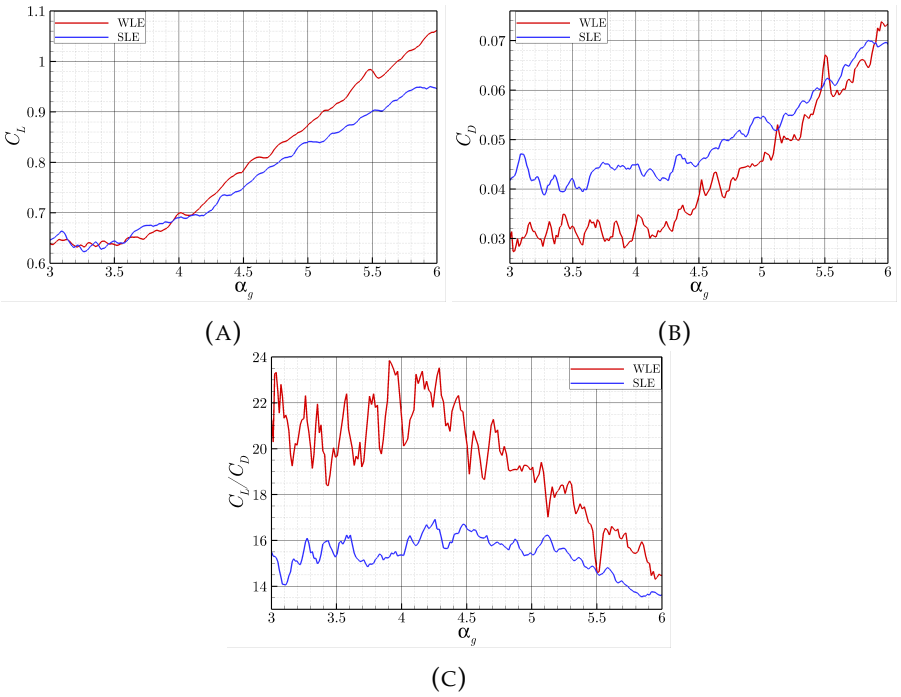

FIGURE 4.2: Lift (a) and drag (b) coefficients and efficiency (c) varying the angle of attack during the quasi-linear part of the heaving motion.

motion for the straight (Figure 4.3a-c) and the wavy (Figure 4.3d-f) aerofoils. At low and moderate angles, pressure waves are generated at the trailing edge and they gather downstream the supersonic region generating a weak shock wave on the upper surface (Figure 4.3a,d). The shock wave moves upstream decreasing its strength until it reaches the leading edge, then it separates from the LE and moves upstream as a free shock. This behaviour can be observed up to $\alpha_g = 5.72^o$ on the baseline aerofoil (Figure 4.3a-c), while at that angle the WLE case shows a λ-shape shock wave (Figure 4.3f). Figure 4.3g-i represents the pressure coefficient distribution over the main sections of the two aerofoils at different AoA. The general trend of the pressure coefficient over the upper surface of the laminar supercritical aerofoil is characterised by a first plateau with a laminar boundary layer, followed by a bump which defines the laminar separation and a second plateau before the laminar-turbulent transition and the pressure coefficient increase (Dandois et al. (2018a)). The pressure distribution at the main sections of the two aerofoils allows to observe some differences in the flow behaviour. First of all, the L-T transition point is moved upstream in the modified aerofoil over a wide range of angles of attack. Table 4.2 shows that increasing the incidence angle, the transition point of the wavy aerofoil tends to the one of the baseline aerofoil. Moreover, downstream the transition, the pressure coefficient increase is steeper over the modified aerofoil and this has an influence on the lift performance. The laminar separation point is moved slightly upstream at low incidence (Figure 4.3g), while it is moved downstream at moderate and high incidence angles (Figure 4.3h,i). The lift and drag coefficients for each aerofoil at the angles of

attack considered are reported in Table 4.1. The WLE lift coefficient is lower only at high angles, while the WLE drag tends to be lower up to $\alpha_g = 5.72^o$, then it is close to the straight one. The lift coefficient at $\alpha_g = 3.08^o$ is increased upstream the L-T transition point over the modified aerofoil even if the leading edge flow itself gives a negative contribution to the lift (Figure 4.3l). At higher angles, the lift increase is concentrated between the SLE laminar separation and the WLE transition point (Figure 4.3m,n). The drag coefficient at low angles of attack is decreased over the modified aerofoil at the LE. The drag gain obtained close to the leading edge decreases when the incidence angle is increased (Figure 4.3o-q). Downstream the L-T transition point, the drag is decreased over the wavy aerofoil and also this behaviour tends to decrease, increasing the incidence angle but it becomes predominant at higher angles. Table 4.3 gives further details integrating in two steps the piecewise distribution of lift and drag along the chord, shown in Figure 4.3l-q. The first part goes from the LE up to the WLE laminar-turbulent transition point and the second part goes from the WLE transition point to the TE. In this way, the effect of the main pressure distribution features are quantified. It is observed that the lift increase with the incidence angle is related to the increased positive contribution upstream the L-T transition point and the decreased negative contribution downstream the transition point. The drag coefficient is decreased upstream the transition point at $\alpha_g = 3.08^o$, while it is increased at $\alpha_g = 5.72^o$. Downstream the transition point, the drag is always decreased by the modified aerofoil but the effect is reduced increasing the angle of attack.

The main outcome of the chordwise performance analysis is that the modified leading edge has a direct positive impact on the performance at low and moderate angles, but it also has an effect on the shock wave-boundary layer interaction region and on the position of the laminar-turbulent transition point. This effect seems to have a positive impact on the performance over a wide range of angles of attack. The next section will try to analyse the flow field close to the leading edge in order to understand both direct and indirect effects.

α_g[deg]	$C_{L_{WLE}}$	$C_{L_{SLE}}$	$C_{D_{WLE}}$	$C_{D_{SLE}}$
3.08	0.646	0.663	0.029	0.047
4.15	0.709	0.694	0.030	0.043
5.72	1.004	0.929	0.062	0.066

TABLE 4.1: Lift and drag coefficients for SLE and WLE aerofoils during quasi-linear part of heaving motion.

	3.08^o	4.15^o	5.72^o
$x_{t_{SLE}}$	0.28	0.23	0.19
$x_{t_{WLE}}$	0.24	0.19	0.18

TABLE 4.2: Laminar-turbulent transition point over the SLE and WLE aerofoils during quasi-linear part of heaving motion.

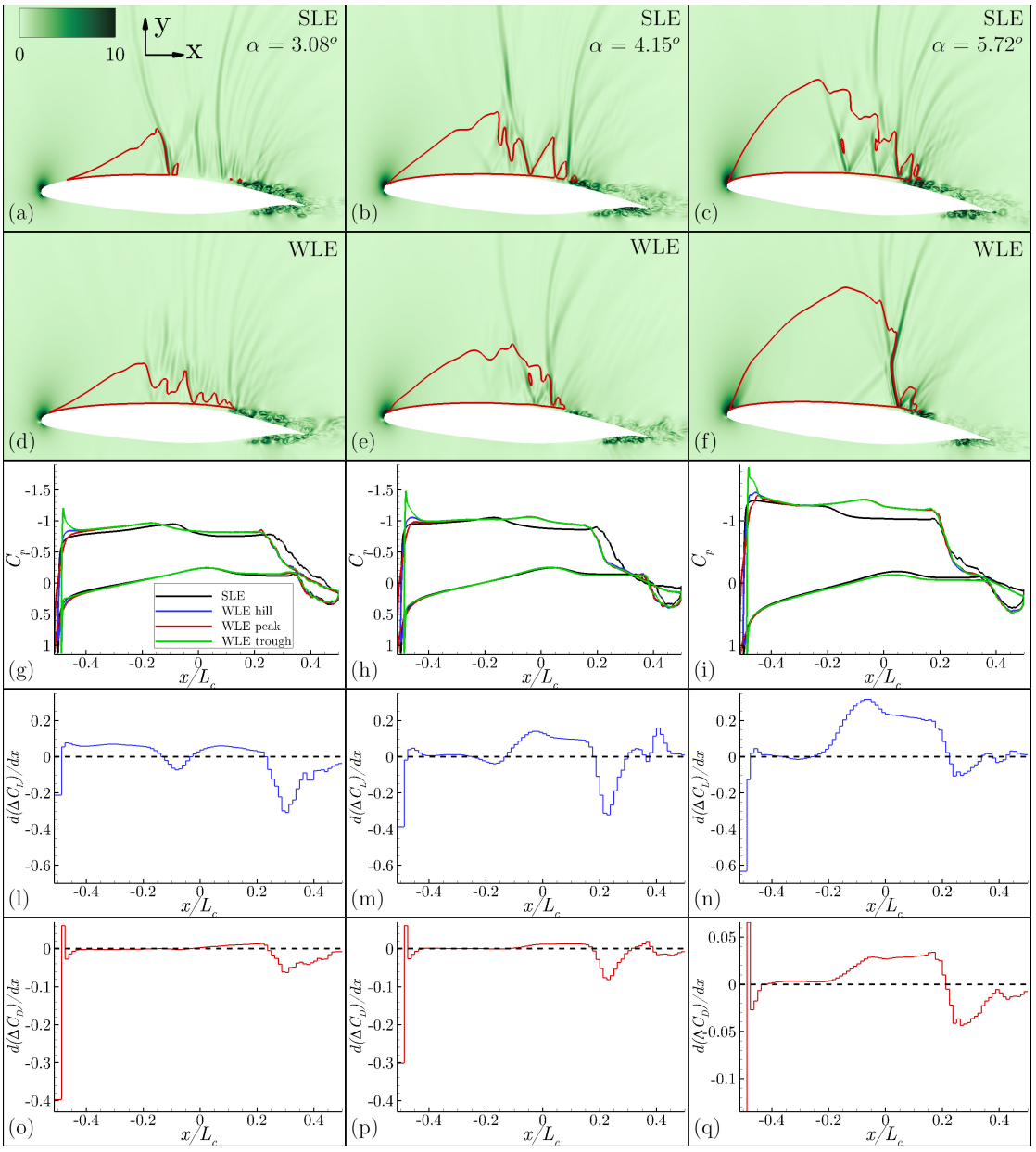

FIGURE 4.3: Aerodynamic performance analysis during the quasi-linear part of heaving motion. Pressure gradient magnitude of SLE (a-c) and WLE hill (d-f) are shown at different angles of attack ($\alpha_g = 3.08^o, 4.15^o, 5.72^o$). The red solid line delimits the supersonic region. Mean pressure coefficient distribution at WLE peak, trough and hill and over SLE (g-i) are compared at different angles of attack. Relative changes in aerodynamic forces between SLE and WLE cases in terms of piecewise distribution of lift (l-n) and drag (o-q) along the chord calculated from wall pressure ($d(\Delta C_L)/dx$ and $d(\Delta C_D)/dx$). The relative difference between SLE and WLE cases are denoted by $\Delta\{.\} = \{.\}_{WLE} - \{.\}_{SLE}$.

Figure 4.4 shows the skin friction coefficient distribution on the upper surface of straight and wavy aerofoils at the incidence angles investigated in this section. First of all, it can be observed that a laminar separation bubble is generated on wavy aerofoils around the trough section close to the leading edge and it grows in length and width increasing the angle of attack. The straight aerofoils present a separation of the

α_g[deg]	$\Delta C_{L_{front}}$	$\Delta C_{L_{rear}}$	ΔC_L	$\Delta C_{D_{front}}$	$\Delta C_{D_{rear}}$	ΔC_D
3.08	0.0246	-0.0348	-0.0103	-0.00375	-0.00773	-0.01148
4.15	0.0255	-0.0112	0.0143	-0.000762	-0.00649	-0.00725
5.72	0.0798	-0.0037	0.0760	0.00829	-0.00579	0.00251

TABLE 4.3: Difference in lift and drag forces between WLE and SLE cases during the quasi-linear part of heaving motion ($\Delta C_L = C_{L_{WLE}} - C_{L_{SLE}}$ and $\Delta C_D = C_{D_{WLE}} - C_{D_{SLE}}$), over two sections of the aerofoil chord (front and rear). The front section is from the LE to the WLE laminar-turbulent transition point and the rear section is from the WLE laminar-turbulent transition point to the TE. Viscous contributions are neglected.

laminar boundary layer which generates a LSB, then the boundary layer reattaches to the aerofoil surface and the laminar-turbulent transition point is located downstream. Both the laminar boundary layer separation and the laminar-turbulent transition locations move upstream increasing the incidence angle. The wavy aerofoil is characterised by a laminar boundary layer separation which varies in the spanwise direction and the laminar-turbulent transition downstream, without boundary layer reattachment like in the straight counterpart. The laminar BL separation is located more downstream around the peak section and more upstream around the trough section because of the flow distortion at the leading edge. Overall, the spanwise mean laminar boundary layer separation is significantly moved downstream on the wavy aerofoil and this might be related to the streamwise vorticity generated at the leading edge which energises the laminar BL but further investigations are needed. Finally, the laminar-turbulent transition location on the wavy aerofoil is moved upstream at low and moderate angles of attack, while it is comparable to the straight case at high angles of attack.

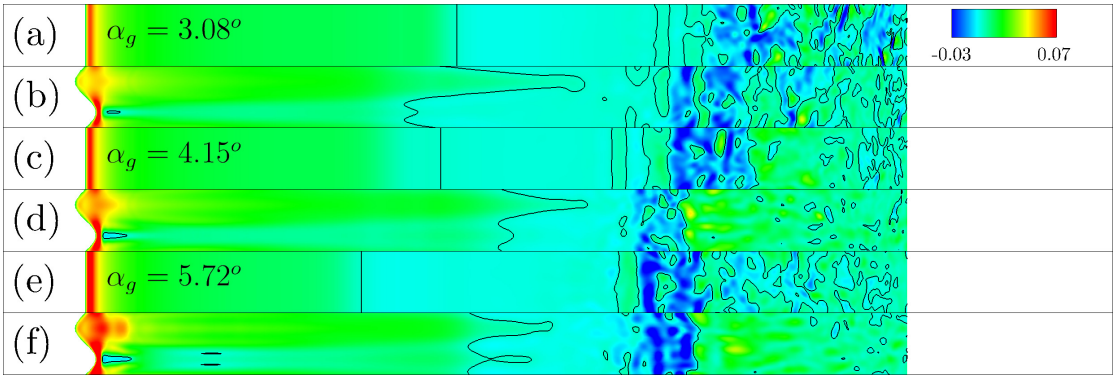

FIGURE 4.4: Skin friction coefficient distribution on the upper surface of SLE (a,c,e) and WLE (b,d,f) aerofoils at $\alpha_g = 3.08^o$ (a,b), $\alpha_g = 4.15^o$ (c,d) and $\alpha_g = 5.72^o$ (e,f).

4.2.2 Spanwise aerodynamic performance details

The wavy geometry introduces three dimensionality in the flow at the leading edge and this has an effect over the whole aerofoil. For this reason, the spanwise

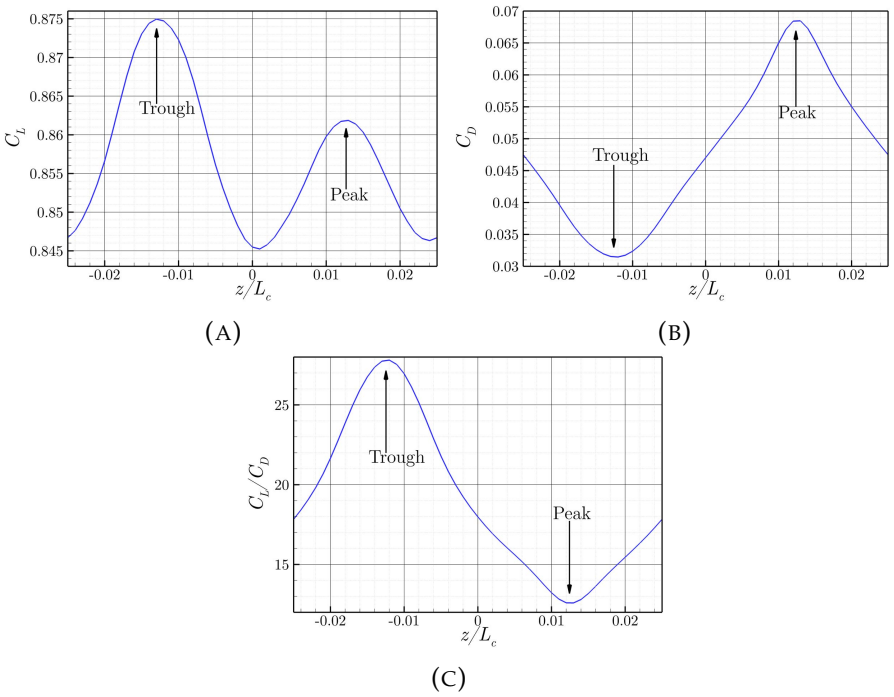

FIGURE 4.5: Lift (a), drag (b) and efficiency (c) spanwise distribution over the wavy aerofoil at $\alpha_g = 4.82^o$.

performance is also analysed in order to define the most significant sections in terms of aerodynamic efficiency.

The spanwise performance of the modified aerofoil is analysed in Figure 4.5 at a specific angle of attack ($\alpha_g = 4.82^o$) but the behaviour is consistent at the other angles. The lift coefficient (Figure 4.5a) shows two different maxima at the peak and trough sections and the minimum close to the hill section. The mean lift coefficient is $C_{L_{mean}} = 0.857$. The lowest value is obtained at the hill section for a geometric reason, the derivative of the surface with respect to the z direction has the highest value so the force has the largest spanwise component. The trough generates a lift higher than the peak because of the pressure distribution close to the leading edge. The result is quite different for the drag coefficient (Figure 4.5b). The highest value is obtained at the peak and the lowest at the trough. The result is consistent for both pressure and skin friction drag even if the first one is almost one order of magnitude larger. The mean drag coefficient is $C_{D_{mean}} = 0.0478$, close to the hill section value. This spanwise distribution can be explained again considering the pressure distribution close to the LE. The peak section is the one where there is the most gradual pressure decrease between the stagnation point and the pressure coefficient peak. This extended high pressure region increases the drag. The opposite behaviour is observed at the trough, the pressure coefficient changes suddenly from the highest to the lowest values of the pressure coefficient. Overall, the efficiency is 1.5 of the mean one at the trough and 0.72 at the peak (Figure 4.5c).

4.3 Leading edge flow details in quasi-linear motion

The previous section has analysed the performance of the modified aerofoil in detail and compared it with the baseline one. The objective of this section is to analyse the leading edge flow field and its influence on the downstream evolution of the flow, trying to compare the main flow characteristics with the ones at low speed. The first part investigates the leading edge pressure distribution along the span and compares it with the straight counterpart. Then the laminar boundary layer downstream the LE region is evaluated in order to quantify the spanwise variation of BL thickness over wavy aerofoil. The second part examines the evolution of streamwise vortices from the LE to the L-T transition point and the spanwise velocity upstream and downstream the LE (channeling effect).

4.3.1 Leading edge acceleration and boundary layer evolution

The chordwise variation of aerodynamic forces has shown that the drag decrease over the modified aerofoil is related to the leading edge shape and the upstream movement of the transition point. The first effect is dominant at low and moderate angles of attack. Figure 4.3 shows that the peak region has a positive effect in decreasing the drag, while the trough region has a negative effect. In particular, a drag drop is obtained in the first chunk $x \in [-0.5125L_c; -0.4875L_c]$, while a drag increase is observed in the second one $x \in [-0.4875L_c; -0.4750L_c]$. Increasing the angle of attack, the favourable effect of the first chunk decreases while the adverse effect of the second one increases and overall the leading edge is not beneficial. The favourable behaviour observed in the first chunk can be explained analysing the spanwise distribution of the maximum pressure coefficient (Figure 4.6) because a high pressure coefficient at the leading edge tends to increase the drag. The maximum pressure coefficient is close to the straight one at the trough and peak sections but it is lower at the other sections. In particular, the maximum pressure coefficient decreases abruptly around the peak, while it decreases gradually around the trough. The spanwise distribution of the streamwise location of the maximum pressure coefficient is not shown but it follows the shape of the wavy geometry. It is located on the lower surface close to the leading edge and it moves further away from the leading edge increasing the angle of attack. The outcome of this pressure distribution is that the first chunk, which takes into account the peak and the hill effects, brings to a drag reduction. The reduction in the first chunk decreases with the incidence angle increase because the maximum pressure coefficient drop decreases at higher angles. On the contrary, in the second chunk the high pressure coefficient in the trough region penalises the wavy aerofoil performance and this effect grows increasing the incidence angle because the high pressure region moves downstream and a higher pressure area is included in the second chunk.

The flow field at the leading edge over the two aerofoils is illustrated in Figure 4.7, where the contour of streamwise velocity is represented together with the sonic line. The first observation is related to the spanwise boundary layer thickness over the wavy aerofoil. At the trough section a reverse flow region develops inside the boundary layer and becomes larger increasing the angle of attack. The effect of this reverse flow region is boundary layer thickening. The effect of the reverse flow seems to be limited to the trough area because the boundary layer is thinner at the hill and peak sections and it seems to be comparable with the boundary layer over the baseline aerofoil.

Figure 4.8 shows the details of the LE bubble around the trough region at $\alpha_g = 6.00^o$. It is shown only one specific condition but the results are consistent at the other incidence angles with the bubble in the trough region growing with the angle of attack increase. The bubble canopy (tangential velocity equal to zero) and the streamlines on both side and top views allow to understand the details of the flow behaviour in the reverse flow region. Two foci are displayed clearly in the top view and they are consistent with previous studies of WLE aerofoils at low speed (Perez Torro and Kim (2017)). The side view showing the velocity vectors allows to analyse the boundary layer details in the bubble. Downstream the laminar separation, the BL in the reverse flow is qualitatively similar to the BL in a channel, the flow is zero at the wall, then it grows in magnitude to a maximum and then it goes to zero again before becoming positive. Further downstream the BL changes, it is negative close to the wall but with a small amplitude and it is almost constant moving away from the wall. In the upper part of the reverse flow region, the magnitude starts growing reaching a negative maximum before going to zero and becoming positive. At the end of the reverse flow region, the BL shape is evolving again. Close to the wall the velocity is negative in a very limited region, then it becomes positive reaching a maximum before showing a strong deceleration and becoming slighty negative again. Finally, outside the reverse flow region it becomes positive and it quickly grows to supersonic conditions.

A reverse flow region has a positive effect on the skin friction drag. However, in this case the skin friction drag is about one order of magnitude lower than the pressure drag mainly because of the aerofoil shape, a laminar supercritical aerofoil is designed to decrease the skin friction drag exploiting the characteristics of a laminar boundary layer. Moreover, the reverse flow region has a limited streamwise and spanwise extension (Figure 4.8), this means that overall the effect of the reverse flow region on the local drag at the LE is a secondary effect.

The second relevant point about the flow field at the leading edge is related to the flow acceleration and the supersonic region. Figure 4.7 shows clearly that the supersonic region is very close to the LE at the trough section, while it moves further downstream at the hill and peak. A possible explanation for the flow behaviour at the trough section will be given in the next section analysing the channeling phenomenon. Table

4.4 gives quantitative information about the position of the sonic point closest to the wall and its distance from the local leading edge point. Obviously, the sonic point tends to move upstream increasing the angle of attack, but the range of variation increases moving from the trough to the peak. The consequence is that at low angles of attack the supersonic region starts quite far from the leading edge over the baseline aerofoil, while it starts close to the leading edge at the trough and this has an effect on the other sections where the sonic point is more upstream than the straight counterpart. On the contrary, when the sonic point moves upstream $x = -0.4875$ (trough LE) over the baseline aerofoil, the sonic point is more downstream at all the sections of the wavy aerofoil because of the trough. The flow behaviour in this region has an impact on the drag performance of the modified aerofoil, where it allows to decrease the drag at low and moderate angles of attack, while it plays a minor role at high angles.

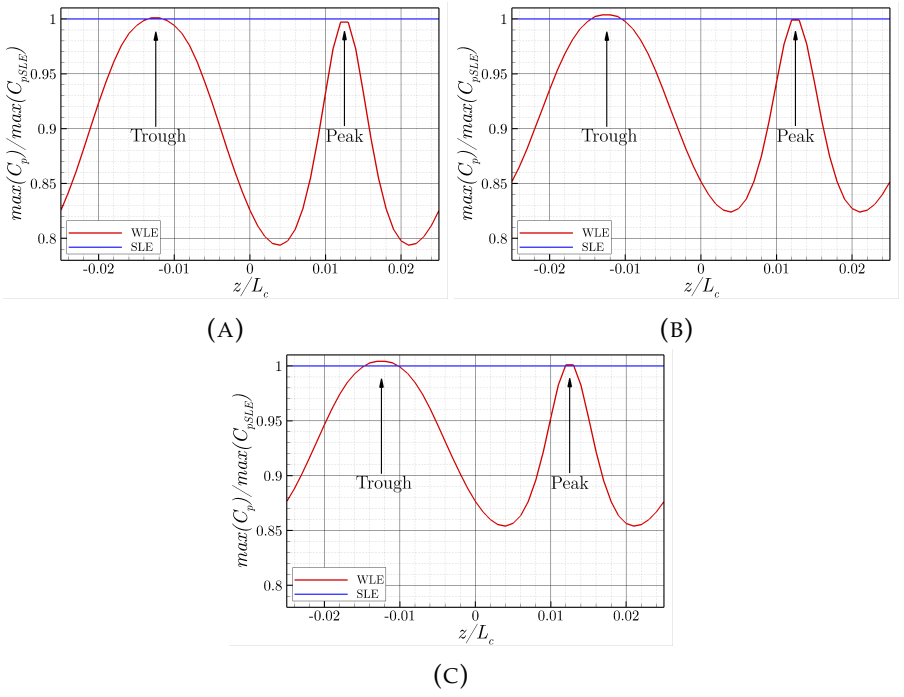

FIGURE 4.6: Spanwise maximum pressure coefficient normalised by the baseline aerofoil one at $\alpha_g = 3.00^o$ (a), $\alpha_g = 4.82^o$ (b) and $\alpha_g = 6.00^o$ (c).

α_g[deg]	x_{trough}	x_{hill}	x_{peak}	x_{SLE}	Δx_{trough}	Δx_{hill}	Δx_{peak}	Δx_{SLE}
3.00	-0.4843	-0.4698	-0.4411	-0.4019	0.0032	0.0320	0.0714	0.0981
4.82	-0.4860	-0.4891	-0.4839	-0.4940	0.0015	0.0109	0.0286	0.0060
6.00	-0.4864	-0.4927	-0.4890	-0.4959	0.0011	0.0073	0.0235	0.0041

TABLE 4.4: Streamwise coordinates of the most upstream position of the sonic line close to the wall and its distance from the local LE for WLE trough, hill, peak and for SLE ($\Delta x_{\{.\}} = x_{LE} - x_{\{.\}}$).

Figure 4.7 shows a large spanwise variation of the boundary layer thickness over the modified aerofoil. The objective is to quantify the thickness and its evolution

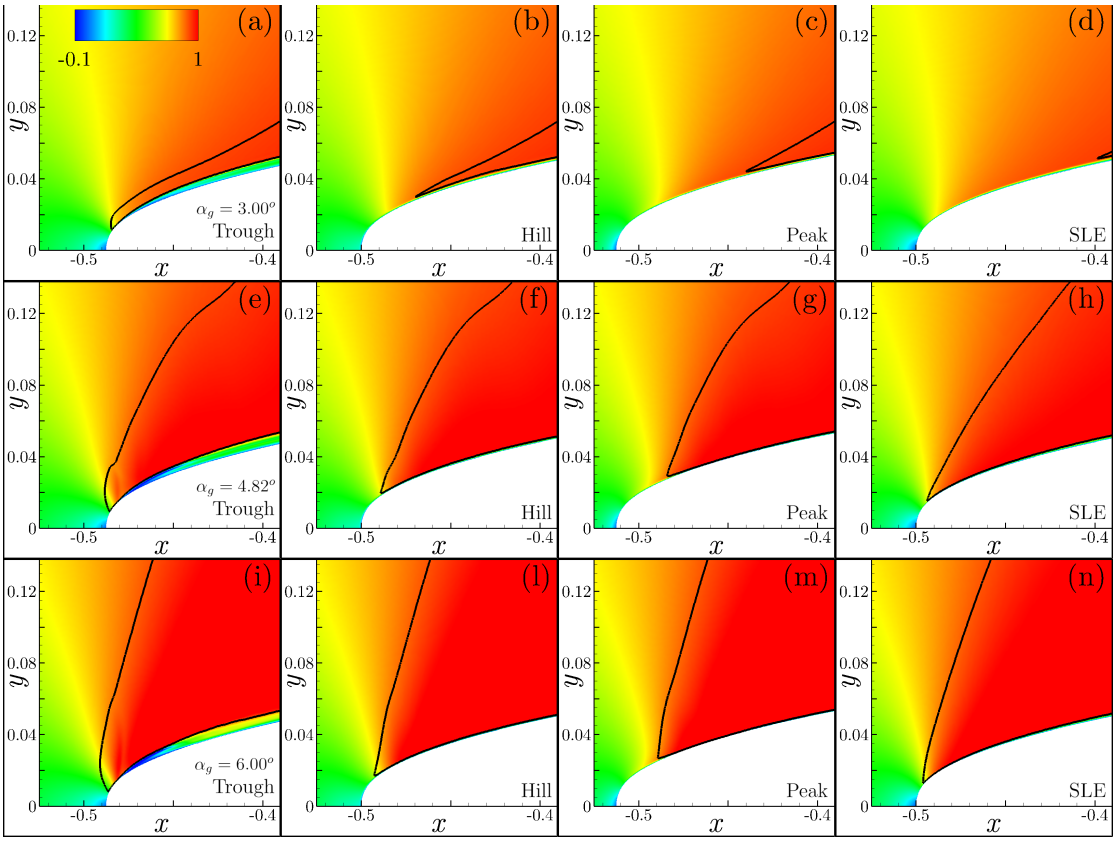

FIGURE 4.7: Streamwise velocity at trough (a,e,i), hill (b,f,l) and peak (c,g,m) sections of WLE aerofoil and over the baseline aerofoil (d,h,n) for $\alpha_g = 3.00^o$ (a-d), $\alpha_g = 4.82^o$ (e-h) and $\alpha_g = 6.00^o$ (i-n). The black line highlights the sonic line.

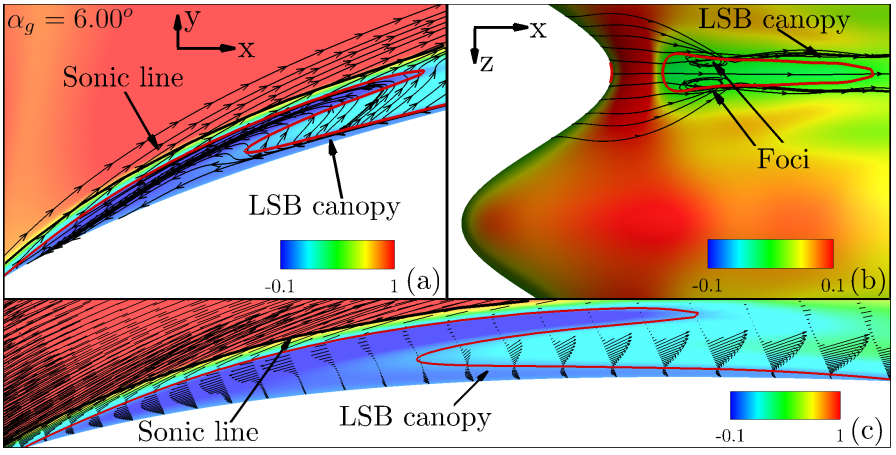

FIGURE 4.8: Streamwise velocity contour on a side view with streamline highlighting the bubble canopy and the sonic line (a), streamwise velocity contour on a top view 10 points above the aerofoil surface with streamlines highlighting the bubble foci and the bubble canopy (b), streamwise velocity contour on a side view with velocity vectors plotted every 3 points in ξ direction highlighting the bubble canopy and the sonic line (c). All the plots highlights the LE region (10% of the chord).

downstream. Since the standard definitions of displacement thickness and boundary layer thickness can not be applied to an aerofoil due to the wall curvature, a different approach is exploited based on Zauner (2019).

- First of all, the solution in the coordinates system (x, y) is transformed in the system (s, η), where s is parallel to the aerofoil surface and the origin is at the leading edge, while η is normal to the surface and the origin is at the wall. This transformation is obtained using inverse distance weighting (IDW) interpolation and an example is illustrated in Figure 4.9a-b.

- The result of the first step is the velocity magnitude profile of the boundary layer $(U - \eta)$ at each streamwise section. The condition to define the boundary layer edge is to have $\partial^2 U/\partial\eta^2 = 0$ for a defined number of points. This means that the velocity magnitude is constant or it is changing linearly, thus it is for sure outside the boundary layer. Figure 4.9c shows the BL profile in (s, η) coordinates and the result of the boundary layer thickness from the described method with a blue line.

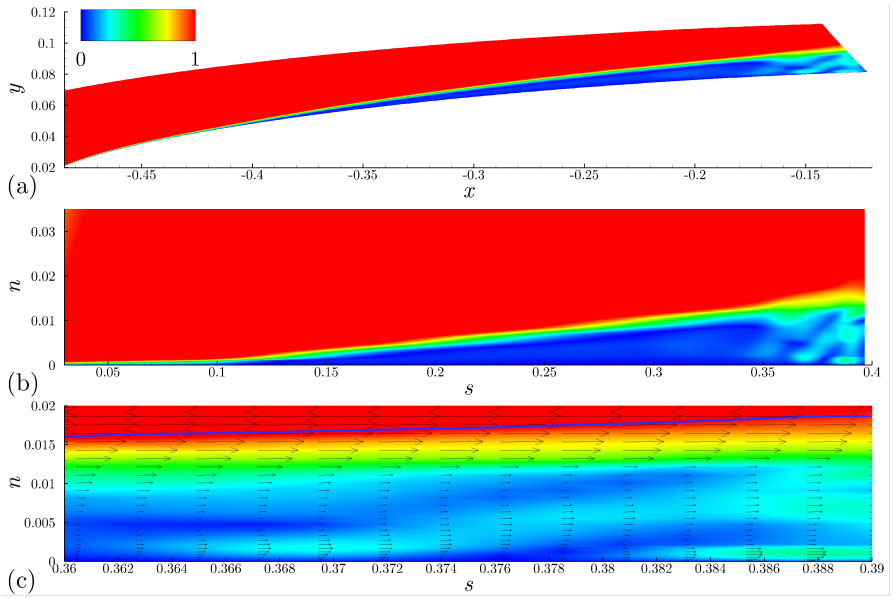

FIGURE 4.9: Velocity magnitude close to the wall in coordinate system (x, y) (a) and (s, η) (b) and boundary layer profile in coordinate system (s, η) and boundary layer thickness in blue line (c).

The boundary layer thickness (δ) is evaluated downstream the leading edge region, where the boundary layer is still laminar. In principle the method can be applied also to a mean turbulent boundary layer but since the aerofoils are performing a heaving motion, it is only possible to analyse the laminar one in this case. Figure 4.10 shows the result for the angles of attack considered in this section. At the trough section the boundary layer tends to grow close to the leading edge, while moving further away it becomes quite constant. A different behaviour is observed over the straight aerofoil and at the peak where the BL increases slowly but constantly. Further details are given in Table 4.5 where the thickness at the trough, at the peak and over the SLE is evaluate at $s = 0.25$ and at the different angles. The result shows that the thickness grows faster increasing the incidence angle at the trough than at the peak where it is quite constant

changing the angle of attack. The growth of the BL over the SLE is similar to the trough section but the shape is quite different due to the evolution of streamwise vortices and the reverse region close to in the trough.

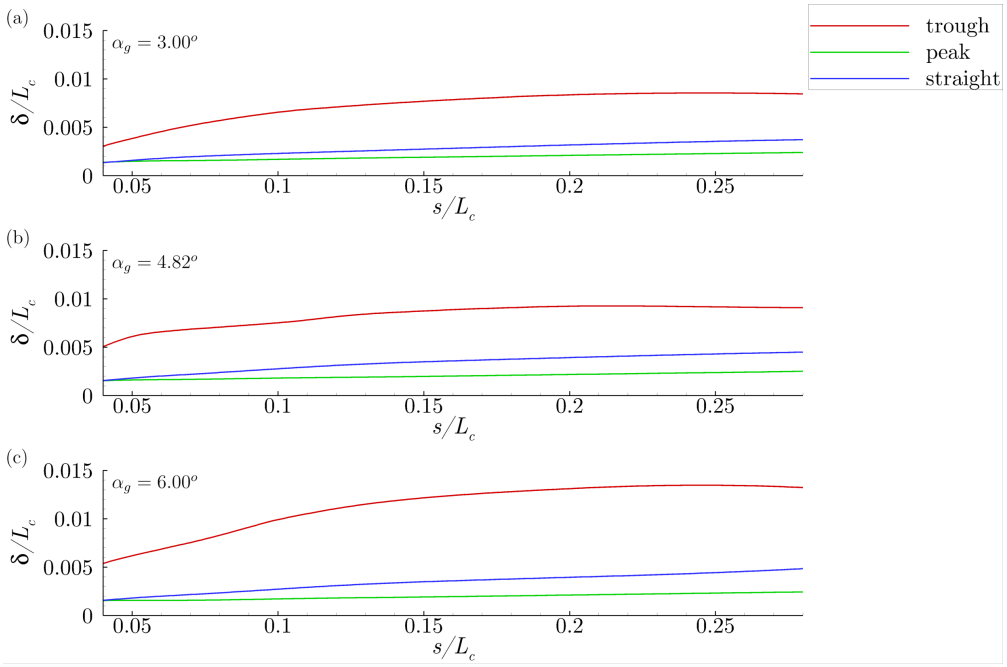

FIGURE 4.10: Boundary layer thickness (δ/L_c) distribution along the curvilinear coordinate s at $\alpha_g = 3.00^o$ (a), $\alpha_g = 4.82^o$ (b) and $\alpha_g = 6.00^o$ (c) for WLE trough and peak and for SLE.

α_g[deg]	δ_{trough}	δ_{peak}	δ_{SLE}
3.00	0.00854	0.00228	0.00354
4.82	0.00917	0.00234	0.00430
6.00	0.01346	0.00232	0.00443

TABLE 4.5: BL thickness at the trough, at the peak and over the SLE at $s = 0.25$ for $\alpha_g = 3.00^o$, $\alpha_g = 4.82^o$ and $\alpha_g = 6.00^o$.

4.3.2 Leading edge flow channeling

The acceleration of the flow to a supersonic condition at the leading edge of the modified aerofoil was observed in Figure 4.7. A possible explanation of this flow behaviour is the flow channeling phenomenon illustrated in Figure 4.11 for $\alpha_g = 4.82^o$. The upstream flow approaching the aerofoil is subsonic, thus it deviates before encountering the peak. This creates a spanwise velocity component towards the trough. The streamlines converge towards the trough and the subsonic flow is accelerated. In a streamwise location between trough and peak ($x = -0.5$) lobes of the spanwise velocity with opposite sign can be observed. The lower lobes indicate that the flow is moving towards the trough, while on the upper side it is moving in the opposite direction, away from the trough section. The sonic line close to the wall is

observed at $x = -0.4860$ (Table 4.4) and at this streamwise location the spanwise velocity component has an opposite direction, thus the streamlines diverge from the trough. The flow is supersonic downstream this location, hence the flow is still accelerated further downstream. Figure 4.11 shows a streamwise position downstream the sonic line at $x = -0.48$. The flow in the boundary layer is influenced by the aerofoil geometry and it moves towards the trough, while outside the boundary layer the flow channeling phenomenon is dominant and the flow diverges from the trough. The opposite spanwise velocity sign inside and outside the boundary layer generates streamwise vorticity downstream.

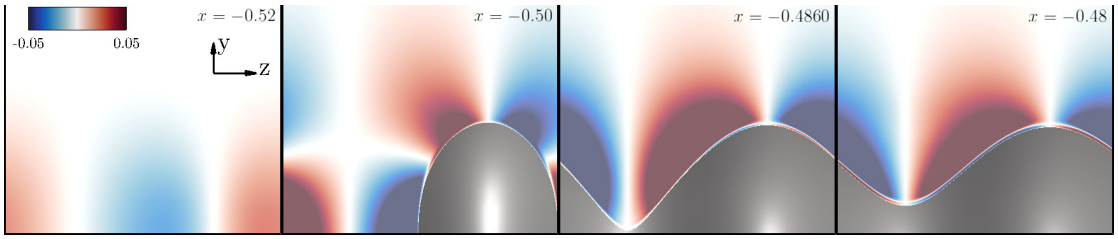

FIGURE 4.11: Contour plots of spanwise velocity at four streamwise positions from $x = -0.52$ to $x = -0.48$ for the wavy aerofoil at $\alpha_g = 4.82^o$. The range shown in the spanwise direction is $[-0.025, 0.025]$ and in the vertical direction it is $[0.0, 0.05]$.

The flow channeling phenomenon can be observed also at low speeds. If the Mach number is low, the flow accelerates upstream the leading edge during the convergence and it slows down during the divergence downstream the leading edge. In this case the flow becomes sonic before the divergence and it continues the acceleration downstream the leading edge. The flow field during the channeling phenomenon can be compared to the one inside a convergent-divergent nozzle where the flow becomes sonic at the throat. The pressure coefficient is plotted in Figure 4.12b along the streamlines illustrated in Figure 4.12a. The pressure coefficient distribution at the trough recalls the one along the axis of a nozzle. The main difference is related to the presence of the body, the flow initially slows down approaching the aerofoil, but it accelerates close to the LE and it reaches sonic condition around the LE position. Downstream the leading edge, the flow close to the wall is decelerated by the presence of a reverse flow region, while moving further away from the wall (grey line) it keeps accelerating up to $x = -0.45$. Upstream the LE, the magnitude of both acceleration and deceleration increase moving closer to the wall, but overall the result is the same because the streamlines have the same pressure coefficient $C_p = 0.4$ at $x = -0.6$ and they reach the critical pressure coefficient (sonic line) around the same position $x \simeq -0.486$. Downstream the LE, the deceleration caused by the reverse flow is stronger close to the wall due to a ramp effect related to the steep boundary layer thickening. Figure 4.12c shows the convergent-divergent shape of the flow. The throat location and the position of the sonic line are not exactly in the same position ($x_{M=1} - x_t = 0.005$). In this short region the spanwise pressure gradient ($\partial p/\partial z$) slows down the flow, but the dominant streamwise pressure gradient ($\partial p/\partial x$) speeds it up to

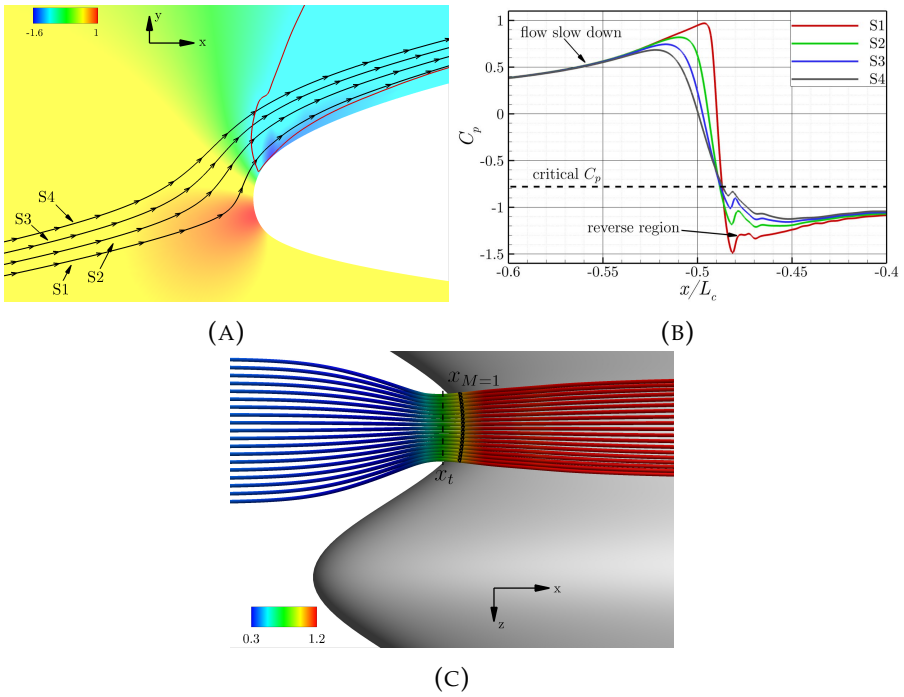

FIGURE 4.12: Channeling phenomenon details. Pressure coefficient contour plot close to the leading edge trough at $\alpha_g = 4.82^o$ (a). Red line represents the sonic line and black lines represent four streamlines. Pressure coefficient distribution close to the leading edge along the streamlines (b). Top view of streamlines coloured by Mach number (c). Dotted black line represents the sonic line and the dashed black line represents the trough section of the convergent-divergent nozzle shape.

sonic condition. Decreasing the upstream flow velocity, the distance between the throat and the sonic line increases because the sonic line moves downstream and, as a consequence, the benefit of the trough section decreases.

The leading edge flow channeling phenomenon on wavy aerofoils is consistent at low and high speed flows but the flow characteristics in transonic flows are different and they can be compared with a convergent-divergent nozzle. In this section, the WLE design parameters, amplitude and wavelength, have not been investigated. The wavy amplitude is expected to have a minor effect on the flow channeling phenomenon. When the amplitude is increased, the upstream flow deviates earlier but overall the flow characteristics should be consistent. The main parameter to characterise the flow channeling phenomenon in transonic flows is expected to be the wavelength. In the analogy with the convergent-divergent nozzle, the wavelength parameter is comparable with the nozzle throat. When the wavelength is decreased, the spanwise acceleration of the upstream flow is increased and the sonic line moves upstream. As a consequence the flow is supersonic in the convergent section and it decelerates. This might have a detrimental impact on the flow acceleration in the LE region and on the overall pressure distribution on the suction side of the wavy aerofoil.

4.3.3 Streamwise vorticity evolution

Figure 4.13 and 4.14 analyse the evolution of streamwise vorticity inside the laminar boundary layer at $\alpha_g = 3.00^o$ and $\alpha_g = 6.00^o$. The streamwise vorticity has been evaluated during the post-processing, using a first order scheme to calculate the velocity derivatives. For $\alpha_g = 3.00^o$ two streamwise vortex (SV) sheets, generated by the turning of spanwise vorticity, are observed at $x = -0.48$ on each side of the peak section. The reverse flow region at the trough generates localised streamwise vorticity ($x = -0.45$). Vorticity sheets pairs are generated above and below the original SV sheets with an opposite sign and they develop downstream the reattachment point ($x = -0.40$). The boundary layer is still laminar downstream the reattachment and the sheets pairs develop at a slow rate and symmetric with respect to the trough section. Streamwise vorticity appears very close to the wall, initially around the trough section ($x = -0.35$) and then also around the peak one ($x = -0.15$). During the downstream motion, the vorticity decay associated with the vorticity spreading is observed. The main result displayed in the streamwise vorticity flow field is the generation of vorticity sheets pairs in the trough region that energise the boundary layer without inducing transition to turbulence. As a consequence, the laminar boundary layer is three dimensional and the vorticity develops at a slow rate.

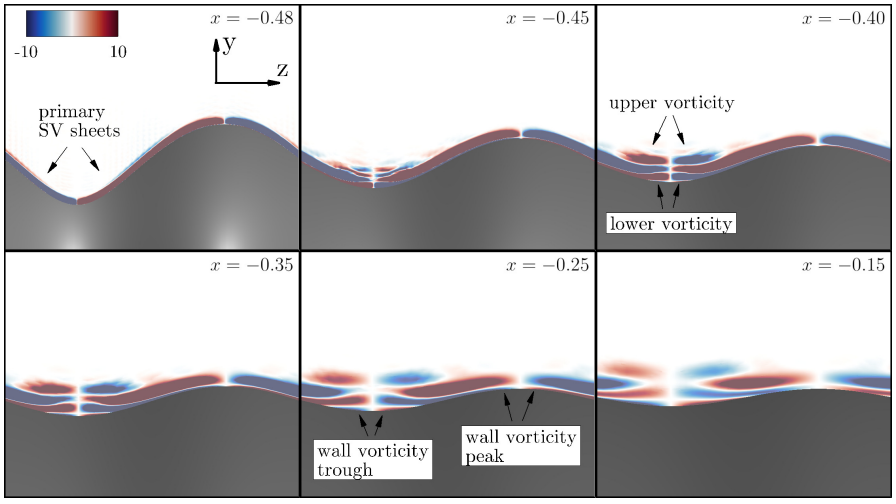

FIGURE 4.13: Contour plots of streamwise vorticity from $x = -0.48$ to $x = -0.15$ for the wavy aerofoil at $\alpha_g = 3.00^o$. The range shown in both spanwise and vertical direction is 0.05, but the estremes vary in the vertical direction to focus on the region close to the aerofoil surface.

Figure 4.14 shows the streamwise vorticity at $\alpha_g = 6.00^o$ in order to observe differences and similarities with the low incidence angle flow field. Streamwise vortex sheets are again generated at the leading edge, but in this case the reverse flow region is thicker and it has a greater influence on the flow field around the trough ($x = -0.45$). Once the flow reattaches, the flow is different from the low incidence case ($x = -0.40$). The upper and lower vorticity regions are generated again above and

below the original vortex sheets but the simmetry with respect to the trough section is lost. An additional vortex pair is generated on top. Moreover, the wall vorticity is observed more upstream at higher angles of attack. Overall, the vorticity region around the trough is thicker at $\alpha_g = 6.00^o$. Moving downstream, the vorticity decay is stronger on the upper part of the boundary layer and the pair on top becomes very weak ($x = -0.25$). The flow field at $\alpha_g = 6.00^o$ shows that downstream the reverse flow region the flow is still laminar and, as a consequence, the flow development further downstream happens at a slow rate and symmetric with respect to the trough section. The streamwise vorticity field shows some differences but the main vorticity pairs are observed as in the low angle case.

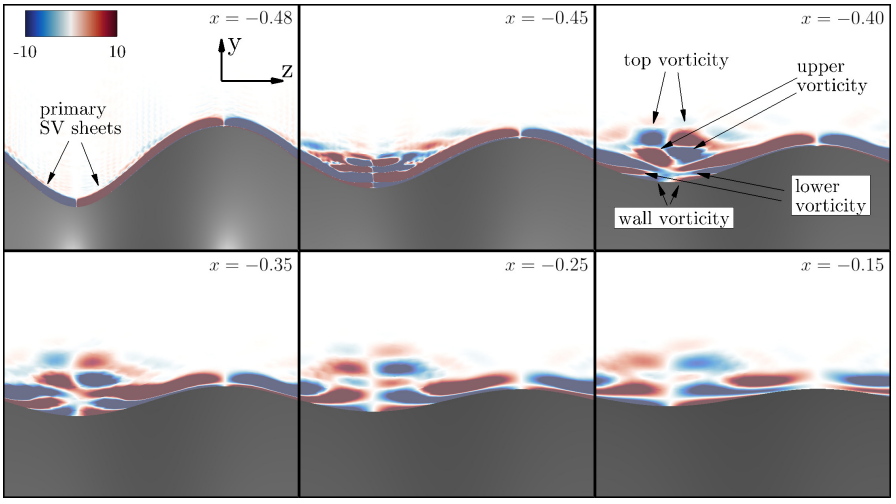

FIGURE 4.14: Contour plots of streamwise vorticity from $x = -0.48$ to $x = -0.15$ for the wavy aerofoil at $\alpha_g = 6.00^o$. The range shown in both spanwise and vertical direction is 0.05, but the estremes vary in the vertical direction to focus on the region close to the aerofoil surface.

4.4 Observations on λ-shock structure

The previous sections have shown that the modified aerofoil introduces new flow features in the leading edge region such as streamwise vorticity and reverse flow at the trough. These have an influence on the flow downstream and this section has the objective to analyse it. Firstly, the shock waves over the baseline and the wavy aerofoils are compared for two different conditions, one with similar structures between the two aerofoils and one with different structures. Then, the condition with major differences is investigated in more details trying to relate the different shock waves structure to the upstream flow characteristics. In addition, the interaction between the shock waves and the laminar and turbulent boundary layer is analysed in further details.

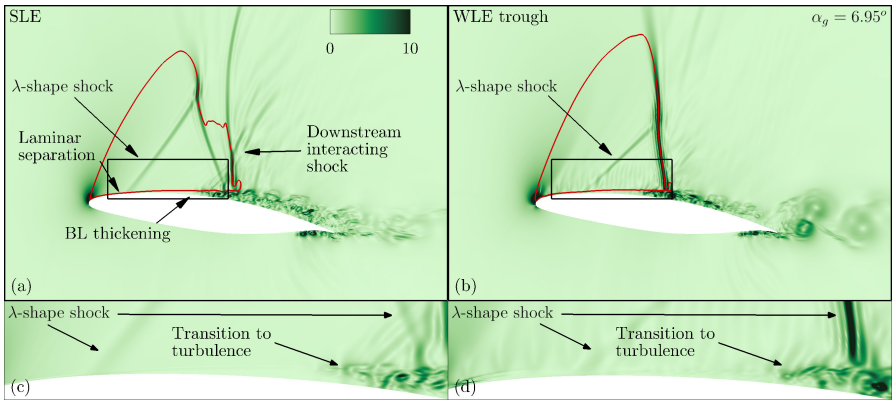

FIGURE 4.15: Pressure gradient magnitude of SLE (a) and WLE trough (b) at $\alpha_g = 6.95^o$. The red line highlights the sonic line and the black rectangle indicates the SBLI region plotted in (c) and (d).

At low incidence angles, weak shock waves travel upstream on the upper surface of both aerofoils, becoming weaker and finally detaching from the aerofoil at the LE. In this condition the main effect on the aerodynamic characteristics is the modified flow in the LE region, hence the shock structure is similar on both aerofoils (Figure 4.3a,d).

Increasing the angle of attack the shock waves become stronger and some differences can be observed. First of all, a λ-shape shock wave is observed over the wavy aerofoil (Figure 4.3f). This behaviour can be explained with the upstream developed streamwise vorticity which energises the BL and decreases the shock waves oscillations. On the contrary, on the straight counterpart shock waves are interacting with each other and with the BL. The consequence of these different shock shapes is a more downstream position of the laminar separation on the wavy aerofoil (Figure 4.3i) which has a positive effect on the lift performance (Figure 4.3n). This can be explained with the positive pressure gradient generated by the shock waves which tends to separate the BL. The presence of moving and interacting shock waves on the baseline aerofoil brings this positive pressure gradient upstream and causes an upstream movement of laminar separation. This intermediate condition is useful to understand the mutual interaction between shock wave structure and BL streamwise development.

At $\alpha_g = 6.95^o$, both aerofoils show a λ-shape shock (Figure 4.15a,b). On the baseline one the λ-shape shock tends to bend upstream and to interact with another shock generated downstream by the strong pressure waves coming from the TE and the turbulent BL. Downstream the λ-shock the flow is still supersonic and it becomes subsonic downstream the interacting shock. The interaction between the λ-shape shock and the laminar boundary layer is crucial to understand the described shock structure. The forward shock of the λ structure separates the laminar boundary layer ($x_s = -0.34$) as it is shown in Figure 4.15c. The separated laminar BL thickens and further downstream L-T transition is observed, sligthly upstream the backward shock

of the λ structure. The separation of a 2D laminar BL tends to move the forward shock upstream and as a consequence, the λ-shock structure bends upstream. The result is that downstream the backward shock, the flow is still supersonic and this allows the development of the interacting normal shock which brings the flow to subsonic conditions.

On the wavy aerofoil the shock structure does not have this detrimental effect on the BL because of the streamwise vorticity generated upstream which energises the BL. This is related to the presence of the counter-rotating streamwise vortices in the trough region which tend to accelerate the fluid in between them increasing the momentum, and thus confer to the fluid the extra amount of kinetic energy necessary to prevent local separation (Favier et al. (2012)). The interaction between the forward shock and the laminar BL is radically changed, the positive pressure gradient separates the BL ($x_s = -0.29$) but there is no upstream movement of the separation point and as a consequence no bending of the λ structure. Figure 4.15d shows that downstream the BL separation the behaviour is similar to the straight counterpart with transition to turbulence and interaction of turbulent BL with backward shock.

On both aerofoils the backward shock of the λ structure interacts with a turbulent BL (Figure 4.15a,b). Whether there is separation downstream the interaction or not, it has been observed (Delery (1985)) a BL thickening due to the interaction with a shock wave. The thickening is higher over the baseline aerofoil for two main reasons: the turbulent BL interaction with both the backward shock and the downstream normal shock over the baseline aerofoil and the more energetic BL over the modified aerofoil. Previous studies (Delery (1985)) show that vortex generators can be used to control the shock turbulent BL interaction and this result seems to be consistent with previous analysis. Figure 4.15b shows some vortices detaching from the aerofoil. They are related to the pressure difference between the upper and the lower surface at the TE.

To sum up, the SBLI over the V2C aerofoil at high angles of attack in transonic flow is characterised by a λ-shape shock, where the forward shock interacts with a laminar BL and the backward one interacts with a turbulent BL. The driving mechanism is the laminar BL separation due to the interaction with the forward shock. An upstream movement of the laminar separation can cause a bending of the λ-shape shock and the generation of an additional normal shock downstream. This can have an impact on the interaction with the turbulent BL, which can thicken because of a stronger interaction with two shocks. The generation of three dimensional laminar boundary layer and streamwise vorticity at the trough of the modified aerofoil is crucial to control the laminar BL separation and avoid its upstream movement.

This different SBLI at high angles can have an important impact on the flow unsteadiness. Previous studies (Szubert et al. (2016)) show that at $\alpha = 7.0^o$ the flow is characterised by the shock buffet phenomenon. The more energetic laminar BL over

the wavy aerofoil can have a major impact on the control of shock waves oscillation and should be analysed in further details with a static analysis.

4.5 Concluding remarks

The wavy leading edges over laminar supercritical aerofoils in transonic flow show promising results. This preliminary study has analysed the performance of the modified aerofoil at different angles of attack through a heaving motion. The main focus has been the quasi-linear part of the heaving motion. In the first part, the aerodynamic performance has been studied in details both in chordwise and spanwise directions. The main results are summarised as follows.

- The wavy geometry generates a distortion of the flow field in the leading edge region and this has an impact on the transition point which is moved upstream. The LE distortion enhances the disturbances initial size and growth.
- The drag coefficient is decreased in two main regions at low and moderate angles of attack: the leading edge and downstream the transition point. Increasing the angle of attack, the beneficial effect of the leading edge is decreased and the second region becomes dominant for the aerofoil performance.

The second part has analysed the flow field at the main sections of the wavy aerofoil (peak, hill and trough) and compared it with the baseline case. The leading edge analysis allows to explain the drag reduction at the LE region. The flow channeling phenomenon explains the acceleration to supersonic conditions of the flow at the trough in a wide range of angles of attack, which has an influence on the enhancement of the lift coefficient. The boundary layer and the streamwise vorticity evolution show that the modified leading edge energises the laminar boundary layer and makes it three dimensional.

In the third part, the results obtained during the previous analysis are exploited to explain the shock waves structure. At low incidence angles, the shock structure is similar over the two aerofoils and the aerodynamic characteristics are driven by the LE flow behaviour. A significant difference can be noticed at high angles of attack. The baseline aerofoil is characterised by the interaction of the main λ-shape shock with a downstream shock due to an upstream movement of the laminar separation, which modifies the shape of the λ shock and thickens the BL. The wavy aerofoil shows a different shock boundary layer interaction without the bending of the λ-shape shock due to a more energetic three dimensional laminar BL, which can be crucial for the control of shock buffet phenomenon.

Chapter 5

Mitigation of transonic shock buffet

This chapter aims to apply WLEs to mitigate shock buffet phenomenon over a supercritical aerofoil in transonic flow. The Dassault Aviation's V2C profile is simulated in a transonic flow with $Re_\infty = 5.0 \times 10^5$ and $M_\infty = 0.7$ at $\alpha = 7.0^o$. The spanwise domain size, denoted by L_z, is set to 0.05. In this chapter, the WLE wavelength is $\lambda_{LE} = 0.05$, thus only one wavelength is considered. Three different amplitudes are analysed $h = 0.0075$, $h = 0.0125$ and $h = 0.0250$ which correspond to an aspect ratio of the wavy geometry ($2h/\lambda$) of 0.3, 0.5 and 1, respectively.

The previous chapter has shown that wavy aerofoils increase the aerodynamic efficiency at low and moderate angles of attack, mainly because they are able to decrease the pressure drag. The results of this preliminary analysis prove that WLEs in transonic flows should be analysed in further details. The first question is, how does the WLE amplitude influence the aerodynamic performance of the modified aerofoil? Three different configurations are considered in order to answer this question, one with a low WLE amplitude ($h = 0.0075$), one with a conventional amplitude ($h = 0.0125$) and one with a high amplitude ($h = 0.0250$), they are called WLE1, WLE2 and WLE3, respectively (Figure 5.1). They are analysed at $\alpha = 7.0^o$ in terms of both mean and unsteady aerodynamic performance. The unsteady aerodynamic performance is a key analysis considering the imposed angle of attack (AoA). One of the main research topics in high speed flows is the mitigation of unsteady oscillations which in transonic flows result in shock buffet. This rises the second important question and justifies the choice of the imposed incidence angle, what is the influence of leading edge (LE) waviness over the shock buffet phenomenon? The unsteady pressure field is analysed in more details trying to understand its behaviour on both straight and wavy aerofoils. Then, a frequency filtering approach on the flow field is applied, trying to characterise all the unsteady phenomena.

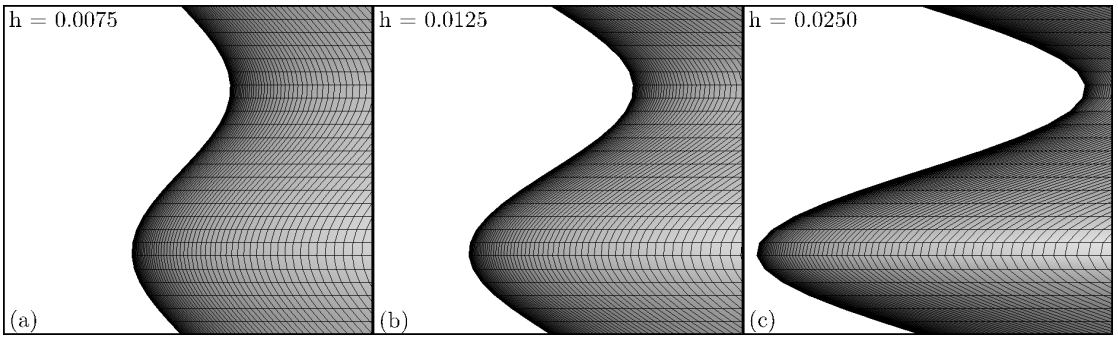

FIGURE 5.1: Leading edge view of WLE1 (a), WLE2 (b) and WLE3 (c) aerofoils with 50% of points shown.

5.1 Time-averaged characteristics

The first part of this chapter analyses the mean aerodynamic characteristics of the wavy aerofoils, comparing them with the straight counterpart. The objective is to define the effect of WLE amplitude on mean aerodynamic performance and determine the most efficient configuration before extending the analysis to the unsteady characteristics. The mean aerodynamic performance is first evaluated in streamwise direction and then in spanwise direction, comparing the results between straight and wavy aerofoils.

5.1.1 Streamwise aerodynamic performance details

Table 5.1 shows the mean aerodynamic performance of straight and wavy aerofoils. The mean lift generated by the modified aerofoil is increased with $h = 0.0075$ and it tends to decrease when the amplitude is enhanced. As a result, WLE3 aerofoil has a lower mean lift than the straight one. The trend of the mean drag is different. The wavy aerofoil tends to decrease the drag coefficient and it is quite constant increasing the WLE amplitude. In order to understand this trend, it is necessary to investigate the drag components. The pressure drag on wavy aerofoils is decreased compared to the one on the baseline case and it seems to decrease when the amplitude is enhanced, while the skin friction drag on wavy aerofoils is increased compared with the one on the baseline case and it grows when the amplitude is increased. The pressure drag is the dominant component in transonic flows and this explains the overall improved aerodynamic performance on wavy aerofoils. Increasing the amplitude, the effects on pressure and skin friction drag components seem to cancel each other. The trend of drag coefficient is expected to change when the amplitude is enhanced to values higher than the ones considered in this study. In this case, the drag should start increasing because of the increased flow distortion at the LE which should bring to an early separation.

	C_L	C_D	C_{Dp}	C_{Df}	C_L/C_D
SLE	0.943	0.084	0.081	0.00314	11.20
WLE1 ($h = 0.0075$)	1.003	0.074	0.070	0.00382	13.56
WLE2 ($h = 0.0125$)	0.944	0.073	0.069	0.00383	12.91
WLE3 ($h = 0.0250$)	0.883	0.072	0.067	0.00460	12.34

TABLE 5.1: Mean aerodynamic performance of wavy and straight aerofoils at $\alpha = 7.0^o$.

Figure 5.2 shows the pressure coefficient over the main sections of the three wavy aerofoils (peak, hill and trough) and compares it with the distribution over the straight one. The pressure distribution shape over the upper surface changes between the straight and the wavy aerofoil. The mean pressure coefficient on the baseline aerofoil increases regularly from the LE moving downstream up to the TE. This is a sign of large and periodic shock wave oscillations over time. On the other hand, the mean pressure coefficient over the modified aerofoils shows a plateau in the laminar BL region followed by a steep pressure increase. The pressure coefficient upstream the L-T transition point is lower over the modified aerofoils and then it becomes higher downstream the L-T transition. The pressure plateau shrinks increasing the WLE amplitude because it starts more downstream due to the amplitude increase and it finishes more upstream due to the L-T transition point movement. The laminar-turbulent transition point moves upstream when the amplitude is increased because the flow distortion at the LE is enhanced; this means that the disturbances generated at the LE are higher when the wavy amplitude is increased and this brings to an earlier L-T transition.

The effect of pressure distribution over the lift coefficient is shown in Figure 5.4 where the relative change between SLE and WLE cases in terms of piecewise distribution of lift is illustrated for the three modified aerofoils. The difference between SLE and WLE aerofoils lift coefficient is computed over small sections along the aerofoil in the chordwise direction. Then, the derivative is computed in order to take into account the different sections' length. The trend is consistent for the three wavy aerofoils, the piecewise distribution of lift is higher over the modified aerofoils between the end of the LE region and the L-T transition point. The main effect of the wavy amplitude can be observed in the LE region where an amplitude increase has a negative impact on the local lift. A second effect is the upstream movement of the L-T transition point which shrinks the region of lift enhancement when the WLE amplitude is enhanced. Overall, the amplitude growth has a negative effect on the aerofoil lift but a small wavy amplitude (WLE1) allows to generate a higher lift than the straight counterpart.

The relative change between SLE and WLE cases in terms of piecewise distribution of pressure drag coefficient (Figure 5.5) shows also a consistent trend changing the WLE amplitude. The LE region has almost a negligible effect with a low amplitude ($h = 0.0075$), while higher amplitudes tend to increase the LE region's drag with respect to the baseline case. The beneficial effect for the drag is observed downstream

the modified aerofoil L-T transition point. These results are consistent with the ones in Chapter 4. The region of L-T transition on the modified aerofoil has a negative contribution on drag coefficient but it decreases when wavy amplitude is increased. The decrease of pressure drag coefficient with the amplitude growth, observed in Table 5.1, is the result of these streamwise positive and negative effects. Overall, the amplitude increase has a positive effect on pressure drag coefficient, even if the LE region shows an opposite trend. This suggests that the flow distortion at the LE does not bring to a local benefit but it has a positive effect on BL development downstream and its interaction with the shock wave.

The skin friction drag increases with WLE amplitude growth (Table 5.1). Figure 5.3 displays the mean skin friction coefficient distribution over the upper surface of straight and wavy aerofoils and shows that the skin friction drag increase is located in the laminar BL region and it is distributed over the aerofoil span. This can be explained with the LE flow distortion which modifies 2D laminar BL, essential to have a low skin friction drag on supercritical aerofoils. Figure 5.3 shows that the mean position of laminar separation is moved downstream by the wavy aerofoil with respect to the straight one. In particular, the trough section shows the most upstream separation and an additional small LSB close to the leading edge, while the peak section has the most downstream separation. This trend is consistent changing the WLE amplitude. The main difference between straight and modified aerofoils is that the first shows laminar separation, reattachment and then L-T transition, while the second one shows laminar separation and then L-T transition.

The relative change between SLE and WLE cases in terms of piecewise distribution of skin friction drag coefficient (Figure 5.6) shows that the modified aerofoils increase the skin friction drag upstream the L-T transition point with the highest increase close to the LE region. This result can be explained considering the profile chosen for this study. A laminar supercritical profile is designed to minimize the skin friction drag by delaying the laminar-turbulent transition on the aerofoil in design condition. The wavy aerofoils generate a distortion in the LE region and a three dimensional laminar BL develops downstream and this has a negative effect on the skin friction drag in the laminar BL region.

The mean aerodynamic analysis shows that modified aerofoils allow to increase the aerofoil efficiency over the range of analysed amplitudes. The best performance is obtained with $h = 0.0075$, where lift coefficient is increased and drag coefficient is decreased with respect to the straight counterpart. Since an aerofoil in transonic flow at moderate angles of attack is characterised by flow unsteadiness, an analysis of the flow oscillations over the aerofoils is essential to define WLEs aerodynamic performance.

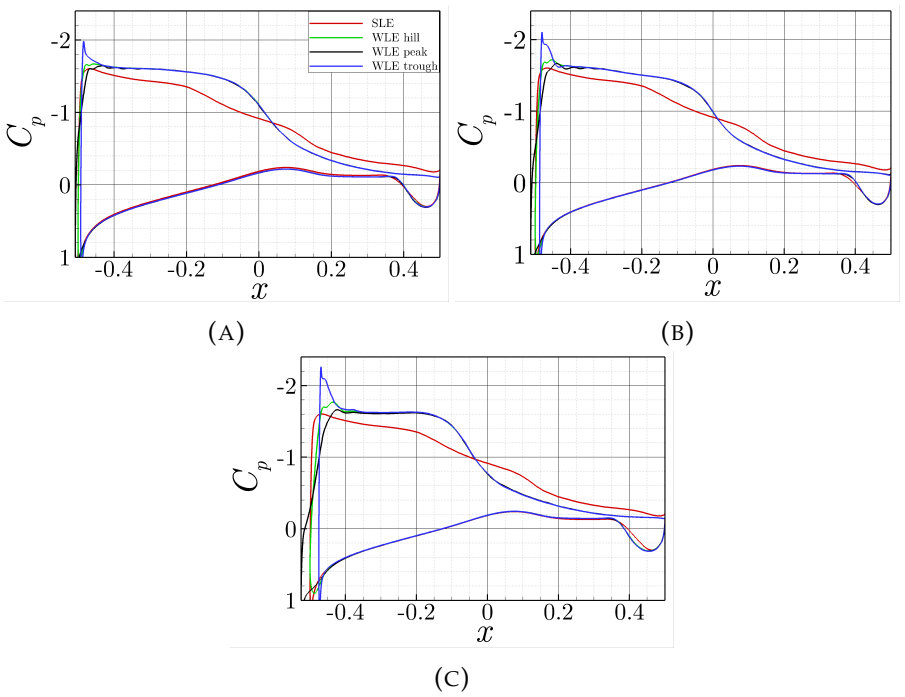

FIGURE 5.2: Mean pressure coefficient distribution at WLE peak, hill and trough and over SLE at $\alpha = 7.0^o$ for WLE1 (a), WLE2 (b) and WLE3 (c) aerofoils.

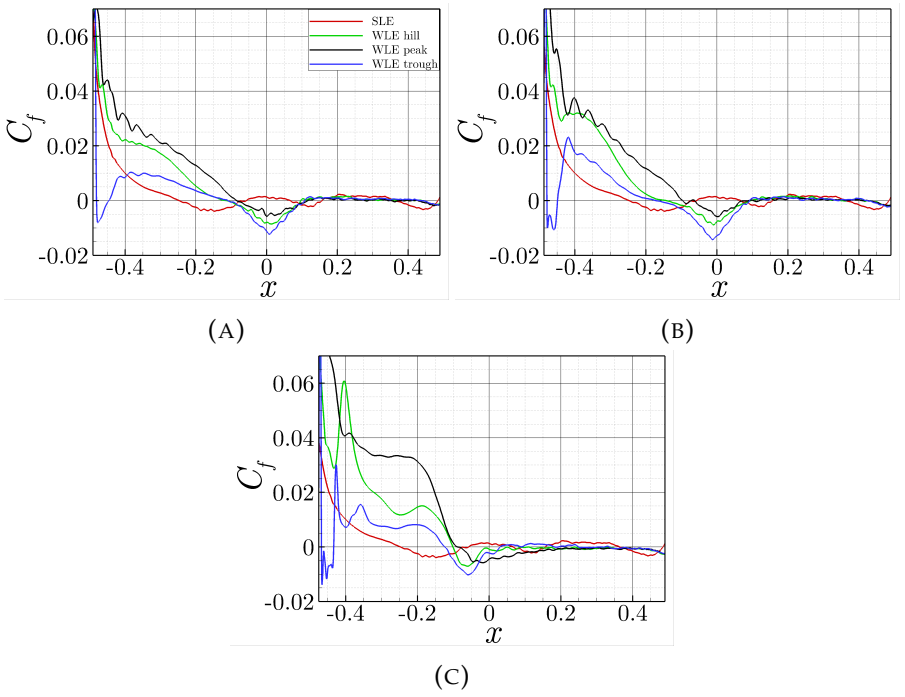

FIGURE 5.3: Mean skin friction coefficient distribution over the suction side at WLE peak, hill and trough and over SLE at $\alpha = 7.0^o$ for WLE1 (a), WLE2 (b) and WLE3 (c) aerofoils.

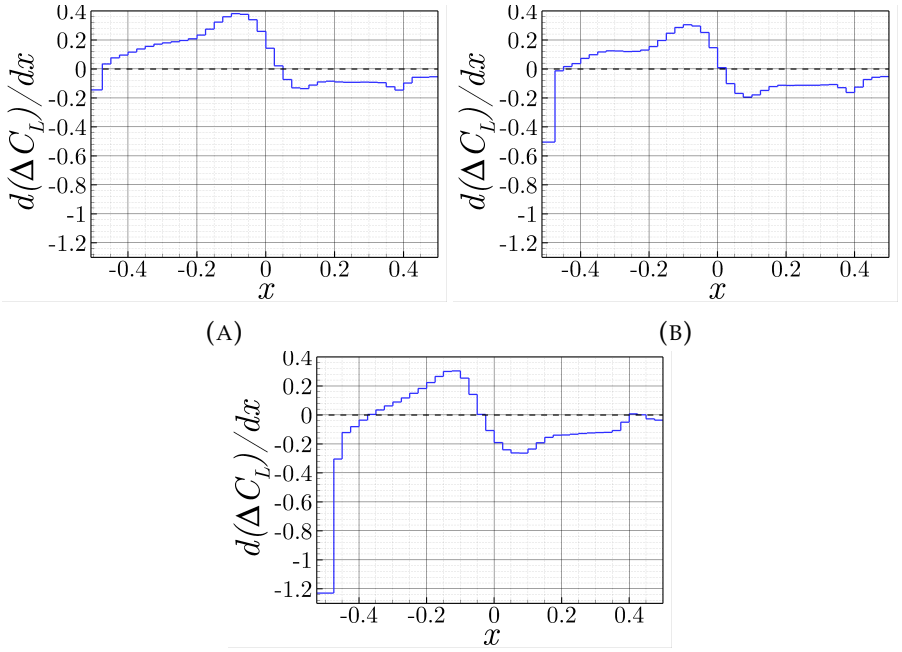

FIGURE 5.4: Relative change in aerodynamic forces between SLE and WLE cases in terms of piecewise distribution of lift along the chord calculated from wall pressure ($d(\Delta C_L)/dx$) for WLE1 (a), WLE2 (b) and WLE3 (c) aerofoils. The relative difference between SLE and WLE cases are denoted by $\Delta\{.\} = \{.\}_{WLE} - \{.\}_{SLE}$.

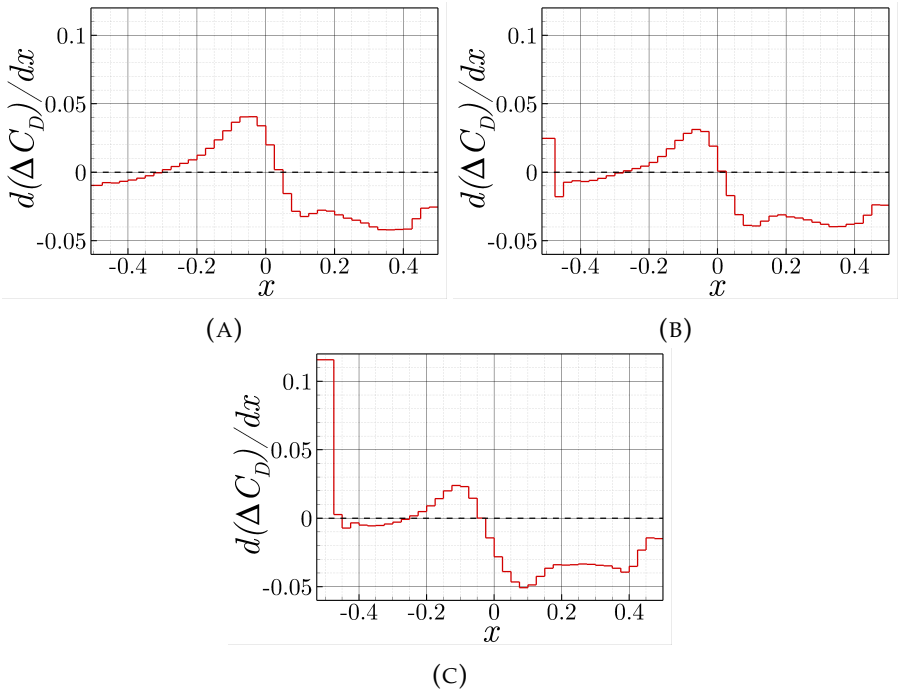

FIGURE 5.5: Relative change in aerodynamic forces between SLE and WLE cases in terms of piecewise distribution of pressure drag along the chord calculated from wall pressure ($d(\Delta C_D)/dx$) for WLE1 (a), WLE2 (b) and WLE3 (c) aerofoils. The relative difference between SLE and WLE cases are denoted by $\Delta\{.\} = \{.\}_{WLE} - \{.\}_{SLE}$.

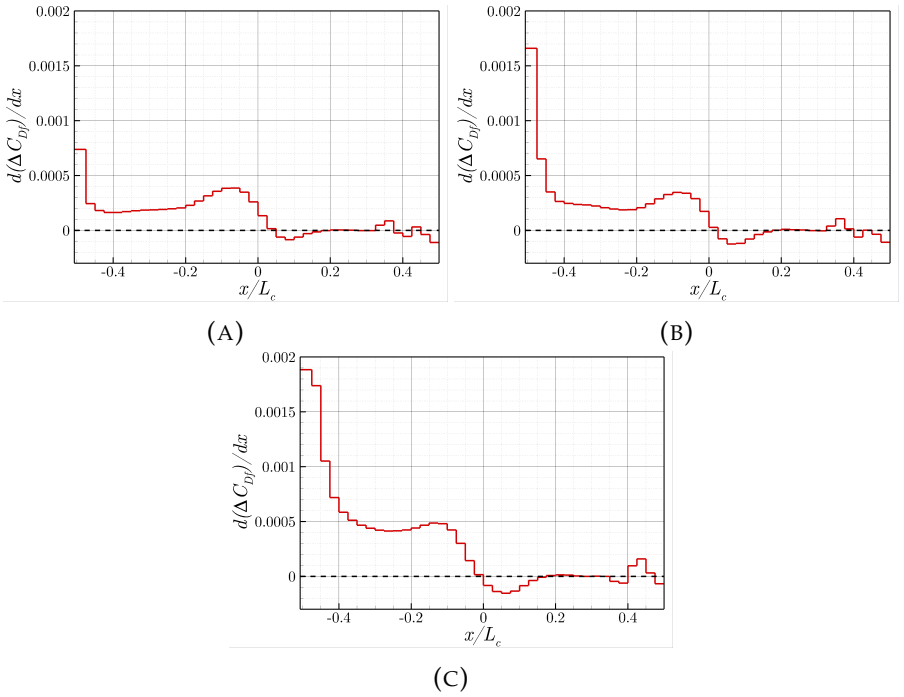

FIGURE 5.6: Relative change in aerodynamic forces between SLE and WLE cases in terms of piecewise distribution of skin friction drag along the chord ($d(\Delta C_{Df})/dx$) for WLE1 (a), WLE2 (b) and WLE3 (c) aerofoils. The relative difference between SLE and WLE cases are denoted by $\Delta\{.\} = \{.\}_{WLE} - \{.\}_{SLE}$.

5.1.2 Spanwise aerodynamic performance details

The spanwise aerodynamic performance of a wavy aerofoil in transonic flows has been analysed in Chapter 4. The objective of this section is to extend previous analysis to a higher incidence angle and to the influence of wavy amplitudes.

The mean lift coefficient distribution shows again two maxima at the peak and at the trough of the wavy geometry, where the first one is lower than the second one (Figure 5.7a). The lowest value is obtained at the hill section because the derivative of the surface with respect to the z direction has the highest value at the hill, thus the force has the largest spanwise component. The trough generates a lift higher than the peak because of the pressure distribution close to the leading edge. Increasing the wavy amplitude, the two maxima grow.

The drag coefficient shows a minimum at the trough and a maximum at the peak (Figure 5.7b). Their amplitude also increases when the wavy amplitude is enhanced. This spanwise distribution can be explained taking into account the pressure distribution close to the LE. The peak section is the one where there is the most gradual pressure decrease between the stagnation point and the pressure coefficient peak. This extended high pressure region increases the drag. The opposite behaviour is observed at the trough; the pressure coefficient changes suddenly from the highest to lowest values of the pressure coefficient (Figure 5.2).

The resulting spanwise efficiency has a maximum at the trough and a minimum at the peak (Figure 5.7c). The efficiency is evenly distributed between the maximum and the minimum at low wavy amplitudes ($h = 0.0075$). Increasing the wavy amplitude to high values ($h = 0.0250$), the efficiency in the trough region shows the maximum increasing quickly and the shape of the distribution becoming sharp, while in the peak region the minimum decreases slowly and the shape becomes quite flat. This is consistent with the overall decreased efficiency when WLE amplitude is increased (Table 5.1).

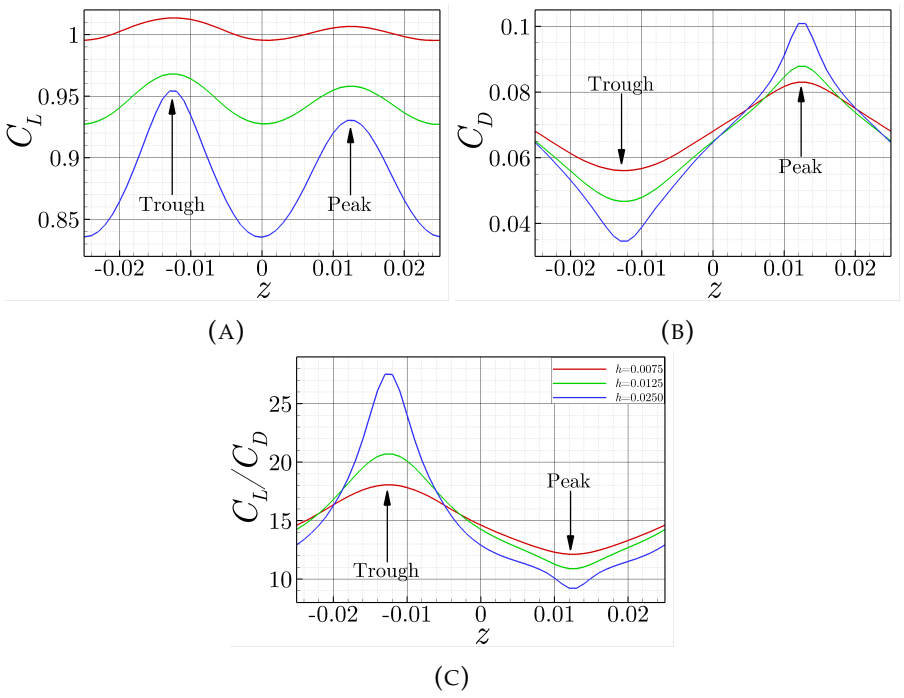

FIGURE 5.7: Mean lift (a), drag (b), and efficiency (c) spanwise distribution over WLE1, WLE2 and WLE3 aerofoils at $\alpha = 7.0^o$.

5.2 Unsteady characteristics

The mean aerodynamic characteristics analysis shows a performance improvement of the modified aerofoil using different WLE amplitudes, but the control of unsteady phenomena is the main focus at moderate and high angles of attack. First of all, the aerodynamic force fluctuations are analysed to give an overview of the unsteady aerodynamic performance and the influence of wavy amplitude on mitigation of flow unsteadiness. Then, the unsteady motion of SLE and WLE aerofoils is studied in details showing the flow characteristics and identifying the different phenomena with a frequency filtering technique.

5.2.1 Aerodynamic force fluctuations

Figure 5.8 illustrates lift and drag coefficient time signal for baseline and modified aerofoils. The baseline case shows large low frequency lift oscillations as main unsteady phenomenon (Figure 5.8a), which are consistent with previous studies (Szubert et al. (2016)) on the same aerofoil at higher Reynolds numbers. A consistent behaviour is observed for the drag coefficient time signal (Figure 5.8b). The power spectral density (PSD) displays two maxima (Figure 5.9), a low frequency one ($St = 0.12$) which might be related to shock buffet and a high frequency one ($St = 1.2$) which seems to be associated with vortex shedding (Szubert et al. (2016)).

On the contrary, the modified aerofoils show different time signals changing the WLE amplitude. WLE1 aerofoil ($h = 0.0075$) presents two main lift and drag oscillations, a low frequency one at $St = 0.1$ and a high frequency one at $St = 0.9$ (Figure 5.9). The PSD shows a mitigation of the low frequency phenomenon with respect to the baseline case, while the high frequency one increases its strength. The nature of these unsteady phenomena needs to be investigated in the following sections. The PSD for WLE2 aerofoil ($h = 0.0125$) shows that the low frequency oscillation ($St = 0.14$) is drastically decreased and the high frequency one ($St = 0.64$) becomes dominant for both lift and drag. At the highest amplitude considered in this study ($h = 0.0250$) the signals change again significantly. The low frequency oscillation ($St = 0.08$) is dominant and it is the strongest on the modified aerofoils, while the high frequency component ($St = 1.0$) is even lower than the one on the straight counterpart.

The main outcome of this unsteady performance analysis is that the leading edge waviness allows to suppress a strong low frequency oscillation, generating a high frequency one. Moreover, the wavy aerofoils' time signal shows always two components and their magnitude changes with different WLE amplitudes. The Strouhal number of the maxima are summarised in Table 5.2. The low frequency maximum initially decreases when WLE amplitude is enahnced and then it increases again. The high frequency maximum has an opposite trend, it initially increases when the WLE amplitude is increased and then it decreases. It seems that the strength of the high frequency oscillation has an influence on the strength of the low frequency one. This hypothesis can be validated once the details of the unsteady phenomena are fully understood. The objective of the next sections is to characterise the phenomena over the baseline aerofoil, already observed in previous studies, and understand the phenomena over the modified aerofoils.

5.2.2 Overview of the unsteady motion

The mitigation of aerodynamic coefficients oscillations shows that leading edge waviness is a promising passive technique for the control of a low frequency

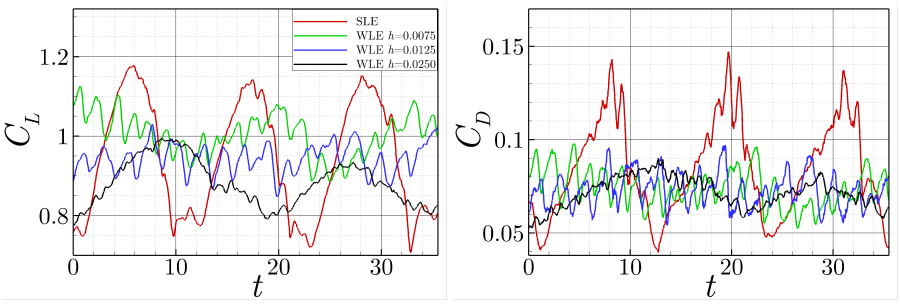

(A) (B)

FIGURE 5.8: Lift (a) and drag (b) coefficient time signal for SLE aerofoil and WLE1, WLE2 and WLE3 aerofoils.

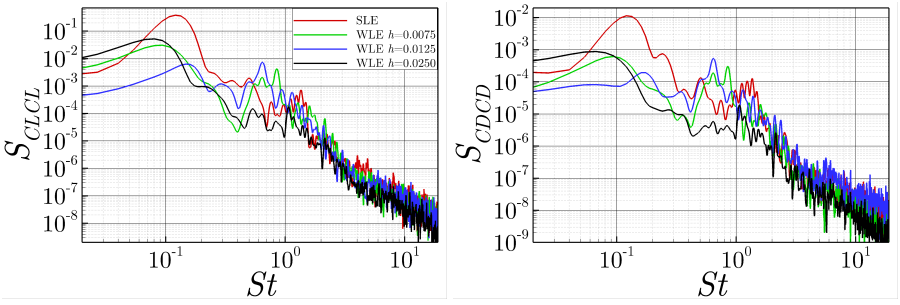

(A) (B)

FIGURE 5.9: Lift (a) and drag (b) coefficient power spectral density with respect to the Strouhal number for SLE aerofoil and WLE1, WLE2 and WLE3 aerofoils.

	I	*II*
SLE	0.12	1.20
WLE1 (h=0.0075)	0.10	0.90
WLE2 (h=0.0125)	0.14	0.64
WLE3 (h=0.0250)	0.08	1.00

TABLE 5.2: Strouhal number of aerodynamic coefficients PSD maxima for SLE aerofoil and WLE1, WLE2 and WLE3 aerofoils.

oscillation which seems related to the shock buffet phenomenon. The analysis of the flow field over the aerofoils has the objective to understand the different phenomena. The main focus is the comparison between baseline and WLE2 aerofoils. The main reason is that the best result in terms of low frequency oscillation control is obtained with $h = 0.0125$. Secondly, the results shown in the previous section display always two maxima in the PSD of the wavy aerofoils which change their magnitude varying the amplitude, so it is assumed that the physical phenomena generating these maxima are the same for the different modified aerofoils. In addition, the characteristics of low frequency oscillations over the wavy aerofoils are compared with the ones over the baseline case.

Figure 5.10 shows the pressure gradient magnitude around the straight aerofoil during a full low frequency cycle, which can be identified with the shock buffet

phenomenon. Initially, the shock wave is at the most upstream position and it generates a large separation of turbulent BL (Figure 5.10a). The pressure waves generated from the vortices passing through the trailing edge decrease their strength because of BL separation. As a consequence, the turbulent boundary layer re-attaches and becomes thinner and the shock wave starts moving downstream (Figure 5.10b). At the most downstream position, there is a complex shock pattern because a λ-shape shock is followed by a normal shock (Figure 5.10c). The upstream shock of the λ structure interacts with the laminar BL and it tends to separate it, generating a positive pressure gradient. Due to this strong interaction with the BL, there is a large separation which moves the transition point and large vortices develop downstream the SBLI region (Figure 5.10d). Strong sound waves are emitted from the TE and both the turbulent BL and the shock wave location move upstream. The shock wave reaches the most upstream position and the cycle starts again.

The unsteady phenomena over the baseline aerofoil are further investigated considering the wall pressure signals at different locations on the upper surface (Figure 5.11). The low frequency peak is observed everywhere on the upper surface but the PSD shows high values close to the TE where large vortical structures are observed and at the most upstream and downstream positions of the SBLI. The high frequency peak shows a different trend, it is observed very close to the trailing edge and it reaches its highest value exactly at the TE, suggesting a relation with the vortex shedding phenomenon which requires further investigations.

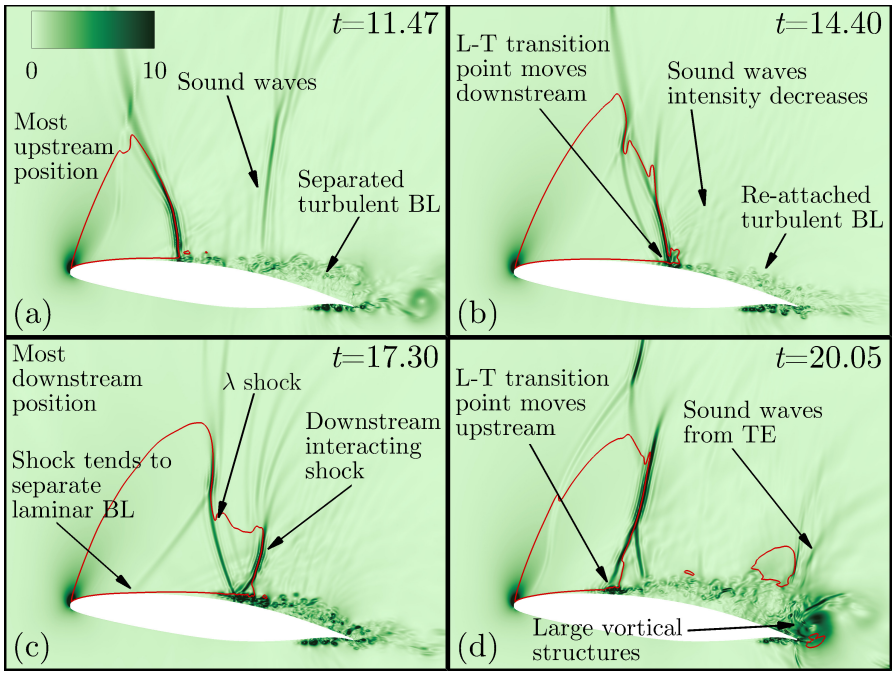

FIGURE 5.10: Pressure gradient magnitude flow field around SLE aerofoil during one cycle of the shock buffet oscillation: most upstream position (a), shock wave downstream movement (b), most downstream position (c) and shock wave upstream movement (d).

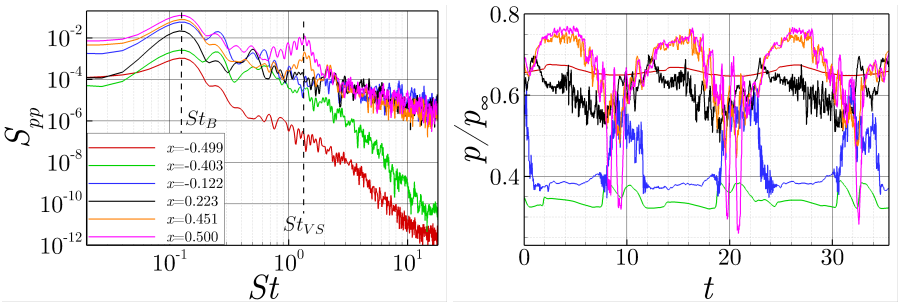

(A) (B)

FIGURE 5.11: Power spectral density with respect to the Strouhal number (a) and time signal (b) of wall pressure at different chordwise locations over the upper surface of SLE aerofoil.

Figure 5.12 shows the pressure gradient magnitude around WLE3 aerofoil during a full cycle of the shock buffet oscillation. This allows to compare the characteristics of the shock buffet phenomenon over the modified aerofoil with the one over the straight counterpart. At the most upstream position the turbulent boundary layer is separated and a λ-shape shock is observed (Figure 5.12a). Once the BL re-attaches, the shock moves downstream up to the most downstream position (Figure 5.12b) where a λ-shape shock is observed again (Figure 5.12c). The interaction between the λ-shape shock and the laminar boundary layer tends to separate the BL and it is responsible for the shock wave upstream movement. As a consequence, large vortical structures develop downstream (Figure 5.12d).

One of the main differences in the shock buffet oscillation between baseline and wavy aerofoils is the amplitude of the shock wave oscillation. Table 5.3 illustrates the details of the shock positions, where x_{SU} is the shock wave most upstream position, x_{DU} is the most downstream position and Δx_S is the oscillation's amplitude. WLE2 aerofoil is not reported because a shock oscillation is not observed. The overall result is that the shock wave over the wavy aerofoils shows a lower amplitude than the straight counterpart, in particular the shock wave displacement over WLE3 is about 45% of the straight one and over WLE1 is about 18% of the straight one (Table 5.3). The WLE amplitude has an influence on the strength of the oscillation, as it was observed at the beginning of this section. The shock wave has a larger oscillation over WLE3 where the high frequency oscillation is weaker. This suggests again a strong connection between low and high frequency oscillations and a more detailed investigation of the high frequency phenomenon is required. The consequences of the shock oscillation lower amplitude is the generation of smaller vortical structures during the upstream movement and the emission of weaker pressure waves from the TE and the turbulent BL. Another major difference is the SBLI at the most downstream position. The baseline aerofoil shows a complex shock structure that interacts with the BL and tends to separate it, while the modified aerofoils display a λ-shape shock where the two shock waves of the λ structure are very close. In addition, wavy leading edges create

streamwise vorticity in the laminar BL which makes it more energetic, as it was observed in the previous chapter. The shock structures together with the three dimensional laminar BL are the main flow characteristics which change the shock buffet phenomenon between straight and wavy aerofoils.

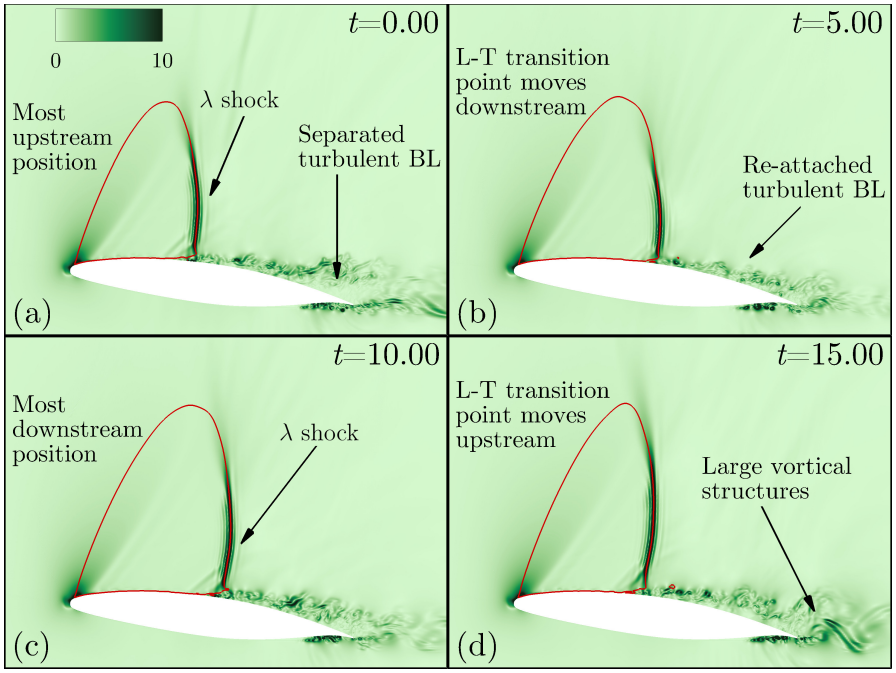

FIGURE 5.12: Pressure gradient magnitude flow field at the hill section of WLE3 aerofoil during one cycle of the shock buffet oscillation: most upstream position (a), shock wave downstream movement (b), most downstream position (c) and shock wave upstream movement (d).

	SLE	WLE1	WLE3
x_{SU}	-0.12	0.00	-0.06
x_{SD}	0.10	0.04	0.04
Δx_S	0.22	0.04	0.10

TABLE 5.3: Shock wave oscillation details for the baseline aerofoil and WLE1 and WLE3 aerofoils.

Figure 5.13 illustrate the pressure signals along the chord of WLE2 aerofoil, from the trough to the TE and its power spectral density with respect to the Strouhal number. The first interesting result is that the low frequency peak is observed only around $x = 0.1$. The reason is that it is not observed a large separation as in the straight counterpart, the shock wave shows very limited upstream-downstream movements. The high frequency pressure peak is observed on different chordwise locations, in particular it reaches the highest value around the SBLI and at the trailing edge. This shows a first difference between the high frequency phenomena on straight and wavy aerofoils. The high frequency phenomenon on the straight aerofoil is detected only close to the TE, while the one on the wavy aerofoil can be observed on different locations of the upper surface. Additional local unsteady phenomena can be observed

from this analysis. First of all, a bump of wall pressure PSD is detected at $x = 0.118$ around $St = 5$ which disappears at the TE. Secondly, a bump appears also at $St = 11$ close to the leading edge. This seems to be related to Kelvin-Helmholtz instability due to the LSB observed at the trough in Figure 5.3. These phenomena do not appear at the other sections and they do not appear also in the PSD of the aerodynamic coefficients, thus they do not have an influence on the unsteady aerodynamic performance. Figure 5.14 shows the pressure gradient magnitude around WLE2 aerofoil during a full high frequency cycle, at the minimum and maximum values. The flow field does not display clearly the driving mechanism of this unsteady oscillation. At the lift minimum there is a BL thickening in the L-T transition region, this bends the λ-shape shock and the forward shock moves upstream (Figure 5.14a). At the lift maximum the BL thins and the λ-shape shock moves in the opposite direction (Figure 5.14b). It is observed downstream the advection of vortical structures, generated from the thickening and thinning of the BL. The high frequency phenomenon seems to be driven by the BL oscillation in the L-T transition region, but further investigations are needed.

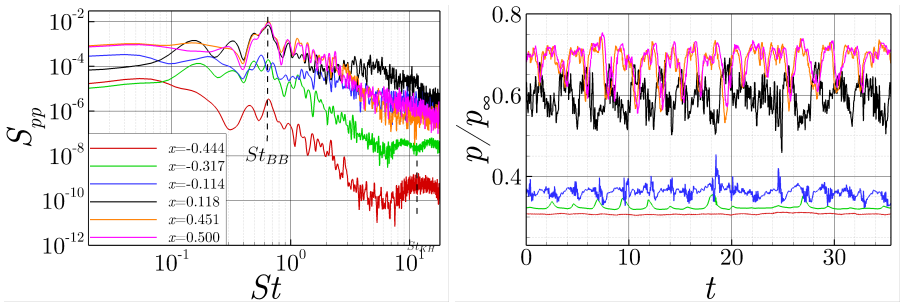

FIGURE 5.13: Power spectral density with respect to the Strouhal number (a) and time signal (b) of wall pressure at different chordwise locations over the upper surface of WLE2 trough section.

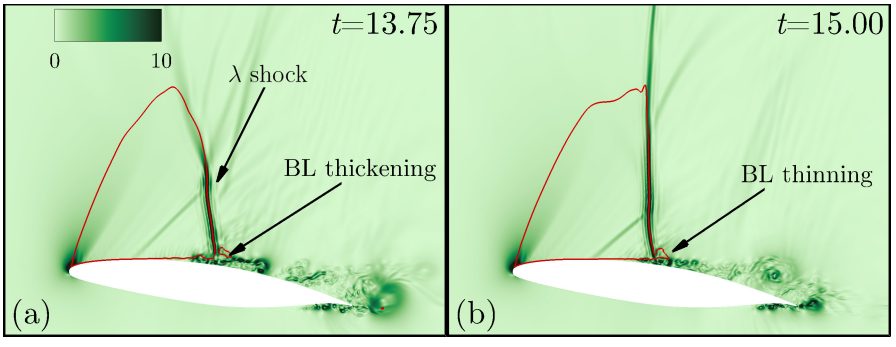

FIGURE 5.14: Pressure gradient magnitude flow field at the hill section of WLE2 aerofoil at the high frequency oscillation's minimum (a) and maximum (b).

5.2.3 Physical phenomena identification and analysis

Previous studies have used different techniques to analyse unsteady phenomena and to identify coherent structures. Proper Orthogonal Decomposition (POD) searches for the most energetic modes whereby coherent structures with high energy content are likely to be represented by POD basis functions (Lumley (1967)). Dynamic Mode Decomposition (DMD) targets the temporal periodicity of the coherent structures and distinguishes modes with respect to their linear amplification (Schmid (2010)). These methods fail when the relevant coherent structures occur at low energies or at multiple frequencies. Spectral Proper Orthogonal Decomposition (SPOD) has been developed to overcome this limitation and enables a clear separation of phenomena that occur at multiple frequencies and energies (Sieber et al. (2016)).

In this study a different approach is used based on a frequency filtering of the flow (Turner and Kim (2020c)). The advantage is that once the flow field is filtered, it is still possible to analyse its evolution over time and the results are not limited to a contour of the modes. The limitation is that the results do not include an energetic representation of the modes like in the SPOD. The details of the method are given as follows.

- The Fourier transform of an arbitrary field variable is evaluated for every grid point.
- Real and imaginary parts are multiplied by a weighting function

$$g(f) = \exp\left[-a(f - f_0)^2\right] + \exp\left[-a(f - f_0)^2\right] \tag{5.1}$$

  where f_0 is the frequency of the unsteady phenomenon and a is an arbitrary parameter that defines the function's wideness. Increasing the value of a, the effect of close frequencies is filtered out.
- The inverse Fourier transform is evaluated for every grid point.

The result is a filtered field of the initial field variable. Figure 5.15 shows an example of the original and filtered spanwise vorticity flow field on WLE2 aerofoil. The high magnitude of the filtered field indicates where the field is more energetic at the given frequency, thus the location of the oscillation's origin and this allows to understand the unsteady phenomenon.

The objective of this section is to exploit the frequency filtering method to analyse the unsteady phenomena on both straight and wavy aerofoils. It was observed at the beginning of this section that each aerofoil shows two main unsteady phenomena and their frequencies are summarised in Table 5.2. It is clear that the low frequency peak

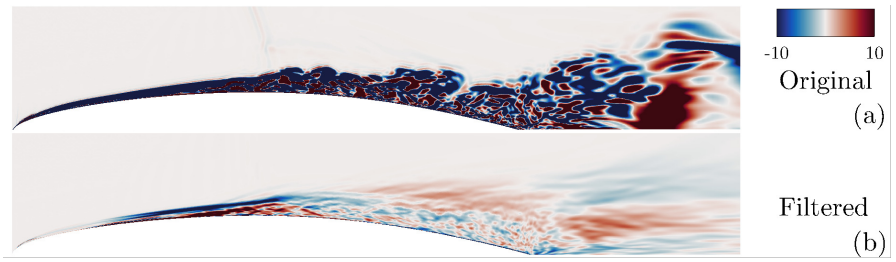

FIGURE 5.15: Instantaneous original (a) and filtered (b) spanwise vorticity at the trough section of WLE2 aerofoil.

(first column of Table 5.2) is caused by the shock buffet phenomenon, thus the main focus is the characterisation of the unsteadiness caused by the second peak.

The high frequency oscillation on the straight aerofoil is detected at the trailing edge. Since Figure 5.10 displays large vortical structures at the TE region, the filtered field is the pressure coefficient. Figure 5.16 shows the filtered field around the TE during one cycle of the high frequency oscillation. The circular structures shown at the trailing edge suggest the periodic release of vortices from the aerofoil. This allows to identify the unsteady oscillation with the vortex shedding. The vortex shedding phenomenon on a circular cylinder is usually detected at $St \simeq 0.2$. The Strouhal number on an aerofoil is calculated with respect to the chord, while on a cylinder it is defined with respect to the diameter. Since the Strouhal number obtained in this case is 6 times larger, the vortex size is expected to be 6 times smaller than the aerofoil chord. A vortex diameter of about 0.16 is observed in Figure 5.10. This validation, together with the frequency filtering analysis, proves that the unsteady phenomenon at high frequency is the vortex shedding. The shock wave is oscillating at a low frequency and the SBLI point is moving backward and forward periodically over the upper surface of the aerofoil. During this oscillation, vortical structures are released periodically at a higher frequency causing the vortex shedding phenomenon. This means that the modification of the high frequency phenomenon with active or passive control techniques can have a positive effect also on the low frequency phenomenon. That's why previous approaches with passive techniques modifying the TE were successfully controlling the shock buffet oscillation (Iovnovich and Raveh (2012)). The problem is that those techniques were drastically decreasing the efficiency of the aerofoil, while active techniques which can be applied only at high angles of attack seem to give better results (Gao et al. (2016)).

The high frequency phenomenon on WLE aerofoil has been already analysed in Figure 5.14. It has been observed a periodic oscillation in the SBLI region. For this reason the field filtered to analyse this phenomenon is the spanwise vorticity. The region highlighted by the filtered field is located in the LSB region up to the SBLI point (Figure 5.17). Figure 5.18 shows the streamwise velocity in the BL region upstream the SBLI. The black line defines the LSB canopy and it shows clearly the high frequency

BL thickening and thinning. This kind of phenomenon has been observed in previous studies (Dandois et al. (2018a)), it is related to the LSB breathing and as a consequence it modifies the shape of the λ-shape shock as shown in Figure 5.14. It is possible to observe the same unsteadiness at the TE with a time lag with respect to the one in the laminar boundary layer (Figure 5.17). This means that the origin of the unsteady phenomenon is in the laminar BL, close to the laminar-turbulent transition point, and this generates vortical structures which are convected up to the TE. This explains why the highest values of the high frequency peak in Figure 5.13 are close to the L-T transition and to the TE. The wavy aerofoil modifies the flow at the leading edge and the development of the flow downstream in the laminar BL is responsible for the introduction of another unsteady phenomenon which is crucial to control the shock buffet oscillation. This allows to explain the bump observed at $x = 0.118$ in Figure 5.13. In this region, small vortices with different sizes are generated and then convected downstream. The range of frequencies detected in Figure 5.13 is consistent with the size of the vortices observed in Figure 5.14.

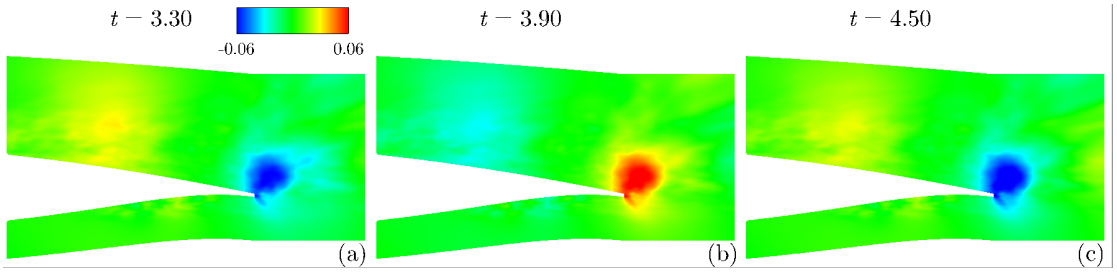

FIGURE 5.16: Filtered pressure coefficient field around the trailing edge of SLE aerofoil during one cycle of the high frequency oscillation. Negative filtered pressure coefficient shows the release of a vortex from the trailing edge (a), followed by a region of positive filtered pressure coefficient (b), then the cycle starts again and another vortex is released (c).

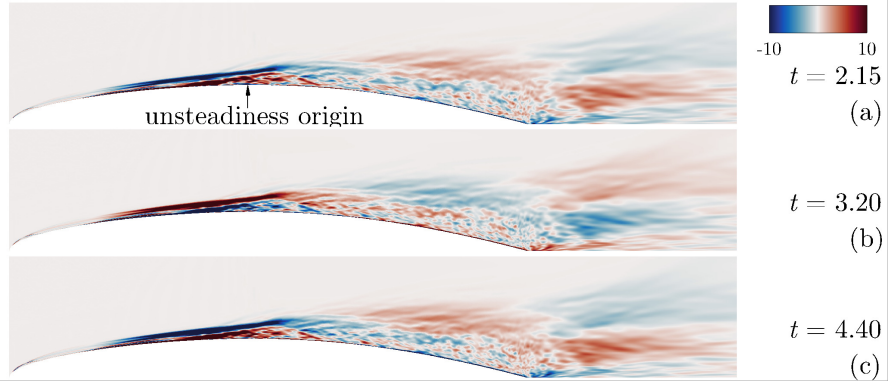

FIGURE 5.17: Filtered spanwise vorticity field at the trough section of WLE2 aerofoil during one cycle of the high frequency oscillation. The minimum (a), maximum (b) and the following minimum (c) of the oscillation are shown.

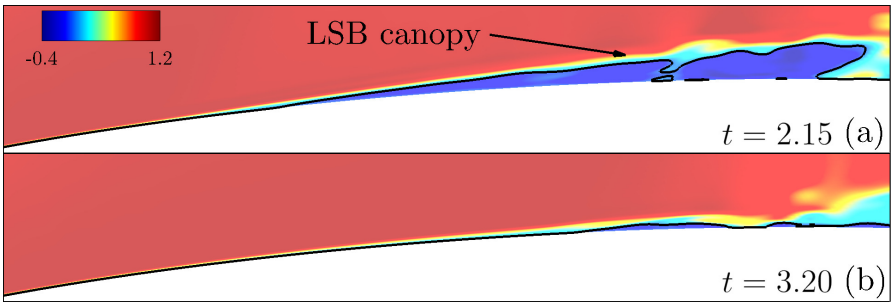

FIGURE 5.18: Streamwise velocity field at the trough section of WLE2 aerofoil showing the minimum (a) and maximum (b) of the LSB breathing oscillation, related to periodic thickening and thinning of the LSB respectively. Black line highlights LSB canopy.

5.2.4 Effect of WLE amplitude on LSB breathing unsteadiness

This section aims to investigate in further details the high frequency unsteadiness identified on WLE2 aerofoil in Section 5.2.3. It is analysed the effect of the wavy amplitude on the unsteadiness and the effect of the unsteadiness on the shock waves structures. Figure 5.19 and 5.20 show that the LSB breathing phenomenon is comparable on WLE1 and WLE2, as it was already highlighted by the overall unsteady performance results (Figure 5.9). The high frequency unsteadiness generates an unsteadiness in the forward shock wave of the λ structure. At the most upstream position of the forward shock wave, the BL is laminar between the forward shock and the SBLI region (Figure 5.19a and 5.20a). The LSB at the leading edge trough creates disturbances that develop downstream and, as a consequence, the BL downstream the forward shock wave becomes turbulent (Figure 5.19b and 5.20b). The forward shock wave is pushed further upstream up to the leading edge where it detaches from the aerofoil. The boundary layer in the downstream LSB region becomes laminar again and another λ-shape shock is generated in the SBLI region (Figure 5.19c and 5.20c). The forward shock of the λ structure moves upstream up to a position upstream the LSB (Figure 5.19d and 5.20d). Then the cycle starts again. The bubble breathing is causing an oscillation of the L-T transition point between $x = -0.17$ and $x = -0.02$ on WLE1 and between $x = -0.25$ and $x = -0.07$ on WLE2. The main difference between these two wavy aerofoils is that the L-T transition oscillation is localised only around the trough section on WLE2.

Figure 5.21 shows that the LSB breathing unsteadiness is not observed on WLE3 aerofoil. The disturbances generated from the LSB at the trough are stronger because of the increased wavy amplitude. A local unsteadiness is generated downstream the leading edge LSB which prevents the downstream BL from being laminar. As a consequence, the forward and backward shocks of the λ structure are close (Figure 5.12) because the upstream BL structure does not allow the forward shock to move further upstream. Interestingly, the effect of the leading edge LSB on the downstream boundary layer is localised in the region downstream the trough section, while the BL

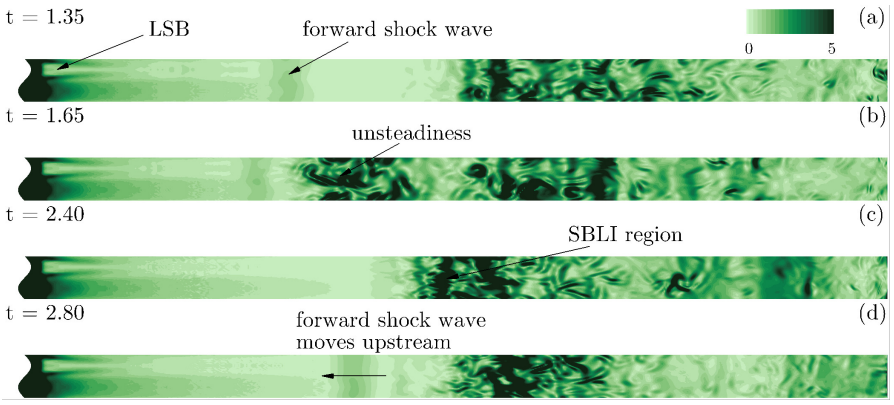

FIGURE 5.19: Pressure gradient magnitude distribution on the upper surface of WLE1 during the high frequency unsteadiness.

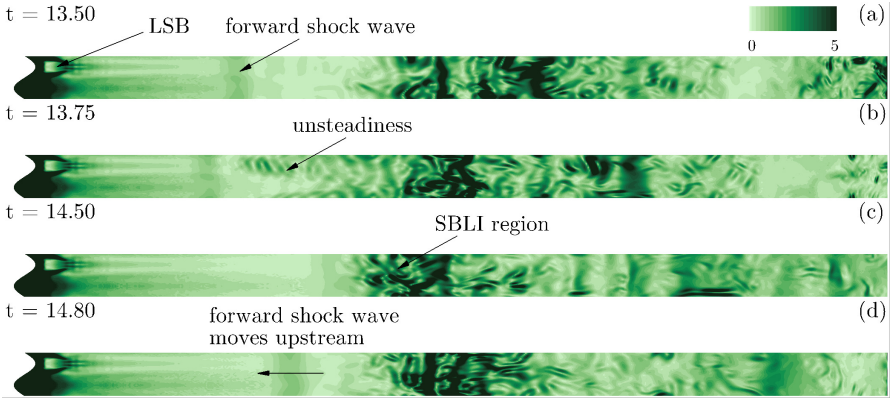

FIGURE 5.20: Pressure gradient magnitude distribution on the upper surface of WLE2 during the high frequency unsteadiness.

downstream the peak section is laminar up to the SBLI region. This results in a significant spanwise difference of the BL upstream the SBLI region which is not observed on WLE1 and WLE2 aerofoils. In this case, the L-T transition point is located around $x = -0.09$.

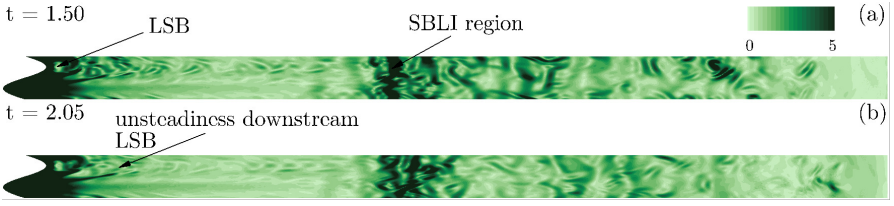

FIGURE 5.21: Pressure gradient magnitude distribution on the upper surface of WLE3 during the high frequency unsteadiness.

Figure 5.22 shows the time evolution of the spanwise averaged pressure gradient magnitude over the three modified aerofoils and it shows clearly that a strong shock buffet unsteadiness is related to a weak bubble breathing unsteadiness and vice versa. The bubble breathing unsteadiness is causing an oscillation of the L-T transition point of about 15% and 20% of the chord on WLE1 and WLE2 aerofoils (Figure 5.22a and

5.22b), respectively. On the contrary, WLE3 aerofoil displays a predominance of shock buffet unsteadiness (Figure 5.22c).

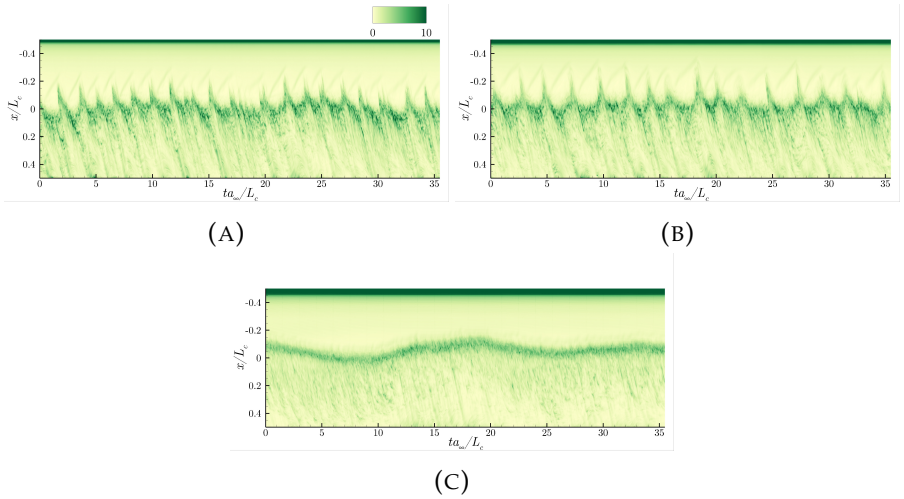

(A) (B)

(C)

FIGURE 5.22: Time evolution of spanwise averaged pressure gradient magnitude for WLE1 (a), WLE2 (b) and WLE3 (c).

5.3 Concluding remarks

Wavy leading edges over supercritical aerofoils in transonic flows show promising results. The study presented in this chapter has considered the effect of WLE amplitude on mean aerodynamic performance and on mitigation of shock buffet unsteady phenomenon.

In Section 5.1 the mean aerodynamic performance has been studied both in streamwise and spanwise directions together with the influence of wavy amplitude on aerofoil performance. The mean efficiency can be increased for a wide range of WLE amplitudes but the best performance is obtained with the lowest one ($h = 0.0075$). The results show that a small waviness is sufficient to create an important drag decrease. The main effect of WLE amplitude on lift coefficient is around the LE region which has a negative effect on lift compared to the SLE case. The effect becomes worse when WLE amplitude is enhanced. A second effect is the upstream movement of the L-T transition point which shrinks the region of lift enhancement when WLE amplitude is increased. The main effect of wavy amplitude on drag coefficient is in the LE region which has almost a negligible effect on drag at low amplitudes, while wavy amplitude growth tends to increase the drag with respect to the SLE case. The beneficial effect on drag is observed downstream of the modified aerofoil's L-T transition point.

Section 5.2 has analysed the unsteady results in detail, starting from the shock buffet phenomenon and the effect of a wavy leading edge on it. Then, high-frequency

phenomena have been identified and studied on both baseline and modified aerofoils. The main results are summarised as follows.

- Shock buffet phenomenon can be controlled by a wavy aerofoil and it changes its strength modifying the wavy amplitude. WLE aerofoils show a decrease in shock wave oscillation's amplitude. The strong interaction between shock wave and BL generates a large separation on SLE aerofoil, while this separation is not observed on the wavy counterpart. This difference during low-frequency oscillations is related to a more energetic BL on wavy aerofoils because of streamwise vorticity created upstream in the LE region.
- The high-frequency oscillation on baseline aerofoils is related to vortex shedding, while the one on modified aerofoils is related to LSB breathing. LSB breathing is responsible for a periodic thickening and thinning of the laminar BL upstream SBLI region. As a consequence, small vortices are generated and they convect downstream creating large vortical structures at the TE. It is observed a strong connection between shock buffet and LSB breathing phenomena on wavy aerofoils. When the shock buffet's strength is decreased, LSB breathing's strength is increased and vice versa.

A limitation of this study is that the effect of the WLE wavelength was not investigated. Previous studies on wavy aerofoils in subsonic flows have shown that a wavelength reduction is beneficial in both pre-stall and post-stall conditions. It is expected a similar effect on the pressure drag in the transonic regime. The reduction of the wavelength might have a positive effect also on the mitigation of shock buffet unsteadiness because of the increased distortion of the flow in the LE region. However, a similar effect observed on the wavy amplitude should be expected also on the wavelength: an initial reduction of the shock oscillation reducing the wavelength and then an increase once the leading edge is creating a high distortion in the laminar BL. The main difference with the wavy amplitude variation is the LSB observed in the LE region at the trough because the area where the bubble can develop becomes narrower reducing the wavelength and thus it is easier to observe a collapse of multiple bubbles further downstream. This is a larger three dimensional effect than the ones investigated in this chapter which can have a significant impact on the aerodynamic performance of wavy aerofoils, thus it should be investigated in details in future studies.

Chapter 6

Shock buffet aeroacoustics

This chapter investigates the aerofoil self-noise produced during the shock buffet phenomenon and its mitigation through wavy leading edges, extrapolating the far-field from the aerodynamic results presented in Chapter 5. A time domain solution to the Ffowcs Williams and Hawkings (FW-H) equation based on Farassat 1A formulation (Williams and Hawkings (1969)), simplified for the current problem, is implemented in order to calculate the current field. Since the focus is on the aerofoil dipole noise, the integration is performed on the aerofoil surface. This neglects direct quadrupole noise, although some signature of quadrupole noise scattered by the wall may be present. The spanwise periodic boundary condition implemented in the aerodynamic simulations is also applied in the far-field noise calculation. In order to perform this, the surface integral is performed iteratively on domains shifted nL_z either side of the aerofoil. This process is repeated until a converged solution is obtained, for the current setup a span of 25 chord lengths was found to be sufficient for converged far-field spectra results.

The previous chapter has shown that wavy aerofoils are able to mitigate the shock buffet oscillations and that a high-frequency unsteadiness, originated upstream the SBLI region, is generated. The main outcome of the unsteady aerodynamic analysis is that the low and high frequency phenomena seem to be tightly related, when the first one is stronger, the second one is weaker and vice versa. The objective of this chapter is to investigate the effect of this passive technique on the far-field noise. The first question is, what is the effect of WLEs on sound propagation in transonic flows? The acoustic field is evaluated solving the FW-H equation on the aerofoil's surface, taking into account the dipole contribution. WLE and SLE aerofoils are analysed at $\alpha = 7.0^o$ where the baseline aerofoil shows both shock buffet and vortex shedding phenomena. A time domain solution to FW-H equation has been recently used to analyse sound propagation of aerofoils at low Mach numbers with a wide range of flow conditions (Turner and Kim (2020b); Gelot and Kim (2020); Turner and Kim (2020a)). The second question is whether the effect of wavy amplitudes on sound propagation is

comparable to the one on near-field hydrodynamics or to the one at low Mach numbers. Three different configurations are considered in order to answer this question, one with a low WLE amplitude ($h = 0.0075$), one with a conventional amplitude ($h = 0.0125$), and one with a high amplitude ($h = 0.0250$), they are referred to as WLE1, WLE2, and WLE3, respectively.

6.1 Far-field extrapolation approach

The acoustic analogy formulation of FW-H is used for acoustic predictions

$$\Box^2 p' = \frac{\partial}{\partial t}[\rho_\infty u_i n_i \delta(f)] - \frac{\partial}{\partial x_i}[p n_i \delta(f)] + \frac{\partial^2}{\partial x_i \partial x_j}[H(f) T_{ij}] \tag{6.1}$$

where $\Box$ is the wave or D'Alembert operator in three dimensional space. The moving surface is described by $f(\mathbf{x}, t) = 0$ such that $\nabla f = \mathbf{n}$, $\mathbf{n}$ is the unit outward normal. This assumption implies that $f > 0$ outside the moving surface (Figure 6.1). Also $p' = c^2 \rho' = c^2(\rho - \rho_0)$, c and ρ_0 are the speed of sound and density in the undisturbed medium, respectively. The symbols $u_i n_i$, p and $T_{ij} = \rho u_i u_j - \sigma_{ij} + (p' - c^2 \rho')\delta_{ij}$ are the local normal velocity of the surface, the local gage pressure on the surface and the Lighthill stress tensor, respectively. In the definition of the Lighthill stress tensor, σ_{ij} is the viscous stress tensor and δ_{ij} is the Kronecker delta. The Heaviside and the Dirac delta functions are denoted $H(f)$ and $\delta(f)$, respectively. In the second term on the right of Equation 6.1, the viscous shear force over the surface acting on the fluid is neglected. Acoustic analogy allowed to convert a nonlinear problem of noise generation by a moving surface to a linear problem. All the nonlinearities are into the Lighthill stress tensor which is assumed known from the near field aerodynamic calculations.

Neglecting quadrupole noise, two wave equations need to be solved, thickness noise and loading noise equation, respectively.

$$\Box^2 p'_T = \frac{\partial}{\partial t}[\rho_0 u_i n_i \delta(f)] \tag{6.2}$$

$$\Box^2 p'_L = -\frac{\partial}{\partial x_i}[p n_i \delta(f)] \tag{6.3}$$

The source terms on the right hand side are also known as monopole and dipole sources, respectively.

The Green's function of the wave equation in the unbounded three dimensional space is

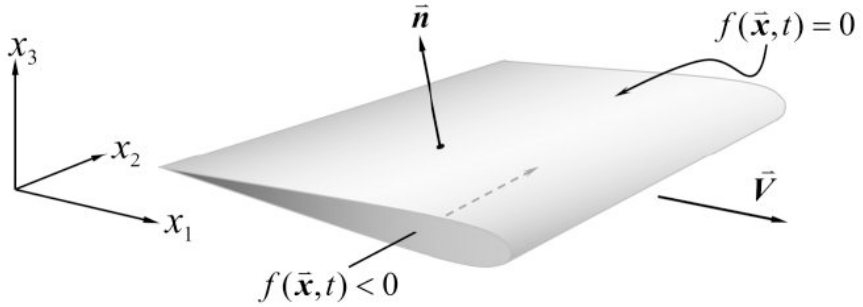

FIGURE 6.1: The definition of the moving surface implicitly as $f(\mathbf{x},t)=0$ (Williams and Hawkings (1969)).

$$G(\mathbf{x},t;\mathbf{y},\tau)=\begin{cases}0 & \tau>t\\ \delta(\tau-t+r/c)/4\pi r & \tau\leq t\end{cases} \tag{6.4}$$

where $r=|\mathbf{x}-\mathbf{y}|$. Here $(\mathbf{x},t)$ and $(\mathbf{y},\tau)$ are the observer and the source space-time variables, respectively. The symbol $\delta(\bullet)$ stands for the Dirac delta function.

The thickness and loading noise of components of Formulation 1A is

$$4\pi p'_T(\mathbf{x},t)=\int_{f=0}\left[\frac{\rho_0\dot{u}_i n_i}{r(1-M_r)^2}+\frac{\rho_0 u_i n_i \hat{r}_i \dot{M}_i}{r(1-M_r)^3}\right]_{ret}dS+ \int_{f=0}\left[\frac{\rho_0 c u_i n_i (M_r-M^2)}{r^2(1-M_r)^3}\right]_{ret}dS \tag{6.5}$$

$$4\pi p'_L(\mathbf{x},t)=\int_{f=0}\left[\frac{\dot{p}\cos\phi}{cr(1-M_r)^2}+\frac{\hat{r}_i\dot{M}_i p\cos\phi}{cr(1-M_r)^3}\right]_{ret}dS+ \int_{f=0}\left[\frac{p(\cos\phi-M_i n_i)}{r^2(1-M_r)^2}+\frac{(M_r-M^2)p\cos\phi}{r^2(1-M_r)^3}\right]_{ret}dS \tag{6.6}$$

where the near field terms (order $1/r^2$) and the far field term (order $1/r^3$) are separated.

The Farassat 1A formulation, simplified for the current problem, can be written as

$$4\pi p_a(\mathbf{x},t)=\int\left[\frac{\dot{p}\cos\phi}{a_\infty r(1-M_r)^2}+\frac{p(\cos\phi-M_i n_i)}{r^2(1-M_r)^2}+ \frac{(M_r-M^2)p\cos\phi}{r^2(1-M_r)^3}+\frac{\rho_\infty a_\infty u_i n_i(M_r-M^2)}{r^2(1-M_r)^3}\right]_{ret}dS \tag{6.7}$$

where $l = p\cos(\phi)$, subscript *ret* indicates variables are analysed at the retarded time $\tau = t - r/a_\infty$, dotted variables indicate the time derivative, and r is the effective acoustic distance calculated from the Garrick triangle (Garrick and Watkins (1953)) extended for two-dimensional mean flow velocity:

$$r = \frac{M_x d_x + M_y d_y + \sqrt{(M_x d_x + M_y d_y)^2 + (1 - M_x^2 - M_y^2)[d_x^2 + d_y^2 + d_z^2]}}{1 - M_x^2 - M_y^2} \tag{6.8}$$

where $(M_x, M_y) = (M_\infty cos(\alpha), M_\infty sin(\alpha))$ and $(d_x, d_y, d_z) = (x_o - x_s, y_o - y_s, z_o - z_s)$, with subscript o and s representing observer and source respectively. Additionally, $M_r = \mathbf{M} \bullet \hat{\mathbf{r}}$, where $r = (M_x r + d_x, M_y r + d_y, d_z)$ is the effective radiation vector, and $\hat{}$ represents a unit length. The local radiation angle ϕ, is determined by $\phi = \arccos(\mathbf{n} \bullet \hat{\mathbf{r}})$, where n is the surface normal. The above integration is therefore performed on the aerofoil surface. This neglects direct quadrupole noise, although some signature of quadrupole sound scattered by the wall may be present. The impenetrable surface integration greatly reduces the cost of the calculation, requiring only the pressure as an input variable. The spanwise periodic boundary condition implemented in the simulations is also applied in the far-field noise calculation. In order to achieve this, the surface integral is performed iteratively on domains shifted nL_z either side of the aerofoil. This process is repeated until a converged solution is obtained, which occurs due to r increasing and $\phi \to \pi/2$ as the z coordinate is increased. For the current setup a span of 25 chord lengths was found to be sufficient for converged far-field spectra results. Validation of the current FW-H implementation is included in Turner (2019).

6.2 Definition of variables for statistical analysis

Data processing and analysis are carried out upon the completion of each simulation. The main property required in this study is the power spectral density (PSD) function of pressure fluctuations on the aerofoil surface and at the far-field observer location. The far-field (acoustic) pressure is defined as

$$p_a(\mathbf{x}, t) = p(\mathbf{x}, t) - \overline{p}(\mathbf{x}) \tag{6.9}$$

where $\overline{p}(x)$ is the time averaged pressure. We also define the vertical wall pressure jump as

$$\Delta p_w(x, z, t) = p_w(x, y_u, z, t) - p_w(x, y_l, z, t) \tag{6.10}$$

where p_w is obtained via Equation 6.9 on the aerofoil surface and the subscripts u and l indicate the upper and lower sides of the aerofoil. The PSD functions of the pressure

fluctuations (based on frequency and one-sided) are then calculated by

$$S_{ppa}(\mathbf{x}, f) = \lim_{T\to\infty} \frac{P_a(\mathbf{x}, f, T)P_a^*(\mathbf{x}, f, T)}{T} \tag{6.11}$$

$$S_{ppw}(\mathbf{x}, f) = \lim_{T\to\infty} \frac{\Delta P_w(\mathbf{x}, f, T)\Delta P_w^*(\mathbf{x}, f, T)}{T} \tag{6.12}$$

where P_a and ΔP_w are an approximate Fourier transform of p_a and Δp_w, respectively, based on the following definitions

$$P_a(\mathbf{x}, f, T) = \int_{-T}^{T} p_a(\mathbf{x}, t)e^{2\pi i f t}dt \tag{6.13}$$

$$\Delta P_w(x, z, f, T) = \int_{-T}^{T} \Delta p_w(x, z, t)e^{2\pi i f t}dt \tag{6.14}$$

and "$*$" denotes a complex conjugate.

The overall acoustic performance of an aerofoil is evaluated considering the overall sound pressure level (OSPL) which is defined as

$$OSPL = \int_{f_{min}}^{f_{max}} SPL_{ppa}(\mathbf{x}, f)df \tag{6.15}$$

where SPL_{ppa} is the PSD of far-field pressure fluctuations in dB and $[f_{min}, f_{max}]$ is the frequency range where the acoustic performance is evaluated.

6.3 Radiated spectra and directivity trends

The objective of this section is to analyse the far-field pressure fluctuations in terms of spectral analysis and directivity trends in order to investigate the aeroacoustic performance of the aerofoils and find a relation between the wall pressure fluctuations and the far-field one. The objective is to identify the main characteristics of the radiated noise and then investigate it in more details in the next section, analysing the pressure fluctuations sources on the aerofoils' surfaces.

The overall acoustic performance of the three wavy aerofoils is firstly compared with the straight counterpart. The overall sound pressure level (OSPL) is computed at different observer angles θ integrating the spectra in the range $0.12 < St < 20$ and the difference between SLE and WLE aerofoils is computed. Figure 6.2 shows that WLE1 and WLE2 have similar overall performance, while WLE3 is able to control the radiated noise over the all directivity plot, showing the best acoustic performance. WLE1 and WLE2 display the main noise reduction in the region upstream and above the aerofoil ($90^o < \theta < 240^o$), while the radiated noise is comparable with the straight case in the region downstream the aerofoil. The objective of the following analysis is

to understand why WLE3 is much better at reducing noise emission and why WLE1 and WLE2 has the best aeroacoustic performance upstream and above the aerofoil with respect to the straight case.

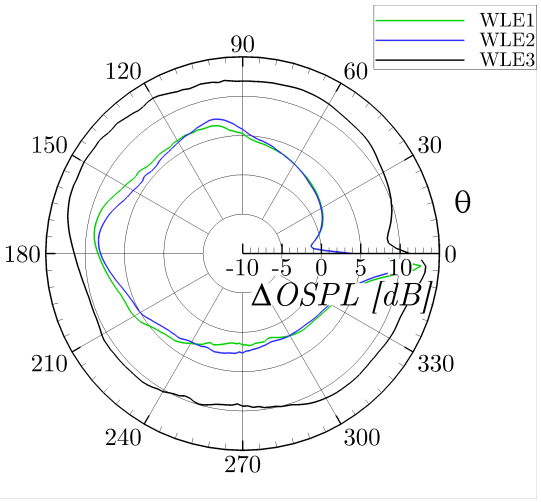

FIGURE 6.2: Directivity plot of the overall sound pressure level (OSPL) difference between straight aerofoil and the three wavy aerofoils.

The predicted radiated noise power spectral density obtained via the FW-H solver are shown in Figure 6.3 for different directivity locations over a narrow observer band of 10^o and a radius of $r = 10L_c$ from the aerofoil mid-chord. The observer angle θ is defined with respect to the downstream position and positive values are defined in anticlockwise direction. An observer angle $\theta = 0^o$ represents the location downstream the aerofoil while an observer angle $\theta = 90^o$ shows the location above the aerofoil and so on. The SLE shock buffet oscillations are radiated in the far-field in all the directions with higher values above and below the aerofoil, while the vortex shedding oscillations present a different trend. The pressure fluctuations related to the vortex shedding phenomenon are mainly radiated downstream where a maximum at $St = 1.2$ is observed (Figure 6.3a), while a bump is detected in the upstream region between $St = 0.5$ and $St = 1.3$. This might be related to the upstream movement of weak shock waves which periodically detach from the straight aerofoil during the shock buffet phenomenon. Interestingly, this unsteady phenomenon has a limited effect on the wall pressure fluctuations but it becomes predominant in this range of frequencies in the far-field. Above and below the aerofoil, a maximum is not observed in the far-field pressure fluctuations spectra, which is expected considering the nature of the unsteady phenomenon on the aerofoil. WLE1 and WLE2 aerofoils show similar trends in the higher frequency phenomena. The unsteady phenomena at $St = 0.85$ and $St = 0.64$ for WLE1 and WLE2, respectively, are predominant downstream, above and below the aerofoils. In the upstream region, the far-field pressure fluctuations are stronger on the straight aerofoil in this frequency range which allows to explain the overall improved aeroacoustic performance of WLE1 and WLE2 in this region. WLE3 shows the best trend overall in decreasing the far-field pressure fluctuations over a

broad frequency range. The higher frequency oscillation observed around $St = 1.0$ is always lower than the other wavy aerofoils and the straight counterpart. Interestingly, in the upstream direction a bump is observed in the frequency range $St = 0.3 - 0.4$ which does not appear in the other directions.

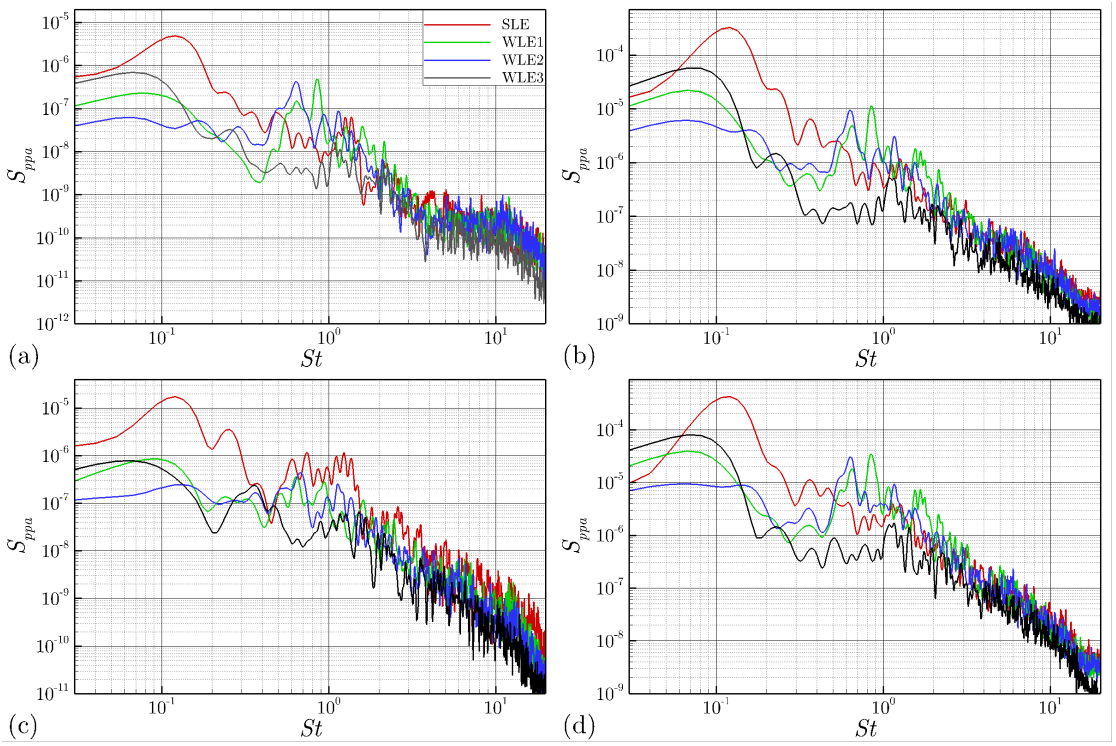

FIGURE 6.3: Power spectral density of far field sound pressure fluctuations over a narrow circular arc with a radius of $r = 10$ centered in the mid-chord of the baseline aerofoil. The data are averaged over 10^o band at $\theta = 0^o$ (a), $\theta = 90^o$ (b), $\theta = 180^o$ (c) and $\theta = 270^o$ (d).

The sound pressure level (SPL) difference between wavy aerofoils and the straight counterpart is investigated in Figure 6.4. In order to have a clear understanding of the high frequency range, a one-sixth-octave band PSD is computed. This allows to better show the range of frequencies where wavy aerofoils decrease the far-field pressure fluctuations. WLE1 and WLE2 decrease the SPL downstream, above and below the aerofoil for $St < 0.5$, while the noise emission is generally increased in the range $0.5 < St < 2.0$. In particular, WLE1 displays higher sound emission around $St = 0.9$ and $St = 1.8$ in the region downstream while WLE2 around $St = 0.64$ and $St = 1.8$. A different trend is observed in the upstream location, the frequency range of decreased SPL is broadened, consistently with the results displayed by the OSPL (Figure 6.2). In the high frequency range ($St > 7.0$), WLE1 and WLE2 decrease the SPL only upstream the aerofoil, while in the other directions the SPL is comparable to the straight counterpart. WLE3 presents a different trend, consistently with the OSPL displayed in Figure 6.2. The SPL is increased around $St = 1.8$ downstream the aerofoil, like for the other wavy aerofoils, but overall the noise emission is reduced in the investigated frequency range.

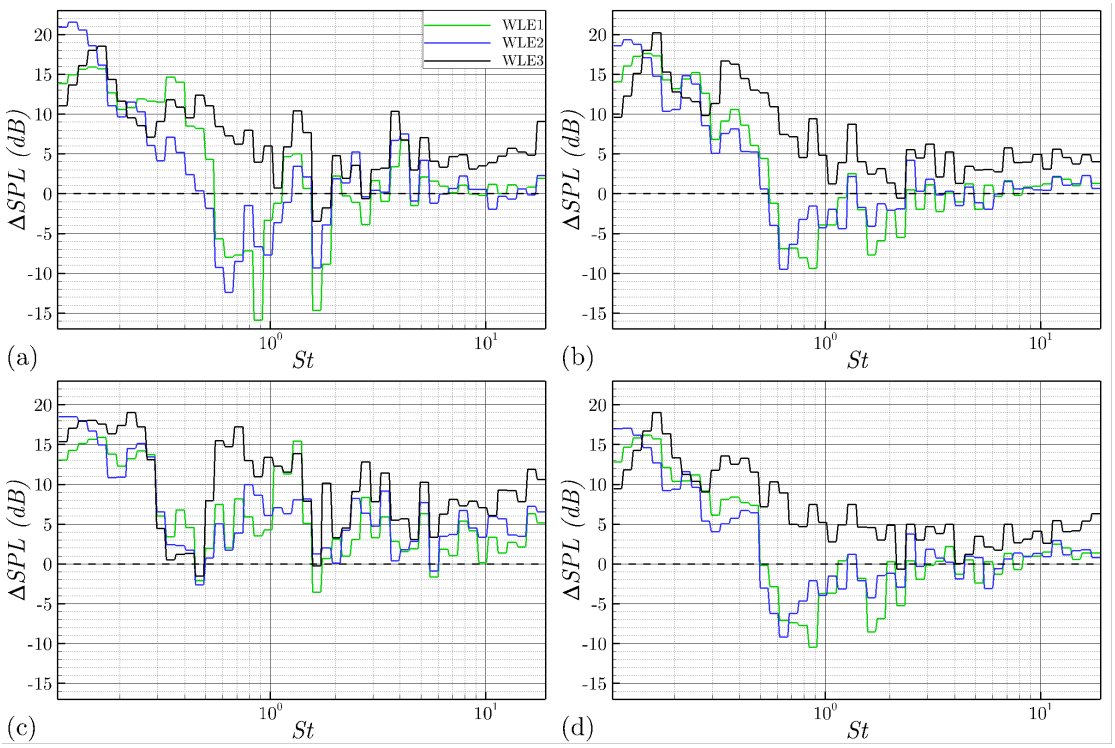

FIGURE 6.4: Sound pressure level (SPL) difference between wavy aerofoils and straight counterpart. One-sixth-octave band power spectral density of far field sound pressure fluctuations over a narrow circular arc with a radius of $r = 10$ centered in the mid-chord of the baseline aerofoil. The data are averaged over 10^o band at $\theta = 0^o$ (a), $\theta = 90^o$ (b), $\theta = 180^o$ (c) and $\theta = 270^o$ (d).

The effect of observer angle on the radiated noise is investigated though the sound directivity in Figure 6.5 at the Strouhal number of the main unsteady phenomena observed on the different aerofoils. At $St = 0.12$ each aerofoil produces the expected dipolar radiation pattern although the straight aerofoil shows a significantly higher noise emission. The directivity patterns are closer at $St = 0.64$ where the bubble breathing phenomenon is observed on WLE2 aerofoil. In this case, WLE1 and WLE2 have similar trends and the asymmetry of the directivity pattern increases causing higher noise emission in the downstream direction. The bubble breathing phenomenon on WLE1 aerofoil is observed at $St = 0.85$ and also in this case the directivity pattern for WLE1 shows an asymmetric shape with higher noise emission in the downstream direction. On the other hand, the straight aerofoil displays higher noise emission in the lower half upstream direction. At $St = 1.2$ the SLE aerofoil's directivity plot does not show a dipolar radiation pattern. A third lobe is observed in the upstream direction where the sound emissions are significantly higher than on the wavy aerofoils. This might be related to the detachment of weak shock waves from the straight aerofoil's leading edge. For the three wavy aerofoils, the expected dipole shape is observed with an asymmetry and a higher noise emission in the downstream direction.

The radiated spectra and the directivity trends have shown that WLE1 and WLE2

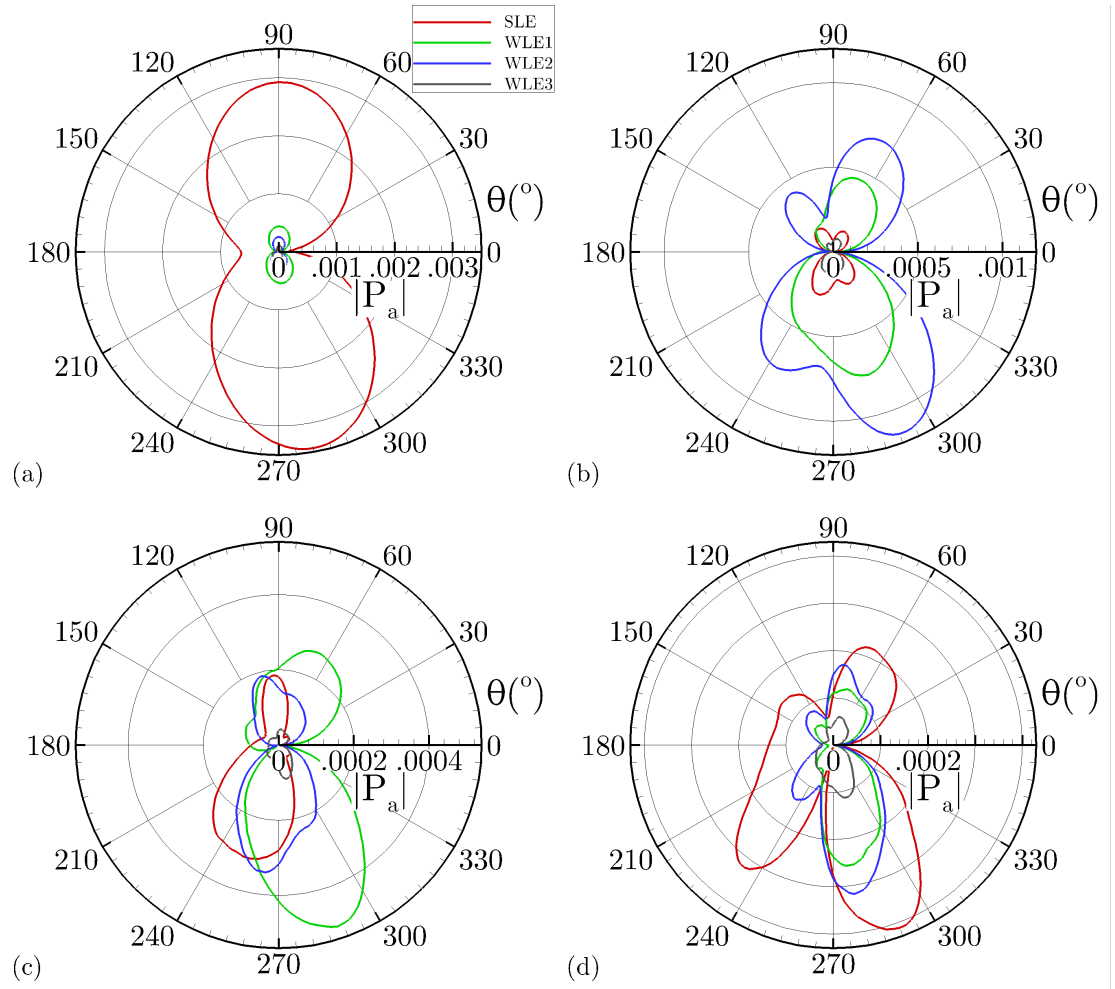

FIGURE 6.5: Sound directivity based on the magnitude of acoustic pressure Fourier transform ($|P_a|$) at observers $(x_o, y_o, z_o) = (10L_c \cos\theta, 10L_c \sin\theta, 0)$. The results are shown for $St = 0.12$ (a), $St = 0.64$ (b), $St = 0.85$ (c) and $St = 1.2$ (d) comparing the three wavy aerofoils and the straight counterpart.

aerofoils present consistent result decreasing the far-field pressure fluctuations in the region upstream and above the aerofoil with respect to the straight case. The noise reduction above the aerofoil is related to the decreased far-field pressure fluctuations when $St < 0.5$ which is related to the mitigation of the shock buffet oscillation in the near field, while in the range between $St = 0.5$ and $St = 2.0$ the two wavy aerofoils generate stronger far-field pressure fluctuations because of the bubble breathing phenomenon observed in the near field. In the region upstream the aerofoil, the far-field pressure fluctuations on the wavy aerofoils are weaker in the range between $St = 0.5$ and $St = 2.0$ because of the nature of the high frequency unsteadiness (LSB thickening and shrinking causes the generation of vortices in the SBLI region). On the contrary, the straight aerofoil shows quite strong far-field pressure fluctuations in this frequency range because of the shock waves travelling upstream and detaching from the leading edge. The WLE3 aerofoil displays a reduction of far-field pressure fluctuations over the investigated frequency range and it is the only wavy aerofoil that

shows pressure fluctuations reduction in the high frequency range. The main reason for the WLE3 aeroacustic performance is the mitigation of the shock buffet and a very weak high frequency unsteadiness in the near field.

This section has shown the aeroacoustic performance of the three wavy aerofoil with respect to the straight counterpart, investigating the benefits of this passive technique both in terms of frequency range and directivity trends. The next section will analyse in details the pressure fluctuations sources in terms of both magnitude and phase distribution on the aerofoil's surface.

6.4 Pressure fluctuations source identification

In this section the pressure fluctuations sources on the aerofoil surface are investigated in details. The source is visualised by considering the part of the leading term in the FW-H equation which varies over the surface. The contours of L_w are plots over the aerofoil surface for an observer located at $\theta = 90^o$ and $R = 10L_c$. The dipole sources are identified by two main contributions.

- The Fourier transform magnitude $|L_w|$, which identifies the noise source strength on the surface, thus the fluctuations amplitude.
- The cosine of Fourier transform phase angle $\cos\phi$, which defines the phase variation over the surface.

Regions of high strength magnitude do not guarantee that the noise radiates from a location, just that pressure fluctuations are large. This is because phase interference may result in a negligible contribution in the FW-H integration. For this reason, both contributions, magnitude and phase, have to be taken into account in order to understand the source mechanism.

Figure 6.6 and 6.7 show the magnitude and phase contributions at $St = 0.12$, respectively, for the straight aerofoil and the three wavy ones. At this frequency large shock wave oscillations are observed on the straight aerofoil and as a consequence the flow displays also oscillations of the laminar-turbulent transition region. The wall pressure fluctuations magnitude presents the higher values in the region between the most upstream and the most downstream position of the laminar-turbulent transition point. The wavy aerofoils present significantly lower magnitude than the straight counterpart at this frequency but the highest magnitude is also located in the laminar-turbulent transition region. Regarding the phase, the straight case shows an in-phase source relationship on the entire aerofoil surface. There is more variation with the wavy aerofoils and in particular the variation increases when the wavy amplitude is increased. WLE1 and WLE2 display an in-phase relation in the high

magnitude source regions while phase variation is observed on WLE3 at the laminar-turbulent transition region which might be an explanation of the significant noise reduction at this frequency on WLE3 aerofoil.

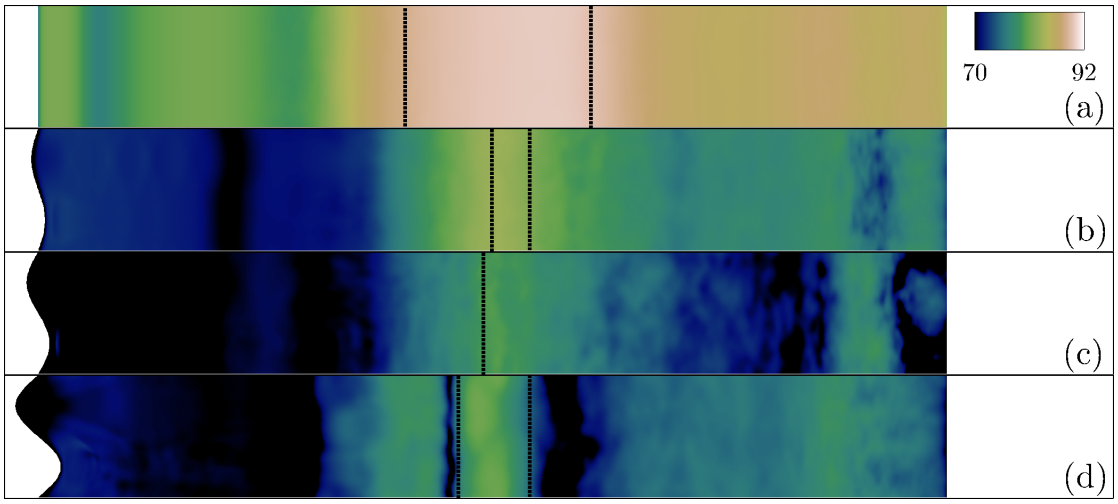

FIGURE 6.6: The magnitude in log scale of the Fourier transform of the wall pressure jump at the tonal frequency $fL_c/a_\infty = 0.12$. Dotted black line displays the spanwise averaged laminar-turbulent transition points.

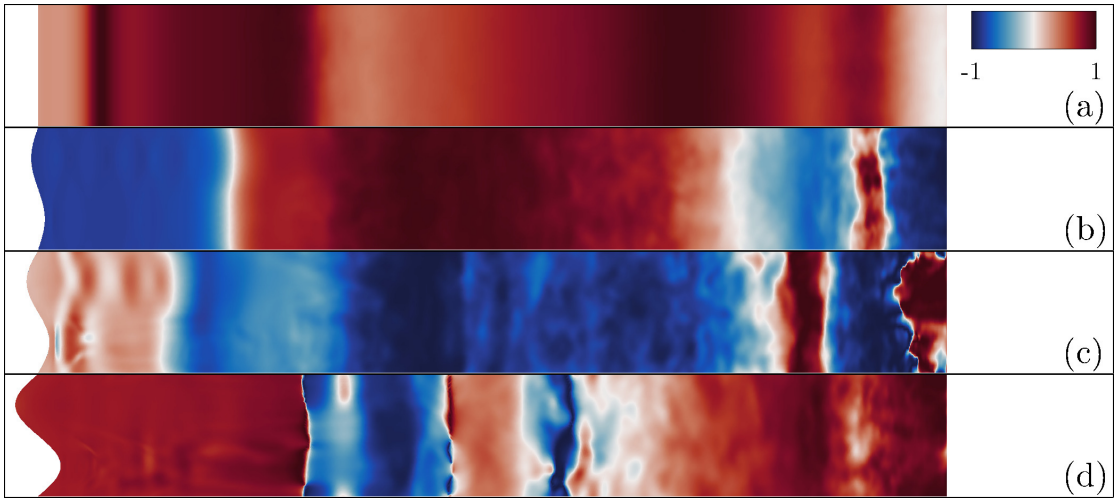

FIGURE 6.7: The phase distribution of the Fourier transform of the wall pressure jump at the tonal frequency $fL_c/a_\infty = 0.12$.

The pressure fluctuations at the frequency of bubble breathing phenomenon on WLE2 ($St = 0.64$) are investigated in Figure 6.8 and 6.9. WLE2 shows regions of high magnitude at the SBLI region and in the downstream region of turbulent boundary layer. This can be explained considering that the bubble breathing phenomenon causes the generation of vortices from the shock boundary layer interaction region and that these vortices are then convected downstream. The dipole solution of FW-H equation does not take into account direct quadrupole sources but in case of vortices convected in a turbulent BL, the pressure fluctuations emitted from the BL are also scattered by the wall so they can be captured by the dipole solution. These two

components define the dominant pressure signature of wall pressure fluctuations at $St = 0.64$, even if they are out-of-phase between each other. WLE1 shows a consistent trend with two main regions of high magnitude and opposite phase. The main difference is the strength of the wall pressure fluctuations which might be an explanation for the lower sound emission. WLE3 shows a similar distribution of wall pressure fluctuations magnitude even if the magnitude is significantly decreased in comparison to both WLE1 and WLE2. The reason why a low amplitude of noise sources is observed on this aerofoil is that WLE3 shows a very weak bubble breathing phenomenon in the near field which is observed on wavy aerofoils between $St = 0.6$ and $St = 1.0$. Another difference between WLE3 and the other modified aerofoils is that the phase distribution displays high variation in the SBLI region which is related to destructive interference. The straight aerofoil displays a different trend, a region of high source is observed in the region upstream the most upstream position of the laminar-turbulent transition point. Regarding the phase, a higher phase variation is observed in the streamwise direction. For this reasons the SLE aerofoil presents lower wall pressure fluctuations at $St = 0.64$.

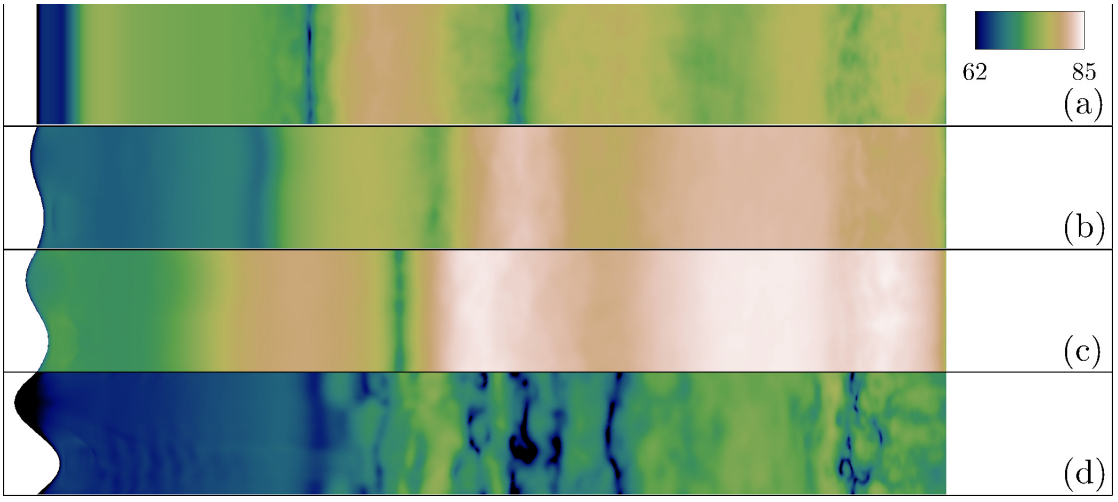

FIGURE 6.8: The magnitude in log scale of the Fourier transform of the wall pressure jump at the tonal frequency $fL_c/a_\infty = 0.64$.

Figure 6.10 and 6.11 display the wall pressure fluctuations magnitude and phase at the frequency of the bubble breathing phenomenon on WLE1 ($St = 0.85$). The results are consistent showing two regions of high magnitude in the SBLI region and in the turbulent BL region which are out-of-phase between each other. Furthermore, Figure 6.11 shows clearly the effect of the wavy amplitude on spanwise destructive interference. Increasing the wavy amplitude, the out-of-phase distribution in the spanwise direction is increased in the regions of high magnitude.

Finally, the pressure fluctuations are investigated at the frequency of the vortex shedding phenomenon on the baseline aerofoil. The pressure fluctuations magnitude is located at the trailing edge on SLE aerofoil (Figure 6.12) and this region of the

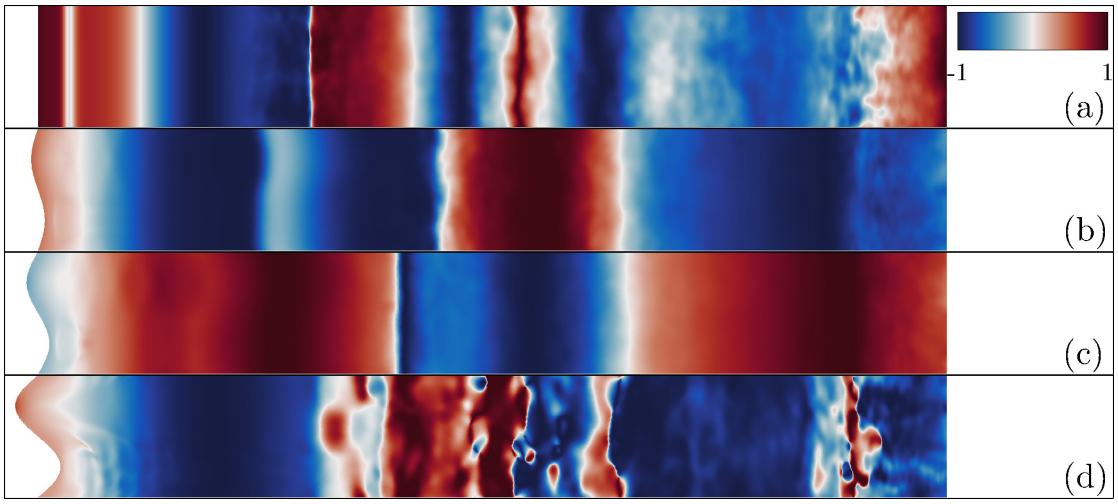

FIGURE 6.9: The phase distribution of the Fourier transform of the wall pressure jump at the tonal frequency $fL_c/a_\infty = 0.64$.

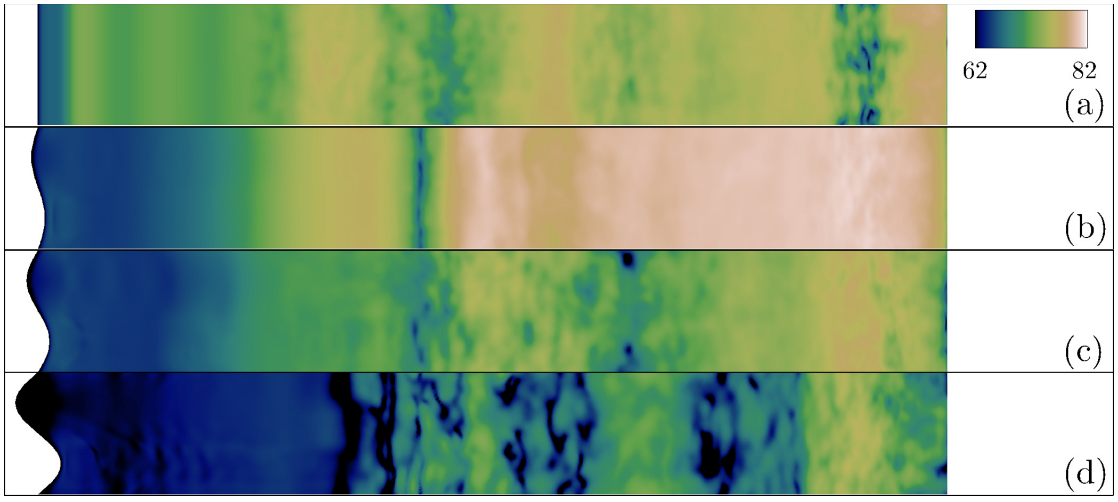

FIGURE 6.10: The magnitude in log scale of the Fourier transform of the wall pressure jump at the tonal frequency $fL_c/a_\infty = 0.85$.

surface shows in-phase source relationship (Figure 6.13). The pressure fluctuations phase distribution on wavy aerofoils is interesting because WLE1 generates spanwise destructive interference mainly downstream the SBLI region, while WLE3 generates spanwise destructive interference in the LE region at the trough and in the mid-chord region. On the contrary, WLE2 displays very limited spanwise destructive interference. Regarding the pressure fluctuations magnitude, WLE2 presents high magnitude regions at the SBLI and close to the TE, while WLE1 and WLE3 displays the high magnitude region close to the TE.

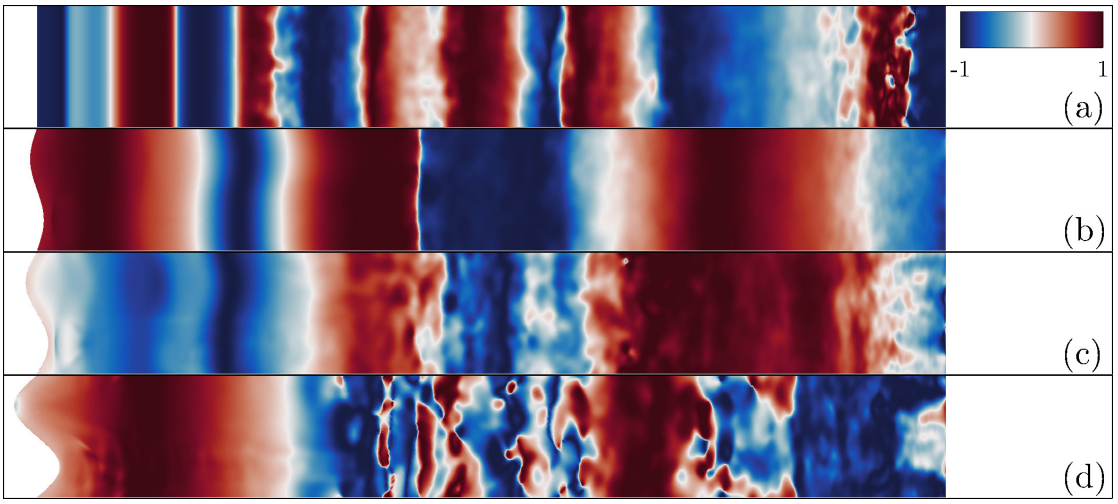

FIGURE 6.11: The phase distribution of the Fourier transform of the wall pressure jump at the tonal frequency $fL_c/a_\infty = 0.85$.

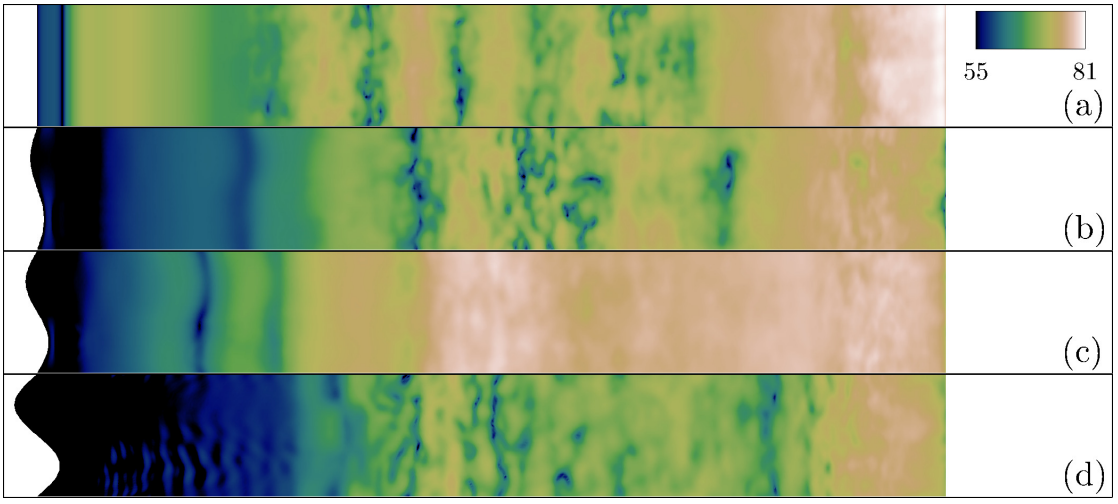

FIGURE 6.12: The magnitude in log scale of the Fourier transform of the wall pressure jump at the tonal frequency $fL_c/a_\infty = 1.20$.

6.5 Concluding remarks

Wavy leading edges over supercritical aerofoils in transonic flows show promising results. This study has extended the previous analysis shown in Chapter 5 on mean and unsteady aerodynamic performance considering the aeroacoustic performance and the effect of wavy amplitude on it. The SLE aerofoil is characterised by low frequency large shock wave oscillations and a higher frequency vortex shedding at the trailing edge. The three wavy aerofoils present a low frequency shock oscillation which can be mitigated by the wavy amplitude and a higher frequency bubble frequency phenomenon.

Section 6.3 presents the aeroacoustic performance in terms of radiated spectra and directivity trends. The main outcomes of this analysis are summarised as follows:

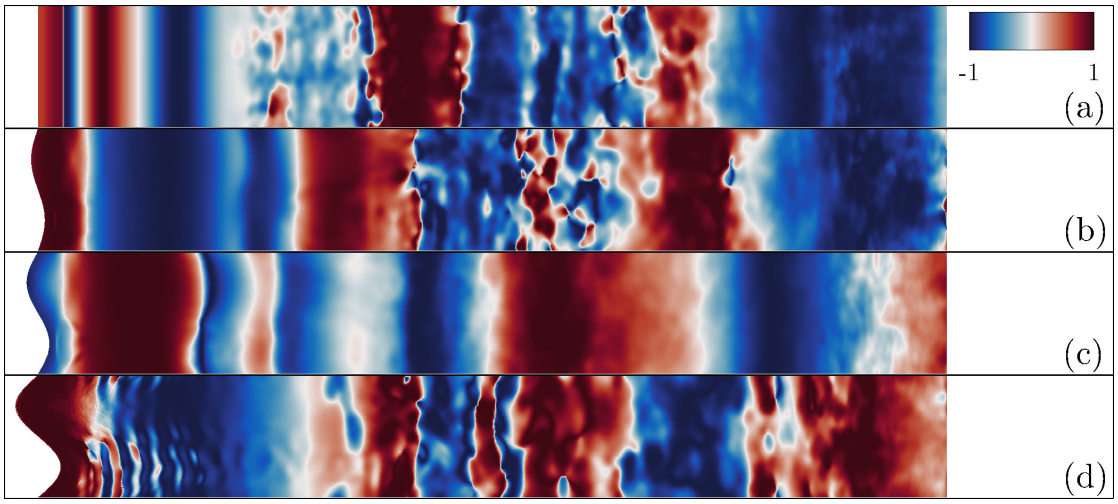

FIGURE 6.13: The phase distribution of the Fourier transform of the wall pressure jump at the tonal frequency $fL_c/a_\infty = 1.20$.

- WLE1 and WLE2 show consistent results decreasing the far-field pressure fluctuations in the region upstream and above the aerofoil and having comparable performance with SLE in the region downstream. In particular, the pressure fluctuations are decreased in the low frequency range ($St < 0.5$) downstream the aerofoil and they are increased at higher frequencies ($0.5 < St < 1.2$).

- WLE3 displays a reduction of far-field pressure fluctuations over the all frequency range considered in this study and at all the observer directions. This is the only investigated aerofoil that presents pressure fluctuations reduction in the high frequency range.

- SLE aerofoil shows significant pressure fluctuations in the low frequency range which are related to the shock buffet phenomenon in the near field. The radiated spectra display a bump at $0.5 < St < 1.3$ which is not observed in the wall pressure unsteady analysis. The effect on the directivity trends is a deviation from the expected dipole shape which is observed at other frequencies.

In the last part of this chapter (Section 6.4), the sources of the wall pressure fluctuations are analysed because they characterise the dipole noise which is the only component taken into account in this study. The main findings of the noise source investigation are summarised as follows.

- The pressure fluctuations on the SLE aerofoil's surface at the shock buffet frequency present high source magnitude in the region between the most upstream and the most downstream position of the L-T transition point. The phase distribution presents an in-phase source relationship in the streamwise and spanwise directions.

- At the frequency of the laminar bubble breathing on WLE1 and WLE2 aerofoils the magnitude is higher at the SBLI region and in the region downstream where the turbulent BL develops. The sources are out-of-phase in the SBLI and the turbulent BL regions.
- At the vortex shedding frequency the source magnitude is high and in-phase close to the TE on the straight aerofoil, as expected by the nature of the aerodynamic phenomenon in the near field.

The investigation of the pressure fluctuations sources allows also to observe the effect of the wavy magnitude. WLE3 aerofoil significantly reduces the pressure fluctuations because of the increased spanwise variation of the phase distribution which brings to an enhanced destructive interference (Figure 6.7, 6.9, 6.11 and 6.13). This is driven by the LE wavy shape. It should be possible to observe a wavy amplitude threshold where a higher wavy amplitude allows to obtain a significant aeroacoustic performance improvement compared with the straight case. Since the aeroacoustic performance improvement is related to the destructive interference, a similar trend in noise reduction should be observed decreasing the WLE wavelength. The wavy amplitude parameter was investigated in this chapter because Hansen et al. (2010) have shown that the amplitude is more effective than the wavelength in self noise mitigation.

The aerodynamic and aeroacoustic performance analysis carried out in this chapter and in the previous one shows that WLE1 presents the best mean aerodynamic performance, while WLE2 presents the best unsteady aerodynamic performance. Finally, WLE3 displays the best aeroacoustic performance. This proves that WLE aerofoils can be beneficial in transonic flows but a trade-off is needed for the overall performance in shock buffet conditions.

Chapter 7

Swept wing effects

This chapter applies WLEs to a swept wing section and analyses the mitigation of shock buffet phenomenon over a supercritical aerofoil in transonic flow. Two different wavy configurations are investigated (Figure 7.1). In the first configuration (WLEc1), the WLE direction has a sweep angle with respect to the upstream flow field, while in the second configuration (WLEc2), the WLE direction is parallel to the upstream flow field. The definition of the waviness direction on wavy swept wing is not straightforward because of the additional spanwise component. In the first configuration, the WLE is in the same direction of the largest component of the upstream flow, while in the second configuration, the WLE is in the same direction of the overall upstream flow. The comparison of these two different wavy configurations on swept wavy wings can not be found in literature at any speed range even if it is not straightforward to define which configuration shows the best aerodynamic performance. This is the reason why both wavy configurations are analysed in this chapter.

WLEc1 simulation is set up using an unswept mesh and imposing a sweep angle to the upstream flow, while WLEc2 requires a swept mesh with an unswept upstream flow. In order to compare the aerodynamic mean and unsteady performance with the unswept case presented in Chapter 5, the upstream Mach number is set to $M_\infty = M_{\infty 2D} / \cos\Lambda$, where $M_{\infty 2D} = 0.7$ is the component of the upstream Mach number parallel to the chord and $\Lambda = 25^o$ is the sweep angle. The upstream Mach number is chosen to be consistent with the unswept cases investigated in previous chapters to allow a fair comparison of the aerodynamic characteristics. Table 7.1 specifies geometry, aerofoil surface mesh and upstream flow setup for both WLE configurations. The mean chord is $L_c = 1$ for both aerofoils, this means that WLEc2 has a spanwise domain size $L_z = L_{zWLEc1} * \cos^2\Lambda$ and an upstream Reynolds number $Re_\infty = Re_{\infty WLEc1} / \cos\Lambda$. Both aerofoils have a WLE wavelength equal to the spanwise domain size, thus only one wavelength is simulated. The application of periodic boundary conditions is a physical approximation because of the increase thickness of

the boundary layer in the spanwise direction. The simulation of the full wing would be needed to avoid this physical approximation which would imply the increase of computational resources by at least one order of magnitude to keep the simulation time to solution unchanged. Previous studies (Franciolini et al. (2018)) have shown the applicability of periodic boundary conditions to model infinite swept wings, which is valid at a reasonable distance from the fuselage and wing tip. The results of this chapter should give a preliminary idea about the aerodynamic performance of wavy swept wing configurations before performing a full wing comparison in future studies.

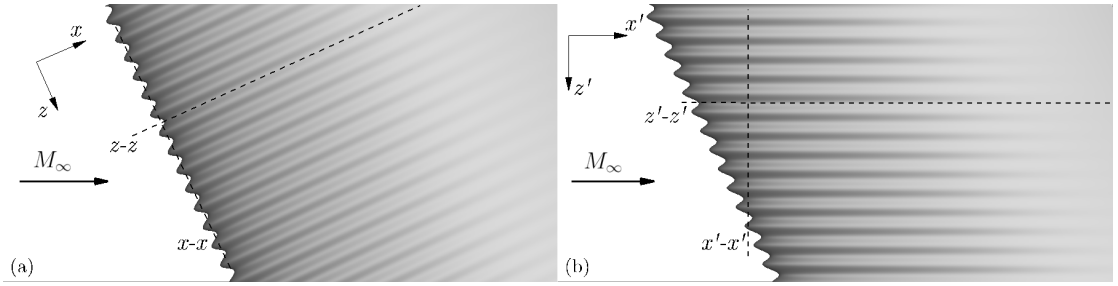

FIGURE 7.1: WLE swept wing with LE waviness in direction of the wing's chord (a) and in direction of the upstream flow (b).

	Re_∞	L_z	λ_{LE}	h_{LE}	$n_{\xi AERO}$	$n_{\zeta AERO}$
WLEc1	500000	0.050	0.050	0.0125	800	50
WLEc2	551690	0.041	0.041	0.0125	900	50

TABLE 7.1: Simulation setup for swept WLE configurations.

Previous chapters have analysed mean and unsteady aerodynamic performance and aeroacoustic performance of WLE aerofoils, showing the mitigation of shock buffet and the control of far-field pressure fluctuations. The objective of this chapter is to apply two wavy configurations to a swept wing section and analyse the aerodynamic characteristics. The first question is, what is the best wavy configuration for shock buffet mitigation? Two WLE configurations, shown in Figure 7.1, are simulated and compared with the straight case. The second query is about the mean and unsteady aerodynamic characteristics. The aim is to investigate if there is a consistency in the mean aerodynamic performance and the unsteady phenomena observed in Chapter 5. The third question is about the leading edge flow structures, how does the introduction of a sweep angle modify the leading edge flow structures with respect to the unswept case?

The results of this chapter represent a preliminary investigation on the effect of WLEs on swept wings. The main limitation of this analysis is the spanwise domain size which covers only one WLE wavelength. This means that it is not possible to simulate buffet cell structures, which are spatially periodic in the spanwise direction. A physical approximation in the simulation setup is introduced by the application of period boundary conditions in the spanwise direction.

7.1 Time-averaged characteristics

The first part of this chapter analyses the mean aerodynamic characteristics of the wavy swept wing sections, comparing them with the straight counterpart. The objective is to define the effect of WLE configurations on mean aerodynamic performance and determine the most efficient configuration before extending the analysis to the unsteady characteristics.

Table 7.2 shows the mean aerodynamic performance of straight and wavy swept wing sections. The mean lift generated by the modified wing is increased and it is comparable between the two wavy configurations. The first difference with previous investigations is observed on the mean drag coefficient. WLEc1 decreases the mean drag coefficient because of the pressure drag reduction, while the skin friction drag is increased, coherently with the two dimensional modified aerofoil. On the other hand, WLEc2 slightly increases the drag coefficient. In this latter case, both the pressure drag and the skin friction drag are increased. Overall, the two wavy configurations show an increased aerodynamic efficiency but WLEc1 presents the highest mean aerodynamic efficiency.

	C_L	C_D	C_{Dp}	C_{Df}	C_L/C_D
SLE	0.664	0.065	0.0626	0.0023	10.22
WLEc1	0.767	0.056	0.0502	0.0056	13.74
WLEc2	0.753	0.070	0.0642	0.0052	10.84

TABLE 7.2: Mean aerodynamic performance of straight and wavy swept wing sections at $\alpha = 7.0^o$.

Figure 7.2 shows the mean pressure coefficient distribution on the upper surface of SLE, WLEc1 and WLEc2 swept wing sections. The wavy wing sections display a plateau of low pressure distribution starting from the leading edge region. The plateau on WLEc1 develops more downstream, this means that the mean position of the shock wave is more downstream. Previous studies on wavy aerofoils have proved that the beneficial decrease of the pressure drag is obtained downstream the laminar-turbulent (L-T) transition. WLEc1 generates higher flow distortion in the leading edge region because of the sweep angle between the upstream flow and the WLE direction. The results is that a steep increase of the pressure coefficient is observed downstream the L-T transition point and this region of high pressure coefficient is beneficial to decrease the pressure drag coefficient. The leading edge pressure coefficient distribution on the two wavy configurations is shown in Figure 7.3. WLEc2 presents a larger region of low pressure coefficient downstream the through section. The area of high pressure coefficient is more extended in the peak region on WLEc2 and, as a consequence, the low pressure coefficient plateau is settled more downstream. The high drag coefficient on WLEc2 can be explained by two physical phenomena, the

high pressure coefficient region at the leading edge and the pressure coefficient distribution downstream the pressure plateau in the laminar BL region.

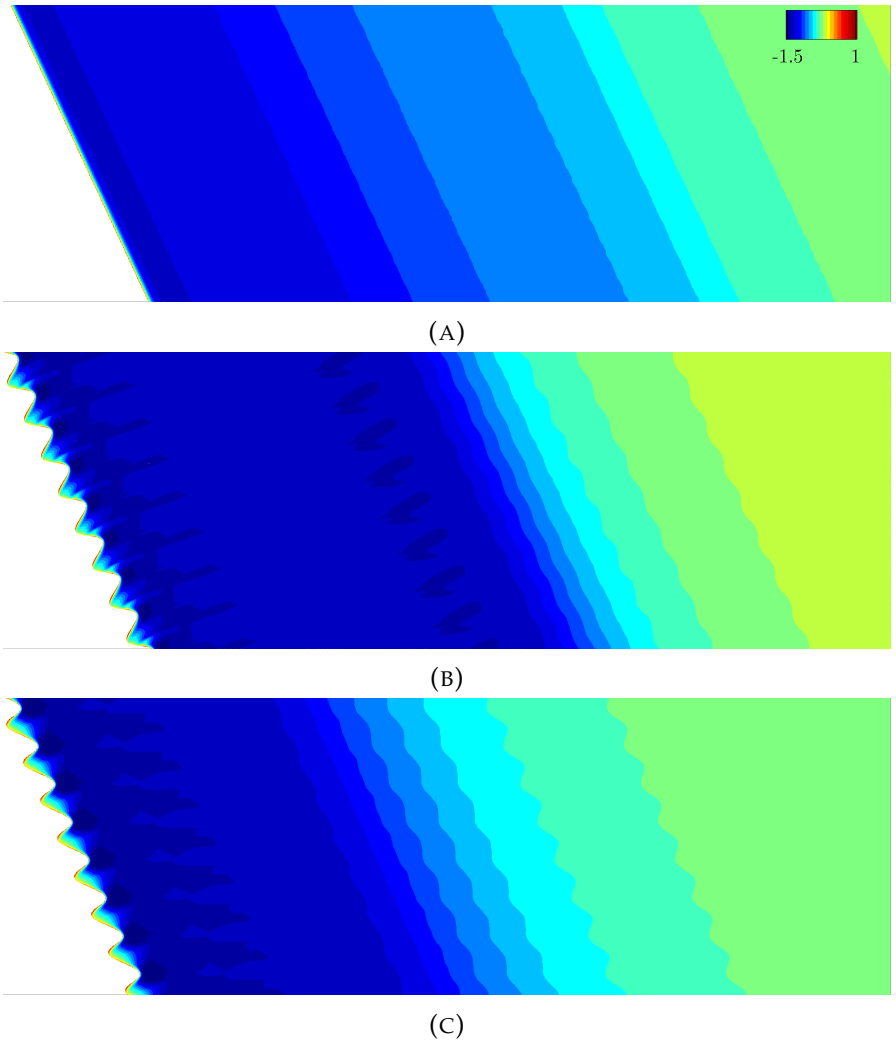

FIGURE 7.2: Mean pressure coefficient distribution on the upper surface of SLE (a), WLEc1 (b) and WLEc2 (c) swept wing sections at $\alpha = 7.0^{o}$. Domain is replicated 8 times in the spanwise direction.

The mean skin friction coefficient distribution on the upper surface is analysed in Figure 7.4. The straight case presents mean laminar separation at about 25% of the chord and the mean L-T transition at about 45% of the chord, while WLEc1 shows a mean laminar separation location more downstream at about 45% of the chord and the mean L-T transition at about 70% of the chord. The skin friction coefficient distribution in the three dimensional laminar boundary layer is characterised by stripes of lower skin friction which develop streamwise in the opposite direction of the upstream flow. WLEc2 presents a different mean flow behaviour, a stripe of lower skin friction coefficient is observed between the peak and through sections. In addition, a localised mean laminar separation bubble is observed between the peak and through sections from 25% to 40% of the chord. Downstream this laminar separation bubble the transition to turbulence is observed at about 50% of the chord.

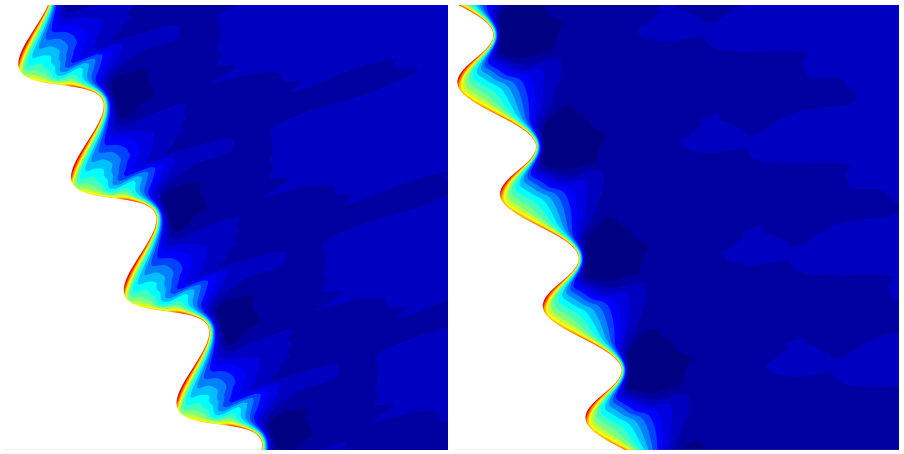

(A) (B)

FIGURE 7.3: Mean pressure coefficient distribution on the LE upper surface of WLEc1 (a) and WLEc2 (b) swept wing sections at $\alpha = 7.0^{o}$. Domain is replicated 4 times in the spanwise direction.

Both wavy configurations present a laminar separation bubble in the through region (Figure 7.5), as it was already observed on previous studies of wavy aerofoils. The sweep angle on WLEc1 introduces an additional separation region at the peak. The different skin friction coefficient distributions on the two wavy configurations suggest different vortex structures on the two swept wing sections, which might explain the difference in the mean and unsteady aerodynamic performance.

Figure 7.6 shows instantaneous streamlines close to the upper surface of the three swept wing sections. The straight case shows that the flow in the laminar boundary layer is moving in the chordwise direction. The transition to turbulence is causing the flow to move in the direction of the upstream flow and further downstream the swept geometry is adding a spanwise component to the velocity (Figure 7.6a). On WLEc1 the streamlines converge towards the LSB at the trough in the LE region. They travel in the chordwise direction in the laminar boundary layer and the transition to turbulence is distorting the flow making it travel in the direction of the upstream flow (7.6b). On WLEc2 the LSB at the trough is smaller but the influence on the flow is stronger and the streamlines collapse in the LSB bubble region at the LE. Then, they travel in the chordwise direction within the laminar boundary layer and downstream the L-T transition, the streamlines coming from the LE peak move in the direction of the upstream flow, while the streamlines coming from the trough show a strong spanwise velocity component generated by the swept geometry (Figure 7.6c). To sum up, the chordwise component of the upstream flow has a major influence on the direction of the flow in the laminar boundary layer for the three swept wing sections. Both wavy configurations present a LSB in the LE region but on WLEc2 it has a stronger influence on the flow evolution downstream.

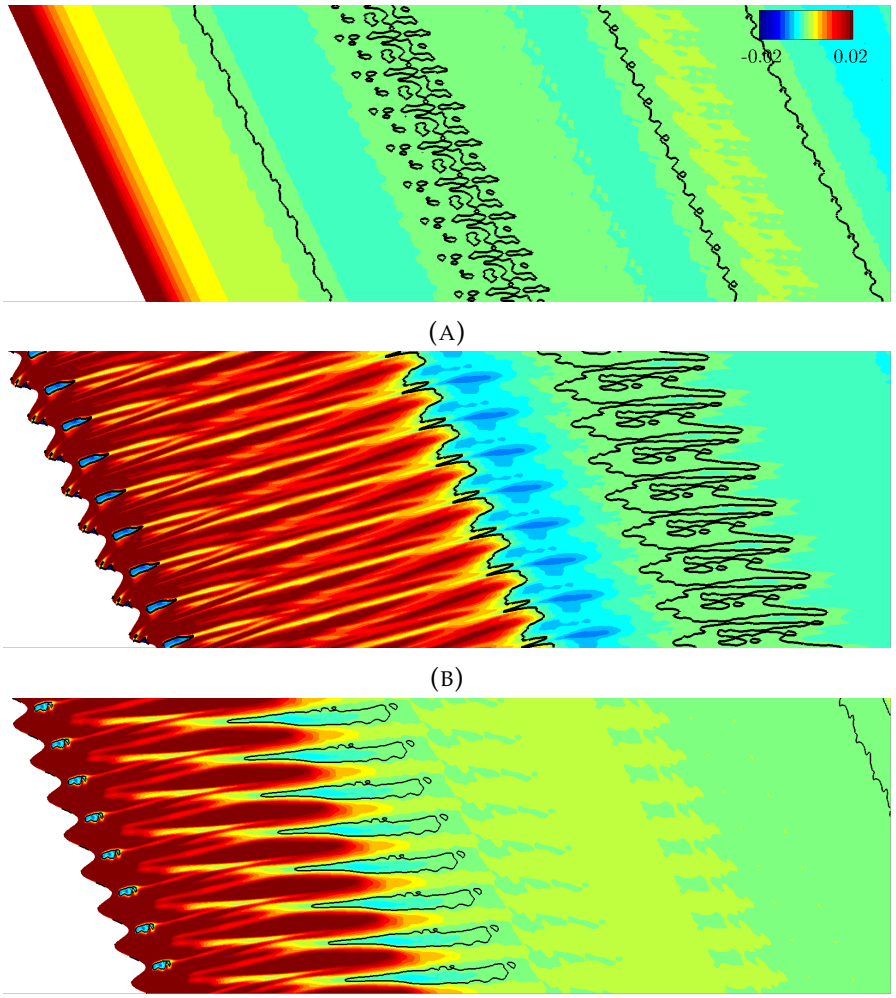

(A)

(B)

(C)

FIGURE 7.4: Mean drag producing skin friction coefficient distribution on the upper surface of SLE (a), WLEc1 (b) and WLEc2 (c) swept wing sections at $\alpha = 7.0^o$. The black line highlights regions where $C_f = 0$. Domain is replicated 8 times in the spanwise direction.

7.2 Unsteady characteristics

The mean aerodynamic characteristics analysis shows a performance improvement of wavy configurations, but the control of unsteady phenomena is the main focus at moderate and high angles of attack. First of all, the aerodynamic force fluctuations are invetigated to have an overview of the unsteady aerodynamic performance. Then, the unsteady motion is investigated in details on the straight and the two wavy configurations, trying to define and identify the different unsteady phenomena.

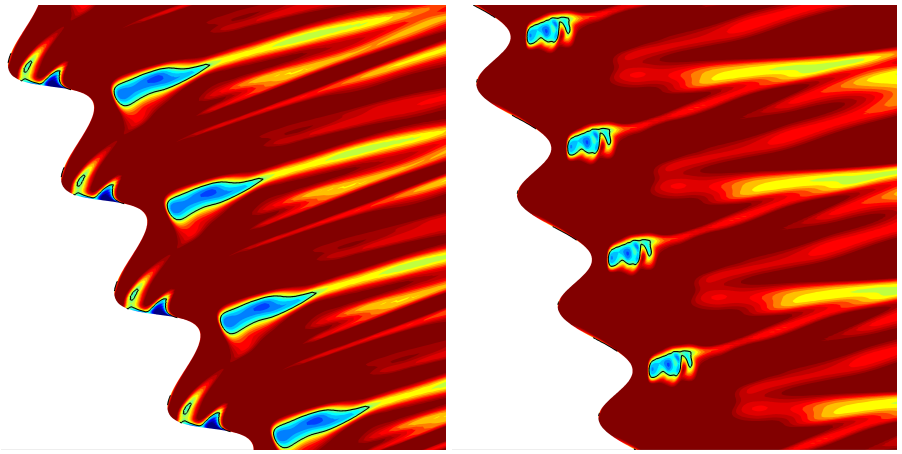

(A) (B)

FIGURE 7.5: Mean drag producing skin friction coefficient distribution on the LE upper surface of WLEc1 (a) and WLEc2 (b) swept wing sections at $\alpha = 7.0^o$. The black line highlights regions where $C_f = 0$. Domain is replicated 4 times in the spanwise direction.

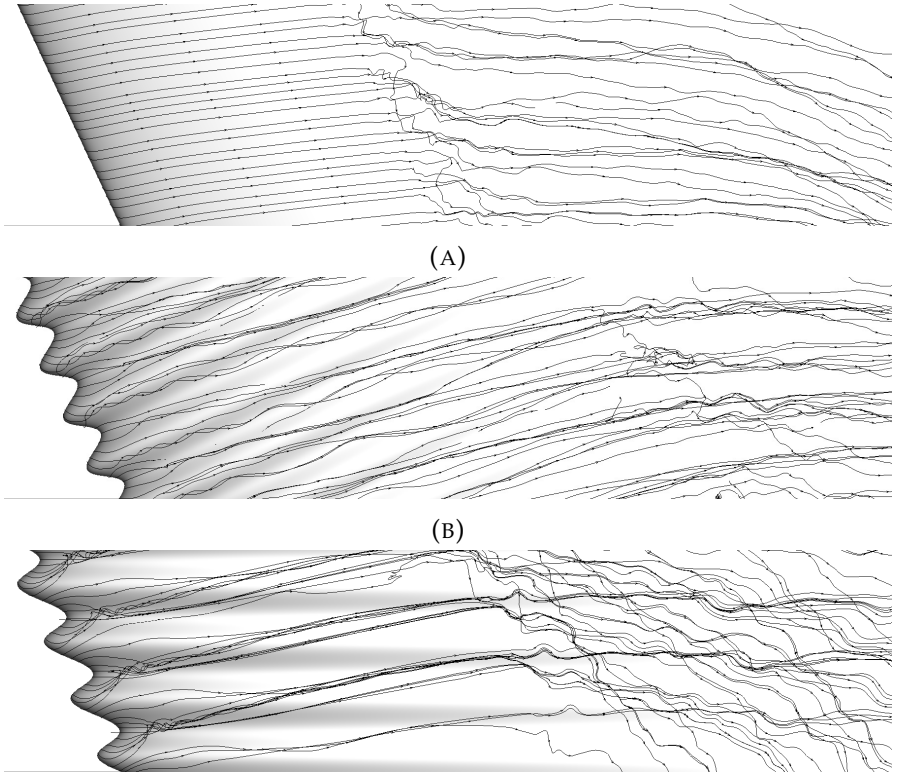

(A)

(B)

(C)

FIGURE 7.6: Instantaneous streamlines close to the upper surface of SLE (a), WLEc1 (b) and WLEc2 (c) swept wing sections at $t = 0.0$. Domain is replicated 4 times in the spanwise direction.

7.2.1 Aerodynamic force fluctuations

Figure 7.7 illustrates lift and drag coefficient time signal for baseline and modified swept wing sections. The baseline wing section displays large low frequency oscillations, consistent with the unswept case analysed in Chapter 5, which are related to the shock buffet phenomenon. The two modified wing sections also present low frequency oscillations with significant lower amplitude. The difference between the wavy configurations is that WLEc1 displays a sinusoidal low frequency lift oscillation, consistent with the baseline case and with previous studies on wavy aerofoils, while WLEc2 displays a more irregular lift signal. The power spectral density of lift and drag coefficients (Figure 7.8) illustrates that both modified wing sections decrease the amplitude of the shock buffet oscillation. In addition to the shock oscillation, the straight swept wing section presents a higher frequency oscillation at $St = 1.0$, which was observed also on the baseline aerofoil in Chapter 5 (Figure 5.9) and it is related to the vortex shedding phenomenon. WLEc2 presents also a higher frequency oscillation at $St = 1.4$ which needs to be investigated in further details. On the other hand, WLEc1 does not show any secondary unsteadiness, analysing aerodynamic forces, but a more detailed investigation on local unsteadiness is needed to fully understand the unsteady behaviour of this swept wing section configuration. The aerodynamic coefficients PSD maxima for the baseline and the modified swept wing sections are summarised in Table 7.3.

	I	II
SLE	0.12	1.0
WLEc1	0.08	-
WLEc2	0.10	1.4

TABLE 7.3: Strouhal number of aerodynamic coefficients PSD maxima for SLE, WLEc1 and WLEc2 swept wing sections.

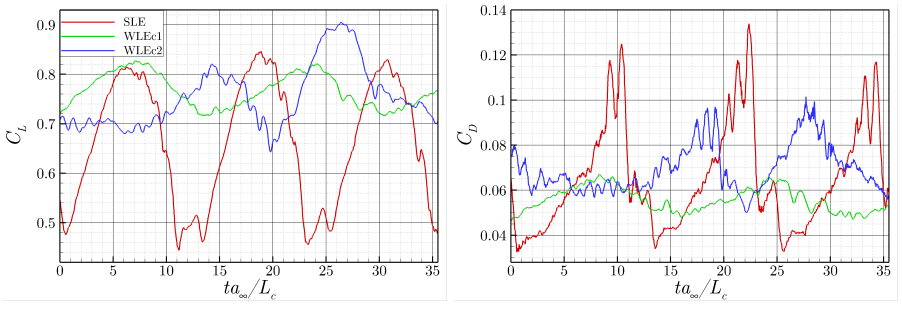

(A) (B)

FIGURE 7.7: Lift (a) and drag (b) coefficient time signal for SLE, WLEc1 and WLEc2 swept wing sections.

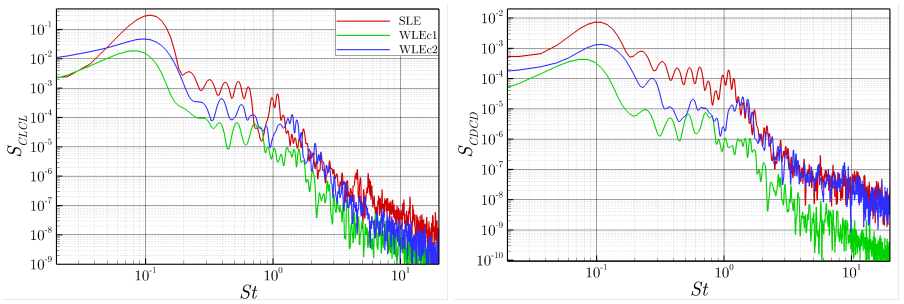

(A) (B)

FIGURE 7.8: Lift (a) and drag (b) coefficient power spectral density with respect to the Strouhal number for SLE, WLEc1 and WLEc2 swept wing sections.

7.2.2 Overview and investigation of the unsteady phenomena

The mitigation of aerodynamic coefficients low frequency oscillations shows that leading edge waviness is a promising passive technique for swept wing applications. The next step of the unsteady analysis is to investigate and understand the different unsteady phenomena on the baseline and the modified swept wing sections. This analysis is conducted through two main steps. Firstly, the wall pressure time signals are investigated in different streamwise locations to give an overview of the local unsteady phenomena and then some physical phenomena are further investigated using the frequency filtering method introduced in Chapter 5.

The local unsteady analysis of the wall pressure on the baseline wing section displays different local maxima in the power spectral density plot (Figure 7.9). The low frequency unsteadiness at $St = 0.12$ related to the shock buffet phenomenon is detected on different streamwise locations on the baseline wing section. On the contrary, the higher frequency unsteadiness at $St = 1.20$ related to the vortex shedding phenomenon is observed only close to the TE, consistently with the nature of the unsteady phenomenon and with previous studies. In addition to these unsteady phenomena, observed already in the unsteady analysis of the aerodynamic forces, two local maxima are detected. The first one is observed between $x = -0.23$ and $x = 0.0$ at $St = 0.70$, while the second one is observed around $x = -0.23$ at a higher frequency ($St = 9.0$).

Figure 7.10 shows the pressure gradient magnitude flow field around the straight wing section during a full cycle of the shock buffet phenomenon. Initially, the shock wave is at the most downstream position and a complex shock waves structure is observed with a λ-shape shock followed by a normal shock (Figure 7.10a). This shock waves structure is consistent with observations on SLE aerofoils in previous chapters. The upstream shock of the λ structure interacts with the laminar BL, introducing a positive pressure gradient. In addition to that, sound waves are generated from the turbulent BL and from vortices passing over the TE and they interact with the normal

shock wave. Due to these interactions, there is a large separation, which moves the L-T transition point and the SBLI region upstream (Figure 7.10b). At the most upstream position, the pressure waves generated from vortices passing over the TE decrease their strength because of turbulent BL separation (Figure 7.10c). As a consequence, the turbulent BL reattaches and becomes thinner, and the shock wave starts moving downstream. Weak shock waves move upstream and detach from the LE (Figure 7.10d). Finally, the shock wave reaches the most downstream position and the cycle starts again.

The unsteadiness observed at $St = 0.70$ is investigated in further details using a frequency filtering method of the pressure coefficient on the swept wing section's upper surface. The unsteady phenomenon is related to the normal and λ-shape shock waves dynamics and their interaction with the BL (Figure 7.11). The result of SBLI is the generation of small vortical structures which develop downstream. This explains why this unsteadiness is detected between the most upstream and the most downstream position of the shock wave. The unsteadiness observed at $St = 9.0$ is detected at the most upstream position of the shock wave and consistently with the unsteadiness at $St = 0.70$, it is related to SBLI at the most upstream position. The higher frequency suggests that this unsteadiness is related to the generation of secondary smaller vortices which then are convected downstream. These local unsteady phenomena do not appear on the baseline unswept aerofoil. This suggests that they are related to a three dimensionality introduced in the laminar BL by the sweep angle.

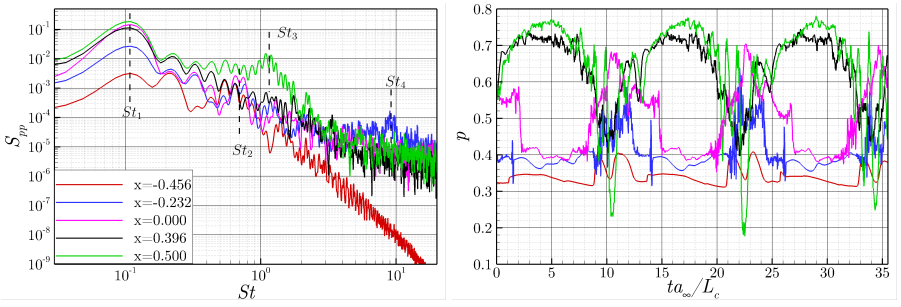

(A) (B)

FIGURE 7.9: Power spectral density with respect to the Strouhal number (a) and time signal (b) of wall pressure at different chordwise locations over the upper surface of SLE swept wing section.

The local unsteady analysis of WLEc1 wing section is displayed in Figure 7.12. A low frequency unsteadiness related to the shock buffet phenomenon is detected at $St = 0.08$ on different streamwise locations. Figure 7.13 shows the pressure gradient distribution at the though during the shock oscillations. A normal shock wave is oscillating periodically on the upper surface of the swept wing section. The oscillation amplitude is significanlty lower compared with the baseline case. Weak shock waves are observed in the supersonic region. In this case, they do not move upstream

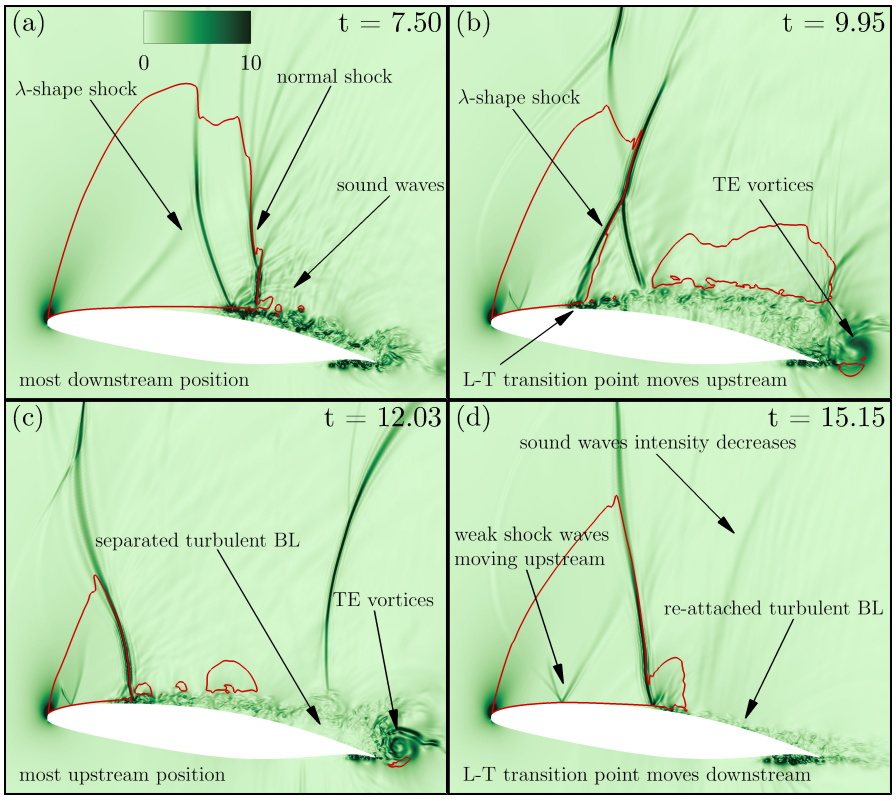

FIGURE 7.10: Pressure gradient magnitude flow field around SLE swept wing section during one cycle of shock buffet oscillation: most downstream position (a), shock wave upstream movement (b), most upstream position (c), and shock wave downstream movement (d). The red line highlights the sonic line. The slices are perpendicular to the z axis of xyz reference frame.

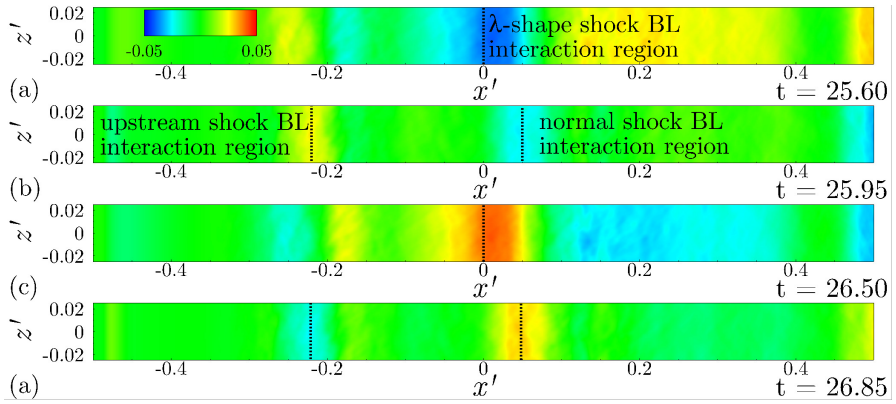

FIGURE 7.11: Filtered pressure coefficient field on the upper surface of the baseline swept wing section during one cycle of the oscillation at $St = 0.7$.

because they are generated from the three dimensional vortical structures within the laminar BL (Figure 7.13a). At the most upstream position of the normal shock wave, the turbulent BL separates and vortices are periodically passing over the TE (Figure 7.13b).

The local surface pressure unsteady analysis displays also a local maximum at $St = 0.75$ on the second half of swept wing section (Figure 7.12a). The unsteady

phenomenon is investigated with the frequency filtering method on the pressure coefficient and the spanwise vorticity. The filtered pressure coefficient displays periodical release of vortical structures downstream the SBLI region (Figure 7.14a). The filtered spanwise vorticity suggests that the origin of the unsteadiness is located in the laminar BL region upstream the SBLI region (Figure 7.14b).

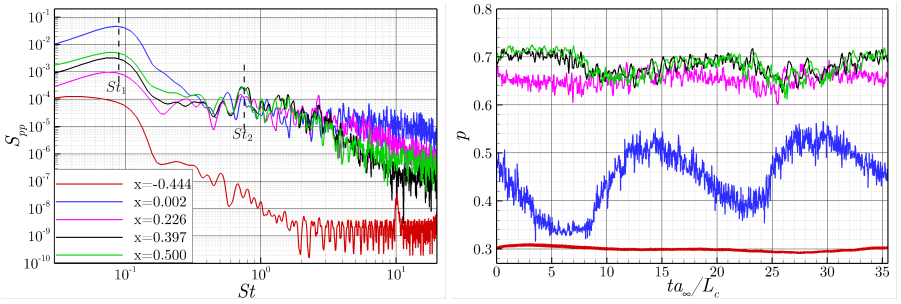

(A) (B)

FIGURE 7.12: Power spectral density with respect to the Strouhal number (a) and time signal (b) of wall pressure at different chordwise locations at the though over the upper surface of WLEc1 swept wing section.

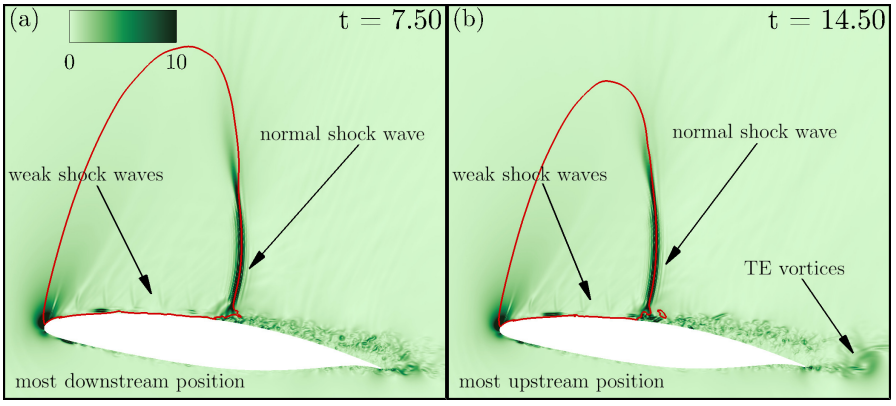

FIGURE 7.13: Pressure gradient magnitude flow field around WLEc1 swept wing section during one cycle of shock buffet oscillation: most downstream position (a), and most upstream position (b). The red line highlights the sonic line. The slices are perpendicular to the z axis of xyz reference frame.

The local unsteady analysis of WLEc2 wing section is shown in Figure 7.15. The low frequency unsteadiness related to the shock buffet is observed at $St = 0.10$. Figure 7.16 shows that the shock wave structures and the shock dynamics is different from the other wavy configuration and from the baseline case. A normal shock wave oscillates periodically on the upper surface of the swept wing section. A periodic separation and reattachment of the turbulent BL downstream the SBLI region is observed (7.16a,c). In addition, weak shock waves not travelling upstream are observed, as in the other wavy configuration. This is related to the vortical structures developing in the laminar BL and they will be analysed in details in the next section. Table 7.4 summarises the amplitude of shock oscillations during the shock buffet phenomenon. The baseline wing section displays the largest oscillation on 23% of the chord. WLEc2

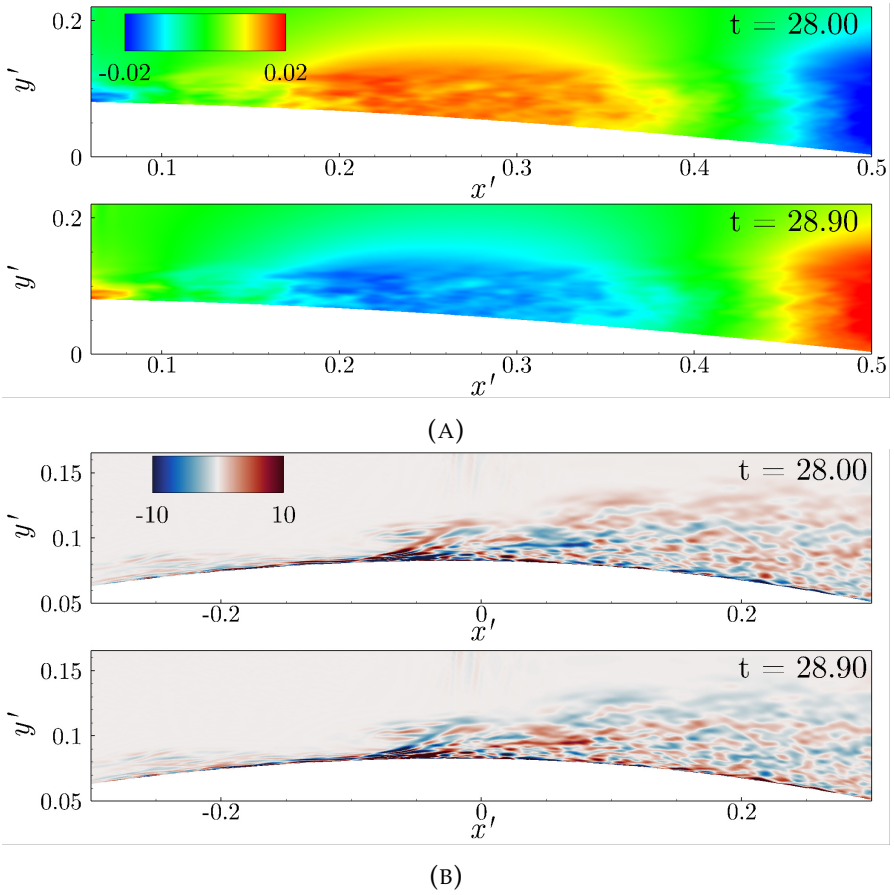

FIGURE 7.14: Filtered pressure coefficient field (a) and filtered spanwise vorticity field (b) at the trough section of WLEc1 swept wing section during one cycle of the oscillation at $St = 0.75$.

is able to decrease it to about 16% of the chord, while on WLEc1 the oscillation is limited to about 7% of the chord. This is consistent with the unsteady analysis of aerodynamic forces in Figure 7.8.

The wall pressure unsteady analysis shows a maximum in the power spectral density plot at $St = 1.30$ (Figure 7.15a). This unsteadiness is localised in the second half of the wing section. The frequency filtering method is applied to the pressure coefficient and the spanwise vorticity. The filtered pressure coefficient shows the periodic release of vortical structures from the SBLI region which develop downstream up to the TE (Figure 7.17a). The origin of this unsteady phenomenon is located in the laminar BL upstream the SBLI region, as it is shown by the filtered spanwise vorticity (Figure 7.17b). This is consistent with the unsteadiness observed on WLEc1 and it characterises the high frequency unsteady phenomena on wavy swept wing sections. However, the origin of the high frequency unsteadiness is localised in a thin region close to the surface on WLEc1, while it is on a thicker region on WLEc2. Another difference between the two wavy configurations is that the high frequency unsteadiness is observed for the aerodynamic forces and the local wall pressure

signals on WLEc2, while it is observed only for the local wall pressure signals on WLEc1.

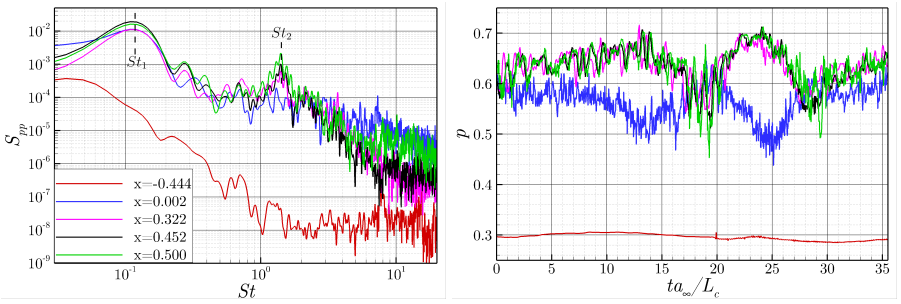

(A) (B)

FIGURE 7.15: Power spectral density with respect to the Strouhal number (a) and time signal (b) of wall pressure at different chordwise locations at the though over the upper surface of WLEc2 swept wing section.

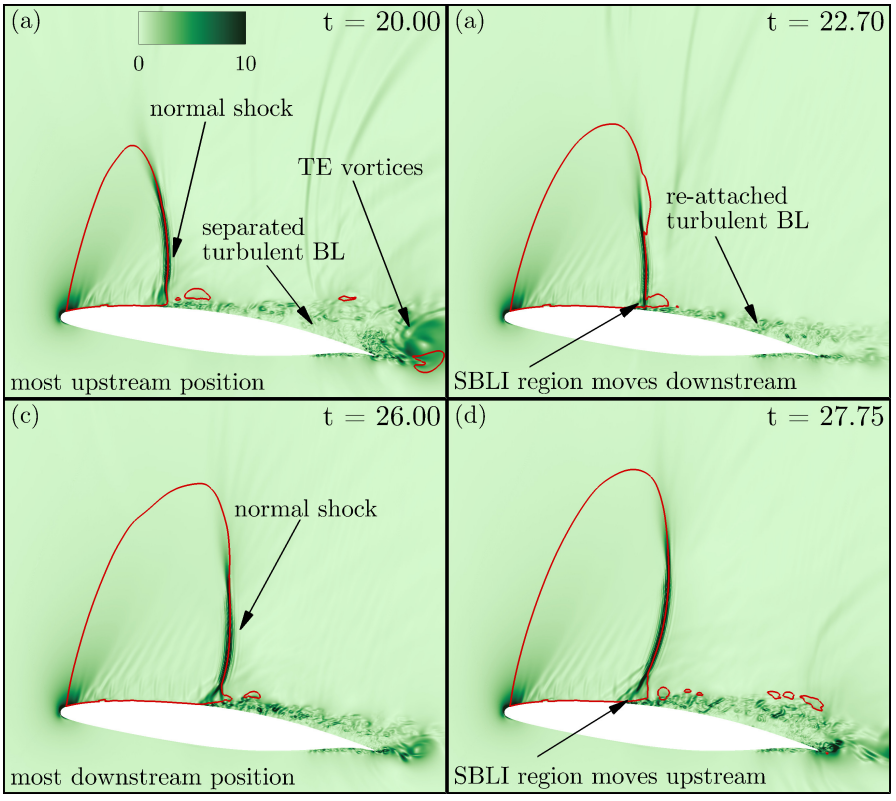

FIGURE 7.16: Pressure gradient magnitude flow field around WLEc2 swept wing section during one cycle of shock buffet oscillation: most upstream position (a), shock wave downstream movement (b), most downstream position (c), and shock wave upstream movement (d). The red line highlights the sonic line. The slices are perpendicular to the z' axis of $x'y'z'$ reference frame.

This section has investigated in details the unsteady phenomena on SLE, WLEc1 and WLEc2 swept wing sections. The main findings can be summarised as follows.

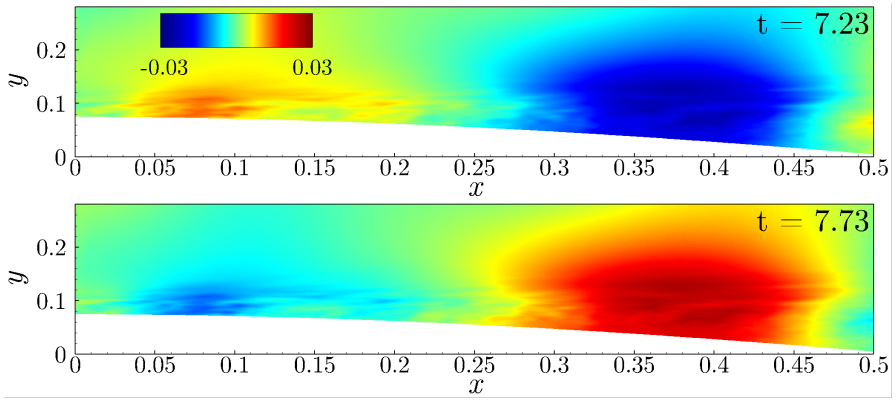

(A)

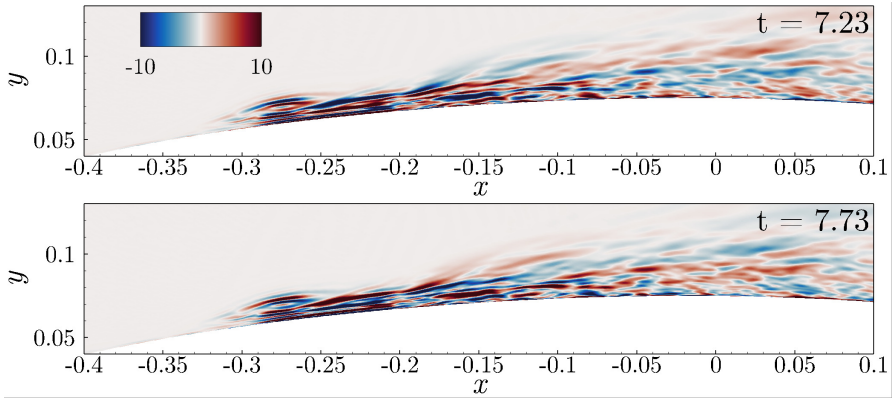

(B)

FIGURE 7.17: Filtered pressure coefficient field (a) and spanwise vorticity field (b) at the trough section of WLEc2 swept wing section during one cycle of the oscillation at $St = 1.30$.

	SLE	WLEc1	WLEc2
x_{SU}	-0.23	-0.02	-0.15
x_{SD}	0.00	0.05	0.01
Δx_S	0.23	0.07	0.16

TABLE 7.4: Shock wave oscillation details for the baseline and WLEc1 and WLEc2 swept wing sections.

- The shock buffet oscillation is observed on the three configurations but WLEc1 shows the best performance in mitigating the low frequency unsteadiness and it is able to significantly decrease the amplitude of shock oscillations.
- The vortex shedding phenomenon is observed on the baseline case, consistently with previous findings on straight aerofoils (Chapter 5). In addition, two unsteady phenomena are observed and they are related to the shock wave interaction with the three dimensional BL at the most upstream and most downstream positions of the shock buffet. As a result of SBLI, vortices are periodically released and they develop downstream.

- The wavy configurations present a high frequency unsteadiness which arises in the laminar BL upstream the SBLI region and generates vortices developing in the turbulent BL and passing over the TE.
- Weak shock waves are observed in the supersonic region of the modified swept wing sections. They are not moving upstream and detaching from the LE, as on the baseline wing section, and they are generated from the three dimensional vortical structures within the laminar BL, introduced by the leading edge waviness.

7.3 Flow structures analysis

This section investigates the flow structures of the two wavy configurations, comparing them with previous studies on modified aerofoils (Chapter 4). In particular, the flow channeling phenomenon is investigated to unsterstand the upstream flow interaction with the wavy leading edge and then the streamwise vorticity evolution is analysed to understand the flow structures developing in the laminar BL. The understanding of flow structures on the wavy configurations leads to a better comprehension of the mean and unsteady aerodynamic perfomance of the modified wing sections.

7.3.1 Leading edge flow channeling

The flow channeling phenomenon on the wavy unswept wing section shows a lobular pattern of the spanwise velocity (Figure 4.11), where on the lower lobes the flow is moving toward the trough, while on the upper lobes it is moving in the opposite direction away from the trough.

WLEc1 introduces an asymmetry because the WLE direction is not parallel to the upstream flow direction. Upstream the swept wing section, two lobes of positive and negative spanwise velocity are observed upstream the peak and trough sections, respectively (Figure 7.18a). This is consistent with the observations on two dimensional wavy aerofoils. The stagnation point on WLEc1 is not at the peak and trough sections like on unswept aerofoils, but on one side of the peak. As a consequence, the spanwise velocity distribution around the peak shows two lobes, one of positive and one of negative spanwise velocity (Figure 7.18b). In particular, negative spanwise velocity is observed in the half of the peak where the stagnation point is located. In the region of positive spanwise velocity, the flow in the laminar BL displays an opposite spanwise flow direction. This region of negative spanwise velocity is thinner where the above positive spanwise velocity is faster and vice versa. This region of opposite spanwise velocity generates streamwise vorticity, as it will be

illustrated later in this section. The leading edge waviness generates two regions of negative spanwise velocity at the peak: a large lobe around the stagnation point and a thin layer in the laminar BL underneath the positive lobe. Moving further downstream, the two regions of negative spanwise velocity grow and they end up merging together upstream the trough (Figure 7.18c,d). In addition the positive lobe is split into two positive lobes on the upper and lower side of the peak. Moving downstream these two positive lobes tend to shrink. Another difference with the unswept case is that the trough section does not present a stagnation point and it breaks the region of negative spanwise velocity. Around the trough a thick and a thin region of negative spanwise velocity are observed (Figure 7.18e). The asymmetry introduced by the sweep angle between the WLE direction and the upstream flow direction significantly changes the flow field around the WLE and it generates more complex vortex structures which have a stronger effect on the flow field than the leading edge flow channeling observed on unswept aerofoils.

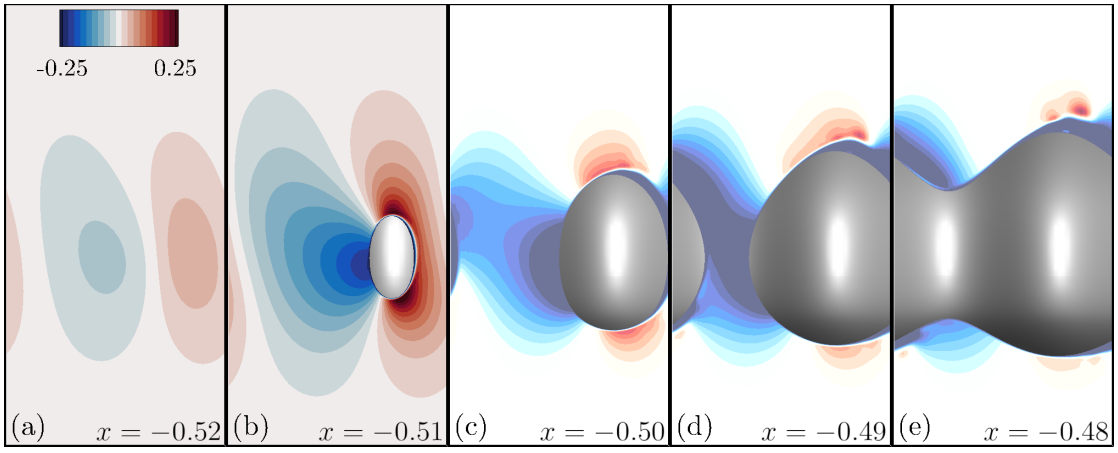

FIGURE 7.18: Contour plots of spanwise velocity at five streamwise positions of WLEc1 swept wing section. The range shown in the spanwise direction is $[-0.025, 0.025]$ and in the vertical direction it is $[-0.05, 0.05]$.

In WLEc2 configuration the WLE direction and the upstream flow direction are parallel. In this case the asymmetry is introduced by the spanwise geometry because two consecutive peaks present different streamwise locations. Upstream the swept wing section the subsonic flow is influenced by the geometry and a positive spanwise velocity is observed with higher amplitude in the peak region (Figure 7.19a). Also this wavy configuration does not present the stagnation point at the peak and trough sections but on one side of the peak like on WLEc1. A tiny lobe of negative spanwise velocity is observed around the stagnation point, while two lobes of high positive spanwise velocity are displayed on the lower and upper side of the peak (Figure 7.19b). Moving further downstream, on one side of the peak the positive lobe grows, while on the other side of the peak a region of negative spanwise velocity is generated within the laminar BL (Figure 7.19c). At $x = -0.47$ the leading edge flow channeling is comparable to the unswept case (Figure 7.19d). On one side of the trough section, a

region of positive spanwise velocity above a region of negative spanwise velocity within the laminar BL is displayed, while on the other side of the trough section, the opposite flow field is observed, a region of negative spanwise velocity above a region of positive spanwise velocity within the laminar BL. The main difference with the unswept case is the asymmetry between the flow fields on the opposite sides of the trough.

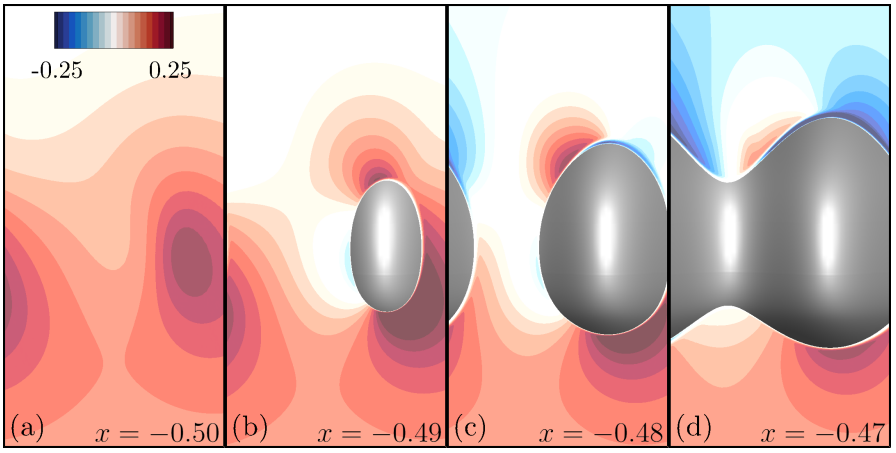

FIGURE 7.19: Contour plots of spanwise velocity at five streamwise positions of WLEc2 swept wing section. The range shown in the spanwise direction is $[-0.025, 0.025]$ and in the vertical direction it is $[-0.05, 0.05]$.

7.3.2 Streamwise vorticity evolution

The streamwise vorticity analysis on the unswept wing section displays streamwise vortex (SV) sheets at the leading edge. The reverse flow region around the trough section generates localized streamwise vorticity. Vortex sheet pairs are generated above and below the original streamwise vortex sheets with an opposite sign and they develop downstream the reattachment point. An additional vortex pair is generated on top of the original SV sheets with high incidence angles (Figure 4.13, 4.14).

WLEc1 presents two SV sheets of opposite sign on one side of the peak (Figure 7.20a). They are generated by the presence of a positive spanwise velocity region on top of the negative spanwise velocity within the laminar BL observed in Figure 7.18c. These SV sheets develop downstream in a streamwise vortex structure around the peak section and SV sheets are generated in the trough section (Figure 7.20b,c). Further downstream the streamwise vortex structures are convected in the spanwise direction and they tend to move away from the surface. Close to the surface additional SV sheets are generated (Figure 7.20d-h).

WLEc2 streamwise vorticity shows a symmetric distribution in the peak region. Two SV sheets of opposite sign are observed on the two sides of the peak section and they end up on top of each other at the peak section (Figure 7.21a). This symmetric

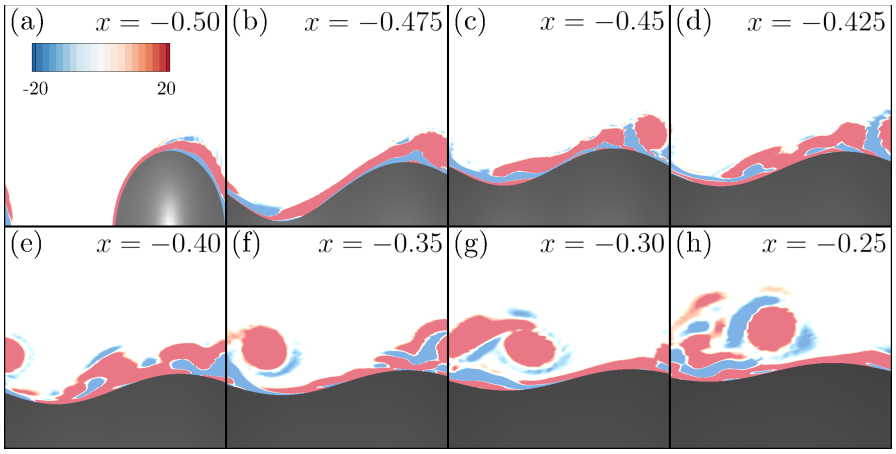

FIGURE 7.20: Contour plots of streamwise vorticity for WLEc1 swept wing section. The range shown in both spanwise and vertical direction is 0.05, but the estremes vary in the vertical direction to focus on the region close to the aerofoil surface.

distribution at the leading edge is because the WLE direction and the upstream flow direction are parallel. Downstream the trough, a main SV sheet is observed around the peak section on top of a wall SV sheet, while additional vorticity is generated around the trough section because of the laminar separation bubble (Figure 7.21b). Further downstream, the main SV sheet and the wall SV sheet are distributed along the span. An additional SV sheet on top of the main one is observed on one side of the though section (Figure 7.21c-e). Streamwise vortical structures are generated further downstream also on WLEc2 configuration and they are also convected in the spanwise direction (Figure 7.21f-h). In this configuration the streamwise vortical structures are close to the wing section surface, so no additional SV sheet is generated underneath them.

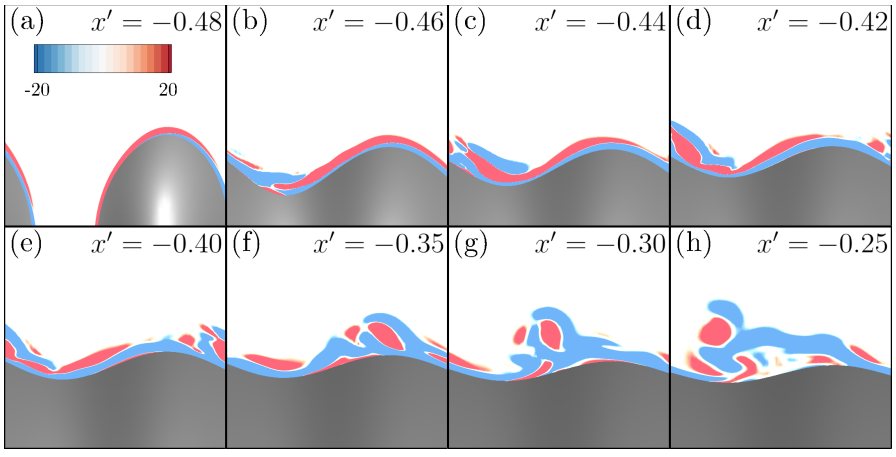

FIGURE 7.21: Contour plots of streamwise vorticity for WLEc2 swept wing section. The range shown in both spanwise and vertical direction is 0.04, but the estremes vary in the vertical direction to focus on the region close to the aerofoil surface.

The streamwise vorticity evolution on wavy swept wing sections is not comparable with the unswept cases because of the flow field asymmetry in the leading edge

region. On both wavy configurations streamwise vortical structures are generated on the upper surface of the wing sections and they are convected in the spanwise direction. The streamwise vortical structures on WLEc1 are generated close to the leading edge (around $x = -0.475$) and then they develop downstream and they are detached from the wing section surface. As a consequence, additional SV sheets are generated close to the surface. On the contrary, on WLEc2 streamwise vortical structures are generated further downstream (around $x = -0.35$) and they develop close to the wing section surface.

7.4 Concluding remarks

The study presented in this chapter has analysed the effect of leading edge waviness on swept wing sections in terms of both mean and unsteady aerodynamic performance. Two wavy configurations have been investigated: in the first one the WLE direction has a sweep angle with respect to the upstream flow, while in the second one the WLE direction is parallel to the upstream flow. The two wavy configurations have been compared with a baseline swept wing section.

Section 7.1 has analysed the time-averaged aerodynamic characteristics. Both wavy configurations increase the lift coefficient with respect to the straight counterpart. The main difference between the two wavy configurations is the drag coefficient. The pressure drag is significantly decreased by WLEc1, which shows the highest mean aerodynamic efficiency. In Chapter 5, it was observed that the leading edge region tends to have a negative effect on the pressure drag because of high pressure coefficient regions, while the region downstream the L-T transition point has a positive effect in decreasing the pressure drag. WLEc2 displays a larger high pressure coefficient region around the leading edge peak which has a negative effect on the pressure drag coefficient. On the contrary, WLEc1 shows a larger pressure coefficient distribution plateau on the upper surface but then a steep pressure coefficient increase and because of this higher pressure coefficient region downstream the L-T transition point, the pressure drag coefficient is decreased. The skin friction drag coefficient is about one order of magnitude lower than the pressure drag coeffient. However, both wavy configurations tend to increase the skin friction drag. The two wavy configurations display different skin friction distribution. On the one hand, WLEc1 shows stripes of lower skin friction in the three dimensional laminar BL. On the other hand, WLEc2 presents a single stripe of lower skin friction between the peak and the trough section. In addition, a localised mean laminar separation bubble is observed.

Section 7.2 has analysed the unsteady aerodynamic characteristics of the three aerofoils in details. The main results are summarised as follows.

- The straight unswept wing section displays two unsteady phenomena already observed on the unswept wing sections, the shock buffet oscillation and the vortex shedding. Two additional unsteady phenomena are observed on the swept wing section. They are related to the shock wave interaction with the BL. As a result of this interaction, vortices are periodically released and they develop downstream.
- The two wavy configurations display two main unsteady phenomena. A low frequency unsteadiness related to the shock wave oscillation and a high frequency unsteadiness which originates in the laminar BL upstream the SBLI region and generates vortices developing in the turbulent BL. The difference between the two wavy configurations is that on WLEc1 this high frequency unstediness is observed locally in the wall pressure analysis, while on WLEc2 it is observed both locally in the wall pressure analysis and globally in the aerodynamic forces analysis.

Section 7.3 is focused on analysing the leading egde flow structure on the two wavy configurations, comparing them with the flow structures on unswept wing sections (Chapter 4). The main observations are summarised as follows.

- The leading edge flow channeling does not show the lobular pattern of spanwise velocity observed on WLE aerofoils. The main difference is that on unswept wing sections a stagnation point is observed at the trough and peak sections, while on swept wing sections an asymmetry is introduced and only one stagnation point is observed on one side of the peak section. On WLEc1 a region of negative spanwise velocity is observed between two consecutive peaks and two lobes of positive spanwise velocity are generated on the upper and lower surface around the peak section. The flow field around WLEc2 leading edge is closer to the unswept case. On one side of the trough section, a region of positive spanwise velocity above a region of negative velocity within the laminar BL is observed, while on the other side of the trough section, a region of negative spanwise velocity above a region of positive velocity within the BL is detected. The main difference with the unswept case for WLEc2 configuration is the amplitude of the positive and negative lobes.
- The asymmetry introduced by the sweep angle has a major effect also on the streamwise vorticity evolution. On both wavy configurations, streamwise vortical structures are generated on the upper surface of the wing sections and they are convected in the spanwise direction. On WLEc1 streamwise vortical structures are generated close to the leading edge and they detach from the wing surface while developing downstream. As a result, additional SV sheets are generated close to the surface. On WLEc2 the streamwise vortical structures generate further downstream and they develop close to the wing surface.

The results presented in this chapter represent a preliminary study on the possibility to apply wavy leading edges to commercial aircraft wings. The outcome of the mean and unsteady aerodynamic analysis shows that a configuration with WLEs having a sweep angle with respect to the upstream flow has a higher mean aerodynamic efficiency than the straight counterpart and is able to mitigate the shock buffet unsteady phenomenon at $\alpha = 7.0^o$ incidence angle. The practical application of this passive technique to commercial aircraft still requires an extensive analysis of the mean and unsteady aerodynamic performance at high efficiency incidence angle. Furthermore, the preliminary analysis presented in this chapter should be further extended with simulations of the full wing. This would allow to investigate in details the following open questions.

- The effect of the spanwise domain size and the possible interaction between laminar separation bubbles in the leading edge region.
- The effect of WLEs on the buffet cells which characterize the flow over a swept wing in commercial aircraft.
- The effect of the physical approximation introduced in this chapter by the application of periodic boundary conditions.

Chapter 8

Conclusions and Future Work

8.1 Summary of findings

This research presents investigations into the aerodynamic and aeroacoustic performance of wavy leading edges (WLEs) in transonic flows. The research methodology consists of high fidelity numerical simulations of the 3D compressible Navier-Stokes equations based on high order implicit schemes. The baseline aerofoil is based on a Dassault Aviation's V2C profile which is a laminar supercritical aerofoil designed for transonic flows, delaying the onset of wave drag and decreasing the skin friction drag. WLEs have been extensively studied in subsonic flows with a special focus on post-stall conditions, but there is a minimal literature about the application of this passive technique in transonic flows. Due to the novelty of the study, an overview of WLEs in transonic flows was given in this work with applications in aerodynamics and aeroacoustics.

The preliminary study has compared the performance of the baseline and the modified aerofoil at difference angles of attack through a heaving motion with a main focus on the quasi-linear part of the heaving motion. The aerodynamic performance analysis has shown that the wavy geometry generates a distortion of the flow field in the leading edge region and this moves the transition point upstream. WLE aerofoils are able to decrease the pressure drag in two main regions at low and moderate angles of attack: the leading egde and downstream the transition point. The second region is dominant at higher incidence angles. The flow field investigations at the leading edge have explained the beneficial effect of the leading edge waviness in this region. The flow channeling phenomenon explains the acceleration of the flow to supersonic conditions at the trough in a wide range of incidence angles, which has a positive effect on the lift coefficient. The boundary layer and the streamwise vorticity evolution prove that the modified LE energises the laminar BL and makes it three dimensional.

After an investigation of mean aerodynamic performance at different angle of attack and a preliminary study of the leading edge flow field, the aerodynamic performance of the wavy aerofoil has been studied at a shock buffet condition ($M_\infty = 0.7$ and $\alpha = 7.0$). The main focus of this second part of the thesis was on the unsteady phenomena and the effect of WLE amplitude on mean and unsteady aerodynamic performance. The results of this study have shown that a small waviness is sufficient to create an important drag decrease. The beneficial effect on drag pressure decrease is observed downstream of the modified aerofoil's L-T transition point. The LE region has a negligible effect on the drag coefficient at low wavy amplitudes, while wavy amplitude growth tends to increase the drag in the LE region with respect to the SLE case. The unsteady aerodynamic analysis investigated both low and high frequency phenomena. The results show that the shock buffet phenomenon can be controlled by a wavy aerofoil and it changes its strength modifying the wavy amplitude. The difference during low frequency oscillations seems to be related to a more energetic BL on the modified aerofoils because of streamwise vorticity created upstream in the LE region. The high frequency oscillation on the wavy aerofoils is related to LSB breathing phenomenon. LSB breathing is responsible for a periodic thickening and thinning of the laminar BL upstream of the SBLI region. The effect on the downstream flow is the generation of small vortices in the SBLI region. It is observed a strong connection between shock buffet and LSB breathing phenomena on wavy aerofoils. When the shock buffet's strength is decreased, the LSB breathing's strength is increased and vice versa. The WLE amplitude is a design parameter to control the interaction between these unsteady phenomena.

In order to provide a complete overview of WLE aerofoils performance in transonic flows, the aeroacoustic performance of the modified aerofoils was analysed in the thesis. The effect of WLE amplitude was considered, consistently with the unsteady aerodynamic investigation. WLE1 and WLE2 show consistent results decreasing the far-field pressure fluctuations in the region upstream and above the aerofoil and having comparable performance with SLE in the region downstream. On the other hand, WLE3 displays a reduction of far-field pressure fluctuations over the all frequency range considered in this investigation and at all the observer directions.

The aerodynamic and aeroacoustic performance analysis on WLE aerofoils displays that WLE1 presents the best mean aerodynamic performance, while WLE2 presents the best unsteady performance. Finally, WLE3 displays the best aeroacoustic performance. This proves that WLE aerofoils can be beneficial in transonic flows but a trade-off is needed for the overall performance.

In the last part of this study, WLEs have been applied to swept wing sections. Two wavy configurations have been investigated and compared to the baseline case: in the first one the WLE direction has a sweep angle with respect to the upstream flow, while in the second one the WLE direction is parallel to the upstream flow. The mean

aerodynamic analysis has shown that the main difference between the two wavy configurations is the drag coefficient. The pressure drag is significantly decreased by WLEc1 because of a larger pressure distribution plateau on the upper surface and a steep pressure increase. This higher pressure coefficient distribution downstream the L-T transition point is responsible for decreasing the pressure drag coefficient. The unsteady analysis shows two additional unsteady phenomena on the straight swept wing section which are related to the release of small vortices from the SBLI region at the most upstream and downstream position of the shock buffet oscillation. The two wavy configurations present a high frequency unsteadiness which originates in the laminar BL upstream the SBLI region and generates vortices developing in the turbulent BL. Finally, the flow field in the leading edge region is investigated for the two wavy configurations. The flow channeling effect is modified by the asymmetry introduced by the sweep angle. In particular, only one stagnation point is observed on one side of the peak. On WLEc1 a region of negative spanwise velocity is observed between two consecutive peaks and two lobes of positive spanwise velocity are generated around the peak section on the upper and lower surface. The flow field around WLEc2 leading edge is closer to the unswept case. The main difference with the unswept case for WLEc2 configuration is the amplitude of the positive and negative lobes. The streamwise vorticity evolution analysis displays on both configurations the generation of streamwise vortical structures. On WLEc1 streamwise vortical structures are generated close to the leading edge and they detach from the wing surface while developing downstream. On WLEc2 the streamwise vortical structures generate further downstream and they develop close to the wing surface.

8.2 Limitations

This study has investigated different aspects of WLEs performance in a transonic flow. The objective was to give an overview on different aspects related to mean and unsteady aerodynamics and aeroacoustics. Due to the extent of the all analysis, some important limitations need to be highlighted in order to tackle them in future studies.

8.2.1 Major limitations

- The spanwise domain size represents an important limitation. All the simulations performed include one WLE wavelength. Previous studies on WLEs in subsonic flows (Perez Torro and Kim (2017)) have shown that the dynamics of vortical structures generated by the LE waviness can increase its complexity when a larger domain span is considered. Recent analyses (Turner and Kim (2020b)) have also shown the importance of the spanwise domain size in aeroacoustic simulations.

- The study has investigated the effect of WLE amplitude parameter in details, but the effect of WLE wavelength was not analysed. Previous studies on WLEs in subsonic flows have shown that the ratio between WLE amplitude and wavelength is a design parameter. It would be interesting to see if the conclusions in subsonic flows are valid also in transonic flows.

8.2.2 Other limitations

- The simulations performed in this study present an upstream flow with a moderate Reynolds number. As a result, the skin friction drag is about one order of magnitude lower than the pressure drag. ILES with a Reynolds number in the order of magnitude of millions should provide results closer to industrial applications.
- After a preliminary analysis of mean aerodynamic performance at different angles of attack through a heaving motion, the main focus of the study was the mitigation of shock buffet phenomenon. A detailed analysis on mean and unsteady aerodynamic performance on high efficiency angles of attack would provide a broader picture of WLE performance in transonic flows.

8.3 Future works arising from this study

The results presented in this thesis give an overview of aerodynamic and aeroacoustic performance of WLEs in transonic flows. In particular, they prove the potential of WLEs to increase the aerodynamic efficiency and mitigate the shock buffet unsteadiness and far-field pressure fluctuations at high incidence angles.

Future works should try to tackle the limitations of this study. In particular, the next step is to compare the straight and the wavy aerofoils with a larger spanwise domain size. This might change the complexity of the flow structures in the three dimentional laminar BL and it might introduce new unsteady phenomena related to large three dimensional vortical structures. In subsonic flows it is observed that the laminar separation bubbles generated at the trough sections tend to interact further downstream creating larger flow structures at high incidence angles (Perez Torro and Kim (2017)). This three dimensional interaction of laminar separation bubbles generated at the trough might have a major impact on the efficiency of a laminar supercritical aerofoil. Because of the additional disturbances within the laminar boundary layer, the L-T transition point might move further upstream decreasing the aerofoil efficiency. The generation of streamwise vorticity within the laminar BL should be localized around the trough section like with three dimensional shock control bumps where the interaction between streamwise vortices generated by

adjacent bumps happens further downstream the location of the bump itself. A simulation with a large spanwise domain is even more important when swept wings are considered. In this case, the full wing should be simulated in order to get rid of the periodic boundary conditions approximation. Three dimensional flow structures called buffet cells are observed on straight swept wings, they move upstream until they reach the shock wave and then they travel at an angle in the spanwise direction. The streamwise vorticity generated at the leading edge in the wavy case would interact with both the shock wave and the buffet cells in the SBLI region.

The analysis of WLE wavelength on the aerodynamic and aeroaoustic performance is necessary to complete the parametric study on WLE wing sections. The wavelength might have a major effect on the flow channeling phenomenon. A wavelength decrease would increase the acceleration upstream the leading edge bringing the flow to sonic conditions and then decelerating it in the convergent region, while a wavelength increase would decrease the acceleration upstream the leading edge and it would not bring the flow to sonic conditions before the divergence where the flow would be decelerated. Both these cases represent off design conditions and would bring to a decrease in the wavy aerofoil's efficiency. The reduction of the wavelength might have a positive effect on the mitigation of shock buffet unsteadiness because of the increased distortion of the flow in the LE region. However, a similar effect observed on the wavy amplitude should be expected also on the wavelength: an initial reduction of the shock oscillation reducing the wavelength and then an increase once the leading edge is generating a high distortion in the laminar BL. Furthermore, the area where the bubble can develop becomes narrower decreasing the wavelength, therefore it is easier to observe a collapse of multiple bubbles further downstream which might decrease the aerofoil efficiency. The wavelength is a secondary parameter affecting the aeroacoustic performance of the wavy aerofoil, which is the reason why the wavy amplitude was investigated in this study. However, a trend similar to the wavy amplitude should be observed decreasing the WLE wavelength.

Once a deep understanding of WLE performance at high incidence angles is reached, the same analysis should be conducted at a high efficiency condition to understand if the conclusions in terms of WLE amplitude, WLE wavelength and swept wing configuration are consistent or a trade off is needed for real applications. The results presented in this thesis have already shown that a trade-off in terms of WLE amplitude is needed in order to reach optimal mean and unsteady aerodynamic performance and aeroacoustic performance.

Finally, a further step is required towards the application of WLEs to aeronautical cases. The Reynolds number should be increased in the order of millions. This would increase the contribution of skin friction drag to the total drag, especially in high efficiency configurations. It was observed in this thesis that WLE aerofoils and swept wing sections tend to increase the skin friction drag. An investigation at high

Reynolds numbers might provide more details on the applicability and the limitations of this passive technique in transonic flows.

Appendix A

Methodology details

A.1 Grid generation

A.1.1 Horizontal interface

The x coordinates of an horizontal interface are distributed using the function introduced in the previous section, then the y coordinates are computed using a combination of trigonometric functions.

$$y(x) = a \sin^2 \frac{\pi}{2} k + b \cos \frac{\pi}{2} k \tag{A.1}$$

where the coefficients a, b and k are specific for left and right interfaces.

$$\begin{cases} a = y_{LE} \qquad b = 0 \\ k = \frac{x - x_{LD}}{x_{LE} - x_{LD}} \end{cases} \quad \text{left interface} \tag{A.2}$$

$$\begin{cases} a = y_{TE_{1,2}} \qquad b = y_{TE_{1,2}} \\ k = -\frac{x - x_{RD}}{x_{TE_{1,2}} - x_{RD}} \end{cases} \quad \text{right interface} \tag{A.3}$$

where (x_{LE}, y_{LE}) are the coordinates of the leading edge, x_{LD} is the coordinate of the domain's left edge, while $(x_{TE_{1,2}}, y_{TE_{1,2}})$ are the coordinates of the trailing edge (considering a general case of a blunt trailing edge) and x_{RD} is the coordinate of the domain's right edge. The function of the horizontal interface $y(x)$ has the first derivative equal to zero at x_{LD} and x_{RD}, thus it is normal to the vertical edges of the domain.

A.1.2 Vertical interface

The vertical interface is the opposite case because the y coordinates are firstly distributed and then the x coordinates are computed as a function of y. A third order polynomial function is used, thus there are four free parameters. The conditions for the upper left vertical interface are

$$\begin{cases} x(y_0) = x_0 & x(y_1) = x_1 \\ \frac{dx}{dy}(y_0) = 1 & \frac{dx}{dy}(y_1) = 0 \end{cases} \tag{A.4}$$

where $y \in [y_0, y_1]$ and $x \in [x_0, x_1]$. The conditions for the other interfaces are analogous. The function of the vertical interface $x(y)$ has the first derivative equal to zero at y_1, thus it is normal to the upper edge of the domain. The first derivative at y_0 is equal to 1 because, in this way, two cells adjacent to the interface have the same dimension in the η direction.

A.1.3 Grid output

Once the boundary points for each block are defined and computed, the interior grid points can be obtained through an interpolation method. It is used a two dimensional multivariate interpolation method because it has the advantage that the boundary points are not changed; this is an essential requirement for a multi-block grid. The drawback is that undesired grid overlapping can be obtained when the interior points are computed. In this case, it is necessary to work on the points distribution and the interfaces shape. The freedom provided by the coordinates distribution becomes essential to obtain an accurate mesh. For example, if the domain is large, the vertical interface shape tends to create an overlapping grid. The solution is to apply the vertical interface function to a limited zone with a relatively small height and then use a vertical line that connects the interface extreme with the domain upper edge (Figure 3.1).

A.2 Numerical methods

A.2.1 Boundary compact finite difference scheme

The use of Fourier analysis to characterise the errors of differencing schemes is a standard technique. It provides an effective way to quantify the resolution characteristics of differencing approximations. Considering a periodic domain $[0, L]$,

the dependent variable $f(x)$ can be decomposed into its Fourier coefficients as

$$f(x) = \sum_{k=-N/2}^{k=N/2} \hat{f}_k \exp\left(\frac{2\pi i k x}{L}\right) \tag{A.5}$$

Introducing a scaled wavenumber $\overline{\kappa} = 2\pi k/N$

$$f(x) = \sum_{\kappa=-\pi}^{\kappa=\pi} \hat{f}_\kappa \exp(i\kappa x) \tag{A.6}$$

The domain of the scaled wavenumber $\overline{\kappa}$ is $[0, \pi]$. The exact first derivative generates a function with Fourier coefficients $\hat{f}'_\kappa = i\kappa\hat{f}_\kappa$, whereas central finite difference schemes give $(\overline{f}'_\kappa)_{FD} = i\overline{\kappa}\hat{f}_\kappa$. Each finite difference approximation corresponds to a particular function $\overline{\kappa}(\kappa)$. The range of wavenumbers where the modified wavenumber approximates the exact differentiation within a specified error tolerance defines the set of well resolved waves. The schemes defined by Equation 3.20 correspond to

$$\overline{\kappa}(\kappa) = \frac{2\sum_{m=1}^{3} a_m \sin m\kappa}{1 + 2\alpha\cos\kappa + 2\beta\cos 2\kappa} \tag{A.7}$$

This equation imposes $\overline{\kappa} = 0$ where $\kappa = \pi$ regardless of the coefficients, which represents the main limitation of this approach.

When non periodic boundary conditions are imposed, a boundary scheme has to be introduced in order to compute the derivatives. In such cases, the scheme is one sided. Kim (2007) proposed an extrapolation method to perform beyond the boundaries. A spline function is devised to extrapolate the profiles of the objective function and its first derivative beyond the boundaries. This method generates a set of non central compact finite difference schemes. The spline function from a point of interest (x_i, f_i) near a boundary is defined as

$$g_i(x^*) = f_i + \sum_{m=1}^{N_A} p_m (x^*)^m + \sum_{m=1}^{N_B} [q_m \cos(\phi_m x^*) + r_m \sin(\phi_m x^*)] \tag{A.8}$$

$$g'_i(x^*) = \frac{dg_i(x^*)}{dx} = \frac{1}{\Delta x}\left[\sum_{m=1}^{N_A} m p_m (x^*)^{m-1} - \sum_{m=1}^{N_B} \phi_m [q_m \sin(\phi_m x^*) - r_m \cos(\phi_m x^*)]\right] \tag{A.9}$$

where $x^* = (x - x_i)/\Delta x$ is the non dimensional coordinate from the point of interest. The extrapolation function is a linear combination of polynomials and trigonometric series. The constants N_A and N_B represent the orders of each series. The coefficients p_m, q_m and r_m are determined to match the interior profile of the original function correctly. This allows the extrapolation to the unknown exterior profile. Finally, the control variables ϕ_m are used to optimise the scheme.

The set of non central boundary compact schemes is given by

$$\begin{cases} \overline{f}'_0 + \gamma_{01}\overline{f}'_1 + \gamma_{02}\overline{f}'_2 = \frac{1}{\Delta x}\sum_{m=0,\neq 0}^{4} b_{0m}(f_m - f_0) & i = 0 \\ \gamma_{10}\overline{f}'_0 + \overline{f}'_1 + \gamma_{12}\overline{f}'_2 + \gamma_{13}\overline{f}'_3 = \frac{1}{\Delta x}\sum_{m=0,\neq 1}^{4} b_{1m}(f_m - f_0) & i = 1 \end{cases} \tag{A.10}$$

Analogous expressions can be obtained at $i = N$ and $i = N - 1$. This formulation closes the pentadiagonal matrix system at the boundaries and maintains eighth order of formal accuracy as well as five-point stencil. The coefficients are obtained with an optimisation procedure based on the Fourier analysis of the schemes. The optimisation objective is to match the real part of $\overline{\kappa}(\kappa)$ with the true wavenumber and the imaginary part with zero in the widest possible range of wavenumbers. The error is generated where these conditions are not respected. The real part represents dispersive error while the imaginary part represents dissipative error. The coefficients obtained from the optimisation are summarised in Table A.1.

coefficients	$i = 0$	$i = 1$
γ_{i0}	-	0.062416827135697
γ_{i1}	7.384981229860590	-
γ_{i2}	5.077471844790880	1.876497111557460
γ_{i3}	-	0.500665382914425
b_{i0}	-	-0.265382412479116
b_{i1}	-5.539132254744410	-
b_{i2}	8.077471844790880	0.561751444221272
b_{i3}	1.025823948263630	1.251441662981250
b_{i4}	-0.057707551244191	0.036520712981561

TABLE A.1: Coefficients of optimised boundary compact schemes

A.2.2 Boundary filter scheme

High order extrapolation is exploited to close the set of boundary filters. A set of fourth-order polynomials is used for the extrapolation near the boundary

$$\begin{cases} g(x^*) & = f_0 + \sum_{m=1}^{4} c_m (x^*)^m \\ \hat{\Delta} g(x^*) & = \hat{\Delta} f_0 + \sum_{m=1}^{4} d_m (x^*)^m \end{cases} \tag{A.11}$$

where $x^* = (x - x_0)/\Delta x$ is a dimensionless distance from the boundary. The extrapolation method brings to the following boundary closure filters

$$\begin{cases} \hat{\Delta} f_0 + \gamma_{01}\hat{\Delta} f_1 + \gamma_{02}\hat{\Delta} f_2 = \sum_{m=0,\neq 0}^{5} b_{0m}(f_m - f_0) & i = 0 \\ \gamma_{10}\hat{\Delta} f_0 + \hat{\Delta} f_1 + \gamma_{12}\hat{\Delta} f_2 + \gamma_{13}\hat{\Delta} f_3 = \sum_{m=0,\neq 1}^{5} b_{1m}(f_m - f_1) & i = 1 \\ \gamma_{20}\hat{\Delta} f_0 + \gamma_{21}\hat{\Delta} f_1 + \hat{\Delta} f_2 + \gamma_{23}\hat{\Delta} f_3 + \gamma_{24}\hat{\Delta} f_4 = \sum_{m=0,\neq 2}^{5} b_{2m}(f_m - f_2) & i = 2 \end{cases} \tag{A.12}$$

Analogous expressions can be obtained at $i = N$, $i = N-1$ and $i = N-2$. The new coefficients can be written as functions of the interior filter coefficients

$$i = 0 : \begin{cases} \gamma_{01} = \alpha C \quad \gamma_{02} = \beta C \\ C = \frac{1}{1+\alpha k_{exr}+\beta k_{exr}^2} \\ b_{01} = C[a_1 - 5R/3] \quad b_{02} = C[a_2 + 10R/21] \quad b_{03} = C[a_3 - 5R/42] \\ b_{04} = C[5R/242] \quad b_{05} = C[-R/630] \\ R = \frac{k_{exr}-1}{\log k_{exr}}[a_1 + a_3 + (k_{exr}+1)(a_2 + k_{exr}a_3)] \end{cases} \tag{A.13}$$

$$i = 1 : \begin{cases} \gamma_{10} = \alpha + \beta k_{exr} \quad \gamma_{12} = \alpha \quad \gamma_{13} = \beta \\ b_{10} = a_1 + a_2 + a_3 + 1627R/1260 \quad b_{12} = a_1 + 10R/21 \quad b_{13} = a_2 - 5R/42 \\ b_{14} = a_2 + 5R/252 \quad b_{15} = -R/630 \\ R = \frac{k_{exr}-1}{\log k_{exr}}[a_2 + a_3(k_{exr}+1)] \end{cases} \tag{A.14}$$

$$i = 2 : \begin{cases} \gamma_{20} = \beta \quad \gamma_{21} = \alpha \quad \gamma_{23} = \alpha \quad \gamma_{24} = \beta \\ b_{20} = a_2 + a_3 + 1627R/1260 \quad b_{21} = a_1 - 5R/3 \quad b_{23} = a_1 - 5R/42 \\ b_{24} = a_2 + 5R/252 \quad b_{25} = a_3 - R/630 \\ R = \frac{a_3(k_{exr}-1)}{\log k_{exr}} \end{cases} \tag{A.15}$$

where k_{exr} is a constant coefficient. The interior filter coefficients are evaluated with a local cut-off wavenumber. The weighting on the cut-off wavenumber is given by

$$\kappa_{c_i} = \begin{cases} \kappa_{c_b} & i = 0 \\ (\kappa_{c_b} - \kappa_c)[1 + \cos(2\pi/3)] + \kappa_c & i = 1 \\ (\kappa_{c_b} - \kappa_c)[1 + \cos(5\pi/6)] + \kappa_c & i = 2 \end{cases} \tag{A.16}$$

where κ_{c_b} is the cut-off wavenumber at the boundary. Kim (2010) proposed a boundary weighting which is a linear function of the interior scheme's cut-off wavenumber, while Kim and Sandberg (2012) proposed a smoother profile near the boundaries.

A.2.3 Parallelisation

The matrices introduced in Equation 3.30 can be explicitly written as

$$\mathbf{P} = \begin{bmatrix} 1 & \gamma_{01} & \gamma_{02} & \cdots & \cdots & \cdots & 0 \\ \gamma_{10} & 1 & \gamma_{12} & \gamma_{13} & \cdots & \cdots & 0 \\ \beta & \alpha & 1 & \alpha & \beta & \cdots & 0 \\ \vdots & \ddots & \ddots & \ddots & \ddots & \ddots & \vdots \\ 0 & \cdots & \beta & \alpha & 1 & \alpha & \beta \\ 0 & \cdots & \cdots & \gamma_{13} & \gamma_{12} & 1 & \gamma_{02} \\ 0 & \cdots & \cdots & \cdots & \gamma_{02} & \gamma_{01} & 1 \end{bmatrix} \tag{A.17}$$

$$\mathbf{Q} = \begin{bmatrix} b_{00} & b_{01} & b_{02} & b_{03} & b_{04} & 0 & \cdots & \cdots & 0 \\ b_{10} & b_{11} & b_{12} & b_{13} & b_{14} & 0 & \cdots & \cdots & 0 \\ -a_2 & -a_1 & 0 & a_1 & a_2 & 0 & \cdots & \cdots & 0 \\ 0 & -a_2 & -a_1 & 0 & a_1 & a_2 & 0 & \cdots & 0 \\ \vdots & \ddots & \ddots & \ddots & \ddots & \ddots & \ddots & \ddots & \vdots \\ 0 & \cdots & \cdots & -a_2 & -a_1 & 0 & a_1 & a_2 & 0 \\ 0 & \cdots & \cdots & 0 & -a_2 & -a_1 & 0 & a_1 & a_2 \\ 0 & \cdots & \cdots & 0 & -b_{14} & -b_{13} & -b_{12} & -b_{11} & -b_{10} \\ 0 & \cdots & \cdots & 0 & -b_{04} & -b_{03} & -b_{02} & -b_{01} & -b_{00} \end{bmatrix} \tag{A.18}$$

$$\mathbf{P}_F = \begin{bmatrix} 1 & \gamma_{F01} & \gamma_{F02} & 0 & \cdots & \cdots & \cdots & \cdots & 0 \\ \gamma_{F10} & 1 & \gamma_{F12} & \gamma_{F13} & 0 & \cdots & \cdots & \cdots & 0 \\ \gamma_{F20} & \gamma_{F21} & 1 & \gamma_{F23} & \gamma_{F24} & 0 & \cdots & \cdots & 0 \\ 0 & \beta_F & \alpha_F & 1 & \alpha_F & \beta_F & 0 & \cdots & 0 \\ \vdots & \ddots & \ddots & \ddots & \ddots & \ddots & \ddots & \ddots & \vdots \\ 0 & \cdots & 0 & \beta_F & \alpha_F & 1 & \alpha_F & \beta_F & 0 \\ 0 & \cdots & \cdots & 0 & \gamma_{F24} & \gamma_{F23} & 1 & \gamma_{F21} & \gamma_{F20} \\ 0 & \cdots & \cdots & \cdots & 0 & \gamma_{F13} & \gamma_{F12} & 1 & \gamma_{F10} \\ 0 & \cdots & \cdots & \cdots & \cdots & 0 & \gamma_{F02} & \gamma_{F01} & 1 \end{bmatrix} \tag{A.19}$$

$$\mathbf{Q}_F = \begin{bmatrix} b_{F00} & b_{F01} & b_{F02} & b_{F03} & b_{F04} & b_{F05} & 0 & \cdots & \cdots & \cdots & 0 \\ b_{F10} & b_{F11} & b_{F12} & b_{F13} & b_{F14} & b_{F15} & 0 & \cdots & \cdots & \cdots & 0 \\ b_{F20} & b_{F21} & b_{F22} & b_{F23} & b_{F24} & b_{F25} & 0 & \cdots & \cdots & \cdots & 0 \\ a_{F3} & a_{F2} & a_{F1} & a_{F0} & a_{F1} & a_{F2} & a_{F3} & 0 & \cdots & \cdots & 0 \\ 0 & a_{F3} & a_{F2} & a_{F1} & a_{F0} & a_{F1} & a_{F2} & a_{F3} & 0 & \cdots & 0 \\ \vdots & \ddots & \ddots & \ddots & \ddots & \ddots & \ddots & \ddots & \ddots & \ddots & \vdots \\ 0 & \cdots & 0 & a_{F3} & a_{F2} & a_{F1} & a_{F0} & a_{F1} & a_{F2} & a_{F3} & 0 \\ 0 & \cdots & \cdots & 0 & a_{F3} & a_{F2} & a_{F1} & a_{F0} & a_{F1} & a_{F2} & a_{F3} \\ 0 & \cdots & \cdots & \cdots & 0 & b_{F25} & b_{F24} & b_{F23} & b_{F22} & b_{F21} & b_{F20} \\ 0 & \cdots & \cdots & \cdots & 0 & b_{F15} & b_{F14} & b_{F13} & b_{F12} & b_{F11} & b_{F10} \\ 0 & \cdots & \cdots & \cdots & 0 & b_{F05} & b_{F04} & b_{F03} & b_{F02} & b_{F01} & b_{F00} \end{bmatrix} \tag{A.20}$$

The matrices introduced in Equation 3.31 can be written as

$$\mathbf{R} = \left[\begin{array}{ccccccc|ccccccc} 1 & \gamma_{01} & \gamma_{02} & \cdots & \cdots & \cdots & \cdots & \cdots & \cdots & \cdots & \cdots & \cdots & \cdots & 0 \\ \gamma_{10} & 1 & \gamma_{12} & \gamma_{13} & \cdots & \cdots & \cdots & \cdots & \cdots & \cdots & \cdots & \cdots & \cdots & 0 \\ \beta & \alpha & 1 & \alpha & \beta & \cdots & \cdots & \cdots & \cdots & \cdots & \cdots & \cdots & \cdots & 0 \\ \vdots & \ddots & \ddots & \ddots & \ddots & \ddots & \ddots & \ddots & \ddots & \ddots & \ddots & \ddots & \ddots & \vdots \\ 0 & \cdots & \beta & \alpha & 1 & \alpha & \beta & \cdots & \cdots & \cdots & \cdots & \cdots & \cdots & 0 \\ 0 & \cdots & \cdots & \beta & \alpha & 1 & \alpha & 0 & \cdots & \cdots & \cdots & \cdots & \cdots & 0 \\ 0 & \cdots & \cdots & \cdots & \beta & \alpha & 1 & 0 & 0 & \cdots & \cdots & \cdots & \cdots & 0 \\ \hline 0 & \cdots & \cdots & \cdots & \cdots & 0 & 0 & 1 & \alpha & \beta & \cdots & \cdots & \cdots & 0 \\ 0 & \cdots & \cdots & \cdots & \cdots & \cdots & 0 & \alpha & 1 & \alpha & \beta & \cdots & \cdots & 0 \\ 0 & \cdots & \cdots & \cdots & \cdots & \cdots & \cdots & \beta & \alpha & 1 & \alpha & \beta & \cdots & 0 \\ \vdots & \ddots & \ddots & \ddots & \ddots & \ddots & \ddots & \ddots & \ddots & \ddots & \ddots & \ddots & \ddots & \vdots \\ 0 & \cdots & \cdots & \cdots & \cdots & \cdots & \cdots & \cdots & \cdots & \beta & \alpha & 1 & \alpha & \beta \\ 0 & \cdots & \cdots & \cdots & \cdots & \cdots & \cdots & \cdots & \cdots & \cdots & \gamma_{13} & \gamma_{12} & 1 & \gamma_{10} \\ 0 & \cdots & \cdots & \cdots & \cdots & \cdots & \cdots & \cdots & \cdots & \cdots & \cdots & \gamma_{02} & \gamma_{01} & 1 \end{array}\right] \tag{A.21}$$

The same can be written for a modified matrix $\mathbf{R}_F$ of the original matrix $\mathbf{P}_F$.

A.3 Boundary conditions

The matrix $\mathbf{M}$ and its inverse can be explicitly written as

$$\mathbf{M} = \begin{bmatrix} 1 & 0 & 0 & 0 & 0 \\ u & \rho & 0 & 0 & 0 \\ v & 0 & \rho & 0 & 0 \\ w & 0 & 0 & \rho & 0 \\ \frac{u^2+v^2+w^2}{2} & \rho u & \rho v & \rho w & \frac{1}{\gamma-1} \end{bmatrix} \tag{A.22}$$

$$\mathbf{M}^{-1} = \begin{bmatrix} 1 & 0 & 0 & 0 & 0 \\ -u/\rho & 1/\rho & 0 & 0 & 0 \\ -v/\rho & 0 & 1/\rho & 0 & 0 \\ -w/\rho & 0 & 0 & 1/\rho & 0 \\ (\gamma-1)\frac{u^2+v^2+w^2}{2} & -(\gamma-1)u & -(\gamma-1)v & -(\gamma-1)w & \gamma-1 \end{bmatrix} \tag{A.23}$$

The flux jacobian matrix $\mathbf{K}'_{\xi}$ can be explicitly written as

$$\mathbf{K}'_{\xi} = \begin{bmatrix} U_{\xi} & \rho\xi_x & \rho\xi_y & \rho\xi_z & 0 \\ 0 & U_{\xi} & 0 & 0 & \xi_x/\rho \\ 0 & 0 & U_{\xi} & 0 & \xi_y/\rho \\ 0 & 0 & 0 & U_{\xi} & \xi_z/\rho \\ 0 & \rho c^2\xi_x & \rho c^2\xi_y & \rho c^2\xi_z & U_{\xi} \end{bmatrix} \tag{A.24}$$

where

$$\begin{aligned} \mathbf{U} &= [u, v, w]^T \\ \xi &= [\xi_x, \xi_y, \xi_z]^T \\ U_\xi &= \mathbf{U} \bullet \xi = u\xi_x + v\xi_y + w\xi_z \end{aligned} \tag{A.25}$$

The eigenvector matrix $\mathbf{P}$ and its inverse, introduced in Equation 3.45, are written explicitly because they will be used to impose the boundary conditions.

$$\mathbf{P} = \begin{bmatrix} \tilde{\xi}_x & \tilde{\xi}_y & \tilde{\xi}_z & 1/2 & 1/2 \\ u\tilde{\xi}_x & u\tilde{\xi}_y - c\tilde{\xi}_z & u\tilde{\xi}_z + c\tilde{\xi}_y & \frac{u+c\tilde{\xi}_x}{2} & \frac{u-c\tilde{\xi}_x}{2} \\ v\tilde{\xi}_x + c\tilde{\xi}_z & v\tilde{\xi}_y & v\tilde{\xi}_z - c\tilde{\xi}_x & \frac{v+c\tilde{\xi}_y}{2} & \frac{v-c\tilde{\xi}_y}{2} \\ w\tilde{\xi}_x - c\tilde{\xi}_y & w\tilde{\xi}_y + c\tilde{\xi}_x & w\tilde{\xi}_z & \frac{w+c\tilde{\xi}_z}{2} & \frac{w-c\tilde{\xi}_z}{2} \\ \mathbf{b} \bullet \mathbf{l}_x & \mathbf{b} \bullet \mathbf{l}_y & \mathbf{b} \bullet \mathbf{l}_z & \frac{H+c\mathbf{u}\bullet\mathbf{l}_\xi}{2} & \frac{H-c\mathbf{u}\bullet\mathbf{l}_\xi}{2} \end{bmatrix} \tag{A.26}$$

$$\mathbf{P}^{-1} = \begin{bmatrix} \mathbf{B}_o \bullet \mathbf{l}_x & \alpha u\tilde{\xi}_x & \alpha v\tilde{\xi}_x + \frac{1}{c}\tilde{\xi}_z & \alpha w\tilde{\xi}_x - \frac{1}{c}\tilde{\xi}_y & -\alpha\tilde{\xi}_x \\ \mathbf{B}_o \bullet \mathbf{l}_y & \alpha u\tilde{\xi}_y - \frac{1}{c}\tilde{\xi}_z & \alpha v\tilde{\xi}_y & \alpha w\tilde{\xi}_y + \frac{1}{c}\tilde{\xi}_x & -\alpha\tilde{\xi}_y \\ \mathbf{B}_o \bullet \mathbf{l}_z & \alpha u\tilde{\xi}_z + \frac{1}{c}\tilde{\xi}_y & \alpha v\tilde{\xi}_z - \frac{1}{c}\tilde{\xi}_x & \alpha w\tilde{\xi}_z & -\alpha\tilde{\xi}_z \\ \beta - \frac{\mathbf{u}\bullet\mathbf{l}_\xi}{C} & \mathbf{C}_+ \bullet \mathbf{l}_x & \mathbf{C}_+ \bullet \mathbf{l}_y & \mathbf{C}_+ \bullet \mathbf{l}_z & \alpha \\ \beta + \frac{\mathbf{u}\bullet\mathbf{l}_\xi}{C} & \mathbf{C}_- \bullet \mathbf{l}_x & \mathbf{C}_- \bullet \mathbf{l}_y & \mathbf{C}_- \bullet \mathbf{l}_z & \alpha \end{bmatrix} \tag{A.27}$$

where

$$\begin{gathered} \tilde{\xi} = \frac{\xi}{|\xi|} \qquad \mathbf{U} = [u, v, w]^T \qquad \delta\tilde{U}_\xi = \tilde{\xi}_x\delta u + \tilde{\xi}_y\delta v + \tilde{\xi}_z\delta w \\ \mathbf{l}_x = [1,0,0]^T \qquad \mathbf{l}_y = [0,1,0]^T \qquad \mathbf{l}_z = [0,0,1]^T \qquad \mathbf{l}_\xi = [\tilde{\xi}_x, \tilde{\xi}_y, \tilde{\xi}_z]^T \\ \mathbf{b} = \left(\frac{\mathbf{u}^2}{2}\right)\mathbf{l}_\xi + c(\mathbf{u} \times \mathbf{l}_\xi) \qquad H = h + \frac{\mathbf{u}^2}{2} \qquad h = \frac{c^2}{\gamma - 1} \\ \mathbf{B}_o = (1-\beta)\mathbf{l}_\xi - \frac{\mathbf{u} \times \mathbf{l}_\xi}{c} \qquad \mathbf{C}_\pm = \pm\frac{\mathbf{l}_\xi}{c} - \alpha\mathbf{u} \qquad \alpha = \frac{\gamma - 1}{c^2} \qquad \beta = \frac{\gamma - 1}{2}M^2 \end{gathered} \tag{A.28}$$

The matrix $\mathbf{R}$, introduced in Equation 3.50, is given by

$$\delta\mathbf{R} = \begin{bmatrix} \tilde{\xi}_x(\delta\rho - \delta p/c^2) + \delta\tilde{\theta}_1 \\ \tilde{\xi}_y(\delta\rho - \delta p/c^2) + \delta\tilde{\theta}_2 \\ \tilde{\xi}_z(\delta\rho - \delta p/c^2) + \delta\tilde{\theta}_3 \\ \delta p/\rho c + \delta\tilde{U}_\xi \\ \delta p/\rho c - \delta\tilde{U}_\xi \end{bmatrix} \tag{A.29}$$

where

$$\begin{aligned} \delta\tilde{\theta}_1 &= \tilde{\xi}_z\delta v - \tilde{\xi}_y\delta w \\ \delta\tilde{\theta}_2 &= -\tilde{\xi}_z\delta u - \tilde{\xi}_x\delta w \\ \delta\tilde{\theta}_3 &= \tilde{\xi}_y\delta u - \tilde{\xi}_x\delta v \end{aligned} \tag{A.30}$$

A.3.1 Non reflective condition

For a subsonic exit plane, four characteristic waves L_1, L_2, L_3 and L_4 leave the computational domain while L_5 enters it. An inviscid boundary condition would generate reflected waves. It is necessary to use only non reflective boundary conditions to avoid this kind of reflections. The non reflective conditions should allow the acoustic waves to radiate through the boundary and they should make the mean flow information feed back from the far field because a subsonic flow is considered. The CBCs method applied to N-S equations allows a non reflective treatment for boundaries which is exact for one dimensional problems and remains well posed for multi-dimensional cases. In multi-dimensional cases the condition is not exact, thus waves which do not reach the boundary at normal incidence are not perfectly transmitted.

The non reflective outflow condition when $u > 0$ and $\xi = \xi_{max}$ can be written as

$$L_5^* = R \tag{A.31}$$

where R can be equal to zero as proposed by Thompson (1987, 1990). In this case, the condition shows ill-posed effects in the whole domain after long time calculation. Alternatively, some physical information on mean static pressure can be added to the set of outflow boundary conditions so that the problem remains well posed.

$$R = K\frac{p - p_\infty}{\rho c} \tag{A.32}$$

where K is defined as

$$K = \sigma_{ref}(1 - M_\infty^2)\frac{c}{l} \tag{A.33}$$

M_∞ is the free stream Mach number. This condition does not fix any of the dependent variables, it is used to obtain the amplitude variation of the incoming wave L_5. On the other hand, the non reflective condition when $u < 0$ and $\xi = 0$ imposes $L_4^* = R$.

The correction term can be written as

$$\frac{\mathbf{P}}{J}(\mathbf{L}^* - \mathbf{L}) = C_R \begin{bmatrix} 1 \\ u + fc\tilde{\xi}_x \\ v + fc\tilde{\xi}_y \\ w + fc\tilde{\xi}_z \\ \frac{c^2}{\gamma - 1} + fc\mathbf{l}_{\tilde{\xi}} \bullet \mathbf{u} + \frac{|\mathbf{u}|^2}{2} \end{bmatrix} \tag{A.34}$$

where C_R is a scalar constant given by

$$C_R = \frac{f}{2c^2}\left[D_1 c^2\left(f\frac{\gamma-1}{2}M^2 - \frac{\mathbf{l}_\xi \bullet \mathbf{u}}{c}\right) - \mathbf{D_{234}} \bullet (c\mathbf{l}_\xi - f(\gamma-1)\mathbf{u}) - fD_5(\gamma-1)\right] + \frac{R}{2} \tag{A.35}$$

$\mathbf{D_{234}} = [D_2, D_3, D_4]$ and

$$f = \begin{cases} +1 & L_4^* = R \\ -1 & L_5^* = R \end{cases}$$

Equation A.34 allows to avoid the standard procedure for GCBCs and to directly correct the characteristic convection term. This means that the matrix multiplications are avoided and the number of mathematical operations decreases.

A.3.2 Wall condition

An inviscid wall shows no penetration of flow imposing the slip condition. This implies that the contravariant velocity normal to the wall is zero or it is given by a function of space and time if the wall behaves as an acoustic source. When the wall pulsates acoustically, the time derivative of the normal velocity $d\tilde{U}/dt$ should be also specified on the wall, where $\delta\tilde{U} = \tilde{\xi}_x\delta u + \tilde{\xi}_y\delta v + \tilde{\xi}_z\delta w$.

For the left-sided wall, L_4 is the incoming wave and L_5 is the outgoing wave, thus the condition can be written as

$$L_4^* = L_5 - 2\frac{d\tilde{U}}{dt}\bigg|_{wall} \tag{A.36}$$

For the right-sided wall, L_5 is the incoming wave and L_4 is the outgoing wave, thus the condition is given by

$$L_5^* = L_4 + 2\frac{d\tilde{U}}{dt}\bigg|_{wall} \tag{A.37}$$

where the wall pulsation term is zero if the wall is stationary.

The wall conditions are formulated using true multidimensionality as proposed by Kim and Lee (2004). The LODI approximation sets the source term in Equation 3.51 equal to zero, but this approach has led to a lack of multidimensionality because the transverse terms are not included. For this reason, convective and viscous fluxes are included inside vector $\hat{\mathbf{D}}$.

The correction term is given by

$$\frac{\mathbf{P}}{J}(\mathbf{L}^* - \mathbf{L}) = C_W \begin{bmatrix} 1 \\ u + fc\tilde{\xi}_x \\ v + fc\tilde{\xi}_y \\ w + fc\tilde{\xi}_z \\ \frac{c^2}{\gamma-1} + fc\mathbf{l}_{\tilde{\xi}} \bullet \mathbf{u} + \frac{|\mathbf{u}|^2}{2} \end{bmatrix} \tag{A.38}$$

where

$$C_W = \frac{f}{c}\left[-\frac{c}{J}\frac{d\tilde{U}}{dt} - \mathbf{D_{234}} \bullet \mathbf{l}_{\tilde{\xi}} + D_1 \mathbf{l}_{\tilde{\xi}} \bullet \mathbf{u}\right] \tag{A.39}$$

and

$$f = \begin{cases} +1 & \text{left-sided wall} \\ -1 & \text{right-sided wall} \end{cases}$$

It is interesting to note that the correction term is given by the same vector for the non reflective outflow conditions and the wall conditions. The difference is the scalar that multiplies the vector and that incorporates the conditions.

A.3.3 Characteristic interface condition

The presence of a body inside the computational domain can generate grid singularities that bring spurious oscillations inside the domain. The grid singularities can be identified where the grid metrics derivatives are not unique because of shared block boundaries. The shared block boundaries are referred as block interface boundaries and they can be constant ξ interfaces or constant η interfaces. It is considered the constant ξ interface in this section. The boundary scheme isolates the blocks not allowing the information to flow. Thus, the interface boundary condition has to be imposed. The discontinuity can be written in terms of the metrics gradient as

$$\nabla\xi^L \neq \nabla\xi^R \tag{A.40}$$

The norm of the gradient is different but the direction is the same because both blocks share the same direction

$$\nabla\tilde{\xi}^L = \nabla\tilde{\xi}^R \tag{A.41}$$

where $\nabla\tilde{\xi}^L = \frac{\nabla\xi^L}{|\nabla\xi^L|}$ and $\nabla\tilde{\xi}^R = \frac{\nabla\xi^R}{|\nabla\xi^R|}$. Peers et al. (2010) proposed that also the characteristic variables time derivatives should match at the interface

$$\frac{\partial \mathbf{R}^L}{\partial t} = \frac{\partial \mathbf{R}^R}{\partial t} \tag{A.42}$$

The condition for the block interface boundaries can be written as

$$\mathbf{L}^L = \mathbf{L}^R \tag{A.43}$$

where $\hat{\mathbf{D}}$ is defined as in the wall condition.

The sign of the convection speeds determines if a wave is entering or exiting a block. The incoming wave of one block is also the exiting wave of the adjacent block. As a consequence, both the incoming and outgoing waves can be obtained from the interior values of the blocks. Every block evaluates the outgoing waves, while the incoming waves are obtained by the outgoing waves of the adjacent block.

$$\begin{cases} L_i^{L^*} = L_i^R & \frac{\lambda_i^L}{|\lambda_i^L|} = \frac{\lambda_i^R}{|\lambda_i^R|} \leq 0 \\ L_i^{R^*} = L_i^L & \frac{\lambda_i^L}{|\lambda_i^L|} = \frac{\lambda_i^R}{|\lambda_i^R|} \geq 0 \end{cases} \quad \text{for i=1,...,5} \tag{A.44}$$

This condition is imposed using matrix multiplication because the final expression of the correction term is not convenient as in the previous cases.

A.3.4 Interface condition using halo points

When the grid is not modified by the presence of a body, the singularities problem is avoided and it is not necessary to impose characteristic interface conditions (CICs). In this case the quasi-disjoint systems are solved in each subdomain inside each block. The only difference is the communication between subdomains at the blocks boundary. In the parallelisation explained previously, two adjacent subdomains are completely separated because they are in the same block, thus the boundary points of the first subdomain are adjacent to the boundary points of the second subdomain. In this case, the boundary points of the first subdomain are coincident with the boundary points of the second subdomain because they are the boundary points of the blocks. The condition requires communication of the halo points without a specific treatment at the boundary.

A.4 Zonal characteristic boundary conditions

Zonal CBC method extends the characteristic analysis inside a zone. This is done because when the CBCs are applied at the boundary, the condition on the amplitude of the incoming characteristic is discontinuous with respect to the values of the amplitude inside the domain. The method allows to impose the condition smoothly inside the zone and decrease the reflections at the boundary. This technique, as the sponge layer one, divides the computational domain into a physical and a non physical region where the BCs are applied.

Sandberg and Sandham (2006) proposed a formulation of the zonal CBCs that does not take into account the physics of the problem. Poinsot and Lele (1992) explained that the exact value of the incoming characteristic wave should also be taken into account at the boundary. For a subsonic non reflecting outflow

$$L_5 = K(p - p_\infty) + L_5^{exact} \tag{A.45}$$

The second term ensures an accurate matching of derivatives between both sides of the boundary while the first term keeps the mean value around p_∞. Since most of the problems are too complicated to find an exact value, L_5^{exact} is usually set to zero. In this case, the condition at the boundary is set equal to an expected value of the incoming characteristic wave

$$L_i^* = g(x)L_i + [1 - g(x)]L_i^{ex} \quad i = 4, 5 \tag{A.46}$$

where L_i^{ex} is the expected value and $g(x)$ is a ramping function. The amplitude of the incoming wave is initially damped and it is not imposed equal to zero at the boundary, but equal to the expected value which is closer to the exact one. The issue is the evaluation of the expected value.

The practical implementation can be divided in three main steps that have to be applied every time step.

- First of all, it is necessary to evaluate and save L_i in a plane.
- After that, the value saved at $t - \Delta T$ is imposed inside the zone. The time shift ΔT is a function of space, thus considering a point with coordinates (x, y) at time t, the time shift is
$$\Delta T = t - \frac{L_{zr} - (x_{max} - x)}{u_\infty} \tag{A.47}$$
- Finally, the characteristic boundary conditions are applied inside the zone. The value of the parameter C_R is given by
$$\begin{aligned} C_R = -f\frac{g(x) - 1}{2c^2}\Bigg[D_1 c^2 \left(f\frac{\gamma - 1}{2}M^2 - \frac{\mathbf{l}_\xi \bullet \mathbf{u}}{c} \right) - \\ \mathbf{D_{234}} \bullet (c\mathbf{l}_\xi - f(\gamma - 1)\mathbf{u}) - fD_5(\gamma - 1) \Bigg] + \frac{L_5^{ex}}{2} \end{aligned} \tag{A.48}$$
where L_5^{ex} is the expected value. In this method the parameter C_R is both a function of space with the damping function $g(x)$ and a function of time with the expected amplitude of the incoming wave.

Figure A.1 presents a 1D reference of the method. The red dot is the border of the zone, where the value of L_5 is saved at each time step. The black dots are inside the zone, where the second and third steps are applied. The proposed method works if

the expected value is accurately calculated, thus if the zone is thin because otherwise the characteristics of the flow would change.

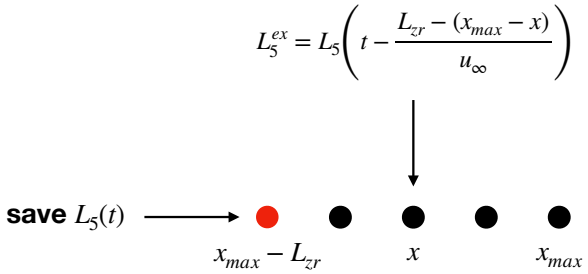

FIGURE A.1: Sketch of the one dimensional zonal CBC method.

References

M Alam and ND Sandham. Direct numerical simulation of short laminar separation bubbles with turbulent reattachment. *Journal of Fluid Mechanics*, 410:1–28, 2000.

AE Alving and HH Fernholz. Turbulence measurements around a mild separation bubble and downstream of reattachment. *Journal of Fluid Mechanics*, 322:297–328, 1996.

A Asghar, RE Perez, and M Ferchichi. Effect of leading edge tubercles on transonic performance of airfoils. In *35th AIAA Applied Aerodynamics Conference*, page 3402, 2017.

M Bernardini, S Pirozzoli, and F Grasso. The wall pressure signature of transonic shock/boundary layer interaction. *Journal of Fluid Mechanics*, 671:288–312, 2011.

J Birkemeyer, H Rosemann, and E Stanewsky. Shock control on a swept wing. *Aerospace Science and Technology*, 4(3):147–156, 2000.

V Brion, J Dandois, JC Abart, and P Paillart. Experimental analysis of the shock dynamics on a transonic laminar airfoil. *Progress in Flight Physics–Volume 9*, 9: 365–386, 2017.

PJK Bruce and H Babinsky. Experimental study into the flow physics of three-dimensional shock control bumps. *Journal of Aircraft*, 49(5):1222–1233, 2012.

PJK Bruce and SP Colliss. Review of research into shock control bumps. *Shock Waves*, 25(5):451–471, 2015.

P Chaitanya, P Joseph, S Narayanan, C Vanderwel, J Turner, JW Kim, and B Ganapathisubramani. Performance and mechanism of sinusoidal leading edge serrations for the reduction of turbulence–aerofoil interaction noise. *Journal of Fluid Mechanics*, 818:435–464, 2017.

TP Chong, A Vathylakis, A McEwen, F Kemsley, C Muhammad, and S Siddiqi. Aeroacoustic and aerodynamic performances of an aerofoil subjected to sinusoidal leading edges. In *21st AIAA/CEAS Aeroacoustics Conference*, page 2200, 2015.

SP Colliss, H Babinsky, K Nübler, and T Lutz. Vortical structures on three-dimensional shock control bumps. *AIAA Journal*, pages 2338–2350, 2016.

JD Crouch, A Garbaruk, D Magidov, and A Travin. Origin of transonic buffet on aerofoils. *Journal of fluid mechanics*, 628:357–369, 2009.

JD Crouch, A Garbaruk, and M Strelets. Global instability analysis of unswept- and swept-wing transonic buffet onset. In *2018 Fluid Dynamics Conference*, page 3229, 2018.

D Custodio, CW Henoch, and H Johari. Aerodynamic characteristics of finite span wings with leading-edge protuberances. *AIAA Journal*, 53(7):1878–1893, 2015.

J Dandois, P Molton, A Lepage, A Geeraert, V Brunet, JB Dor, and E Coustols. Buffet characterization and control for turbulent wings. *AerospaceLab*, (6):p–1, 2013.

J Dandois, I Mary, and V Brion. Large-eddy simulation of laminar transonic buffet. *Journal of Fluid Mechanics*, 850:156–178, 2018a.

J Dandois, I Mary, and V Brion. Large-eddy simulation of laminar transonic buffet. *Journal of Fluid Mechanics*, 850:156178, 2018b. .

JM Delery. Experimental investigation of turbulence properties in transonic shock/boundary-layer interactions. *AIAA journal*, 21(2):180–185, 1983.

JM Delery. Shock wave/turbulent boundary layer interaction and its control. *Progress in Aerospace Sciences*, 22(4):209–280, 1985.

P Dupont, C Haddad, and JF Debieve. Space and time organization in a shock-induced separated boundary layer. *Journal of Fluid Mechanics*, 559:255–277, 2006.

T Fan, Q Weiyang, C Weijie, H Cheng, W Renke, and W Xunnian. Numerical analysis of broadband noise reduction with wavy leading edge. *Chinese Journal of Aeronautics*, 31(7):1489–1505, 2018.

J Favier, A Pinelli, and U Piomelli. Control of the separated flow around an airfoil using a wavy leading edge inspired by humpback whale flippers. *Comptes Rendus Mecanique*, 340(1-2):107–114, 2012.

GB Filho, AL Da Costa, AA De Paula, and GR De Lima. A numerical investigation of the wavy leading edge phenomena at transonic regime. In *2018 AIAA Aerospace Sciences Meeting*, page 0317, 2018.

M Franciolini, A Da Ronch, J Drofelnik, DE Raveh, and A Crivellini. Efficient infinite-swept wing solver for steady and unsteady compressible flows. *Aerospace Science and Technology*, 72:217–229, 2018.

C Gao, W Zhang, and Z Ye. Numerical study on closed-loop control of transonic buffet suppression by trailing edge flap. *Computers & Fluids*, 132:32–45, 2016.

DJ Garmann, MR Visbal, and PD Orkwis. Comparative study of implicit and subgrid-scale model large-eddy simulation techniques for low-reynolds number airfoil applications. *International Journal for Numerical Methods in Fluids*, 71(12): 1546–1565, 2013.

IE Garrick and CE Watkins. A theoretical study of the effect of forward speed on the free-space sound-pressure field around propellers. 1953.

F Gea Aguilera, JR Gill, D Angland, and X Zhang. Wavy leading edge airfoils interacting with anisotropic turbulence. In *23rd AIAA/CEAS Aeroacoustics Conference*, page 3370, 2017.

MBR Gelot and JW Kim. Effect of serrated trailing edges on aerofoil tonal noise. *Journal of Fluid Mechanics*, 2020.

NF Giannelis, GA Vio, and O Levinski. A review of recent developments in the understanding of transonic shock buffet. *Progress in Aerospace Sciences*, 92:39–84, 2017.

KL Hansen, RM Kelso, and BB Dally. The effect of leading edge tubercle geometry on the performance of different airfoils. In *7th World Conference on Experimental Heat Transfer, Fluid Mechanics and Termodynamics*, 2009.

KL Hansen, RM Kelso, and C Doolan. Reduction of flow induced tonal noise through leading edge tubercle modifications. In *16th AIAA/CEAS Aeroacoustics Conference*, page 3700, 2010.

KL Hansen, N Rostamzadeh, RM Kelso, and BB Dally. Evolution of the streamwise vortices generated between leading edge tubercles. *Journal of Fluid Mechanics*, 788: 730–766, 2016.

A Hartmann, A Feldhusen, and W Schröder. On the interaction of shock waves and sound waves in transonic buffet flow. *Physics of Fluids*, 25(2):026101, 2013.

KA Hoffmann and ST Chiang. *Computational Fluid Dynamics*, volume 2. Engineering Education System, 4th edition, 2000.

HA Holden and H Babinsky. Effect of microvortex generators on separated normal shock/boundary layer interactions. *Journal of Aircraft*, 44(1):170–174, 2007.

J Huang, Z Xiao, J Liu, and S Fu. Simulation of shock wave buffet and its suppression on an oat15a supercritical airfoil by iddes. *Science China Physics, Mechanics and Astronomy*, 55(2):260–271, 2012.

M Iovnovich and DE Raveh. Transonic unsteady aerodynamics in the vicinity of shock-buffet instability. *Journal of Fluids and Structures*, 29:131–142, 2012.

A Jameson, W Schmidt, and E Turkel. Numerical solution of the euler equations by finite volume methods using runge kutta time stepping schemes. In *14th fluid and plasma dynamics conference*, page 1259, 1981.

LE Jones, RD Sandberg, and ND Sandham. Stability and receptivity characteristics of a laminar separation bubble on an aerofoil. *Journal of Fluid Mechanics*, 648:257–296, 2010.

JW Kim. Optimised boundary compact finite difference schemes for computational aeroacoustics. *Journal of Computational Physics*, 225(1):995–1019, 2007.

JW Kim. High-order compact filters with variable cut-off wavenumber and stable boundary treatment. *Computers & Fluids*, 39(7):1168–1182, 2010.

JW Kim. Quasi-disjoint pentadiagonal matrix systems for the parallelization of compact finite-difference schemes and filters. *Journal of Computational Physics*, 241: 168–194, 2013.

JW Kim and DJ Lee. Generalized characteristic boundary conditions for computational aeroacoustics. *AIAA journal*, 38(11):2040–2049, 2000.

JW Kim and DJ Lee. Adaptive nonlinear artificial dissipation model for computational aeroacoustics. *AIAA journal*, 39(5):810–818, 2001.

JW Kim and DJ Lee. Generalized characteristic boundary conditions for computational aeroacoustics, part 2. *AIAA journal*, 42(1):47–55, 2004.

JW Kim and RD Sandberg. Efficient parallel computing with a compact finite difference scheme. *Computers & Fluids*, 58:70–87, 2012.

JW Kim, ASH Lau, and ND Sandham. Caa boundary conditions for airfoil noise due to high-frequency gusts. *Procedia Engineering*, 6:244–253, 2010a.

JW Kim, ASH Lau, and ND Sandham. Proposed boundary conditions for gust-airfoil interaction noise. *AIAA journal*, 48(11):2705–2710, 2010b.

JW Kim, S Haeri, and PF Joseph. On the reduction of aerofoil–turbulence interaction noise associated with wavy leading edges. *Journal of Fluid Mechanics*, 792:526–552, 2016.

M Kiya and K Sasaki. Structure of a turbulent separation bubble. *Journal of Fluid Mechanics*, 137:83–113, 1983.

M Kiya and K Sasaki. Structure of large-scale vortices and unsteady reverse flow in the reattaching zone of a turbulent separation bubble. *Journal of Fluid Mechanics*, 154: 463–491, 1985.

B König, M Pätzold, T Lutz, E Krämer, H Rosemann, K Richter, and H Uhlemann. Numerical and experimental validation of three-dimensional shock control bumps. *Journal of Aircraft*, 46(2):675–682, 2009.

ASH Lau and JW Kim. The effects of wavy leading edges on airfoil-gust interaction noise. In *19th AIAA/CEAS Aeroacoustics Conference*, page 2120, 2013.

BHK Lee. Self-sustained shock oscillations on airfoils at transonic speeds. *Progress in Aerospace Sciences*, 37(2):147–196, 2001.

SK Lele. Compact finite difference schemes with spectral-like resolution. *Journal of computational physics*, 103(1):16–42, 1992.

JL Lumley. The structure of inhomogeneous turbulent flows. *Atmospheric turbulence and radio wave propagation*, 1967.

O Marxen, U Rist, and S Wagner. Effect of spanwise-modulated disturbances on transition in a separated boundary layer. *AIAA journal*, 42(5):937–944, 2004.

R Mayer, T Lutz, E Krämer, and J Dandois. Control of transonic buffet by shock control bumps on wing-body configuration. *Journal of Aircraft*, pages 1–13, 2019.

P Molton, J Dandois, A Lepage, V Brunet, and R Bur. Control of buffet phenomenon on a transonic swept wing. *AIAA journal*, 51(4):761–772, 2013.

Y Na and P Moin. Direct numerical simulation of a separated turbulent boundary layer. *Journal of Fluid Mechanics*, 374:379–405, 1998.

S Narayanan, P Chaitanya, S Haeri, P Joseph, JW Kim, and C Polacsek. Airfoil noise reductions through leading edge serrations. *Physics of Fluids*, 27(2):025109, 2015.

H Ogawa, H Babinsky, M Pätzold, and T Lutz. Shock-wave/boundary-layer interaction control using three-dimensional bumps for transonic wings. *AIAA journal*, 46(6):1442–1452, 2008.

Y Ohmichi, T Ishida, and A Hashimoto. Modal decomposition analysis of three-dimensional transonic buffet phenomenon on a swept wing. *AIAA Journal*, 56 (10):3938–3950, 2018.

LL Pauley. Response of two-dimensional separation to three-dimensional disturbances. *Journal of fluids engineering*, 116(3):433–438, 1994.

E Peers, X Zhang, and JW Kim. Patched characteristic interface condition for high-order multiblock aeroacoustic computation. *AIAA journal*, 48(11):2512–2522, 2010.

R Perez Torro. *A Numerical Study on the Unsteady Aerodynamic Characteristics of Thick Aerofoils with Wavy Leading Edges*. PhD thesis, University of Southampton, 2015.

R Perez Torro and JW Kim. A large-eddy simulation on a deep-stalled aerofoil with a wavy leading edge. *Journal of Fluid Mechanics*, 813:23–52, 2017.

S Pirozzoli, M Bernardini, and F Grasso. Direct numerical simulation of transonic shock/boundary layer interaction under conditions of incipient separation. *Journal of Fluid Mechanics*, 657:361–393, 2010.

F Plante, J Dandois, and É Laurendeau. Similitude between 3d cellular patterns in transonic buffet and subsonic stall. In *AIAA Scitech 2019 Forum*, page 0300, 2019.

TJ Poinsot and SK Lele. Boundary conditions for direct simulations of compressible viscous flows. *Journal of computational physics*, 101(1):104–129, 1992.

S Pröbsting and S Yarusevych. Laminar separation bubble development on an airfoil emitting tonal noise. *Journal of Fluid Mechanics*, 780:167–191, 2015.

S Raghunathan, JM Early, C Tulita, E Bénard, and J Quest. Periodic transonic flow and control. *The Aeronautical Journal*, 112(1127):1–16, 2008.

N Rostamzadeh, KL Hansen, RM Kelso, and BB Dally. The formation mechanism and impact of streamwise vortices on naca 0021 airfoil's performance with undulating leading edge modification. *Physics of Fluids*, 26(10):107101, 2014.

N Rostamzadeh, RM Kelso, and BB Dally. A numerical investigation into the effects of reynolds number on the flow mechanism induced by a tubercled leading edge. *Theoretical and Computational Fluid Dynamics*, 31(1):1–32, 2017.

M Rybalko, H Babinsky, and E Loth. Vortex generators for a normal shock/boundary layer interaction with a downstream diffuser. *Journal of Propulsion and Power*, 28(1): 71–82, 2012.

RD Sandberg and ND Sandham. Nonreflecting zonal characteristic boundary condition for direct numerical simulation of aerodynamic sound. *AIAA journal*, 44 (2):402–405, 2006.

F Sartor, G Losfeld, and R Bur. Piv study on a shock-induced separation in a transonic flow. *Experiments in fluids*, 53(3):815–827, 2012.

F Sartor, C Mettot, and D Sipp. Stability, receptivity, and sensitivity analyses of buffeting transonic flow over a profile. *AIAA Journal*, 53(7):1980–1993, 2014.

PJ Schmid. Dynamic mode decomposition of numerical and experimental data. *Journal of fluid mechanics*, 656:5–28, 2010.

TK Sengupta, A Dipankar, and AK Rao. A new compact scheme for parallel computing using domain decomposition. *Journal of Computational Physics*, 220(2): 654–677, 2007.

D Serson, JR Meneghini, and SJ Sherwin. Direct numerical simulations of the flow around wings with spanwise waviness at a very low reynolds number. *Computers & Fluids*, 146:117–124, 2017.

L Siconolfi, S Camarri, and JHM Fransson. Boundary layer stabilization using free-stream vortices. *Journal of Fluid Mechanics*, 764, 2015.

M Sieber, CO Paschereit, and K Oberleithner. Spectral proper orthogonal decomposition. *Journal of Fluid Mechanics*, 792:798–828, 2016.

A Skillen, A Revell, A Pinelli, U Piomelli, and J Favier. Flow over a wing with leading-edge undulations. *AIAA Journal*, 53(2):464–472, 2015.

M Skote and DS Henningson. Direct numerical simulation of a separated turbulent boundary layer. *Journal of Fluid Mechanics*, 471:107–136, 2002.

LJ Souverein, P Dupont, JF Debiève, BW Van Oudheusden, and F Scarano. Effect of interaction strength on unsteadiness in shock-wave-induced separations. *AIAA journal*, 48(7):1480–1493, 2010.

E Stanewsky, J Délery, J Fulker, and W Geißler. *EUROSHOCK-Drag Reduction by Passive Shock Control: Results of the Project EUROSHOCK, AER2-CT92-0049 Supported by the European Union, 1993–1995*, volume 56. Springer Science & Business Media, 2013.

D Szubert, F Grossi, AJ Garcia, Y Hoarau, JCR Hunt, and M Braza. Shock-vortex shear-layer interaction in the transonic flow around a supercritical airfoil at high reynolds number in buffet conditions. *Journal of Fluids and Structures*, 55:276–302, 2015.

D Szubert, I Asproulias, F Grossi, R Duvigneau, Y Hoarau, and M Braza. Numerical study of the turbulent transonic interaction and transition location effect involving optimisation around a supercritical aerofoil. *European Journal of Mechanics-B/Fluids*, 55:380–393, 2016.

CKW Tam. Computational aeroacoustics-issues and methods. *AIAA journal*, 33(10): 1788–1796, 1995.

KW Thompson. Time dependent boundary conditions for hyperbolic systems. *Journal of computational physics*, 68(1):1–24, 1987.

KW Thompson. Time-dependent boundary conditions for hyperbolic systems, ii. *Journal of computational physics*, 89(2):439–461, 1990.

N Titchener and H Babinsky. Shock wave/boundary-layer interaction control using a combination of vortex generators and bleed. *AIAA journal*, 51(5):1221–1233, 2013.

E Touber and ND Sandham. Large-eddy simulation of low-frequency unsteadiness in a turbulent shock-induced separation bubble. *Theoretical and Computational Fluid Dynamics*, 23(2):79–107, 2009.

JM Turner. *Aerodynamic noise from undulated leading edge aerofoils*. PhD thesis, University of Southampton, 2019.

JM Turner and JW Kim. Aeroacoustic source mechanisms of a wavy leading edge undergoing vortical disturbances. *Journal of Fluid Mechanics*, 811:582–611, 2017.

JM Turner and JW Kim. Aerofoil dipole noise due to flow separation and stall at a low reynolds number. *International Journal of Heat and Fluid Flow*, 86:108715, 2020a.

JM Turner and JW Kim. Effect of spanwise domain size on direct numerical simulations of airfoil noise during flow separation and stall. *Physics of Fluids*, 32(6): 065103, 2020b.

JM Turner and JW Kim. Trailing-edge noise generation from a flat-plate aerofoil interacting with a prescribed vortex. *Journal of Sound and Vibration*, page 115654, 2020c.

JH Watmuff. Evolution of a wave packet into vortex loops in a laminar separation bubble. *Journal of Fluid Mechanics*, 397:119–169, 1999.

JEF Williams and DL Hawkings. Sound generation by turbulence and surfaces in arbitrary motion. *Philosophical Transactions for the Royal Society of London. Series A, Mathematical and Physical Sciences*, pages 321–342, 1969.

C Wollblad, L Davidson, and LE Eriksson. Large eddy simulation of transonic flow with shock wave/turbulent boundary layer interaction. *AIAA journal*, 44(10): 2340–2353, 2006.

WS Wong, N Qin, N Sellars, H Holden, and H Babinsky. A combined experimental and numerical study of flow structures over three-dimensional shock control bumps. *Aerospace Science and Technology*, 12(6):436–447, 2008.

S Yarusevych, PE Sullivan, and JG Kawall. On vortex shedding from an airfoil in low-reynolds-number flows. *Journal of Fluid Mechanics*, 632:245–271, 2009.

HS Yoon, PA Hung, JH Jung, and MC Kim. Effect of the wavy leading edge on hydrodynamic characteristics for flow around low aspect ratio wing. *Computers & Fluids*, 49(1):276–289, 2011.

M Zauner. *Direct numerical simulation and stability analysis of transonic flow around airfoils at moderate Reynolds numbers*. PhD thesis, University of Southampton, 2019.

M Zauner, N De Tullio, and ND Sandham. Direct numerical simulations of transonic flow around an airfoil at moderate reynolds numbers. *AIAA Journal*, 57(2):597–607, 2018a.

M Zauner, N De Tullio, and ND Sandham. Unsteady behaviour in direct numerical solutions of transonic flow around an airfoil. In *2018 Fluid Dynamics Conference*, page 2911, 2018b.